



ROYAL MILITARY ACADEMY
Polytechnical Faculty
Department of Ballistics and Weapon Systems
Department of Mechanical Engineering

UNIVERSITY OF LIÈGE
Department of Aerospace and Mechanical Engineering

**SMALL-CALIBER EXTERIOR BALLISTICS:
AERODYNAMIC COEFFICIENTS DETERMINATION BY CFD**

Thesis presented by Véronique de Briey in order to obtain
the Ph.D. Degree in "Applied Sciences", Royal Military Academy
and in "Engineering Sciences & Technology", University of Liège.

Co-directors :

Prof. Dr. Ir. Marc Pirlot, Royal Military Academy
Prof. Dr. Ir. Jean-Philippe Ponthot, University of Liège
Prof. Dr. Ir. Benoit G. Marinus, Royal Military Academy

Evaluation Committee:

Prof. Dr. Ir. Vincent Terrapon, University of Liège
Dr. Ir. Ana Ferreira, Royal Military Academy
ICM Pierre Wey, French-German Research Institute of Saint-Louis
Ir. Philippe Drapela, armasuisse Sciences & Technology

Remerciements

Je tiens tout d'abord à exprimer ma reconnaissance envers mes trois promoteurs, et en premier lieu au professeur Marc Pirlot, pour son suivi, même en dehors de son expertise "de confort", son soutien et sa confiance, si précieuse à mes yeux. Ce travail aura été une de ses dernières pierres à l'édifice de sa carrière et j'espère avoir pu lui apporter la satisfaction attendue. De par sa personnalité pour le moins surprenante et charismatique, mais aussi très humaine et terre à terre, il est pour moi un très bel exemple à suivre. J'en profite d'ailleurs pour le remercier pour sa gestion du département de balistique et son soutien bienveillant au sein de notre école.

Ensuite, je n'en serais pas là sans la présence du Major Benoit Marinus. Je le remercie d'abord pour sa disponibilité, sa patience et sa rigueur, ainsi que pour ses debuggages, tant au niveau software que hardware, mais surtout pour les nombreuses réflexions partagées qui m'ont fait avancer et apprécier ce que je faisais. Ce fut un réel plaisir de travailler avec lui, ainsi qu'un véritable apprentissage, et je me réjouis d'ores et déjà des projets de collaboration à venir.

Je remercie enfin mon promoteur de l'Université de Liège, le professeur Jean-Philippe Ponthot, qui m'a permis de compléter ma formation avec la partie numérique et la rencontre avec le professeur Terrapon, que je remercie au passage pour la qualité de ses cours. Le regard plus neutre du professeur Ponthot sur la balistique, associé toutefois à sa rigueur de numéricien, m'a forcée à remettre en question certaines de mes approches et je lui suis également très reconnaissante pour sa relecture méticuleuse.

Je n'oublie pas le laboratoire de balistique, avec le Cdt Jurgen Grossen que je remercie pour la disponibilité et l'énergie de sa belle équipe. Je remercie en particulier le Cdt Joeri Weckx, l'Adjt Alain Vanhove, le 1SC Gabriel Kempeneers et le 1CC Bart Verhulst, mais aussi... l'Adjt Pascal Delhaye, qui nous a quitté trop tôt mais avec qui je n'oublierai pas le plaisir de travailler, tant son enthousiasme et sa curiosité étaient toujours de la partie.

J'aimerais par ailleurs faire un clin d'oeil à la communauté du "tir longue-distance", et en particulier au Sgt Jan Tibau, pour leurs nombreuses questions pratiques qui m'ont d'une certaine façon forcée à garder les pieds sur terre et à systématiquement faire le lien entre les calculs "théoriques" et la réalité sur le terrain.

Mes pensées les plus chaleureuses reviennent enfin naturellement à mon mari Cédric, qui m'a toujours soutenue, malgré la longueur de ce parcours et mes nombreuses remises en question. A côté de sa charge professionnelle non négligeable (pardon pour l'oeuphémisme), il a (sup)porté ce qu'il pouvait -quand c'était possible- pour me soutenir un maximum. Avec lui bien sûr, ma réserve d'énergie: mes deux petits bonhommes, Cyril & Axel, qui m'ont rendue fière de réaliser cette thèse et tant encouragée à terminer "mon livre".

Finalement, je remercie ma famille et mes amis, et en particulier mes deux Sophie, Inès et Marie-Eve, pour leur patience également, mais surtout pour les moments de décompression et leurs encouragements sincères, qui m'ont également motivée à avancer, j'ai beaucoup de chance de les avoir à mes côtés.

Abstract

The models used to calculate small-caliber projectile trajectories are often only drag-based, given the presumed short ranges and the assumed small variation of the aerodynamic parameters in flight. Depending on the type of application, "field" calibrations are then performed to compensate for the observed deviations. However, with the new small-caliber applications and the inherent increased challenges, these simplified methods do not yield satisfactory results anymore in terms of accuracy and attitude upon impact.

In the first part, next to reviewing existing trajectography models, we discuss their implementation in our own trajectory program *VTraj*, developed in LabVIEW. The six degrees of freedom (6-DoF) model allows to compute the flight of any symmetrical or asymmetrical projectile (spin- or fin- stabilized). Its parameters include a complete set of static and dynamic contributions, including Magnus and pitch damping forces & moments. This model allows the analysis of all translation and angular motions of the projectile's body. The models give good agreement with published results on standard reference projectiles for the trajectory parameters.

In part two, we focus on the methodology to capture the static and dynamic aerodynamic coefficients by steady and unsteady RANS methods for subsonic, transonic and supersonic flight conditions. Accurate resolution of the flow in the boundary layer and in the wake of the projectile proved to be of utmost importance for the correct determination of the coefficients. The coefficient extraction methods are assessed with published results for canonical shapes and good agreement is achieved. The results highlight the strong dependency of the pitch damping coefficient on the reduced pitch frequency which varies along the flight path.

Rigid Body Dynamics (RBD) as well as Computational Fluid Dynamics (CFD) are finally combined in order to evaluate the behavior of specific small-caliber applications: non-lethal projectiles operating in the low subsonic domain, long-range projectiles with focus on transonic domain crossing, and asymmetric configuration are studied. The resolution of the dynamic flow around the projectile and the prediction of stability upon impact are confronted with experimental results and the match is very promising. The research also gives new insight into the diverse phenomena at hand in the transonic domain, or for projectiles with mass unbalance, and the change they impart on static and dynamic stability characteristics.

Résumé

Les modèles utilisés pour calculer les trajectoires de projectiles de petit calibre sont souvent uniquement basés sur la traînée, étant donné les courtes portées présumées et la faible variation supposée des paramètres aérodynamiques en vol. Selon le type d'application, des calibrations sur le "terrain" sont alors effectuées pour compenser les déviations observées. Cependant, étant donné les nouvelles applications en petit calibre et les défis croissants inhérents, ces méthodes simplifiées ne donnent plus de résultats satisfaisants en termes de précision et de comportement à l'impact.

Dans la première partie, après avoir passé en revue les modèles de trajectographie existants, nous discutons de leur mise en œuvre dans notre propre programme de trajectographie *VTraj*, développé dans LabVIEW. Le modèle à six degrés de liberté (6-DoF) permet de calculer le vol de n'importe quel projectile symétrique ou asymétrique (stabilisé par rotation ou par ailette). Ses paramètres comprennent un ensemble complet de contributions statiques et dynamiques, y compris Magnus et le moment d'amortissement en tangage. Les modèles correspondent bien avec les résultats publiés pour des projectiles conventionnels au niveau des paramètres de la trajectoire au point d'arrivée.

Dans la deuxième partie, nous nous concentrons sur la méthode pour déterminer les coefficients aérodynamiques statiques et dynamiques par des méthodes RANS stationnaires et instationnaires, et pour des conditions de vol subsonique, transsonique et supersonique. La résolution précise de l'écoulement dans la couche limite et dans le sillage du projectile s'est avérée être de première importance pour la détermination correcte des coefficients. Les méthodes d'extraction des coefficients sont évaluées sur base de résultats publiés pour des géométries canoniques et la correspondance est bonne. Les résultats soulignent la forte dépendance du coefficient d'amortissement en tangage à la fréquence de tangage réduite qui varie le long de la trajectoire de vol.

La dynamique des corps rigides (RBD) ainsi que la dynamique des fluides numérique (CFD) sont finalement combinées afin d'évaluer le comportement d'applications spécifiques de petit calibre : des projectiles non létaux opérant dans le domaine largement subsonique, des projectiles longue-distance avec un accent sur la traversée du domaine transsonique, ainsi qu'une configuration asymétrique. La résolution de l'écoulement dynamique autour du projectile et la prédiction de la stabilité à l'impact sont confrontées aux résultats expérimentaux, et la correspondance est très prometteuse.

Samenvatting

De modellen die worden gebruikt om de banen van kleinkaliberprojectielen te berekenen zijn vaak alleen op de luchtweerstand gebaseerd, gezien de veronderstelde korte drachten en de vermoede geringe variatie van de aërodynamische parameters tijdens de vlucht. Afhankelijk van het type toepassing worden dan "veld"-kalibraties uitgevoerd om de waargenomen afwijkingen te compenseren. Gezien de nieuwe toepassingen met klein kaliber en de inherente grotere uitdagingen, leveren deze vereenvoudigde methoden echter geen bevredigende resultaten meer op in termen van nauwkeurigheid en oriëntatie bij impact.

In het eerste deel bespreken we, naast een overzicht van de bestaande baanberekeningsmodellen, hun implementatie in ons eigen baanberekeningsprogramma *VTraj*, ontwikkeld in LabVIEW. Het model met zes vrijheidsgraden (6-DoF) maakt het mogelijk de vlucht van elk symmetrisch of asymmetrisch projectiel (spin- of vingestabiliseerd) te berekenen. De parameters omvatten een volledige reeks statische en dynamische bijdragen, met inbegrip van Magnus en pitch dempingskrachten en momenten. De modellen geven een goede overeenkomst met gepubliceerde resultaten over standaard referentieprojectielen voor baanparameters op het eindpunt.

In deel twee, richten we ons op de methodologie om de statische en dynamische aerodynamische coëfficiënten vast te leggen met behulp van steady en unsteady RANS-methoden voor subsonische, transonische en supersonische vluchtcondities. De nauwkeurige resolutie van de stroming in de grenslaag en in het zog van het projectiel bleek van het grootste belang te zijn voor de juiste bepaling van de coëfficiënten. De coëfficiënt-extractiemethoden zijn vergeleken met gepubliceerde resultaten voor generieke projectielen en er is een goede overeenkomst bereikt. De resultaten benadrukken de sterke afhankelijkheid van de pitch-dempingcoëfficiënt van de gereduceerde pitch-frequentie, die varieert langsheen de baan.

Rigid Body Dynamics (RBD) en Computational Fluid Dynamics (CFD) worden tenslotte gecombineerd om het gedrag van specifieke klein-kaliber toepassingen te evalueren: Niet-letale projectielen opererend in het lage subsonische domein, lange-dracht projectielen met focus op de crossing van het transonische domein, en asymmetrische configuratie. De resolutie van de dynamische stroming rond het projectiel en de voorspelling van de stabiliteit bij impact worden geconfronteerd met experimentele resultaten en de overeenkomst is veelbelovend.

Contents

Contents	ix
Nomenclature	xiii
Glossary	xxiii
List of Figures	xxvii
List of Tables	xxxvii
1 Introduction	1
I Exterior Ballistics	7
2 Prologue to stability	11
3 Trajectory Models	15
3.1 Trajectory computation	15
3.2 The 6-DoF Model	18
3.2.1 Coordinate Systems & Transformation Matrices	18
3.2.2 Equations of Motions	27
3.2.3 Definition of forces and moments	30
3.2.4 Other forces...	44
3.3 Practical implementations	46
3.3.1 Meteorological Conditions: ISO standards	46
3.3.2 Integration Methods	47
3.3.3 End of the trajectory	49
3.3.4 Initial conditions & choices	50

3.4	The Lieske-McCoy model for symmetric bodies	51
3.5	Validation of the 6-DoF models	54
3.6	Projectile Linear Theory	58
3.6.1	Linearized aeroballistic equation	60
3.6.2	Yaw of repose	64
3.7	The Modified Point Mass Model - MPMM	66
3.7.1	Fitting factors	69
3.7.2	Validation of the code	70
3.8	The Point Mass Model - PMM	72
3.8.1	Analytical Solution with drag Modeling	74
3.8.2	Siacci's Method vs Ballistic Coefficient	75
4	Existing software in practice	79
5	Stabilization concepts	85
5.1	Gyroscopic stability	87
5.2	Dynamic stability	88
5.3	Overstabilization	91
6	Coefficient collection process	93
6.1	Experimental measuring techniques	94
6.1.1	Full scale firings	94
6.1.2	Aeroballistic Ranges (or Spark Ranges)	95
6.1.3	Wind Tunnels	96
6.2	Software simulation techniques	98
6.2.1	Computational Fluid Dynamic Codes	98
6.2.2	Semi-Empirical Interpolation Codes	98
6.3	Conclusion on Part I	102
II	CFD Methodology	103
7	Fluid Properties and Governing Equations	107
7.1	Conservation Laws & Navier-Stokes Equations	107
7.2	Inviscid Flow	111
7.2.1	Incompressible Inviscid Flow	111
7.2.2	Compressible Inviscid Flow	113
7.3	Viscous Flow	113

7.3.1	Laminar BL	114
7.3.2	Transition	114
7.3.3	Turbulent BL	115
7.3.4	Separation	116
7.4	Turbulence modeling	116
7.4.1	Available CFD methods	116
7.4.2	RANS Modeling	118
7.4.3	Choice of the RANS Models with ANSYS Fluent	120
7.5	BL-research for projectiles so far...	123
8	Computational Fluid Dynamics	125
8.1	Discretization of the equations & Solver settings	127
8.2	Temporal discretization	128
8.3	Spatial Considerations	129
8.3.1	Domain Definition	129
8.3.2	Spatial Discretization	130
8.4	Initial and Boundary conditions	144
8.5	Physical properties	147
8.5.1	Callorically Perfect gas	147
8.5.2	Thermally Perfect gas	147
8.6	Digression on Uncertainty Quantification	149
9	Aerodynamic coefficients extraction	151
9.1	Static aerodynamic coefficients	152
9.1.1	Zero-yaw computations	152
9.1.2	Small angle computations	156
9.1.3	Curved trajectory	157
9.2	Dynamic aerodynamic coefficients	159
9.2.1	Magnus coefficients	159
9.2.2	Pitch Damping coefficients	161
9.2.3	AoA Limitations	170
9.3	Conclusion on Part II	171
III	Small-Caliber Applications	173
10	Non-Lethal Application	177

10.1	Methodology	178
10.1.1	Computational Approach	178
10.1.2	Experimental Approach	179
10.2	Results	181
10.2.1	Experimental comparison of the static coefficients	181
10.2.2	Dynamic Coefficients	182
10.2.3	Boundary Layer Analysis	184
10.3	Trajectory Computations: PMM versus 6-DOF	188
10.4	Conclusion on the non-lethal field...	190
11	Precision Ammunition & Transonic Domain	191
11.1	Methodology	193
11.1.1	Experimental Approach	195
11.1.2	Computational Approach	196
11.2	Results	197
11.2.1	Flow Visualization	197
11.2.2	Aerodynamic Coefficients	201
11.3	Stability Analysis	203
11.4	Conclusion on long-range shooting...	206
12	Mass Unbalance	207
12.1	Mass unbalance in small caliber	209
12.2	Experimental Approach	210
12.3	Analytical predictions	211
12.4	Comparison live firing with analytical predictions	214
12.5	Numerical Results	216
12.5.1	Aerodynamic coefficients without unbalance	216
12.5.2	Aerodynamic coefficients with unbalance	217
12.5.3	6-DoF computations	222
12.6	Conclusion on the mass unbalance...	224
IV	Conclusions	225
	References	235

Nomenclature

Abbreviations

6-DoF	6 Degrees of Freedom (Model)
ABAL	Armament BALListics Department (Royal Military Academy)
AFM	Atmospheric Flight Mechanics
AoA	Angle of Attack
AOP	Allied Ordnance Publication
AP	Armour Piercing
APDS	Armour Piercing Discarding Sabot
APFSDS	Armour Piercing Fin Stabilized Discarding Sabot
APHC	Armour Piercing Hard Core
ARDEC	Armament Research, Development and Engineering Center
ARL	Army Research Laboratory - Maryland
BC	Ballistic Coefficient
BL	Boundary Layer
BOS	Background Oriented Schlieren
BRL	Ballistic Research Laboratory (Old ARL)
CEP	Circular Error Probable
CFD	Computational Fluid Dynamics
CG	Center of Gravity
CP	Center of Pressure

DES	Detached Eddy Simulation
DNS	Direct Numerical Simulation
DRDC-VRC	Defence Research and Development Canada Valcartier Research Centre
EOS	Equation of State
FCI	Fire Control Inputs
FCT	Fire Control Trajectories
FTaB	Firing Tables and Ballistics Division (part of ARDEC/ARL)
GCI	Grid Convergence Index
GNC	Guidance, Navigation & Control
ICAO	International Civil Aviation Organization
IRT	InfraRed Thermography
ISA	International Standard Atmosphere
ISL	Institut franco-allemand de recherche de Saint Louis
LES	Large Eddy Simulation
MPI	Middle Point of Impact
MPMM	Modified Point Mass Model
MSL	Mean Sea Level
MV	Muzzle Velocity
NAAG	NATO Army Armament Group
NABK	NATO Armament Ballistic Kernel
NETD	Noise Equivalent Temperature Difference
PMM	Point Mass Model
RANS	Reynolds Averaged Navier-Stokes
RBD	Rigid Body Dynamics
SD	Sectional Density

SOCBT	Secante-Ogive Cylindrical Boat-Tail
SST	Shear Stress Transport
STANAG	NATO Standardization Agreement
STANREC	NATO Standardization Recommendation
TKE	Turbulent Kinetic Energy
TOF	Time of Flight
ZDES	Zonal-Detached-Eddy Simulation

Coordinate Reference Systems

$\vec{X}_i, \vec{Y}_i, \vec{Z}_i$	Inertial reference frame
$\vec{X}, \vec{Y}, \vec{Z}$	Ground-fixed (or Earth-fixed) reference frame ($=\vec{1}, \vec{2}, \vec{3}$)
$\vec{x}, \vec{y}, \vec{z}$	Body-fixed reference frame (rolling frame, spinning frame) or Plane-fixed reference frame (non-rolling frame) or Aeroballistics reference frame (non-rolling, non-spinning frame)
$\vec{x}_a, \vec{y}_a, \vec{z}_a$	Velocity reference frame (relative to the total velocity vector)

Rigid Body Dynamics

α or AoA	Pitch (overturning, angle of attack) angle (relative to velocity vector)	rad
β	Yaw (sideslip) angle (relative to velocity vector)	rad
δ	Total yaw angle ($\delta \approx \sqrt{\alpha^2 + \beta^2}$ for $\delta \ll$)	rad
δ_F	Fin cant angle (geometric parameter)	°
δ_R	Yaw of repose	rad
$\dot{\alpha}, \dot{\beta}$	transverse angular velocities relative to velocity vector	rad/s
ϵ_H, ϵ_D	Precision tolerances in Height and Distance	m
λ_F	Fast mode damping factor	1/m
λ_S	Slow mode damping factor	1/m
Ω	Angular speed of the earth	rad/s
ω_C	Angular velocity of the coordinate system due to Ω	rad/s

$\Omega_x, \Omega_y, \Omega_z$	Angular velocity components of a coordinate system	rad/s
ϕ, θ, ψ	Bryant's angles (commonly called Euler angles) for conversion between Ground to Body-fixed coordinates	rad
Φ_0	Roll orientation angle of the CG, at emergence from the muzzle	rad
ϕ_0	Roll orientation angle of m_E at emergence from the muzzle	rad
ϕ_F	Fast mode frequency	rad/m
ϕ_S	Slow mode frequency	rad/m
$\vec{1}_V$	Unit vector in the velocity vector direction = \vec{V}/V	
$\vec{1}_x, \vec{1}_y, \vec{1}_z$	Body-fixed unit vectors ($\vec{1}_x$ along symmetry rotational axis)	
$\vec{\Lambda}$	Coriolis force	N
$\vec{\omega}$	Total angular velocity vector (p, q, r) in body-fixed coordinates	rad/s
\vec{g}	Gravity acceleration vector	m/s ²
\vec{h}	Specific angular momentum vector ($\vec{h} = \vec{I}\vec{\omega}/I_y$)	rad/s
$\vec{u}, \vec{v}, \vec{w}$	Velocity vector components in the body axes coordinates	m/s
\vec{V}_0	Muzzle Velocity vector	m/s
\vec{V}_W	Velocity vector with respect to the air ($\vec{V}_W = \vec{V} - \vec{W}$)	m/s
\vec{V}	Velocity vector relative to earth-fixed coordinates (tangent to the trajectory)	m/s
\vec{W}	Wind velocity vector, relative to earth-fixed coordinates	m/s
Az or θ_0	Azimuth of \vec{X} -axis measured clockwise from true North	mils
d or cal	Caliber (diameter) of the projectile	m
g_0	Constant of acceleration due to gravity at MSL	m/s ²
G_x, G_y, G_z	Gravity forces in body coordinates ($\vec{G} = m\vec{g}$)	N

I_x	Axial principal moment of inertia relatives to body axes	kg·m ²
I_y, I_z	Transverse principal moments of inertia relatives to body axes For symmetric configurations : $I_T = I_y = I_z$	kg·m ²
J_A	Aerodynamic Jump	m
J_x, J_y, J_z	Products of inertia ($= I_{yz}, I_{xz}, I_{xy}$)	kg·m ²
K_F	Fast mode amplitude	rad
K_S	Slow mode amplitude	rad
K_T	Trim amplitude	rad
L	Length of the projectile	m
Lat	Latitude of the firing position	°
m	Mass of the projectile	kg
m_E	Removed mass from a mass-symmetric projectile ($m_E \ll m$)	kg
p, q, r	Angular rates in body coordinates ($p =$ roll/spin rate, $q =$ yaw rate, $r =$ pitch rate)	rad/s
q_t	Total transverse angular rate: $q_t = \sqrt{q^2 + r^2}$	rad/s
QE or ψ_0	Quadrant Elevation = initial vertical orientation of the gun relatives to Earth X-Z plane (6400 mils = 360° = 2πrad)	mils
R	Radius of the projectile	m
R_E	Earth Radius, locally approximating the geoid	m
r_E, L_E	Radial and longitudinal positions of the mass m_E	m
S_d	Dynamic stability factor	
S_g	Gyroscopic stability factor	
T_L	Lateral Throwoff (tangent of the deflection angle)	m
Tw	Rifling twist rate at the gun muzzle	d/turn
V	Magnitude of the velocity vector	m/s

V_0 or MV	Magnitude of the Muzzle Velocity vector	m/s
---------------	---	-----

Aerodynamics/Thermodynamics

ρ	Air density	kg/m ³
γ	isentropic coefficient = 1.4 under 800K	
λ	Stokes coefficient or second viscosity coefficient	kg/(m·s)
μ	Dynamic Viscosity	kg/(m·s)
ν	Kinematic Viscosity	m ² /s
\vec{q}	Heat flux vector	W/m ²
\vec{D}	Drag force vector along velocity axes	N
\vec{E}	Pitch damping force vector along velocity axes	N
\vec{H}	Pitch damping moment vector around velocity axes	N·m
\vec{J}	Magnus moment vector around velocity axes	N·m
\vec{L}	Lift force vector along velocity axes	N
\vec{M}	Pitch moment vector around velocity axes	N·m
\vec{Q}	Magnus force vector along velocity axes	N
\vec{S}	Spin damping moment vector around velocity axes	N·m
\vec{V}_{δ_F}	Rolling moment vector around velocity axes	N·m
c	Sound velocity	m/s
C_f	Skin friction coefficient	
C_p	Pressure coefficient	
c_p	Heat capacity at constant pressure	J/(kg·K)
c_v	Heat capacity at constant volume	J/(kg·K)
e	Internal energy per unit mass	J/kg
e_0	Total energy per unit mass	J/kg
F_N	Normal Force	N
F_X	Axial Force	N

F_x, F_y, F_z	Aerodynamic forces in body coordinates	N
G_x	Zero yaw drag of a standard projectile x	N
h	Specific enthalpy	J/kg
h_0	Total specific enthalpy	J
i_x	Form factor	
k	Thermal conductivity	W/(m·K)
M_x, M_y, M_z	Aerodynamic moments in body coordinates	N·m
Ma	Mach number	
p	Air static pressure	Pa
Pr	Prandtl number	
R	specific dry air constant = 287.057 [J/(kg·K)]	J/(kg·K)
Re	Reynolds number	
T	Air static temperature	K

Aerodynamic Coefficients

C_R	Generic aerodynamic coefficient
C_R^*	Starred aerodynamic coefficient = $\frac{\rho S d}{2m} C_R$
C_X or C_A	Force coefficient in \vec{x} -direction or axial coefficient
C_Y or C_N	Force coefficient in \vec{y} -direction or normal coefficient
C_Z	Force coefficient in \vec{z} -direction
C_D	Total drag coefficient
C_{D_0}	Zero-yaw drag coefficient derivative
$C_{D_\delta^2}$	Quadratic-yaw drag coefficient derivative
C_L	Total lift Coefficient
C_{L_δ}	Lift force coefficient derivative
C_{N_δ}	Normal force coefficient derivative
$C_{L_{\delta_0}}$	Zero-yaw lift force coefficient derivative

$C_{L_{\delta^3}}$	Quadratic-yaw lift force coefficient derivative
C_M	Total pitch moment Coefficient
$C_{M_{\delta}}$	Pitch moment coefficient derivative
$C_{M_{\delta_0}}$	Zero-yaw pitch moment coefficient derivative
$C_{M_{\delta^3}}$	Quadratic-yaw pitch moment coefficient derivative
$C_{N_{p\delta}}$	Magnus force coefficient
$C_{N_{p\delta_0}}$	Zero-yaw Magnus force coefficient derivative
$C_{N_{p\delta^3}}$	Quadratic-yaw Magnus force coefficient derivative
$C_{M_{p\delta}}$	Magnus moment coefficient
$C_{M_{p\delta_0}}$	Zero-yaw Magnus moment coefficient derivative
$C_{M_{p\delta^3}}$	Quadratic-yaw Magnus moment coefficient derivative
C_{l_p}	Spin damping moment coefficient derivative
$C_{l_{\delta_F}}$	Rolling moment coefficient derivative
$C_{N_q} + C_{N_{\dot{\alpha}}}$	Pitch damping force coefficient
$(C_{N_q} + C_{N_{\dot{\alpha}}})_0$	Zero-yaw Pitch damping force coefficient derivative
$(C_{N_q} + C_{N_{\dot{\alpha}}})_{\delta^2}$	Quadratic-yaw Pitch damping force coefficient derivative
$C_{M_q} + C_{M_{\dot{\alpha}}}$	Pitch damping moment coefficient (here $q = q_t = \sqrt{q^2 + r^2}$)
$(C_{M_q} + C_{M_{\dot{\alpha}}})_0$	Zero-yaw Pitch damping moment coefficient derivative
$(C_{M_q} + C_{M_{\dot{\alpha}}})_{\delta^2}$	Quadratic-yaw Pitch damping moment coefficient derivative

Computational Fluid Dynamics

$\delta(x)$	Boundary Layer thickness	m
ϵ	Turbulent Dissipation Rate	J/(kg·s)
η	Kolmogorov scale	m
γ	Intermittency	
Λ	Vorticity Thikness Mixing Layer	m

μ_t	Turbulent/Eddy viscosity	kg/(m·s)
ω	Planar pitching angular frequency	rad/s
ω	Specific Dissipation Rate	1/s
$\overline{\rho u'' v''}$	Reynolds Shear Stresses	Pa
τ_w	Wall shear stress	Pa
τ_{ij}	Deviatoric stress tensor	Pa
A	Pitching Amplitude for the forced oscillation	rad
h	Area-Weighted Average of the cell wall distance	m
i	Number of inner iterations per global iteration	
k	Reduced pitch frequency	rad
k	Turbulent kinetic Energy (TKE)	J/kg
L	Length of the body, for the computation of Re	m
L	Large scale containing TKE	m
L_R	Recirculation Length	m
N	Number of global iterations per oscillation cycle	
u^+	Dimensionless velocity u parallel to the wall	
u_i	Total velocity of the flow	m/s
U_∞	Upstream Freestream Velocity	m/s
u_τ	Friction velocity or shear velocity	
y^+	Normalized Distance from the wall	

Operators

*	Multiplication sign used to separate the different physical factors in an equation
·	Scalar product
×	Vectorial product
δ_{ij}	Kronecker symbol

$\vec{\nabla}T$ T is a scalar function
 $\vec{\nabla}T = \text{grad } T = \frac{\partial T}{\partial x} \vec{1}_x + \frac{\partial T}{\partial y} \vec{1}_y + \frac{\partial T}{\partial z} \vec{1}_z$

$\vec{\nabla} \cdot \vec{V}$ \vec{V} is a vector
 $\text{div } \vec{V} = \frac{\partial V_x}{\partial x} + \frac{\partial V_y}{\partial y} + \frac{\partial V_z}{\partial z}$

\equiv Equivalent to

Other Symbols

Γ Temperature lapse rate K/m

Definitions in Ballistics

6/7-DoF While the 6-DoF model is used to describe the motion of single rigid bodies, the 7-DoF model allows the description of a projectile which consists of two coaxial rigid bodies that can spin independently [272]. The 6/7-DoF model is standardized for artillery projectiles for the NATO Naval and Army Forces in AEP-96 [1]. 82, 151

aerodynamic coefficients Parameters defined as a function of the Mach number, Reynolds Number, shape and yaw angle, to quantify the forces and moments acting on a body in flight [14]. 4

AOP The Allied Ordnance Publications are technical documents established under the cover of a reference STANAG. 44, 45, 66, 81

Center of Gravity Point of application of the resultant of the gravity forces. Also considered in this work as the centre of mass, (through which pass the principal moments of inertia. 13

Center of Pressure Point of application of the resultant of aerodynamic forces. 13

direct fire Fire delivered on a target that is visible to the aiming unit (Ex. : Small arms, tank) [14]. xxvii, 2

direct problem Trajectory calculation to determine the impact position of the projectile on the basis of the given FCI. 3

drift Also called spin-drift. Lateral deviation of the projectile due to gyroscopic response. For a right hand (clockwise) direction of rotation this component will be to the right. For a left hand (counterclockwise) direction of rotation

this component will be to the left. The magnitude of the drift is directly related to the magnitude of the curvature. 17, 39

FCI Fire Control Inputs = Set of fixed technical data for a gun-ammunition combination used by fire control computers in order to initiate a trajectory calculation (this includes Gun Elevation and Azimuth) [14]. xxiii, xxiv

indirect fire Fire delivered on a target that is not itself used as the point of aim for the weapon, i.e. the target cannot be seen by the aimer, he will receive the **FCI** from another source (Ex. : artillery, mortars, most naval fire) [14]. xxvii, 2

indirect problem Iterative trajectory calculations (in direct mode) to determine the **FCI** in order to reach a target whose position is given. 2

initial percussion This phenomenon studied in intermediate ballistics (between internal and external ballistics) includes all the effects associated with the exit of the projectile from the tube, such as the re-inflammation of the gases, which will generate a rise in pressure that will further accelerate the projectile, but also the various shocks that can disrupt its stability (orientation and angular rates). 1

Muzzle Velocity (*MV*) Speed of the projectile when it leaves the barrel. In interior ballistics the speed can be estimated using an interior ballistic model. In exterior ballistics the speed is obtained by extrapolating down range measurements of projectile velocity (vs time or position) to the muzzle position [14]. 2

nutation Additional rotation frequency superimposed to the , due to additional perturbations. 14, 61

pitch vs yaw: Two scalar angular velocities. **Pitch** is used for the vertical angular velocity about \vec{z} (= angle of attack), while **Yaw** is used for the horizontal angular velocity about \vec{y} (= sideslip angle). The term "Yaw" is also used for the resultant or total angle between the \vec{x} -axis and the velocity vector \vec{V} . 16

precession Continuous Slow angular movement of the longitudinal axis of a gyroscopically stabilized projectile around the velocity vector, following the action of the pitching moment in flight. xxix, 13, 14, 61, 64

spin vs roll: Two scalar angular velocities. **Spin** is used for the "very fast" axial angular velocity of the projectile induced by the barrel grooves, while **Roll** is used for the other "slower" axial angular rates (between reference frames or angular velocity induced by canted fins). 13, 14

STANAG A NATO standardization document is a normative document that records an agreement among NATO member states – ratified at the authorized national level – to implement a standard, in whole or in part, with or without reservation in order to meet an interoperability requirement¹. STANAG's are available via the NSO Website (depending on security clearances). xxiii, 46, 66

STANREC NATO Standardization Recommendation document specifying one or more NATO or NON-NATO standards relevant for a specific activity of the alliances, but not related to interoperability. STANRECs are prepared and used in the materiel-related fields of standardization only². 81

¹<https://www.nato.int/cps/en/natohq/publications.htm>

²<https://edsis.eda.europa.eu/Files/NATO%20STANAG.pdf>

List of Figures

1.1	Initial percussion with Background Oriented Schlieren (BOS) imaging technique, processed by A. Moumen - ABAL [154].	1
1.2	Direct fire - M1A2C Abrams tank with a 120-mm smooth bore.	2
1.3	Indirect fire - 120-mm mortar.	2
1.4	Complete ballistics cycle from weapon to target.	3
1.5	LabVIEW Graphical Interface VTraj - Direct generalized 6-DoF Model.	10
2.1	Conventional symmetric bullet.	11
2.2	Static stability.	12
3.1	Local extrapolation & Influence of the generated error ε based on the time step used.	16
3.2	Typical angular rates in ballistic conventions. $\vec{x}, \vec{y}, \vec{z}$ referring to the body axis system and $\vec{x}_a, \vec{y}_a, \vec{z}_a$ to the velocity vector, with \vec{x}_a tangent to the trajectory and \vec{y}_a, \vec{z}_a perpendicular to the latter.	17
3.3	From the Inertial to the Body-fixed Coordinates.	19
3.4	Body and Velocity frames vs Ground-fixed coordinates.	20
3.5	Y-Z-X sequence of rotations with Bryant's angles: 1 st Rotation around Y.	22
3.6	Y-Z-X sequence of rotations with Bryant's angles: 2 nd Rotation around z1.	23
3.7	Y-Z-X sequence of rotations with Bryant's angles: 3 rd Rotation around x.	23
3.8	Decomposition of air resistance for both types of stabilization, \vec{M} is illustrated positively.	32
3.9	Drag force coefficient components as a function of Mach number for the 120-mm mortar [137] and the 5.56-mm projectile [217].	33
3.10	Drag coefficient at Ma 0.8 as a function of δ for the 120-mm mortar [137].	34
3.11	Zero-Yaw Drag coefficient for different geometries, estimated with AeroFI [210].	34

3.12	Lift force coefficient components as a function of Mach number for the 120-mm mortar [137] and the 5.56-mm projectile [217].	35
3.13	Lift force coefficient at Mach number 0.8 as a function of δ for the 120-mm mortar [137] and the 5.56-mm projectile [217].	35
3.14	Drag and Lift versus Axial and Normal forces.	36
3.15	Pitch moment coefficient components as a function of Mach number for the 120-mm mortar [137] and the 5.56-mm projectile [217].	37
3.16	Pitch moment coefficient at Mach number 0.8 as a function of δ for the 120-mm mortar [137] and the 5.56-mm projectile [217].	37
3.17	Rotation around longitudinal axis.	38
3.18	Spin damping moment coefficient as a function of the Mach number for the 5.56-mm projectile [217].	38
3.19	A representation of Magnus' force \vec{Q}	40
3.20	Magnus moment coefficient components as a function of Mach number for the 5.56-mm projectile [217].	41
3.21	Magnus moment coefficient as a function of δ for the 5.56-mm projectile [217].	41
3.22	Fitted Magnus moment coefficient as a function of Mach number for the 5.56-mm projectile [217].	41
3.23	Pitch and Yaw damped oscillations for a 5.56-mm projectile. Initial conditions: $MV = 800\text{m/s}$, $QE = 20\text{mils}$, $q_0 = r_0 = 20\text{rad/s}$	42
3.24	Pitch damping coefficient components as a function of Mach number for the 120-mm mortar [137] and the 5.56-mm projectile [217].	43
3.25	Pitch damping coefficient at Mach number 0.8 as a function of δ for the 120-mm mortar [137].	44
3.26	Initial Velocity and Position vectors. The colors are used to enhance the visualization of the different reference systems.	53
3.27	Initial position unit vector triad.	53
3.28	Time increment convergence for cases 4, 8 and 9 from table 3.2 and two integration schemes. The relative error is calculated on the basis of the results given by McCoy [137].	55
3.29	Comparison Pitch Angle in function of the Time of Flight (ToF)- Case 3 on the left - Case 6 on the right.	56
3.30	Comparison XY and XZ projections for scenario 7 [217].	57
3.31	Comparison isolate Pitch (α) and Yaw (β) angles for scenario 7 [217].	57

3.32	Epicyclic Pitching and Yawing Motion for non-trimming rolling projectile. According to equation 3.118, both arms K_S & K_F turn in the same direction.	63
3.33	Tricyclic Pitching and Yawing Motion for a finned projectile with control deflection. According to Eq.3.118, both arms K_S & K_F turn in opposite directions.	63
3.34	Trajectory beginning of a 5.56 mm caliber projectile - scenario 7 from table 3.2. Left : Epicyclic Pitching and Yawing Motion during the first 10 meters because of initial perturbations. Right : No initial perturbations ($q_0, r_0 = 0$), only the precession motion is to be seen with a slight yaw of repose δ_R from the very beginning. . .	64
3.35	Damping exponents λ_F and λ_S as a function of the range for a 5.56 mm projectile with $MV = 405\text{m/s}$ on the left (case 7 from table 3.2) and $MV = 800\text{m/s}$ on the right.	64
3.36	Solution VTraj included in the FTaB corridor for elevation[73]. . . .	71
3.37	Solution VTraj included in the FTaB corridor for azimuth [73]. . . .	71
3.38	"n"-power approximation for different projectile geometries.	74
3.39	G1 vs G7 standard projectile's geometries.	76
3.40	C_{D_0} coefficient shapes for G1 and G7 standard projectiles[137]. . . .	76
3.41	Ballistic coefficient for the .338-inch projectile, according to G1 and G7.	76
4.1	PRODAS Analysis options [16]	81
4.2	NABK Software Architecture	82
5.1	Gyroscopic versus Dynamic Stability Criterion. The orange part implies gyroscopic stability but not dynamic stability.	89
5.2	Representation of an overstabilized projectile. This makes it actually a better gyroscope since it is less sensitive to perturbations. . .	91
6.1	Yaw cards installed on the shooting range of Bourges (FRA) consisting of wooden posts between which are stretched sheets of kerosene, paper or cardboard, to disrupt the flight as little as possible [41, 52].	95
6.2	DRDC Valcartier Aeroballistics Range [62].	96
6.3	ISL's trisonic blow down wind tunnel with high speed camera's for stereovision-technique[134, 155].	97

6.4	CAD model of the semi-free oscillation test bench with instrumented projectile, to use within the VKI S-1 Supersonic-Transonic wind tunnel [112].	97
6.5	Expected Aerodynamic Coefficient Percent Errors from PRODAS Program [16] par rapport aux différentes.	99
6.6	Evolution of AeroPrediction Code with major new added capabilities[149].	100
	105figure.caption.90	
7.1	Schematic development of the boundary layer along the nose of a projectile, with an imperfectly defined transition zone. L is the total length of the projectile facing air. The laminar zone has been stretched for clarity, but it is in fact hardly perceptible in reality. . .	114
7.2	Schematic velocity profile in the inner layer of a turbulent BL. . . .	120
7.3	Three SST models' activation.	122
8.1	SOCBT configuration dimensions ($d = 0.0572\text{m}$).	126
8.2	Spinner configuration dimensions ($d = 0.0162\text{m}$).	126
8.3	ANF configuration dimensions ($d = 0.03\text{m}$).	127
8.4	Computational domain for supersonic case (unstructured mesh). .	130
8.5	Trade-off domain for supersonic to subsonic calculations (unstructured mesh).	130
8.6	y^+ values along the 2D-axisymmetric body for the five meshes detailed in table 8.1.	133
8.7	2D axisymmetric structured mesh 1 from table 8.1 with zoom around the projectile and its boundary layer.	134
8.8	2D axisymmetric structured mesh 3 from table 8.1 with zoom around the projectile and its boundary layer.	134
8.9	2D axisymmetric structured mesh 5 from table 8.1 with zoom around the projectile and its boundary layer.	134
8.10	Grid convergence according to C_{D_0} and C_{l_p} as a function of the area-weighted average h	135
8.11	Ratio of pressure and viscous contributions at different speeds. The viscous relative contribution for drag increases as the speed decreases.	136

8.12	Pressure C_p and skin friction C_f coefficients at Mach 3 and 0° AoA for different 2D Axi-meshes and SST models. Experimental data from Reklis & Sturek [184].	136
8.13	2D-extrusion of a structured mesh, with negative quality zone upstream of the nose.	137
8.14	3D unstructured mesh (left) with density boxes (right).	138
8.15	Unstructured mesh with a 50-layers prismatic boundary layer. Zoom represented with "cut plane" from ICEM CFD [7] giving a partial 3D representation of the different layers (it can give the impression of non-smooth geometry, but it is obviously smooth).	139
8.16	Grid convergence according to C_{D_0} and C_{l_p} as a function of the number of prism layers at the wall for a transonic and a supersonic velocity.	139
8.17	Pressure Coefficient on the windward side of the SOCBT configuration at Ma 0.96 and 10° AoA for three different meshes. Experimental data from [106].	140
8.18	Pressure Coefficient on the leeward side of the SOCBT configuration at Ma 0.96 and 10° AoA for three different meshes. Experimental data from [106].	140
8.19	Skin friction Coefficient on the windward side of the SOCBT configuration at Mach 0.96 and 10° AoA for three different meshes.	140
8.20	Skin friction Coefficient on the leeward side of the SOCBT configuration at Mach 0.96 and 10° AoA for three different meshes.	140
8.21	Pressure Coefficient on the windward side of the SOCBT configuration at 10° AoA for three different transonic velocities. Experimental data from [106].	141
8.22	Pressure Coefficient on the leeward side of the SOCBT configuration at 10° AoA for three different transonic velocities. Experimental data from [106].	141
8.23	Skin friction Coefficient on the windward side of the SOCBT configuration at 10° AoA for three different transonic velocities.	142
8.24	Skin friction Coefficient on the leeward side of the SOCBT configuration at 10° AoA for three different transonic velocities.	142
8.25	Mach contour in the xy plane for a flight speed of Mach 0.91 and 10° AoA.	142
8.26	$\nabla\rho$ contour in the xy plane for a flight speed of Mach 0.91 and 10° AoA.	142

8.27	Mach contour in the xy plane for a flight speed of Mach 0.98 and 10° AoA.	143
8.28	$\nabla\rho$ contour in the xy plane for a flight speed of Mach 0.98 and 10° AoA.	143
8.29	Mach contour in the xy plane for a flight speed of Mach 1.1 and 10° AoA.	143
8.30	$\nabla\rho$ contour in the xy plane for a flight speed of Mach 1.1 and 10° AoA.	143
8.31	Boundary Conditions in 2D.	144
8.32	Boundary Conditions in 3D.	144
8.33	Mach contours around the Spinner configuration in the xy plane in ideal gas conditions - Ma 4.5 - 10° AoA.	148
8.34	Mach contours around the Spinner configuration in the xy plane in real gas conditions - Ma 4.5 - 10° AoA.	148
8.35	Pressure coefficient comparison in ideal and real gas conditions - Ma 4.5 - 10° AoA.	148
8.36	Skin friction coefficient comparison in ideal and real gas conditions - Ma 4.5 - 10° AoA.	148
8.37	Variable heat capacity with the cubic EOS van Soave-Redlich-Kwong [226].	149
9.1	Zero-Yaw drag coefficient for the Spinner [16, 55, 179, 210].	154
9.2	Spin damping coefficient for the Spinner [16, 55, 179, 210].	154
9.3	Zero-Yaw drag coefficient for the ANF configuration [69, 210].	155
9.4	Lift coefficient derivative computed for the Spinner configuration and $\delta = 3^\circ$ [16, 55, 179, 210].	156
9.5	Pitch moment coefficient derivative computed for the Spinner configuration and for $\delta = 3^\circ$ [16, 55, 179, 210].	156
9.6	Lift coefficient derivative computed for the ANF configuration and for $\delta = 1^\circ$ [69, 210].	157
9.7	Pitch moment coefficient derivative computed for the ANF configuration and for $\delta = 1^\circ$ [69, 210].	157
9.8	Evolution of the drag coefficient with respect to the yaw angle δ for the Spinner configuration.	158
9.9	Evolution of the lift and pitch moment coefficients with respect to the yaw angle δ for the Spinner configuration.	158
9.10	Quadratic Drag coefficient with respect to the Mach number for the Spinner configuration.	159

9.11	Cubic Lift (on the left) and Pitch moment (on the right) coefficients with respect to the Mach number for the Spinner configuration. . .	159
9.12	Magnus Moment Coefficient computed for a yaw angle of 3° [16, 55, 179, 210].	160
9.13	Pitching reaction (in blue) of a spin-stabilized projectile following a forced oscillation α in the vertical plane (in black). The same time-history is found for the lift.	163
9.14	Schematic representation of axial/normal forces vs Drag/Lift. . . .	163
9.15	Schematic of a pitch hysteresis loop, used to identify the pitch damping coefficients from points of maximum and minimum pitch rate. . . .	165
9.16	Pitch moment history as a function of time (on the left) and of the Angle of Attack (on the right) for different forced oscillations amplitudes A	168
9.17	Pitch moment history as a function of time (on the left) and of the Angle of Attack (on the right) for different amounts of time-steps per period of oscillation N	168
9.18	Pitch moment history as a function of time (on the left) and of the Angle of Attack (on the right) for different reduced pitch frequencies k	168
9.19	Influence of the different inputs parameters for the determination of the pitch damping moment.	169
9.20	Pitch Damping Moment Coefficient as a function of the Mach number. Experimental data from [178] - CFD RANS results from [59]. . .	169
9.21	Pitch Damping Moment Coefficient as a function of the Mach number for the ANF. Experimental data from [69].	170
10.1	12-GAUGE finned projectile dimensions in mm.	178
10.2	Left : Aerodynamic balance for drag, lift and pitch measurements. Right : IR FlexCam for the temperature profiles visualization. . . .	180
10.3	Wind Tunnel experiments compared with numerical results for the Drag and Lift Force Coefficients as a function of the Angle of Attack (AoA), according to the representation of Fig. 3.14.	181
10.4	Wind Tunnel experiments compared with numerical results for the Pitch Moment Coefficient as a function of the Angle of Attack. . . .	182
10.5	Lift coefficient response for different forced oscillation frequencies with $A = 1^\circ (= 0.017\text{rad})$	182

10.6 Pitch moment coefficient response for different forced oscillation frequencies with $A = 1^\circ (= 0.017\text{rad})$	183
10.7 Pitch moment coefficient response for different forced oscillation frequencies k with $A = 1^\circ (= 0.017\text{rad})$ and $N = 200$ global iterations per oscillation.	183
10.8 Pressure and Skin Friction Coefficients along the projectile for comparison with experimental visualizations at 0° . Lower temperature in blue and higher temperatures in red.	185
10.9 Pressure and skin friction coefficients along the exposed (windward) and unexposed (leeward) sides for different angles of attack (4, 6, 8 and 10 degrees) together with the corresponding IRT-images.	186
10.10PMM vs 6DoF comparison for three elevation angles QE and no initial perturbations.	188
10.11Pneumatic launcher with smooth barrel cal 12.	189
10.12Separation of the sabot behind the projectile at the tube exit.	189
10.13PMM vs 6DoF comparison for three elevation angles QE and no initial perturbations.	189
10.14Pitch and yaw angles for extreme initial conditions.	190
11.1 Dimensions of the three configurations studied in .338 in - all dimensions in mm.	193
11.2 Experimental setup for the flow visualization around the projectile: Classical Schlieren technique on the left, BOS technique on the right.	195
11.3 Projectile 250 at Mach 1.2: Experiments on the left (classical Schlieren at the top, BOS at the bottom), CFD contours on the right (Mach at the top, density gradient at the bottom).	197
11.4 Spitzer projectile at Mach 1.15: Experiments on the left (classical Schlieren at the top, BOS at the bottom), CFD contours on the right (Mach at the top, density gradient at the bottom).	198
11.5 Projectile 250 at Mach 1.02: Experiments on the left (classical Schlieren at the top, BOS at the bottom), CFD contours on the right (Mach at the top, density gradient at the bottom).	198
11.6 Projectile 250 at Mach 0.97: Experiments on the left (classical Schlieren at the top, BOS at the bottom), CFD contours on the right (Mach at the top, density gradient at the bottom).	199

11.7 Projectile 300 at Mach 0.93: Experiments on the left (classical Schlieren at the top, BOS at the bottom), CFD contours on the right (Mach at the top, density gradient at the bottom).	199
11.8 Numeric density contours with three parametric zones where the density was evaluated using the BOS technique on the .338-in. 300gr.-projectile.	200
11.9 Density tracking at three distances from the 300 gr.-projectile wall.	200
11.10 Total Zero Yaw Drag Coefficient for all geometries.	201
11.11 Body drag (Ogive+Cylinder) comparison between the 250 and 300 gr. projectiles.	201
11.12 Tip drag for all geometries.	202
11.13 Base drag for all geometries.	202
11.14 Lift coefficient for all geometries.	202
11.15 Pitch moment coefficient for all geometries.	202
11.16 Spin damping coefficient for all geometries.	203
11.17 Magnus moment coefficient for all geometries.	203
11.18 Pitch Damping coefficient with stability margins based on linear analysis.	205
12.1 Schematic representation of a 9-mm caliber projectile from which a piece has been removed (green contour) to generate an unbalance.	210
12.2 Angular definition of m_E and the new CG position.	210
12.3 Schematic Tricyclic trim pitch and yaw arm K_T	212
12.4 Schematic illustration of the different deviations that can accumulate, in this case to the right.	212
12.5 Experimental and analytical MPI deviations due to a mass unbalance.	214
12.6 Visualization with the high speed camera of the departure of the projectile according to the position of the unbalance.	215
12.7 Drag coefficients for a 9-mm balanced projectile.	216
12.8 Lift coefficients for a 9-mm balanced projectile.	216
12.9 Pitch coefficients for a 9-mm balanced projectile.	217
12.10 Spin damping coefficient for a 9-mm balanced projectile.	217
12.11 Different positions of the unbalance in the yz plane of the projectile.	217
12.12 Pitch moment coefficient evolution as a function of the yaw angle, for different unbalanced projectiles (radial offset).	218

12.13 Spin damping moment coefficient evolution as a function of the yaw angle, for different unbalanced projectiles (radial offset). . . .	218
12.14 Vertical shift in pitch moment coefficient as a function of the velocity, for the unbalanced projectiles considered in figure 12.12.	219
12.15 Slope increment in spin damping moment coefficient as a function of the velocity, for the unbalanced projectiles considered in figure 12.13.	219
12.16 Average pitch slopes as a function of the velocity, for the unbalanced projectiles considered in figure 12.12.	220
12.17 Average spin damping offset as a function of the velocity, for the unbalanced projectiles considered in figure 12.13.	220
12.18 Linear pitch contribution to be added as a function of the radial vertical offset of the CG.	220
12.19 Linear spin damping contribution to be added as a function of the radial horizontal offset of the CG.	220
12.20 Pitch moment coefficient evolution as a function of the yaw angle, for different unbalanced projectiles (radial + longitudinal offset). .	221
12.21 Linear pitch contribution to be added as a function of the longitudinal offset of the CG.	221
12.22 Pitch and yaw angles for a balanced (B) and unbalanced (U) projectile without initial perturbations. QE=1.4mils and MV=460m/s.	222
12.23 Height and drift deviations for a balanced (B) and unbalanced (U) projectile without initial perturbations. QE=1.4mils and MV=460m/s.	222
12.24 Pitch angle for a balanced (B) and unbalanced (U) projectile with $r = \pm 500 \text{ rad/s}$. QE=1.4mils and MV=460m/s.	223
12.25 Zoom on the first meter from figure 12.24.	223
12.26 Vertical deviation for a balanced (B) and unbalanced (U) projectile with $r = \pm 500 \text{ rad/s}$. QE=1.4mils and MV=460m/s.	224
12.27 Horizontal deviation for a balanced (B) and unbalanced (U) projectile with $r = \pm 500 \text{ rad/s}$. QE=1.4mils and MV=460m/s.	224

List of Tables

3.1	Characteristics of a conventional bullet and mortar.	30
3.2	Additional inputs for control scenario's	55
3.3	Comparison data on the Range for the 120mm mortar.	56
3.4	Firing scenario for FCT 155-AM-B.	70
3.5	Additional data as a function of the propellant charges.	70
3.6	Elevation control data.	71
3.7	Azimuth control data.	71
8.1	Grid characteristics for the SOCBT configuration in 2D axisymmetric	133
8.2	Grid Convergence Index [33] for the SST-T3 Model.	135
10.1	Thermal properties of the projectiles.	180
11.1	Geometric data allowing the stability analysis ($Tw = 27.6$ cal/turn).	204
11.2	Stability factors computations based on aerodynamic coefficients calculated using CFD.	205
12.1	9-mm bullet characteristics with and without mass unbalance. . . .	211
12.2	9-mm bullet with unbalance: analytical offset predictions.	213

Chapter 1

Introduction

Once the projectile has left the propulsion environment, i.e. the barrel and the exit effects known as the **initial percussion** (Fig.1.1¹), it enters the field of **exterior ballistics**.

The projectile in flight is thus no longer constrained in its movements, which were previously limited by the walls of the barrel, and like any free body, it is able to develop complex movements that are sometimes considered unpredictable for an unsuspecting user.

As soon as it transitions out of the barrel, it is mainly subjected to gravity

and to the forces applied by the complex flow around its body, but also to the force induced by its rotation, whether it was induced by the grooves of the barrel or whether it is induced later thanks to the fins designed for this purpose.

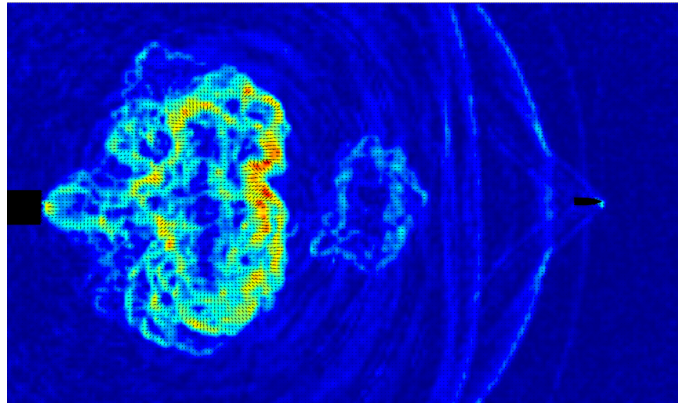


Figure 1.1: Initial percussion with Background Oriented Schlieren (BOS) imaging technique, processed by A. Moumen - ABAL [154].

¹Background Oriented Schlieren (BOS) = Technique for flow visualization and quantification of density gradients in fluids.

Although exterior ballistics is often generalized as the science that studies the trajectories of projectiles in flight, there is a need to clarify its practical applications and the benefits of studying these trajectories in detail.

The problem for any user of a weapon system is the so-called **indirect problem**: knowing the position of a target, he wants to obtain the orientation to give to the barrel in order to hit that target. Depending on whether or not he is able to see his target, we will speak of **direct fire** or **indirect fire**, illustrated with two examples on figures 1.2 and 1.3.



Figure 1.2: **Direct fire** - M1A2C Abrams tank with a 120-mm smooth bore.



Figure 1.3: **Indirect fire** - 120-mm mortar.

In terms of calculation, the indirect problem is actually the last layer in a long calculation process, the first layer being the **design process** (Fig.1.4). For each type of application, terminal ballistics has already determined the effects to be achieved on the target and interior ballistics has given its position on certain limitations inherent to the projectile's propulsion, such as the maximum **Muzzle Velocity** (MV).

The aim of the design phase is consequently to give the projectile a geometry such that it will be able to guarantee optimal stability throughout its trajectory while ensuring the desired effects on impact. This notion of stability is essential in external ballistics and is often very popularized because of its complexity (literally and figuratively!).

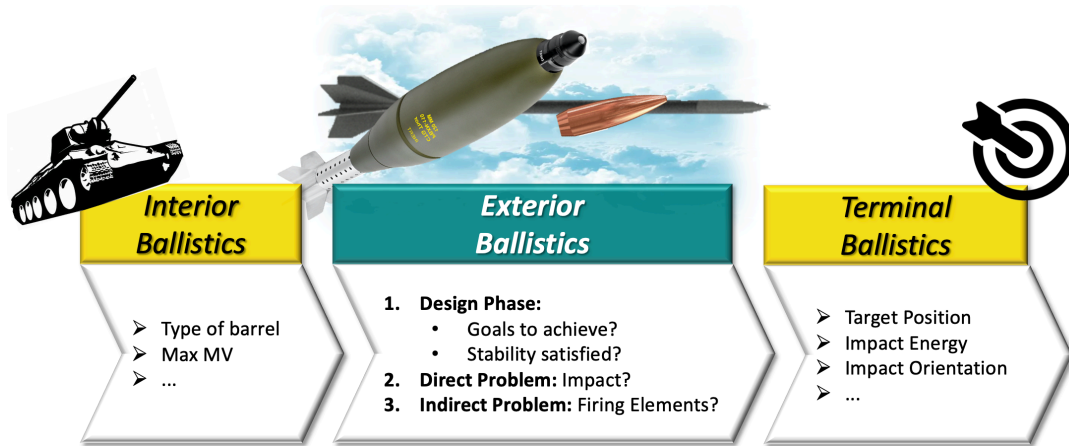


Figure 1.4: Complete ballistics cycle from weapon to target.

Together with the design phase comes the **direct problem**, which is to describe analytically or numerically the trajectory of the Center of Gravity (CG) of the projectile. In an ideal world, the permanent use of a super-complete and standardized model to predict the reality almost perfectly, would be an evidence. However, as in any real world, compromises have to be made to align accuracy and lightness of computation. Of course, these compromises cannot be made without a precise understanding of each physical phenomenon occurring in the air. The study of flight properties also allows the optimization of the choice of a certain type of projectile for a weapon system in a well-defined context. The market offers a multitude of products combining weapons and ammunition, but here again, to make the right choices, the right arguments based on reliable theories and calculations must be available.

- It is with this in mind that the first part of this work compiles the most relevant trajectory models and deals with the sensitive points of stability. This part also details the different tools implemented within the framework of this research to simulate the flight and behavior of a projectile. Starting from the most complete model, the 6 degrees of freedom model (6-DoF) [3], it will be possible to fully define the movements of the projectile and then make simplifications to lighten the calculations and the necessary input data [32, 137], within the limits of the different fields of application [11]. Indeed, the 6-DoF model will shed light on the need to have many basic input data, constituting a significant obstacle to the calculation of some trajectories, far more constraining than the computational load itself. And it is exactly this constraint that this work attempts to minimize.

- Besides the initial flight conditions that are often difficult to know, the most challenging inputs are the **aerodynamic coefficients**, necessary for the calculation of the various forces and moments applied to the projectile, as well as their damping, under the effect of the atmosphere. Several approaches can be used to determine these coefficients and have been the subject of much research for decades. The most recent being Computational Fluid Dynamics (CFD), it will be the subject of the second part of this work. In this part, the essential notions of CFD will be discussed in order to make the transition to the techniques developed to provide aerodynamic coefficients. The present research does not aim to optimize calculation methods for each type of projectile and each type of application, but is intended to present a global approach in order to determine in an efficient way a set of coefficients that can respond to the different layers of external ballistics: design and stability by means of parametric studies, direct calculation and indirect calculation.
- Finally, the third part will consider some more singular but also more concrete small-caliber applications for a ballisticians. The different speed regimes as well as the transition from one regime to another, the calculation features linked to the type of stabilization, or even the possibility of an asymmetrical projectile will be discussed.

If an exhaustive evolution of external ballistics has to be reconstructed, it would be necessary to retrace the military history over centuries, since already in the 18th century some literature is found that has improved the precision and efficiency of Western armies artillery [75, 186], with concepts that are still relevant today. The artillery community is by the way always at the origin of a lot of publications and attempts of standardization in the field of external ballistics. The best example is the NATO Artillery Ballistic Kernel (NABK), now renamed NATO Armaments Ballistic Kernel, which is a set of software packages dedicated to fire control, as part of the NAAG AC/225 LCG/3 SG/2 Sharable Software Suite (S4) [227]. While the first version appeared in 1998, in 2018 it was implemented in more than 20 countries, thanks to an increasingly wide and effective standardization².

²<https://www.army.mil/article/215516>. Feb 2021.

In another field, Franklin Ware Mann was one of the first ballisticians to publish theories for small arms bullets, with his work entitled "*The Bullet's Flight from Powder to Target*" in 1909 [127]. Ninety years later, after providing a large amount of experimental resources, Robert L. McCoy published his book entitled "*Modern Exterior Ballistics: The Launch and Flight Dynamics of Symmetric Projectiles*" [137], which is a key and unavoidable reference for many who have experienced ballistics.

However, ballistics has long remained an application based on analytic and empirical models [163, 245], with many rules of good practice. In parallel to this, publications in computational fluid dynamics have abounded in various aeronautical applications and many articles focus on the determination of what are known as projectile's aerodynamic coefficients. Still, only a few of them make the link between Rigid Body Dynamics (RBD) and CFD, by really showing the influence of input data on physical phenomena, as ballisticians have always done with experimental data. In sectors where it is a matter of designing complex systems such as vehicles or aircraft, performing calculations, even very heavy ones, has long been far less expensive than modifying the actual aircraft and testing it in flight³. In ballistics, on the other hand, the cost of testing has long been a more bearable effort than investment in computation, leaving ballistics experts lagging behind and numericians taking the lead in the field. This slow transition, together with numerous empirical upgrades, have nevertheless allowed the appearance of new projectile and missile configurations that are much more complex and sophisticated.

Virtual Fly-out is a more recent concept, instigated by Jubarah Sahu and Paul Weinacht with their teams from the US Army Research Laboratory (ARL) in the year 2000s [197, 200, 202, 260], relying on impressive computational resources and allowing the digital coupling of RBD and CFD. This concept has clearly motivated the advancement of this thesis and it is actually within this framework that this work finds its place: straddling the numerical and physical interpretation of concrete small-caliber applications, until now brought by analytical theories.

³<https://aerospaceamerica.aiaa.org/departments/why-were-not-there-yet-on-cfd>. Jan 2021.

The main strength and contribution of this thesis is to establish a strong link between two complementary but different scientific fields, namely that of exterior ballistics and CFD. This includes:

- A detailed and broad historical review of trajectory models, with didactic supporting illustrations, and of existing software packages.
- The implementation of an in-house 6-DoF model, allowing all the flexibility of handling in the context of research and user support:
 - Comparison with simplified models;
 - Choice of force and moment contributions;
 - Choice of integration method;
 - Fully controllable inertia tensor;
 - Immediate stability analysis.
- The development of a semi-automated CFD methodology, validated by published experiments and numerical results, to extract static and dynamic coefficients of fin- and spin-stabilized projectiles in the supersonic, transonic and subsonic regimes.
- An analysis of the Planar Pitching Method: The method is not new, but the discussion on input frequency is brought forward to nuance what seemed to be the norm for large caliber finned projectiles.
- The application of the CFD-RBD methodology to three small-caliber projectiles:
 - A non-lethal low-speed fin-stabilized projectile;
 - A spin-stabilized precision ammunition crossing the transonic domain;
 - A supersonic/transonic blunt spin-stabilized projectile with mass unbalance, extending the state-of-the-art that had mostly focused on large-caliber weapons.
- The design of three experimental setups to study the applications mentioned above, requiring the tailored manufacturing of the projectiles and specific adaptations to a pneumatic launcher for low velocities.

Part I

Exterior Ballistics

UNDERTAKING any kind of explanation in exterior ballistics confronts us with the chicken-and-egg situation: **Where to start?**

Is it necessary to first discuss the stability of a projectile, which can be understood by means of the forces that apply to it, before talking about the forces themselves, or should we first of all talk about the forces that apply but that depend on the type of stability? The choice has been made to approach stability in a simple intuitive way and then approach trajectory models as a function of forces and stability, and thereafter supplement this with a more detailed analysis of stability based on the results of this work.

All the models discussed in part I have been implemented in LabVIEW 2020⁴, with detailed explanations and supporting validation illustrations. The implementations performed will be presented under the name **VTraj** in order to make the distinction with the references used. LabVIEW programming language is clearly not the most optimized for this type of calculation from a CPU-time perspective, but thanks to the built-in graphical user interface (Fig. 1.5), it allows visualizing simultaneously a large number of phenomena isolated from one another, which is one of the didactic objectives of this research. This piece of software is also ABAL Department's software of choice, used by the majority of technicians in the ballistics laboratory.

Since ballistics is a specific application of classical mechanics, it could claim to have its own conventions. However, as there is no real major reference in the field of external ballistics, these conventions are clearly embedded in all sorts of conventions specific to the laboratory from which they emanate, which makes any review very challenging. The numerous existing 6-DoF codes use various mathematical models, with different notations and numerical schemes, which leads to confusion, individually as well as in international working groups [272].

⁴<https://www.ni.com/fr-be/shop/labview.html>

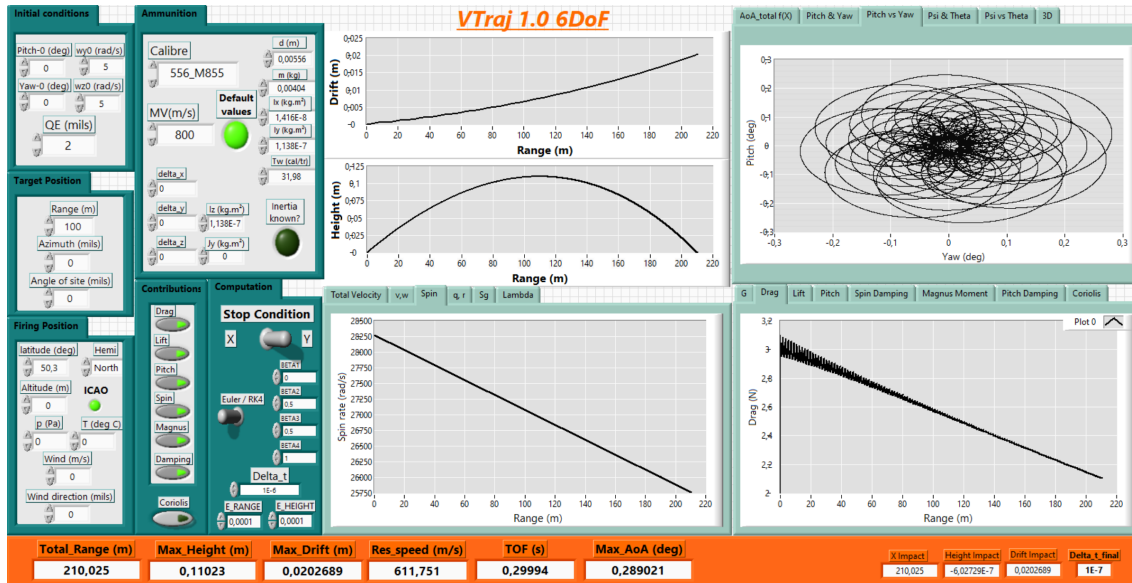


Figure 1.5: LabVIEW Graphical Interface VTraj - Direct generalized 6-DoF Model.

Standardization via NATO is progressing well, but the software suite⁵ which is maintained by professional programmers is difficult to access and considers operational much more extensive aspects than the flight of the projectile, which makes the amount of subroutines and inputs/outputs considerable. The effort of this first part is then really to analyze in details all the "active" models and to keep as much as possible the conventions specific to ballistics, according to the bases which are taught in the ABAL department.

Many articles allowing the implementation of theories as well as the validation of results come from the US Army Research Laboratory⁶ (ARL, formerly called BRL), which has an impressive library of archives and instrumental, experimental and computational resources, difficult to equal here in Belgium. One of their branches also has the lead of the NATO group for NABK development and quality assurance. References to and from this department will therefore regularly appear in the course of this work.

⁵NAAG AC/225 LCG/3 SG/2 Sharable Software Suite (S4)[227]

⁶<https://www.army.mil/>

Chapter 2

Prologue to stability

Everybody has already in his youth (youth being a relative notion...) built a paper airplane thinking it was going to fly very well, but very quickly saw himself completely defeated because after not even two meters that airplane crashed miserably. This upsetting event is actually caused by a stability problem. The mass distribution of this aircraft, combined with the exposure of the surfaces facing the airflow, resulted in an uncontrolled tilting of the aircraft's nose leading to its loss.

Of course, we cannot afford this kind of phenomenon with a projectile that has to travel several hundred or even several thousand meters in a carefully predictable way. Let's take a so-called "classical" projectile (Fig.2.1). This projectile generally consists of a cylindrical part, an ogive at the front, with a hole or a meplat, and

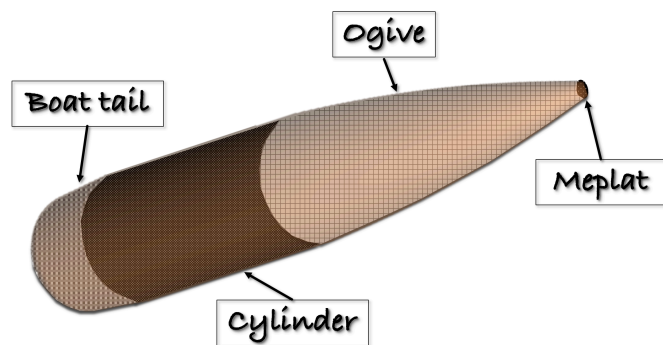
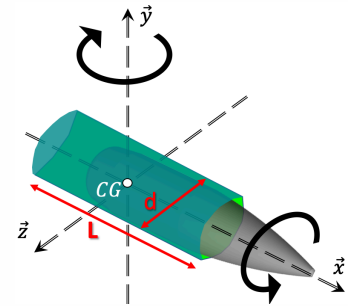


Figure 2.1: Conventional symmetric bullet.

sometimes a boat-tail at the rear. This projectile should be rotationally symmetrical about its longitudinal axis and is considered as rigid: this implies that each transverse axis passing through the center of gravity is considered as a principal axis of inertia (Box 2.1).

Box 2.1: The axial and transverse moments of inertia...

A moment of inertia determines the resistance required to perform a certain angular acceleration about an axis of rotation and depends on the body's mass distribution. Given the axisymmetric shape of a projectile, only I_x and I_y which are respectively the principal moments of inertia in the longitudinal and transversal directions, are expressed. Those moments are given here for a cylinder, to give an idea of the dimensions' influence on the respective moments of inertia, which are essential for further study.



$$I_x = \frac{1}{2}m\left(\frac{d}{2}\right)^2$$

$$I_y = \frac{I_x}{2} + \frac{mL^2}{12}$$

In addition to its own weight and inertia, when this projectile is moving in the air, it is confronted with two types of forces at each point on its surface: skin friction forces and pressure forces¹. These forces have distinct mechanisms at the contact surface but what is considered, is the resultant of these forces at each point of the trajectory, and it is known that given the speed of a projectile, the amplitude of the pressure forces are far greater than the friction forces [95]. Their effect is therefore what is highlighted here intuitively in figure 2.2.

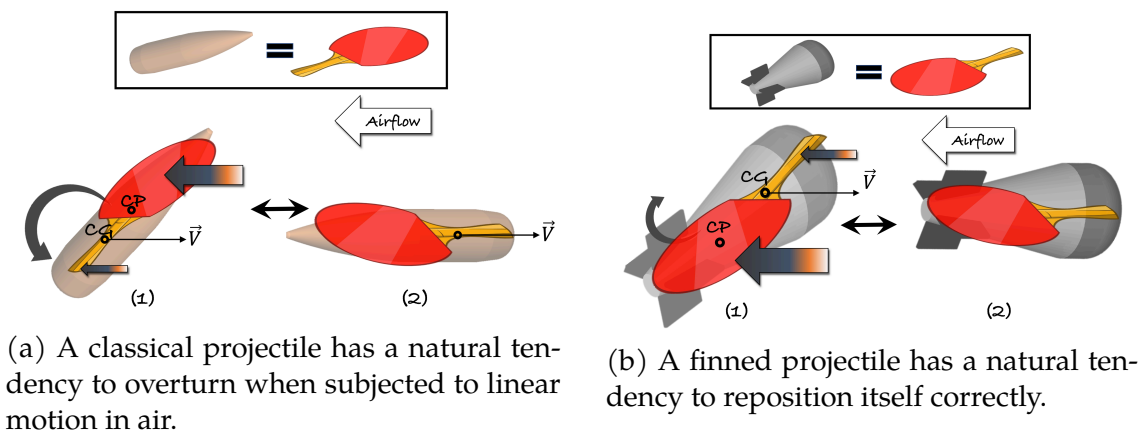


Figure 2.2: Static stability.

If a tennis table racket is flown with the handle backwards at first, and with a certain inclination, also called an **angle of attack** (Fig.2.2a-1), the force exerted by the air on the playing surface will be much greater than the force exerted on the handle, causing the playing surface to tilt upwards and backwards (Fig.2.2a-2).

¹With possible extra pressure force generated when shock waves are formed due to a local velocity near the surface of the projectile near Mach 1 [29].

However, if the same racket is flown with the handle forward (Fig.2.2b-1), the force exerted on the playing surface being always higher, it will swing backwards again, but in the opposite motion, with a more direct movement (Fig.2.2b-2). The larger surface area at the rear is associated to the fins of the projectile illustrated on the right.

For a conventional projectile (Fig.2.2a), the mass distribution (position of the **Center of Gravity**(CG)) is more rearward and the pressure distribution (position of the **Center of Pressure**(CP)) is more forward, which causes the projectile to tumble nose backwards if no further action is taken. In this case we are talking about a **statically unstable** projectile. To avoid this overturning problem and to ensure that the projectile remains stable on its trajectory, we take advantage of the gyroscopic effect (See Box.2.2). Thanks to the grooves in the weapon, rigorously designed for each type of projectile, an axial rotational motion is "imprinted" on the projectile, hence the name **gyroscopically stabilized** or **spin stabilized** projectiles [64]. This motion will generate a **precession** motion around the velocity vector, similar to that of a gyroscope, making the projectile's orientation much more robust in contact with air. The pressure forces that had a very unfavorable impact on an unstabilized projectile will now have only a limited influence on the latter. Moreover, it will be able, just like the gyroscope, to recover a stable position, even if an additional disturbance is added (See Chapter 5). In this case the projectile is said to be **dynamically stable**.

Thanks to the damping phenomena that will be detailed in chapter 5, the projectile remains on a predictable trajectory. However, this possible stabilization by gyroscopic effect has limits: when the projectile becomes too long, its transversal moment of inertia I_y becomes oversized and stability is no longer guaranteed, it is then necessary to switch to another stabilization method, which is the stabilization by fins [63].

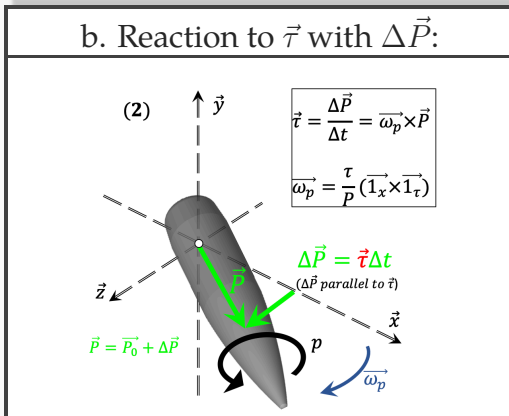
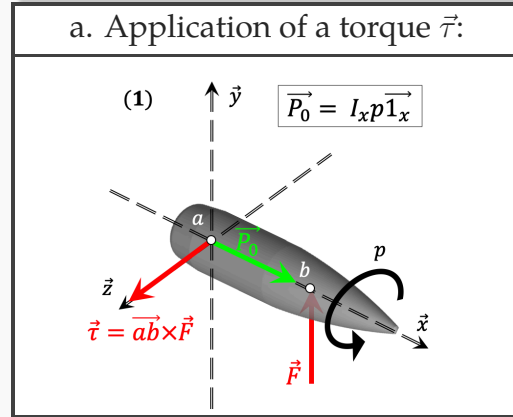
In that case, we take advantage of the situation of the inverted tennis table racket (Fig.2.2b) by placing fins at the rear of the projectile to reverse the distribution of mass and pressure. This means that when an angle of attack appears (which is almost always the case in the beginning of a trajectory), the projectile will naturally reposition itself correctly on its path. That's why the term **statically stable** is used to describe a **fin-stabilized** projectile (Box 5.1).

Box 2.2: Gyroscope principle

The reaction of a gyroscope is not what one might call "intuitive". However, it is interesting to understand the simple origin of this rather surprising reaction; the two schematics below explain the reaction of the gyroscope, directly materialized by a projectile.



Box (a) represents the initial situation where \vec{P}_0 is the initial spin angular momentum along the longitudinal axis of the projectile, the latter having been set in clockwise rotation in the direction of flight by the grooves of the barrel at rate p [rad/s]. If a force \vec{F} is applied for a time interval Δt in the \vec{y} -direction and at a distance \vec{ab} from the center of gravity, a torque $\vec{\tau}$ is created in the \vec{z} -direction.



This torque causes a change in angular momentum with a quantity $\Delta\vec{P}$ proportional to $\vec{\tau}$ and Δt in exactly the same direction as $\vec{\tau}$. The reaction of the nose of the projectile will then be to follow the resultant $\vec{P} = \vec{P}_0 + \Delta\vec{P}$ and therefore exert a clockwise movement at angular rate $\vec{\omega}_p$, shown in box (b).

Consequently, if a projectile has for instance an initial vertical yaw angle, a perturbing torque (=overturning moment) will occur and will tend to push the nose more upwards, but given the axial rotation, the nose will turn to its right. The total yaw angle will finally be the resultant of the original yaw (vertical) and the so-called gyroscopic yaw (horizontal). The nose therefore moves clockwise and this movement will be repeated continuously given the omnipresence of the overturning moment. This rotation motion is called the **Precision**, with angular rate $\vec{\omega}_p$. If another perturbation is added (such as the initial percussion or the curvature of the trajectory), an additional rotation frequency will be superimposed to the precession and is called the **Nutation** [63].

Chapter 3

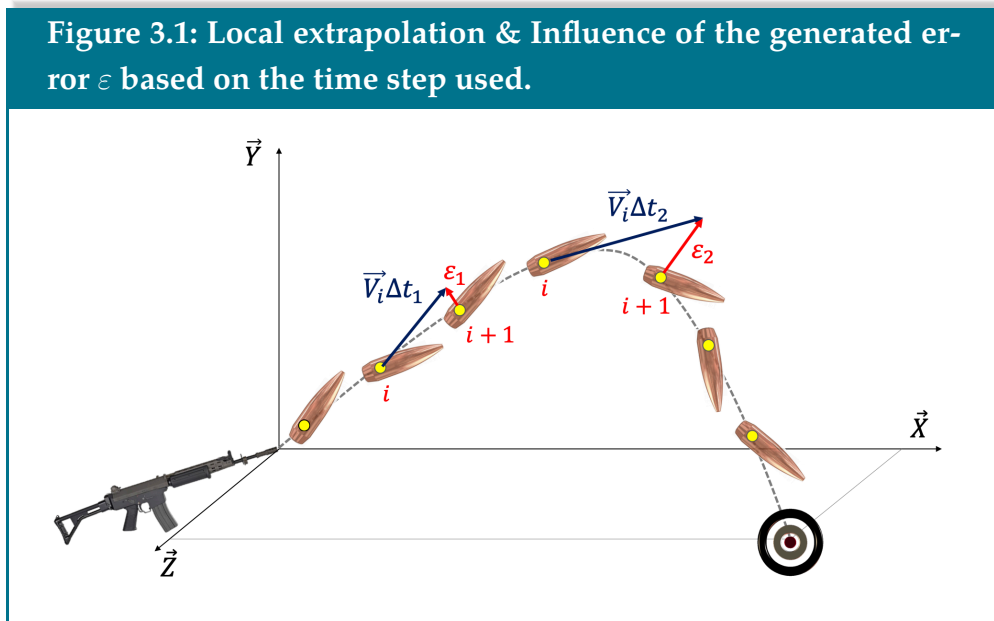
Trajectory Models

3.1 Trajectory computation

There are different trajectory models depending on the equations and the terms that are included, which will be discussed in this chapter. There is even the possibility of considering hybrid crossovers between the models for particular applications. Since in most cases there is no analytical solution, the practical construction of a trajectory is always done in the same way by discretizing the model's equations in time. Next, it is a matter of considering the initial position and initial conditions of a projectile that exits the tube, materialized by its center of gravity, and progressing in time in order to calculate the successive positions of this center of gravity. Between each calculation point, the external forces acting on the projectile will change, which means the calculation must adapt to these changes as a function of time throughout the trajectory. It is clear that the smaller the time increment, the closer the calculation gets to reality, since it is able to capture more changes. Figure 3.1 shows that for a time step $\Delta t_2 > \Delta t_1$, the magnitude of the error induced (ε) on the position of the center of gravity will be much larger. The curvature of the trajectory will also have an impact on the choice of the time step, which can also be variable in order to adapt to this curvature. Of course, a reduced time step has a cost, which must be borne in mind, along with the model that will be used.

Starting from a model that considers a maximum of effects (6-DoF model), where it will be essential to use a very small time step, it is possible for some applications to accept the hypothesis that the effects on the projectile remain constant for a longer period of time and that the time step can therefore increase drastically (MPMM - PMM). This aspect may seem obvious, but it is still the reason why the

operational models we have today in our weapon systems are not yet the most complete model we know: **because of the calculation time**¹.



Before starting detailing the models, it is also important to specify that in order to align with the academic conventions and the NATO agreement dealing with trajectory models, the axis system used for the ground (capital letters) as well as for the body (lowercase) is the ballistic one and not the conventional Atmospheric Flight Mechanics (AFM) coordinates system, as it is found in most publications dealing with 6-DoF models. Although both models use a right hand coordinate system with \vec{X} positive forward, \vec{Y} is pointing upwards and \vec{Z} is pointing to the right when looking downrange (also represented in figure 3.1 for the ground), as opposed to the conventional reference system where the \vec{Z} -axis points downwards and the \vec{Y} -axis points to the right. Depending on the frame of reference in which we are located (sec. 3.2.1), different notations of angles and angular velocities are used, but it will always be referred to **pitch** motion for the vertical rotation rate about \vec{z} -axis (r or $\dot{\alpha}$ if expressed with respect to \vec{z}_a in figure 3.2) and to **yaw** motion for the horizontal rotation rate about \vec{y} -axis (q or $\dot{\beta}$ if expressed with respect to \vec{y}_a in figure 3.2)². The spinning or rolling motion is about the \vec{x} -axis (p in figure 3.2).

¹The illustration was given for an Euler-type integration, the most commonly used integration scheme are the Runge-Kutta 4th and 7th order [137], which will be detailed in section 3.3.2.

²Pitching- and yawing-axis motions are therefore reversed compared to the Atmospheric Flight Mechanics conventions.

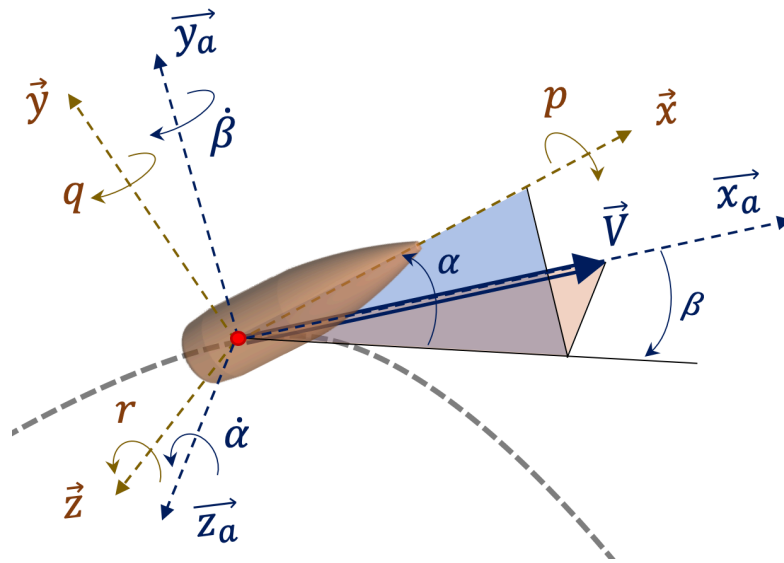


Figure 3.2: Typical angular rates in ballistic conventions. $\vec{x}, \vec{y}, \vec{z}$ referring to the body axis system and $\vec{x}_a, \vec{y}_a, \vec{z}_a$ to the velocity vector, with \vec{x}_a tangent to the trajectory and \vec{y}_a, \vec{z}_a perpendicular to the latter.

This conversion is a priori trivial, but for the 6-DoF model and the necessary work with rotation matrices, the unaware reader could encounter difficulties when converting variables between different frames, given the non-commutativity of the rotation matrices, and could make mistakes in the conventions to determine the initial and final conditions.

For trajectory computations, the ballistic coordinate system is more convenient for different reasons:

- * As most weapon systems have a right-hand twisted barrel, clockwise rotations as well as upward and rightward motions will be defined positively in this coordinate system. The lateral deviation of the projectile from the launch axis is called the **drift**.
- * For simpler models where lateral drift is not taken into account, the model is then displayed in two dimensions $X - Y$. The ballistic system then allows to simply "drop" the third axis Z to keep the same conventions as in more "complete" models.

3.2 The 6-DoF Model

This Rigid Body Dynamic (RBD) model is widely used outside the field of ballistics, mainly in aeronautics, and the references describing it are excessively abundant. Nicolaidis [163] is one of the first references cited in the field of ballistics in the early 1950s, but many technical notes from different defense research laboratories also appeared between the 60s and the 90s [18, 19, 40, 66, 67, 86, 131, 158, 213].

The works of Vaughn [245] and Amoruso [3] were however taken as a baseline for the implementation of our in-house 6-DoF model. These documents respectively make the link with the linear theory which will be discussed in section 3.6 and the different body-fixed, plane-fixed and aeroballistic coordinate systems explained in the following paragraphs. As the calculations in these references have been made in the AFM reference frame, all the steps have been converted here into a ballistic point of view, and are illustrated in this section.

3.2.1 Coordinate Systems & Transformation Matrices

The complexity of the 6-DoF model for a single rigid body does not come from the equations that compose it but rather from the need to switch between different reference frames, fixed and mobile, in order to give the user a set of coordinates (in the case of the direct problem) or a set of firing elements (in the case of the indirect problem) that can be used in the reference frame of his weapon system. The various coordinate systems are defined below and can be seen in figures 3.3-3.4.

Inertial Reference Frame

Although Earth is not an inertial (unaccelerated) reference frame, it is convenient as baseline to observe the motion of a projectile in flight. This is why the Earth is used as a so-called inertial frame of reference in classical mechanics to be able to use Newton's laws, and the Coriolis and Centripetal accelerations are added a posteriori to account for its rotation (Sec. 3.2.4). This first frame has therefore its origin at the center of the Earth (Fig. 3.3).

→ Notation : $\vec{X}_i, \vec{Y}_i, \vec{Z}_i$ with \vec{X}_i positioned at the intersection of the Equator and the Greenwich meridian, \vec{Y}_i passing through geographic North Pole and \vec{Z}_i completing the triad.

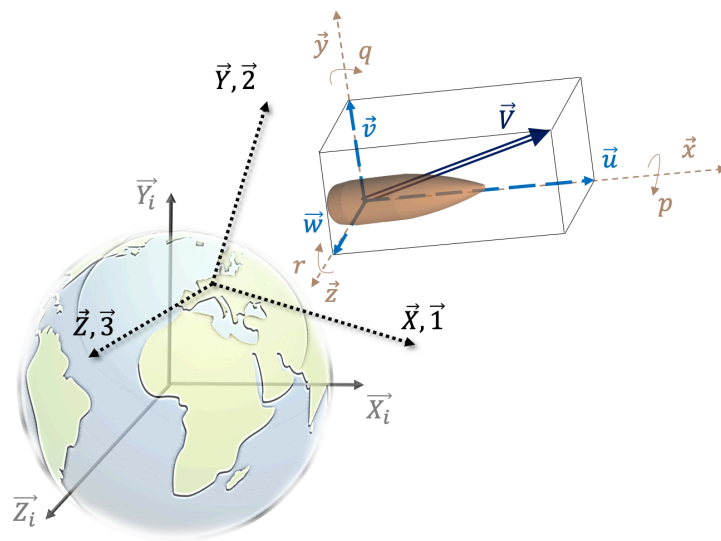


Figure 3.3: From the Inertial to the Body-fixed Coordinates.

Ground-fixed Frame

The Ground-fixed (or Earth-fixed) frame has its origin fixed at the launch point. In principle, this is where the fixed user is located. If the latter is mobile, this reference frame will still be the basis for the interception calculation (Fig. 3.3).

→ Notation : $\vec{X}, \vec{Y}, \vec{Z}$ or $\vec{1}, \vec{2}, \vec{3}$.

Body-fixed Frame

This frame has its origin at the center of gravity (CG) of the projectile and spins with the projectile, sharing all its angular motions. This frame is mostly used for fin-stabilized projectiles trajectories [84]. The x-direction corresponds to the axial axis of symmetry of the projectile (Fig. 3.4).

→ Notation : $\vec{x}, \vec{y}, \vec{z}$ with respective rotation rates p, q, r .

Plane-fixed Frame

This frame is a non-rolling body-fixed coordinate frame⁴ often used for 6-DoF computer simulations of spin stabilized projectiles: the frame yaws and pitches with the projectile but does not roll with it [3, 268]. As spin stabilized projectiles reach typical spin rates of hundreds of revolutions per second, the body-fixed frame would require an extremely small integration time step and totally unsatisfactory simulation times.

→ Notation : $\vec{x}, \vec{y}, \vec{z}$ with respective rotation rates Ω_x ⁵, q, r .

³The notation $\vec{1}, \vec{2}, \vec{3}$ is used for the Lieske-McCoy 6-DOF Model (Sec. 3.4)

⁴Called zero-roll frame in NATO terms [1]

⁵ Ω_x is detailed hereafter and given in equation 3.13

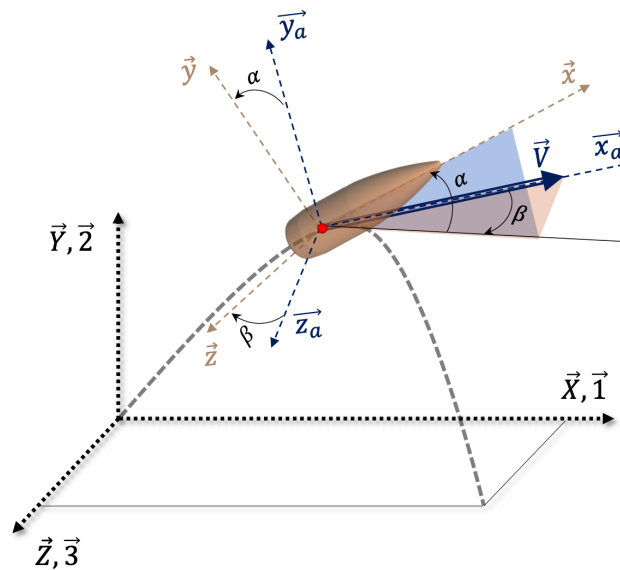


Figure 3.4: Body and Velocity frames vs Ground-fixed coordinates.

Aeroballistic Frame

This is a non-rolling, non spinning body-fixed coordinate frame⁶ used as starting point for the linearized 6-DoF Theory (Sec. 3.6.)

→ Notation : $\vec{x}, \vec{y}, \vec{z}$ with respective rotations rates $0, q, r$.

Velocity Frame

This frame has its origin at the center of gravity of the projectile and is aligned with the velocity vector [245]. The axis \vec{x}_a is tangent to the trajectory, \vec{y}_a perpendicular to the trajectory and pointing upwards in the plane of the trajectory, while \vec{z}_a completes the triad to the right when looking downrange. This frame does not roll with the projectile but is useful for the description of aerodynamic forces and moments [2]. A pitch angle, α , is defined as positive when the projectile's nose points upwards with respect to the velocity vector and an angle of yaw (= sideslip), β , is defined as positive when the projectile's nose points to the right (again, when looking downrange) with respect to the velocity vector (Fig. 3.4).

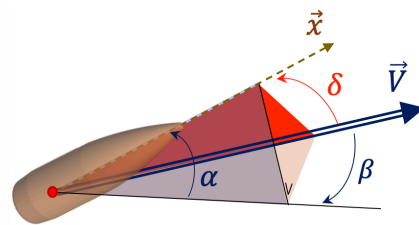
→ Notation : $\vec{x}_a, \vec{y}_a, \vec{z}_a$ with respective rotation rates $0, \dot{\beta}, \dot{\alpha}$.

⁶Called zero-spin frame in NATO terms.

It is usual to find transformation matrices for rotations with Euler angles from the Ground-fixed coordinates (considering in the first instance that the earth is fixed) to the moving body-fixed coordinates. Yet, the necessary transformation for trajectory simulations is the reverse one : it is first necessary to compute the acceleration, velocity and position of the projectile in its own frame and then convert it into the Ground-fixed coordinates, in order to give a solution to the user. Furthermore, for this application, Bryant's angle will be rather used, because the three rotations occur around the three different axes [77].

Box 3.1: Yaw vs Yaw...

Modern Exterior Ballistics uses the terms "yaw" or "yawing motion" to describe any movement of the nose of the projectile with respect to its velocity vector [137]. AOP-65 [14] defines with other words the yaw as *"the angle between the longitudinal axis of a projectile at any moment and the tangent to the trajectory."* However, it is sometimes necessary to make a distinction between the vertical movement of the nose of the projectile, which is the **"pitch", or "angle of attack", in the form of α** , and the horizontal movement of the nose of the projectile, which is the **"yaw" or "angle of sideslip", β** . Any combination of pitching and yawing motion will however be referred as "yaw" when no ambiguity is possible, in the form of δ .



Nose angles relative to velocity vector.

For small angles:

$$\sin \delta = \sqrt{\sin^2 \alpha + \sin^2 \beta \cos^2 \alpha} \\ \approx \sqrt{\alpha^2 + \beta^2}$$

NB: The plane containing \vec{x} and \vec{V} is called the **yaw plane**.

Linear Motion

Figures 3.5-3.7 show the three sequences of the transformation from Ground to Body-fixed axis. The sequence order is important since rotations do not commute.

1. The first rotation starts from the Ground-fixed coordinates and is about the second axis, Y , with amplitude θ . Since a drift to the right is considered to be positive (as shown in figure 3.5), the rotation matrix must be considered with $-\theta$ ($-\pi < \theta < \pi$)⁷. This leads to the new coordinates x_1, Y, z_1 .

$$R_Y(-\theta) = \begin{bmatrix} \cos \theta & 0 & \sin \theta \\ 0 & 1 & 0 \\ -\sin \theta & 0 & \cos \theta \end{bmatrix} \quad (3.1)$$

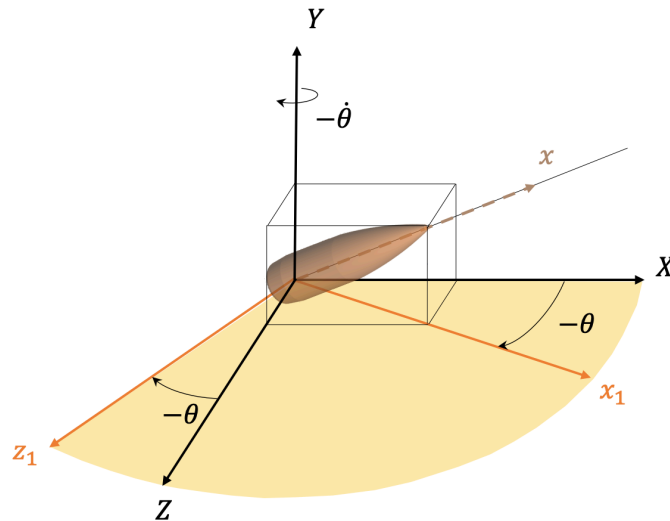


Figure 3.5: Y-Z-X sequence of rotations with Bryant's angles: 1st Rotation around Y.

2. The second rotation is about the third "new" axis z_1 with an angle ψ , positive when the nose is pointing upwards ($-\frac{\pi}{2} < \psi < \frac{\pi}{2}$). This leads to new coordinates x, y_2, z_1 (Fig. 3.6).

$$R_{z_1}(\psi) = \begin{bmatrix} \cos \psi & \sin \psi & 0 \\ -\sin \psi & \cos \psi & 0 \\ 0 & 0 & 1 \end{bmatrix} \quad (3.2)$$

⁷ $-\theta$ is used to keep the same orientation conventions as the rotation matrices.

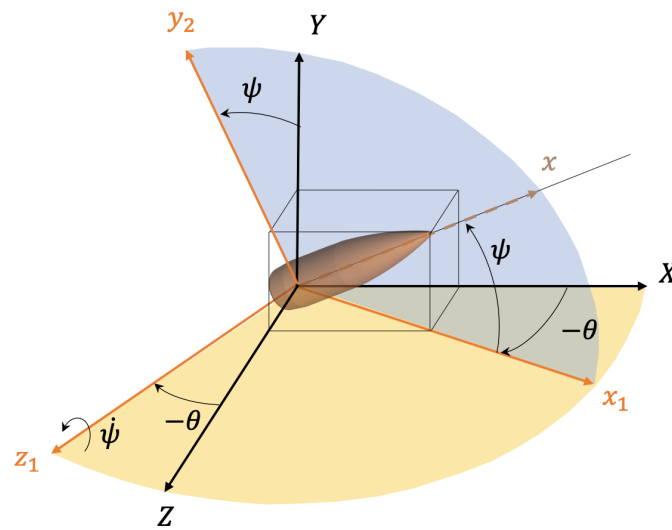


Figure 3.6: Y-Z-X sequence of rotations with Bryant's angles: 2nd Rotation around z_1 .

3. The third rotation about x is the roll angle ϕ , positive clockwise ($0 \leq \phi < 2\pi$, and this leads finally to the Body-fixed coordinates x, y, z (Fig. 3.7).

$$R_x(\phi) = \begin{bmatrix} 1 & 0 & 0 \\ 0 & \cos \phi & \sin \phi \\ 0 & -\sin \phi & \cos \phi \end{bmatrix} \quad (3.3)$$

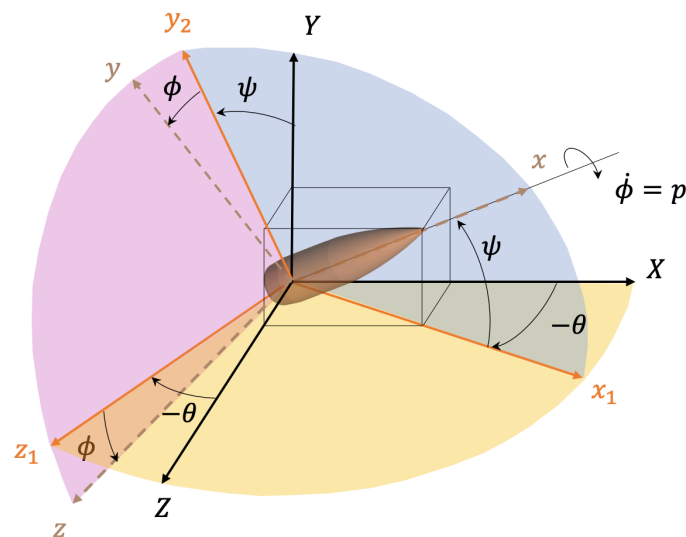


Figure 3.7: Y-Z-X sequence of rotations with Bryant's angles: 3rd Rotation around x .

The global conversion is finally ($c \equiv \cos$; $s \equiv \sin$):

$$\begin{pmatrix} x \\ y \\ z \end{pmatrix} = R_x(\phi)R_{z_1}(\psi)R_Y(-\theta) \begin{pmatrix} X \\ Y \\ Z \end{pmatrix} \quad (3.4)$$

$$\begin{pmatrix} x \\ y \\ z \end{pmatrix} = \begin{bmatrix} c\theta c\psi & s\psi & s\theta c\psi \\ -c\theta s\psi c\phi + s\theta s\phi & c\psi c\phi & -s\theta s\psi c\phi - c\theta s\phi \\ -c\theta s\psi s\phi - s\theta c\phi & c\psi s\phi & -s\theta s\psi s\phi + c\theta c\phi \end{bmatrix} \begin{pmatrix} X \\ Y \\ Z \end{pmatrix} \quad (3.5)$$

To finally obtain the transformation from Body to Ground-fixed axis, rotation matrix 3.5 has to be inverted: the order of the rotation sub-matrices has to be reversed, together with the signs of the angles. Or, since matrix 3.5 is orthogonal, the inverse matrix is simply the transpose one.

$$\begin{pmatrix} X \\ Y \\ Z \end{pmatrix} = R_Y(\theta)R_{z_1}(-\psi)R_x(-\phi) \begin{pmatrix} x \\ y \\ z \end{pmatrix} \quad (3.6)$$

**Transformation Matrix for Linear Motion
from Body to Ground-fixed coordinates:**

$$\begin{pmatrix} X \\ Y \\ Z \end{pmatrix} = \begin{bmatrix} c\theta c\psi & -c\theta s\psi c\phi + s\theta s\phi & -c\theta s\psi s\phi - s\theta c\phi \\ s\psi & c\psi c\phi & c\psi s\phi \\ s\theta c\psi & -s\theta s\psi c\phi - c\theta s\phi & -s\theta s\psi s\phi + c\theta c\phi \end{bmatrix} \begin{pmatrix} x \\ y \\ z \end{pmatrix} \quad (3.7)$$

The work with a plane-fixed approach implies by definition that $\phi = 0$ and therefore the third rotation matrix does not interact with the global transformation matrix.

Angular Motion

In the same way as the conversion of linear motions, angular rates $\vec{\Omega}$ will have to be converted using the Bryant angular rates [3, 48].

$$\vec{\Omega} = \vec{\Omega}_\theta + \vec{\Omega}_\psi + \vec{\Omega}_\phi = \Omega_x \vec{1}_x + \Omega_y \vec{1}_y + \Omega_z \vec{1}_z \quad (3.8)$$

Using matrices 3.2 and 3.3, it comes that:

$$\vec{\Omega}_\theta = R_\phi R_\psi \begin{pmatrix} 0 \\ \dot{\theta} \\ 0 \end{pmatrix} = \begin{pmatrix} \dot{\theta} \sin \psi \\ \dot{\theta} \cos \phi \cos \psi \\ -\dot{\theta} \sin \phi \cos \psi \end{pmatrix} \quad (3.9)$$

$$\vec{\Omega}_\psi = R_\phi \begin{pmatrix} 0 \\ 0 \\ \dot{\psi} \end{pmatrix} = \begin{pmatrix} 0 \\ \dot{\psi} \sin \phi \\ \dot{\psi} \cos \phi \end{pmatrix} \quad (3.10)$$

Since the components of $\vec{\Omega}_\phi$ are parallel to the x-axis, $\vec{\Omega}_\phi = \begin{pmatrix} \dot{\phi} \\ 0 \\ 0 \end{pmatrix}$.

**Angular velocity $\vec{\Omega}$ of the frame
in terms of Bryant's angles derivatives:**

$$\begin{pmatrix} \Omega_x \\ \Omega_y \\ \Omega_z \end{pmatrix} = \begin{bmatrix} 1 & \sin \psi & 0 \\ 0 & \cos \phi \cos \psi & \sin \phi \\ 0 & -\sin \phi \cos \psi & \cos \phi \end{bmatrix} \begin{pmatrix} \dot{\phi} \\ \dot{\theta} \\ \dot{\psi} \end{pmatrix} \quad (3.11)$$

**Bryant's angles derivatives
in terms of Angular velocity $\vec{\Omega}$ of the frame:**

$$\begin{pmatrix} \dot{\phi} \\ \dot{\theta} \\ \dot{\psi} \end{pmatrix} = \begin{bmatrix} 1 & -\cos \phi \tan \psi & \sin \phi \tan \psi \\ 0 & \frac{\cos \phi}{\cos \psi} & -\frac{\sin \phi}{\cos \psi} \\ 0 & \sin \phi & \cos \phi \end{bmatrix} \begin{pmatrix} \Omega_x \\ \Omega_y \\ \Omega_z \end{pmatrix} \quad (3.12)$$

For the plane-fixed approach ($\dot{\phi} = \dot{\theta} = 0$, $\Omega_y = q$, $\Omega_z = r$):

$$\Omega_x = \dot{\theta} \sin \psi = q \tan \psi \quad (3.13)$$

$$\dot{\theta} = -\frac{q}{\cos \psi} \quad (3.14)$$

$$\dot{\psi} = r \quad (3.15)$$

Remark: Although this parameter is not the most important one, it is possible a posteriori to estimate the roll angle which had been assumed to be null with the plane-fixed approach via relation 3.16 [268].

$$\phi(t) = \int_0^t (p + \dot{\theta} \sin \psi) dt \quad (3.16)$$

The use of Bryant (or Euler) angles implies the occurrence of singularities in the transformation matrices and in particular for $\psi = \pm \frac{\pi}{2}$ in matrix 3.12. Considering the definition $-\frac{\pi}{2} < \psi < \frac{\pi}{2}$, this does not represent a problem in most cases (except for some vertical climb and dive trajectories) since in fact, exceeding this limit would physically correspond to a total vertical overturning of the projectile. On the other hand, this demonstrates the need to reconsider the whole reasoning of the rotations with a physical sense for each angle: the 90° conversion of the AFM procedure would not at all have the same implications in terms of singularities and results!

Another approach to avoid these singularities when working with the body coordinates is the use of quaternions (the singularity remains in the aeroballistic frame [3]). The procedure is less visual and more mathematical but is implemented in the new codes supporting indirect fire, for the attitude integration [52, 84]. Amuroso [3] provided the link between Euler's angles and quaternions in the 6-DoF implementation. Quaternions are a quadruplet of operators (3 rotation operators and a scalar part), that can be considered as generalized complex numbers. For instance, the complex number $i = \sqrt{-1}$ can be considered as a rotation operator from real to the imaginary axis (90°). Rotations around X , Y and Z can therefore be handled with such imaginary rotation operators (i , j and k). What the quaternions formalism lacks in intuitive representation of rotations - compared to the Euler angle representation - is compensated by the simplicity of its rotation matrix, which is more efficient in terms of calculation than its Euler counterpart. Indeed, quaternions allow to speed up the calculations by lightening the code (4 elements instead of 3×3 matrices) and by increasing the time step by imposing constraints to the operators on the basis of the error evaluated at each previous iteration [83, 240].

As this work was the first implementation of a full 6-DoF model in ABAL department, without reference software to validate the calculations, the use of Bryant's angles was preferred to ensure physical understanding. A later version will use quaternions to optimize the code.

3.2.2 Equations of Motions

Implementation of the 6-DoF model follows Newton's laws of motion which state that the time rate of change of linear momentum equals the sum of all the externally applied forces, and the time rate of change of angular momentum equals the sum of all the externally applied moments [137]. This forms two major equations, one in **translation** (Eq.3.17) and the other in **rotation** (Eq.3.18), with constant I and m :

$$\Sigma \vec{F} + m\vec{g} = m \frac{d\vec{V}}{dt} \quad (3.17)$$

$$\Sigma \vec{M} = \bar{I} \frac{d\vec{\omega}}{dt} \quad (3.18)$$

Where:

- m Projectile mass;
- \bar{I} Projectile moment of inertia tensor;
- \vec{g} Acceleration due to gravity;
- \vec{V} Total linear velocity vector (u, v, w) in body-fixed coordinates;
- $\vec{\omega}$ Total angular velocity vector (p, q, r) in body-fixed coordinates ;
- $\Sigma \vec{F}$ Vector sum of all the aerodynamic forces;
- $\Sigma \vec{M}$ Vector sum of all the aerodynamic moments
(with respect to the center of gravity);

Equations 3.17 and 3.18 are only valid in an inertial coordinate frame, which is not the case for a projectile in a moving reference frame. These equations must therefore include an additional term to account for the frame rotations and become:

$$\Sigma \vec{F} + m\vec{g} = m \frac{d\vec{V}}{dt} + \vec{\Omega} \times m\vec{V} \quad (3.19)$$

$$\Sigma \vec{M} = \bar{I} \frac{d\vec{\omega}}{dt} + \vec{\Omega} \times I\vec{\omega} \quad (3.20)$$

where $\vec{\Omega}$ is the angular velocity of the coordinate system.

The force vector \vec{F} contains applied forces such as aerodynamic (and thrust) forces, but also fictitious forces such as **centrifugal and Coriolis forces**, since we

are still referring to a non-inertial system (when the projectile flies in the air, the earth continues to rotate...). These forces will be detailed following the aerodynamic forces.

By rearranging expressions 3.19 and 3.20 and developing the different vectors and tensors, three translation equations (3.21-3.23), as well as three rotation equations (3.24-3.26) are obtained, leading to the most complete set of equations for any unarticulated moving body. However, as mentioned above, this complete model is only used for guided missiles or fin-stabilized projectiles. For spin-stabilized projectiles, plane-fixed coordinates are used in order to maintain a reasonable time-step. This means that one axis is constrained to remain in one plane and p equals Ω_x (cfr Eq. 3.13). Moreover, the terms in color in equations 3.30-3.32 vanish for a projectile with a perfect rotational symmetry, since $I_y = I_z = I_T$ and the products of inertia disappear.

The 6-DoF model implemented in LabVIEW is based on the plane-based approach, which considers the products of inertia for the calculation of inertial asymmetrical projectile trajectories as well.

A final step of simplification is still possible and consists in considering $\Omega_x = 0$. In this case we are talking about the aeroballistic equations (Eq. 3.33-3.38), meaning that while the body is rolling at the rate p , the axis system is not rolling at all. These equations will in particular be used as starting point for the linear theory (Sec. 3.6).

Complete 6-DoF Body-fixed Equations of Motion:

$$\dot{u} = \frac{F_x + G_x}{m} - qw + rv \quad (3.21)$$

$$\dot{v} = \frac{F_y + G_y}{m} - ru + pw \quad (3.22)$$

$$\dot{w} = \frac{F_z + G_z}{m} - pv + qu \quad (3.23)$$

$$\dot{p} = \frac{M_x + (I_y - I_z)qr - I_{yz}(r^2 - q^2) - I_{xz}(-qp - \dot{r}) - I_{xy}(rp - \dot{q})}{I_x} \quad (3.24)$$

$$\dot{q} = \frac{M_y + (I_z - I_x)pr - I_{yz}(pq - \dot{r}) - I_{xz}(p^2 - r^2) - I_{xy}(-qr - \dot{p})}{I_y} \quad (3.25)$$

$$\dot{r} = \frac{M_z + (I_x - I_y)pq - I_{yz}(-pr - \dot{q}) - I_{xz}(qr - \dot{p}) - I_{xy}(q^2 - p^2)}{I_z} \quad (3.26)$$

Plane-fixed Equations of Motion:

$$\dot{u} = \frac{F_x + G_x}{m} - qw + rv \quad (3.27)$$

$$\dot{v} = \frac{F_y + G_y}{m} - ru + \Omega_x w \quad (3.28)$$

$$\dot{w} = \frac{F_z + G_z}{m} - \Omega_x v + qu \quad (3.29)$$

$$\dot{p} = \frac{M_x + (I_y - I_z)qr - I_{yz}(r^2 - q^2) - I_{xz}(-qp - \dot{r}) - I_{xy}(rp - \dot{q})}{I_x} \quad (3.30)$$

$$\dot{q} = \frac{M_y - I_x pr + I_z r \Omega_x - I_{yz}(\Omega_x q - \dot{r}) - I_{xz}(\Omega_x p - r^2) - I_{xy}(-qr - \dot{p})}{I_y} \quad (3.31)$$

$$\dot{r} = \frac{M_z + I_x pq - I_y \Omega_x q - I_{yz}(-\Omega_x r - \dot{q}) - I_{xz}(qr - \dot{p}) - I_{xy}(q^2 - \Omega_x p)}{I_z} \quad (3.32)$$

Aeroballistic Equations of Motion:

$$\dot{u} = \frac{F_x + G_x}{m} - qw + rv \quad (3.33)$$

$$\dot{p} = \frac{M_x}{I_x} \quad (3.36)$$

$$\dot{v} = \frac{F_y + G_y}{m} - ru \quad (3.34)$$

$$\dot{q} = \frac{M_y - I_x pr}{I_T} \quad (3.37)$$

$$\dot{w} = \frac{F_z + G_z}{m} + qu \quad (3.35)$$

$$\dot{r} = \frac{M_z + I_x pq}{I_T} \quad (3.38)$$

3.2.3 Definition of forces and moments

Although we can "isolate" each effect in writing, each force and each moment has clearly an implication on the forces and moments that will be calculated at the next time step. In the following, these different forces and moments (See Box 3.2) will be defined individually. They will be sequenced starting with the effects related to the translation motion of the projectile in free air (without taking into account the induced rotational motions), also known as static derivatives, and then continue with the dynamic implications, related to the underlying effects of the different rotations, such as damping and Magnus effects. To best illustrate the explanations, two complementary applications will support the given formulas with experimental data.

5,56 mm M855 Projectile

The NATO standardized 5.56 x 45 mm⁸ projectile [229], is fired from rifles at close range (up to 400 m) in straight fire. The data for this spin-stabilized projectile come from an extensive testing campaign carried out by Silton and Howell [217] from the ARL⁹ on firing ranges [15] and exploited by the software ARFDAS [76], allowing among other things, the extraction of aerodynamic coefficients in flight and the reconstruction of 6-DoF trajectories. The test report is also supplied with previous measurements from Robert McCoy [135]. Table 3.1 sums up the various characteristics of this projectile for the calculations that will follow.

120 mm Mortar Projectile

Mortar is a completely different application than the previous one, since it is first of all a finned projectile and it is fired at high angle of elevation and at low velocity. The baseline data is provided by the work of Robert McCoy [137]. Table 3.1 sums up the various characteristics of this projectile for the calculations that will follow.

Parameter	5.56 mm	120 mm
d [m]	$5.56 \cdot 10^{-3}$	$1.1956 \cdot 10^{-1}$
m [kg]	$4.04 \cdot 10^{-3}$	13.585
I_x [kg·m ²]	$1.416 \cdot 10^{-8}$	$2.335 \cdot 10^{-2}$
I_T [kg·m ²]	$1.138 \cdot 10^{-7}$	$2.3187 \cdot 10^{-1}$
Tw [d/turn]	31.98	∞

Table 3.1: Characteristics of a conventional bullet and mortar.



⁸45 mm is the length of the nominal cartridge case. The length of the projectile varies from one type to another, the M855 projectile has a length of 23.1 mm.

⁹Army Research Laboratory - formerly known as Ballistic Research Laboratory - BRL.

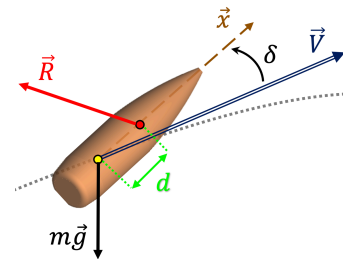
Box 3.2: What are aerodynamic forces and moments?

Aerodynamic forces and moments are the manifestation of the mechanical action of air on the projectile. The forces and moments result from the integration of the surface stresses over the projectile's surface (the shear stress that is tangential and the pressure that is normal to the surface). Depending on the system of axes studied, the expression of the forces exerted by the air can vary. After introduction of the conventions for non-dimensionalization, the forces and moments are typically expressed through the product of three quantities. First the **dynamic pressure**, which is the pressure exerted by the moving fluid: the denser the air or the fastest the flow velocity, the greater the force exerted. Then, a surface arbitrarily chosen as the **projectile cross-section**, i.e. the transversal section of the projectile ($S = \frac{\pi d^2}{4}$). Logically, if the angle of attack varies, the cross-section changes as well but this surface variation is included in the expression of the third term, the **aerodynamic coefficient**.

Given the geometry of the projectiles, the point of application of the resultant of the aerodynamic forces, the so-called **center of pressure** (CP), is generally not colocalized with the **center of gravity** (CG), it is either in front for statically unstable projectiles or behind for statically stable projectiles with respect to the nose of the projectile (Fig.2.2). However, the calculation of a trajectory is necessarily done with respect to the projectile's CG, which leads to express each forces whose point of application is not the center of gravity by means of this force from the CG **and** the inherent moment relatives to the CG, expressed in [N.m]. From the expression of a force it is thus necessary to add a lever arm corresponding to the distance between the CG and the CP.

Lever arm for aerodynamic moment...

Again, like the cross section, this distance varies according to the angle of attack, but by convention this distance is considered constant and equal to the caliber, the difference being also accounted for by the aerodynamic coefficient linked to the moment under consideration.



If the force or moment considered is what is called dynamic, i.e. depending on a rotational movement generated voluntarily or involuntarily, the expression must also contain this rotational velocity ($\omega = p, q$ or r depending on the dynamic force or moment at hand) which is made dimensionless to respect the units of the force or moment in consideration, by means of $\frac{d}{2V}$ ⁱ.

$$\text{Aerodynamic Force Magnitude} = \frac{1}{2} \rho V^2 \cdot \frac{\pi d^2}{4} \cdot C_{R_F} \left(\cdot \frac{\omega d}{2V} \right) \quad (3.39)$$

$$\text{Aerodynamic Moment Magnitude} = \frac{1}{2} \rho V^2 \cdot \frac{\pi d^2}{4} \cdot d \cdot C_{R_M} \left(\cdot \frac{\omega d}{2V} \right) \quad (3.40)$$

Generic Aerodynamic Coefficient $C_R = f(\text{shape}, \delta, Ma, Re^*)$

* Ma = Mach Number, Re = Reynolds Number \rightarrow See Box 7.2.

ⁱThere are two conventions to express dimensionless angular velocities, McCoy uses $\frac{d}{V}$ [137] as in AEP-96 [1], while many studies about coefficients use the NACA aeroballistic system convention $\frac{d}{2V}$ [217]. It does not make any difference for the resultant forces and moments but it is important to maintain consistency.

Static forces & moment

Air resistance is the combination of an aerodynamic force opposing the forward velocity of the projectile, called the drag force (\vec{D}) and an aerodynamic force perpendicular to the trajectory, tending to pull the projectile in the direction its nose is pointed, called the lift force (\vec{L}) [14]. As the point of application of air resistance is not necessarily the CG, it is required to consider in addition a pitching moment to compensate for the offset between CG and CP. The pitching (or overturning) moment (\vec{M}) is defined as positive when it destabilizes the projectile (nose up moment for a positive angle of attack), and negative when it stabilizes it. Figure 3.8 gives a representation of these two forces and moment in two dimensions, supposing a positive angle of attack in the XY -plane. Of course, as the nose of the projectile "rotates" around the velocity vector (precession), the orientation of the lift vector will also rotate while respecting the perpendicularity with the vector perpendicular to the yaw plane (Box 3.1). Equation 3.41, as well as the other expressions of forces and moments are given in vector form and are to be developed according to the unit vectors $\vec{1}_x$ and $\vec{1}_V$, but it is also possible to express them according to the angles α and β , which in turn are expressed in terms of the components of the velocity vector (u, v, w) [268].

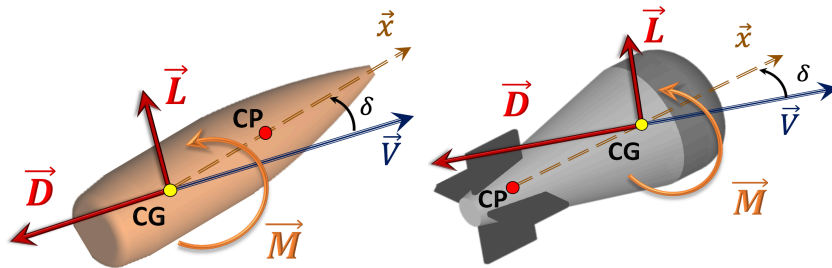


Figure 3.8: Decomposition of air resistance for both types of stabilization, \vec{M} is illustrated positively.

Drag Force =

$$\vec{D} = -\frac{1}{2}\rho V^2 \cdot \frac{\pi d^2}{4} \cdot C_D \cdot \vec{1}_V \quad (3.41)$$

$$C_D = C_{D_0} + C_{D_{\delta^2}} \sin^2 \delta \quad (3.42)$$

Both references from Siltan & Howell [217] and McCoy [137] express the geometric properties of the projectiles but also the aerodynamic coefficients as a function of the Mach number (Box. 7.2). For each force and moment, these data are shown below in graphical form, as far as they are available. In addition to experimental measurements, fittings were also produced so that these coefficients could be implemented in the trajectography programs. How these coefficients have to be handled will be discussed with more detail in chapter 6. Figure 3.9 shows the different components of the drag force for both types of projectiles. As announced, the 120 mm flies at very low speeds, entirely subsonic, while the 5.56 mm begins its flight at large supersonic speed. C_D is mainly depending on the Mach number and yaw angle; therefore a " δ -derivative" $C_{D_{\delta^2}}$ is introduced next to C_{D_0} (Eq. 3.42). The latter translates most of the non-linear Mach number dependency but is independent of δ . $C_{D_{\delta^2}}$ translates the yaw angle dependency and part of the Mach number dependency. This is the conventional approach in ballistics applied here on a force coefficient with a quadratic dependency.

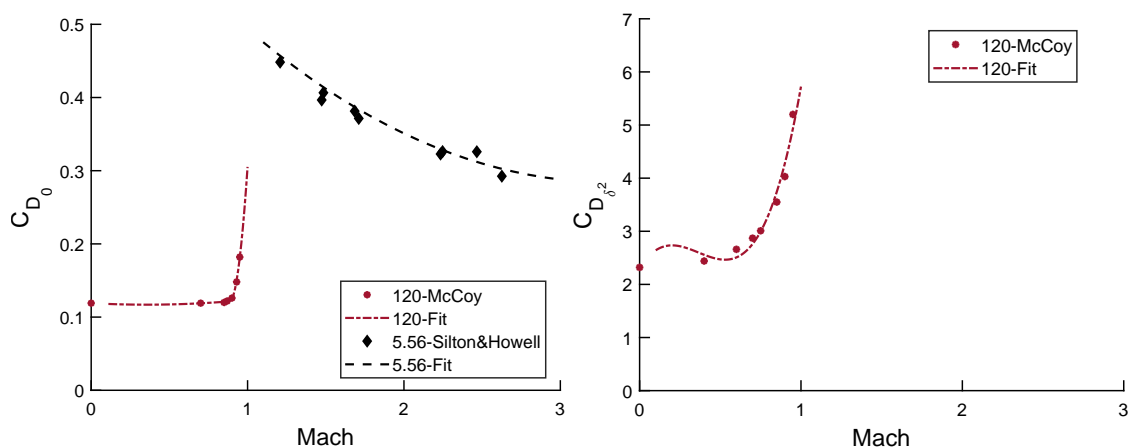


Figure 3.9: Drag force coefficient components as a function of Mach number for the 120-mm mortar [137] and the 5.56-mm projectile [217].

There is no coefficient $C_{D_{\delta^2}}$ for the 5.56 mm, this does not mean that no dependency on the angle of attack is to be expected, but it is negligible for "typical operational" angles. On the other hand, as shown in figure 3.10, the dependency on δ is obvious for the 120 mm and it is therefore essential to take this into account given the high elevation angles of this application, leading to larger oscillations of δ (Sec. 3.5).

C_{D_0} systematically presents a quadratic shape in the supersonic domain, an abrupt drop in the transonic transition and then a low and more or less constant sub-

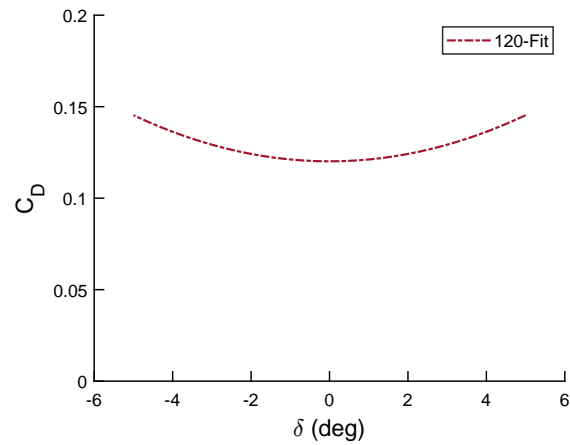


Figure 3.10: Drag coefficient at Ma 0.8 as a function of δ for the 120-mm mortar [137].

sonic part, for both spinning and fin-stabilized projectiles. This is illustrated in figure 3.11 for two types of spin- and fin-stabilized projectiles with different nose shapes¹⁰.

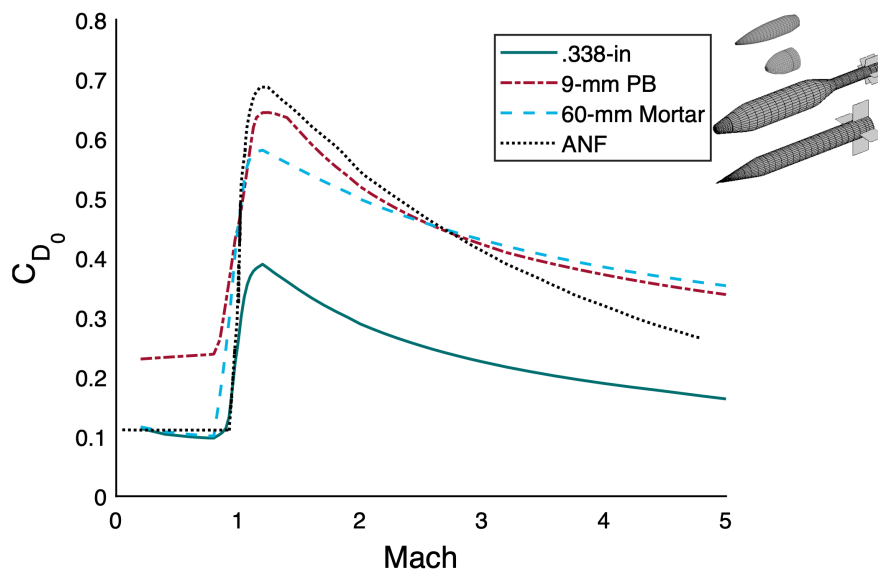


Figure 3.11: Zero-Yaw Drag coefficient for different geometries, estimated with AeroFI [210].

¹⁰The .338-in and 9-mm PB projectiles will be used in chapter III. The ANF configuration is detailed in chapter 8, Fig. 8.3.

Lift Force =

$$\vec{L} = \frac{1}{2}\rho V^2 \cdot \frac{\pi d^2}{4} \cdot C_{L\delta} \cdot \left[\vec{1}_V \times (\vec{1}_x \times \vec{1}_V) \right] \tag{3.43}$$

$$C_L = C_{L\delta} \sin \delta \tag{3.44}$$

$$= C_{L\delta_0} \sin \delta + C_{L\delta_3} \sin^3 \delta \tag{3.45}$$

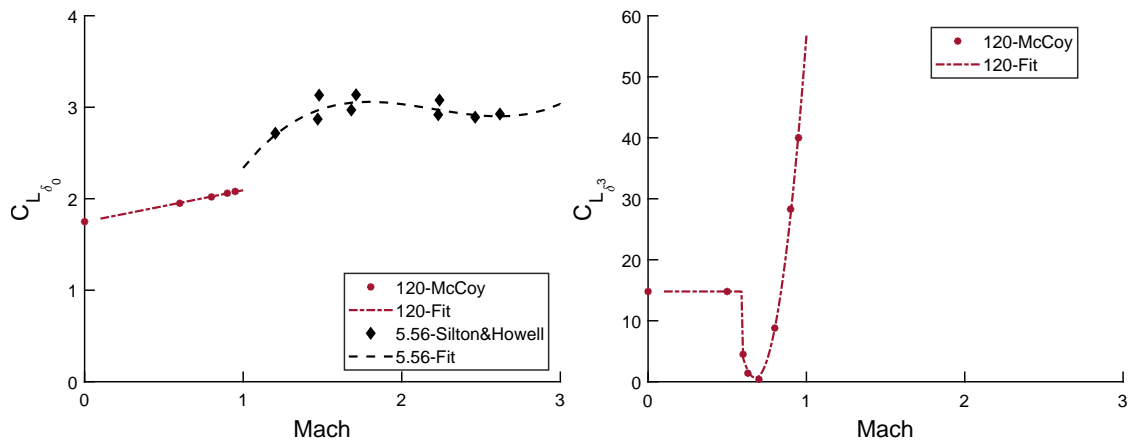


Figure 3.12: Lift force coefficient components as a function of Mach number for the 120-mm mortar [137] and the 5.56-mm projectile [217].

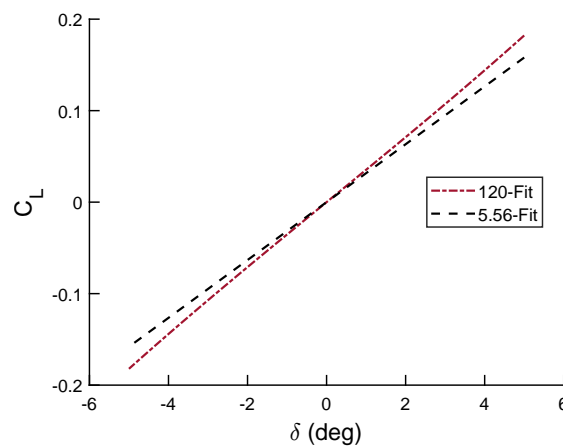


Figure 3.13: Lift force coefficient at Mach number 0.8 as a function of δ for the 120-mm mortar [137] and the 5.56-mm projectile [217].

Unlike the drag, for symmetric projectiles, the lift force is canceled when there is no angle of attack, and can be approximated with a cubic function for large angles. The coefficients derivatives are presented in figures 3.12 as a function of the Mach number. Again, the cubic dependency is not taken into account for the 5.56 mm projectile, as it is insignificant on the final result. Given the cubic shape, the lift pulls the projectile towards the ground if the yaw is negative. Figure 3.13 shows that the total lift coefficient curve is very similar for both types of projectiles at

Mach number 0.8, this may seem surprising but given the order of magnitude of the velocities and angles of attack, the magnitude of \vec{L} will be completely different.

In some references, including Silton & Howell [217], the drag and lift forces are expressed in body axes and not with respect to the velocity vector. These are the axial and normal forces F_x and F_y or F_N , as shown in figure 3.14. The conversion between these forces was used to illustrate the coefficients from figures 3.9 to 3.13.

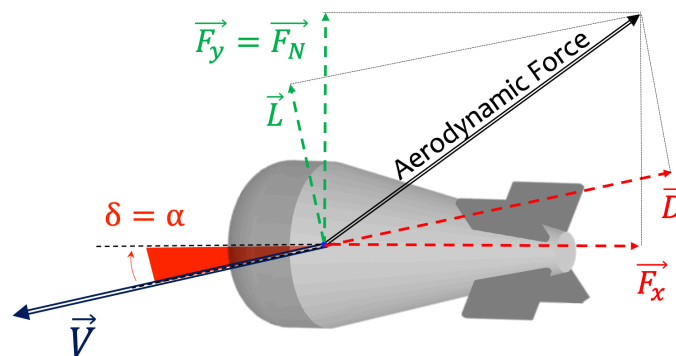


Figure 3.14: Drag and Lift versus Axial and Normal forces.

Pitching/Overturning Moment =

$$\vec{M} = \frac{1}{2}\rho V^2 \cdot \frac{\pi d^2}{4} \cdot d \cdot C_{M\delta} \cdot (\vec{1}_V \times \vec{1}_x) \quad (3.46)$$

$$C_M = C_{M\delta} \sin \delta \quad (3.47)$$

$$= C_{M\delta_0} \sin \delta + C_{M\delta_3} \sin^3 \delta \quad (3.48)$$

Figure 3.15 gives the pitch moment derivatives, according to the same principles as for the lift force. This time the cubic derivatives is given for the 5.56 mm projectile because the influence of the moment is more important than that of the forces on the stability (Chap.5), but still it remains quite small in the subsonic regime and becomes important near Mach number 1, reinforcing the instabilities of the transonic domain. Figure 3.16 shows the stabilizing pitching moment for the 120 mm and destabilizing moment for the 5.56 mm projectile.

As stated in box 3.2, the distance taken between the CG and the CP is by convention the caliber, but it is possible to calculate this effective distance on the basis of the determination of the normal force and the pitching moment coeffi-

icients by means of expression 3.49 [56, 137]:

$$(CG - CP) = \frac{C_{M_\delta}}{C_{N_\delta}} \tag{3.49}$$

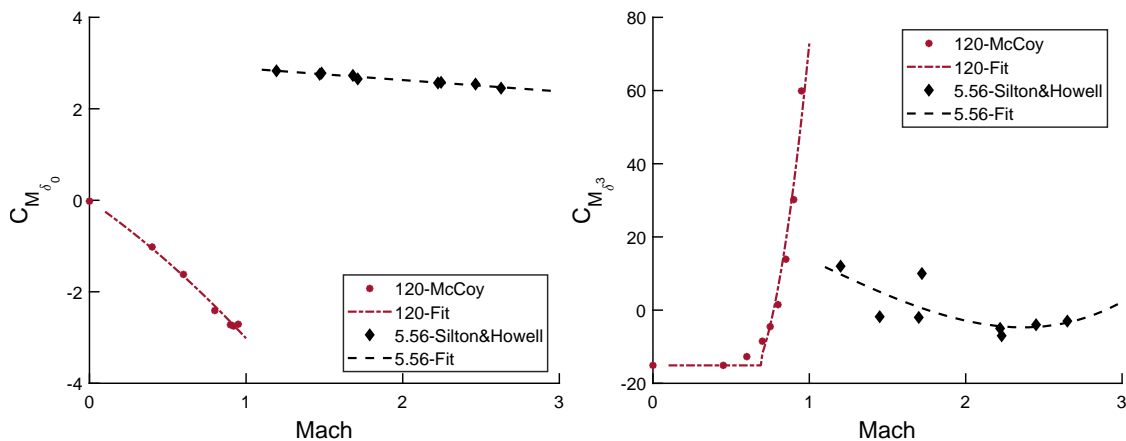


Figure 3.15: Pitch moment coefficient components as a function of Mach number for the 120-mm mortar [137] and the 5.56-mm projectile [217].

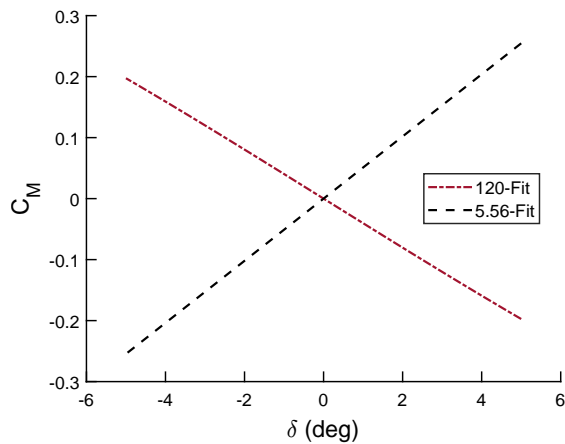


Figure 3.16: Pitch moment coefficient at Mach number 0.8 as a function of δ for the 120-mm mortar [137] and the 5.56-mm projectile [217].

Dynamic forces & moments

- **Spin Damping Moment vs Rolling Moment**

The spin damping moment, noted \vec{S} , characterizes the decrease in spin rate p during flight [14] (Fig.3.17a-Eq.3.50).

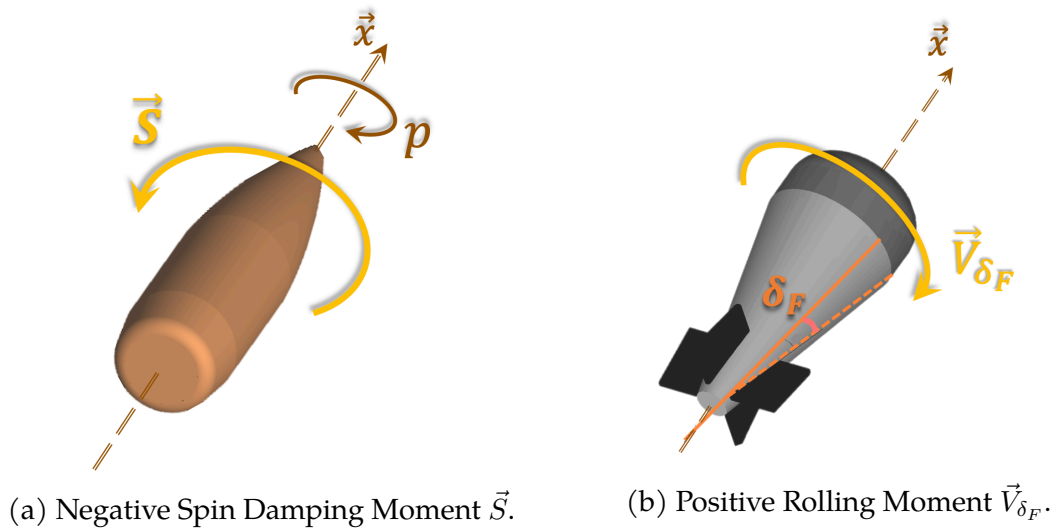


Figure 3.17: Rotation around longitudinal axis.

Spin Damping Moment =

$$\vec{S} = -\frac{1}{2}\rho V^2 \cdot \frac{\pi d^2}{4} \cdot d \cdot C_{l_p} \cdot \frac{pd}{2V} \cdot \vec{1}_x \quad (3.50)$$

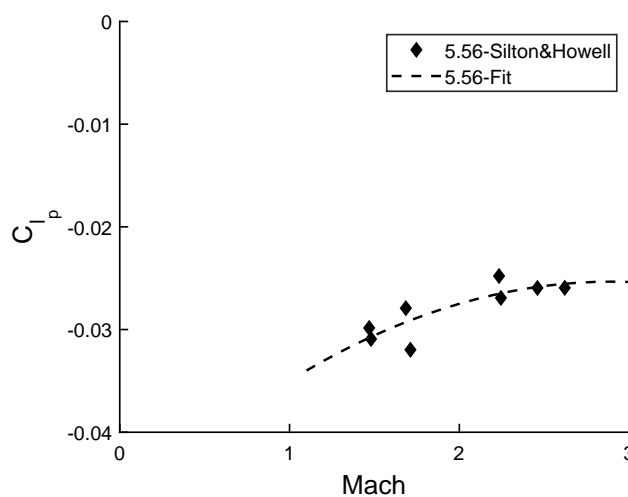


Figure 3.18: Spin damping moment coefficient as a function of the Mach number for the 5.56-mm projectile [217].

In some applications of finned projectiles, canted fins are used in order to compensate the influence of any mass unbalance. The purpose of the fin cant angle δ_F illustrated in figure 3.17b is to "generate" an additional aerodynamic moment around the longitudinal axis, called rolling moment \vec{V}_{δ_F} , so that flight perturbations lead to steering adjustments [64]. The induced rotation is far less pronounced than for a projectile stabilized from the twisted barrel, but this roll is not negligible on the drift of the projectile and has to be considered (Eq.3.51).

Rolling Moment =

$$\vec{V}_{\delta_F} = \frac{1}{2} \rho V^2 \cdot \frac{\pi d^2}{4} \cdot d \cdot C_{l_{\delta_F}} \cdot \vec{1}_x \quad (3.51)$$

Unlike previous coefficients, the spin damping (C_{l_p}) and rolling ($C_{l_{\delta_F}}$) coefficients only begin to depend on the yaw at large amplitudes ($\delta > 15^\circ$, which is why these coefficients are considered "for operational use" independent of $\sin \delta$ (Fig.3.18). This will be discussed in the numerical study of these coefficients (Sec. 9.1.1).

The rolling moment for projectiles with canted fins tends to increase spin while spin damping moment is always present, even if less noticeable for finned projectiles. The consequence is that the two moments are opposed to each other and tend to generate a steady-state rotation [137].

- **Magnus effect**

If a spinning projectile performs a linear motion with an angle of attack, a free stream velocity component will be added to the surface velocity on one side of the projectile, while on the other side the velocity will be reduced. The resultant of the velocities being different in the boundary layer from one side to the other side of the projectile, an under-pressure will be created on one side of the body surface streamline, which will drive the projectile in that direction. This movement is said to be the consequence of the Magnus force \vec{Q} (Fig.3.19-Eq.3.52).

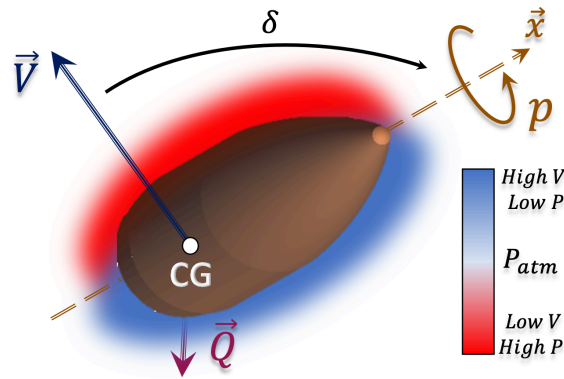


Figure 3.19: A representation of Magnus' force \vec{Q} .

Again, as the point of application of this force is not necessarily the CG, a Magnus moment is to be added (Eq.3.54). The Magnus force is considerably smaller than the drag and lift forces and is ignored in many applications, however, the Magnus moment plays a significant role in the stability of the projectile [29] and will therefore affect the time of flight and the maximum ordinate [14]. A significant crosswind will also generate a Magnus force, with a direction depending on the wind direction [63].

Magnus Force =

$$\vec{Q} = \frac{1}{2}\rho V^2 \cdot \frac{\pi d^2}{4} \cdot C_{N_{p\delta}} \cdot \frac{pd}{2V} \cdot (\vec{1}_V \times \vec{1}_x) \quad (3.52)$$

$$C_{N_p} = C_{N_{p\delta}} \sin \delta = C_{N_{p\delta_0}} \sin \delta + C_{N_{p\delta^3}} \sin^3 \delta \quad (3.53)$$

Magnus Moment =

$$\vec{J} = \frac{1}{2}\rho V^2 \cdot \frac{\pi d^2}{4} \cdot C_{M_{p\delta}} \cdot d \cdot \frac{pd}{2V} \cdot \left[\vec{1}_x \times (\vec{1}_V \times \vec{1}_x) \right] \quad (3.54)$$

$$C_{M_p} = C_{M_{p\delta}} \sin \delta = C_{M_{p\delta_0}} \sin \delta + C_{M_{p\delta^3}} \sin^3 \delta \quad (3.55)$$

Magnus coefficients are undoubtedly the most complicated to determine experimentally, given their dependence on other phenomena that are difficult to isolate. The values represented in figure 3.20 as a function of Mach number and in figure 3.21 for different speeds, are therefore illustrated below so that the reader can consider the order of magnitude and the dispersion of the measurement, but the final shape that was implemented (Fig.3.22)

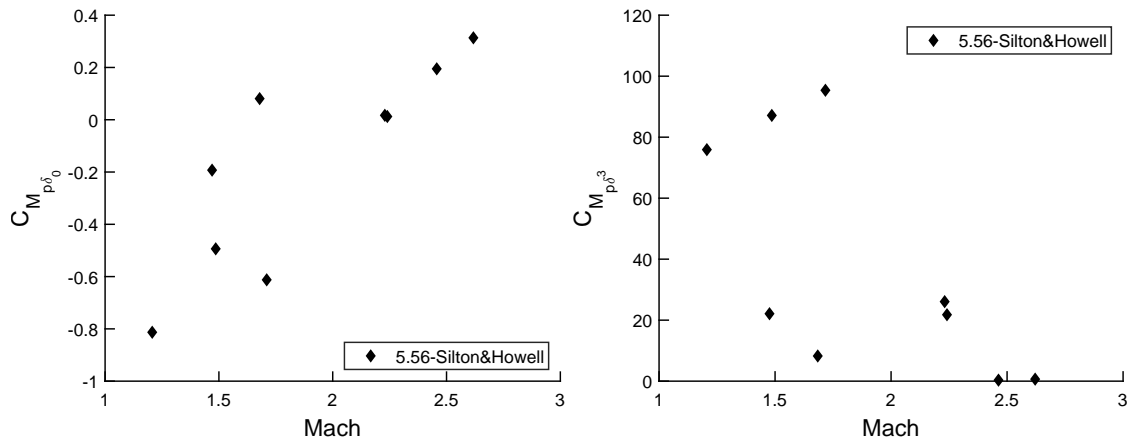


Figure 3.20: Magnus moment coefficient components as a function of Mach number for the 5.56-mm projectile [217].

is proposed directly in Silton & Howell’s article for small angles of attack [217]. All these figures show that, compared to other coefficients, Magnus coefficients do not behave in a linear way at all, neither with respect to the angle of attack, nor with respect to the Mach number, and its intensity also varies according to the spin rate. Therefore, it has always been a real challenge to determine them. As mentioned by the pioneering aerodynamicists [273], several test campaigns spread over several years had to be carried out to try to obtain the coefficients for a single projectile for all the speeds and angles of attack required. Today these coefficients can be determined with 6-DoF data reduction techniques from spark ranges - Sec. 6.1.2 (still with an error margin of 10 to 20% (Fig.6.5)), but when the Linear Theory (Sec.3.6) was used, results were mainly dependent on the analyst [16].

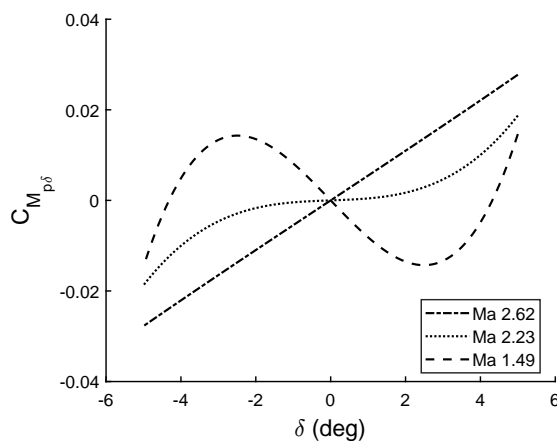


Figure 3.21: Magnus moment coefficient as a function of δ for the 5.56-mm projectile [217].

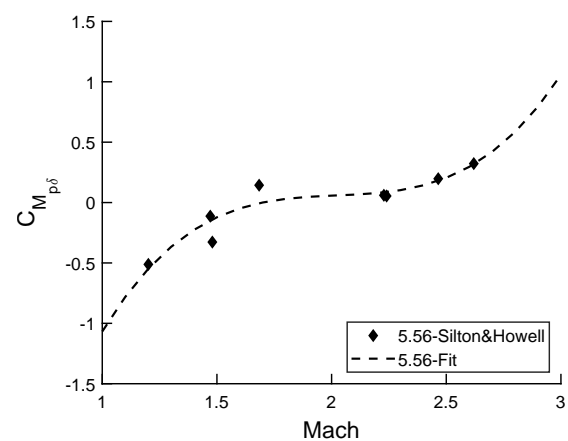


Figure 3.22: Fitted Magnus moment coefficient as a function of Mach number for the 5.56-mm projectile [217].

• Pitch Damping

The term "Pitch damping" is commonly used but it is actually the propensity of a projectile to reduce its oscillatory motion in three dimensions. Figure 3.23 gives a representation of pitch and yaw precession (small frequency-large amplitude) and nutation (high frequency-small amplitude) dampings, i.e. in the respective xy and xz planes of the projectile body. In addition to a gun elevation (Quadrant Elevation - QE) of 20 mils¹¹, initial perturbations were simulated through the transverse angular velocities q_0 and r_0 to visualize the nutation phenomenon.

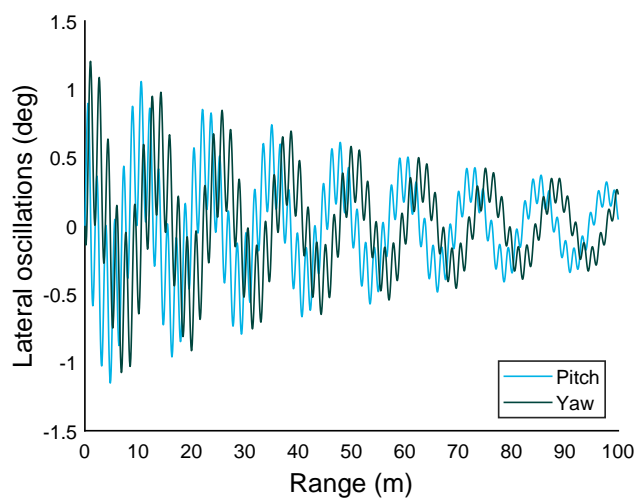


Figure 3.23: Pitch and Yaw damped oscillations for a 5.56-mm projectile. Initial conditions: $MV = 800\text{m/s}$, $QE = 20\text{mils}$, $q_0 = r_0 = 20\text{rad/s}$

The pitch damping force acts in the plane of transverse angular velocity (Eq. 3.56). This force therefore inevitably contains a term proportional to the transverse angular velocity, q_t (Eq.3.57), but also a part proportional to the rate of change of the total yaw angle, $\dot{\delta}$, since the plane in which the force acts is not necessarily the same as the plane of yaw. In most cases, though, these two terms are grouped together because of the very small difference between these two angular velocities [137, 158]. Given the small influence of these coefficients for the two applications presented, the pitch damping force is not presented here, but a calculation on another geometry will be done in chapter 10. Like Magnus effect, the pitch damping moment has much more influence than the pitch damping force in terms of stabilization [24].

¹¹6400 mils = 360°.

Pitch Damping Force =

$$\vec{E} = \frac{1}{2}\rho V \cdot \frac{\pi d^2}{4} \cdot (C_{N_q} + C_{N_{\dot{\alpha}}}) \cdot d \cdot (\vec{\omega} \times \vec{1}_x) \quad (3.56)$$

$$q \equiv q_t = \sqrt{q^2 + r^2} \quad (3.57)$$

$$C_{N_q} + C_{N_{\dot{\alpha}}} = (C_{N_q} + C_{N_{\dot{\alpha}}})_0 + (C_{N_q} + C_{N_{\dot{\alpha}}})_{\delta^2} \cdot \sin^2 \delta \quad (3.58)$$

Pitch Damping Moment =

$$\vec{H} = \frac{1}{2}\rho V \cdot \frac{\pi d^2}{4} \cdot (C_{M_q} + C_{M_{\dot{\alpha}}}) \cdot d^2 \cdot (\vec{1}_x \times (\vec{\omega} \times \vec{1}_x)) \quad (3.59)$$

$$C_{M_q} + C_{M_{\dot{\alpha}}} = (C_{M_q} + C_{M_{\dot{\alpha}}})_0 + (C_{M_q} + C_{M_{\dot{\alpha}}})_{\delta^2} \cdot \sin^2 \delta \quad (3.60)$$

Figures 3.24 and 3.25 give the different pitch damping coefficient values as well as the general dependency on δ . It will be seen later on that largely negative values ensure better gyroscopic and dynamic stability (Chap.5).

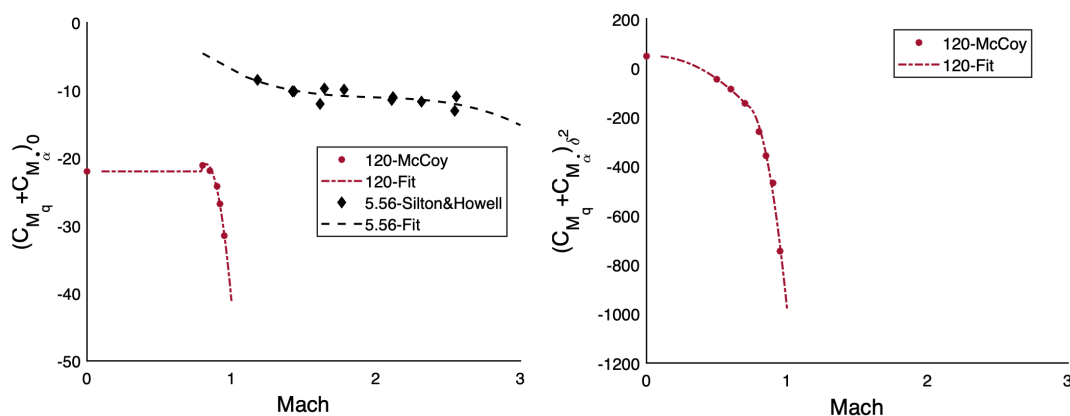


Figure 3.24: Pitch damping coefficient components as a function of Mach number for the 120-mm mortar [137] and the 5.56-mm projectile [217].

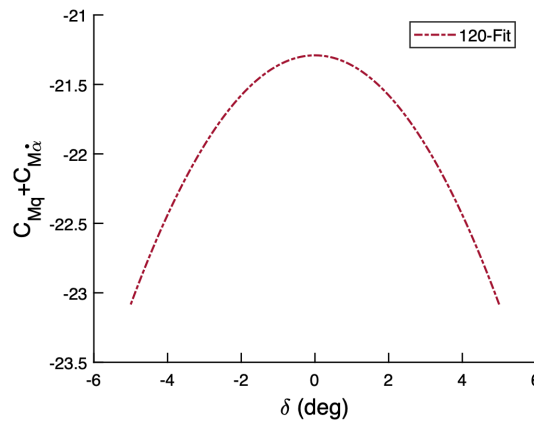


Figure 3.25: Pitch damping coefficient at Mach number 0.8 as a function of δ for the 120-mm mortar [137].

3.2.4 Other forces...

- **Coriolis Acceleration**

As mentioned with equation 3.19, external fictitious¹² forces like the Coriolis force have to be considered to account for the non-inertial reference frame while using classical Newtonian mechanics [63]. It is therefore clear that this effect is only to be taken into account if the time of flight is significant, this will be dependent on the application and the desired precision. For small arms operational ranges (maximum 600 m), this effect can safely be neglected. Coriolis and Gravity forces are expressed as in the AOP-4355 NATO document [11].

Vector Coriolis force =

$$\vec{\Lambda} = -2m(\vec{\omega}_C \times \vec{V}) \quad (3.61)$$

$$\vec{\omega}_C = \begin{pmatrix} \Omega \cos(Lat) \cos(Az) \\ \Omega \sin(Lat) \\ -\Omega \cos(Lat) \sin(Az) \end{pmatrix} \quad (3.62)$$

$\Omega = 7.292115 \cdot 10^{-5}$ rad/s is the angular rate of the earth

Az is the Azimuth of \vec{X} -axis measured clockwise from true North

Lat is the Latitude of the firing position with respect to the Equator

NB: For Southern Hemisphere, Lat is negative in equation 3.62

¹²The term fictitious is used because it is not generated by a real force but introduced to correct assumptions.

$\vec{\omega}_C$ is the angular velocity of the ground-fixed coordinate system due to the rotation of the earth, while \vec{V} is the velocity of the projectile with respect to these ground-fixed axes. In order to work with plane-fixed coordinates, it is necessary to use matrix 3.7 to convert $\vec{V} = (u, v, w)$ in the Ground-fixed coordinates, otherwise the Coriolis effect will be overestimated.

- **Acceleration due to gravity**

$$\vec{g} = -g_0 \begin{pmatrix} \frac{X}{R_E} \\ 1 - \frac{2Y}{R_E} \\ \frac{Z}{R_E} \end{pmatrix} \quad (3.63)$$

g_0 is the acceleration due to gravity at mean sea level (MSL);

$R_E (=6.356766 \cdot 10^6 \text{m})$ is the radius of the earth, locally approximating the geoid [109, 253].

Equation 3.63 is the one given in AOP-4355 [11], but it refers to earth-fixed coordinates. It will therefore be used in the following models, but for the plane-fixed approach, it is necessary to use the transformation matrix from equation 3.5 to convert the gravity vector :

Vector Gravity force =

$$\vec{G} = \begin{pmatrix} -mg_0 \sin \psi \\ -mg_0 \cos \psi \\ 0 \end{pmatrix} \quad (3.64)$$

$$g_0 = 9.80665 \cdot (1 - 0.0026 \cos(2Lat)) [\text{m/s}^2]$$

3.3 Practical implementations

3.3.1 Meteorological Conditions: ISO standards

Weather conditions have a direct impact on the dynamic pressure used to calculate the forces and moments acting on a projectile in flight, as well as on the Mach number on which these same coefficients depend. By default, the implemented programs follow the Standard Atmosphere ISO-2533 [100], redacted under the technical instruction of the International Civil Aviation Organization (ICAO) [170] (Eq. 3.65-3.67). ICAO atmosphere is since 1962 the world-wide standard atmosphere for both aviation and ballistics use [137]. In parallel to this, the ambient pressure and temperature on the firing position can be introduced as input parameters. It would also be possible to implement weather reports¹³ for very long range and/or high altitude applications, to reflect current climate variations, but this falls beyond the direct interest of this work.

$$p_{ICAO} = p_0 \left(1 - \frac{\Gamma Y}{T_0}\right)^{\frac{g_0}{\Gamma R}} \quad (3.65)$$

$$T_{ICAO} = T_0 - \Gamma Y \quad (3.66)$$

$$\rho = \frac{p_{ICAO}}{RT_{ICAO}} \quad (3.67)$$

$$p_0 = 101325[\text{Pa}] (= p_{MSL})$$

$$T_0 = 288.15[\text{K}] (= T_{MSL})$$

$$\Gamma = 0.0065[\text{K/m}]$$

$$R = 287.057[\text{J}/(\text{kg} \cdot \text{K})]$$

The velocity of the wind measured on the firing position can also be taken into account, through the expression of the speed. Vector \vec{V} is then replaced by $\vec{V}_W = \vec{V} - \vec{W}$ and it becomes the velocity vector of the projectile with respect to air, while \vec{W} is the wind velocity vector. The wind is considered equal to zero throughout this work to focus on the permanent forces.

¹³These are also standardized, in particular according to **STANAG 4082** for artillery: *Adoption of a standard artillery computer meteorological message*.

3.3.2 Integration Methods

The problem here is to numerically solve twelve differential equations with respect to time t ¹⁴. Each equation can be expressed as follows:

$$\frac{dx}{dt} = f(t, x(t)) \quad (3.68)$$

With x corresponding to the vector containing the 12 dependent variables:

$$[u, v, w, p, q, r, x, y, z, \phi, \theta, \psi]$$

Although the simplest method to code is the so-called forward Euler integration method which is first-order accurate, the history of trajectography has shown that the fourth-order Runge-kutta (RK4) integration method was the most appropriate [137] because it is a good balance between accuracy and cost of computation. Euler's method is conditionally stable so it requires a sufficiently small time step. However, for identical initial conditions, RK4 allows to multiply the integration time step size by a factor of 10^3 for spin-stabilized projectiles, where typically the Δt of a calculation with Euler is about 10^{-6} s (See Fig. 3.28). The Runge-Kutta method is an algorithm designed to approximate the Taylor series solution [252]. One of the variant used is the one implemented in the 6-DoF model of the ARL which uses the Gill constants [20]. This method was first implemented to optimize computer storage space and then remained the "default" method for their HTRAJ program [132] (Chap. 4).

h being the integration step size, Euler's scheme is implemented as follows:

$$x_{i+1} - x_i = hf(t_i, x_i) \quad (3.69)$$

The Runge-Kutta methods have the same basic expression to determine the dependent variable x :

$$x_{i+1} - x_i = \sum_{n=1}^m w_n k_n \quad (3.70)$$

$$k_n = hf(t_i + c_n h, x_i + \sum_{j=1}^{n-1} \beta_{nj} k_j) \quad (3.71)$$

¹⁴Equations 3.21 to 3.26 to get the velocities and then integrate them again to obtain the positions.

With m the integration order and w_n, c_n, β_{nj} some constants dependent on the method used.

The fourth-order RK methods use $w_n = \frac{1}{6}$ and the following c_n constants:

$$c_1 = 0, c_2 = \frac{1}{2}, c_3 = \frac{1}{2}, c_4 = 1$$

The common RK4 method foresees that:

$$\begin{aligned} \beta_{21} &= \frac{1}{2} & k_1 &= hf(t_i, x_i) \\ \beta_{31} &= 0, \beta_{32} = \frac{1}{2} & k_2 &= hf(t_i + \frac{1}{2}h, x_i + \frac{1}{2}k_1) \\ \beta_{41} &= 0, \beta_{42} = 0, \beta_{43} = 1 & k_3 &= hf(t_i + \frac{1}{2}h, x_i + \frac{1}{2}k_2) \\ & & k_4 &= hf(t_i + h, x_i + k_3) \end{aligned}$$

$$x_{i+1} = x_i + \frac{1}{6}(k_1 + 2k_2 + 2k_3 + k_4) \quad (3.72)$$

while the RK-Gill method uses [20]:

$$\begin{aligned} \beta_{21} &= \frac{1}{2} & k_1 &= hf(t_i, x_i) \\ \beta_{31} &= \frac{1}{\sqrt{2}} - \frac{1}{2}, \beta_{32} = 1 - \frac{1}{\sqrt{2}} & k_2 &= hf(t_i + \frac{1}{2}h, x_i + \frac{1}{2}k_1) \\ \beta_{41} &= 0, \beta_{42} = -\frac{1}{\sqrt{2}}, \beta_{43} = 1 + \frac{1}{\sqrt{2}} & k_3 &= hf(t_i + \frac{1}{2}h, \\ & & & x_i + [-\frac{1}{2} + \frac{1}{\sqrt{2}}]k_1 + [1 - \frac{1}{\sqrt{2}}]k_2) \\ & & k_4 &= hf(t_i + h, x_i - \frac{1}{\sqrt{2}}k_2 + [1 + \frac{1}{\sqrt{2}}]k_3) \end{aligned}$$

$$x_{i+1} = x_i + \frac{1}{6}(k_1 + (2 - \sqrt{2})k_2 + (2 + \sqrt{2})k_3 + k_4) \quad (3.73)$$

Before starting the calculation, it is then necessary to choose the Euler or RK4 integration scheme with in the latter case the possibility to choose the Gill option. The latest reference software developed use an accurate seventh-order Runge-Kutta scheme [52, 84, 272] (Sec. 4). This one has not been implemented with LabVIEW but it will be the subject of a future implementation in another environment.

3.3.3 End of the trajectory

The numerical integration process must be stopped at some point. Depending on the application, different stop conditions are used. The trajectory is usually stopped when the projectile reaches a specific height, but sometimes the trajectory has to be stopped at a specific range. Other rocket mechanisms require a stop after a certain number of rotations [277], a certain deceleration or after a certain time of flight, etc...

In this work, only the height and range stop conditions have been implemented. The stop condition is implemented in two steps. In the first step, the trajectory is stopped as soon as the projectile has passed the target (whether fixed in height ($=Y_T$ - Eq. 3.76) or in distance ($=X_T$ - Eq. 3.79)). For the stop condition in height it is also necessary to specify whether the trajectory has to stop in the ascending or descending phase of the trajectory (Eq.3.75-3.77). In a second step, the distance between the last calculation point and the position of the target (horizontal or vertical depending on the input choice) is compared to a given tolerance, ϵ_X in range or ϵ_Y in height. If the distance lies within the tolerance, the calculation stops definitively, otherwise the calculation resumes one step backward with a reduced time step.

Stop conditions in Height:

Ascending part:

$$Y > Y_T \quad (3.74)$$

$$v > 0 \quad (3.75)$$

Descending part:

$$Y < Y_T \quad (3.76)$$

$$v < 0 \quad (3.77)$$

$$|Y - Y_T| < \epsilon_Y \quad (3.78)$$

Stop conditions in Range:

$$X > X_T \quad (3.79)$$

$$|X - X_T| < \epsilon_X \quad (3.80)$$

3.3.4 Initial conditions & choices

The tables below include all the input parameters necessary to compute a 6-DoF-trajectory for any single moving rigid body in air with the plane-based method.

Position-related Inputs	
QE (ψ_0)	First elevation angle
Az (θ_0), Lat and Hemisphere	For Coriolis force
Altitude	For initial Y_0 and air density (0 by default)
Pressure & Temperature	To consider instantaneous conditions
Wind and Wind direction	To compute V_W if wind is considered
Weapon-related Inputs	
V_0 or MV	Initial Velocity or Muzzle Velocity
Tw	Twist rate to compute p
α_0, β_0	Initial Pitch and Yaw angles
q, r	Initial transversal angular velocities
Projectile-related Inputs	
d, m	Diameter (=caliber), mass
I_x, I_y, I_z	Principal moments of inertia
I_{xy}, I_{xz}, I_{yz}	Products of inertia
$C_{D_0}, C_{D_{\delta^2}}, C_{L_{\delta_0}}, C_{L_{\delta^3}}$	Drag & Lift force coefficients
$C_{M_{\delta_0}}, C_{M_{\delta^3}}$	Pitch moment coefficients
C_{l_p} and/or $C_{l_{\delta_F}}$	Spin or rolling moment coefficients
$C_{N_{p\delta_0}}, C_{N_{p\delta^3}}, C_{M_{p\delta_0}}, C_{M_{p\delta^3}}$	Magnus force & moment coefficients
$(C_{M_q} + C_{M_{\delta}})_0, (C_{M_q} + C_{M_{\delta}})_{\delta^2}$	Pitch damping moment coefficients
Computation-related Inputs	
Δt	Initial timestep
Euler or RK4	Integration Method
Gill option	If RK4 is chosen
Stop Condition	In Range or in Height
ϵ_H, ϵ_D	Precision tolerances

3.4 The Lieske-McCoy model for symmetric bodies

Another approach to the 6-DoF model was first proposed by Robert Lieske and Robert McCoy in 1964 in a BRL report[120] and then further detailed by McCoy in his book[137] for rigid projectiles with rotational symmetry ($I_T = I_y = I_z$). This method aims to express the equations of motion not in the projectile's reference frame but directly in the earth's reference frame. This makes the expressions of forces and moments and initial conditions somewhat more complex, but no rotation matrix is then required.

As long as the projectile is symmetrical, any transverse axis passing through the center of gravity of the projectile is considered to be a main transverse axis of inertia. The total angular momentum vector $\bar{I}\vec{\omega}$ in equation 3.18 can then be decomposed into two parts: an angular momentum about $\vec{1}_x$ and an angular momentum about an axis perpendicular to $\vec{1}_x$, passing through the projectile' CG. This leads to :

$$\bar{I}\vec{\omega} = I_x p \vec{1}_x + I_y (\vec{1}_x \times \frac{d\vec{1}_x}{dt}) \quad (3.81)$$

By dividing equation 3.81 on both sides by I_y and taking the scalar product and the vector product of the left term with $\vec{1}_x$, the outcomes are respectively¹⁵:

$$\frac{\bar{I}\vec{\omega}}{I_y} \cdot \vec{1}_x = \vec{h} \cdot \vec{1}_x = \frac{I_x p}{I_y} \quad (3.82)$$

$$\frac{\bar{I}\vec{\omega}}{I_y} \times \vec{1}_x = \vec{h} \times \vec{1}_x = \frac{d\vec{1}_x}{dt} \quad (3.83)$$

The vectorial expressions of forces and moments allow then to reconsider the equations of motion (3.17 & 3.18) applied to a projectile in the Earth-fixed coordinates, in terms of two vectorial differential equations:

Linear Motion of projectile's center of mass:

$$\begin{aligned} \frac{d\vec{V}}{dt} = & -\frac{\rho\pi d^2 V_W}{8m} C_D \vec{V}_W + \frac{\rho\pi d^2}{8m} C_{L\delta} [V_W^2 \vec{1}_x - (\vec{V}_W \cdot \vec{1}_x) \vec{V}_W] - \\ & \frac{\rho\pi d^3}{8m} C_{N_{p\delta}} \left(\frac{I_y}{I_x}\right) (\vec{h} \cdot \vec{1}_x) (\vec{1}_x \times \vec{V}_W) + \\ & \frac{\rho\pi d^3 V_W}{8m} (C_{N_q} + C_{N_\delta}) (\vec{h} \times \vec{1}_x) + \vec{g} \end{aligned} \quad (3.84)$$

¹⁵ \vec{h} is defined as the specific angular momentum $\bar{I}\vec{\omega}/I_y$

Projectile's angular motion about it's center of mass:

$$\begin{aligned}
\frac{d\vec{h}}{dt} = & \frac{\rho\pi d^4 V_W}{8I_x} C_{l_p} (\vec{h} \cdot \vec{1}_x) \vec{1}_x + \frac{\rho\pi d^3 V_W^2 \delta_F}{8I_y} C_{l_\delta} \vec{1}_x + \frac{\rho\pi d^3 V_W}{8I_y} C_{M_\delta} (\vec{V}_W \times \vec{1}_x) + \\
& \frac{\rho\pi d^4}{8I_x} C_{M_{p\delta}} (\vec{h} \cdot \vec{1}_x) [\vec{V}_W - (\vec{V}_W \cdot \vec{1}_x) \vec{1}_x] + \\
& \frac{\rho\pi d^4 V_W}{8I_y} (C_{M_q} + C_{M_\delta}) [\vec{h} - (\vec{h} \cdot \vec{1}_x) \vec{1}_x]
\end{aligned} \tag{3.85}$$

Initial Conditions

Just as important as the equations of motion are the initial conditions allowing to accurately start the calculations. The graphical representations in figures 3.26-3.27 show the starting angles in the Ground-fixed coordinate system $(\vec{1}, \vec{2}, \vec{3})$ as well as the representation of the three unit vectors originating at the projectile's CG, with $\vec{1}_x$ along the symmetry axis, $\vec{1}_z$ lying in the horizontal plane and $\vec{1}_y$ defined by the cross product $\vec{1}_y = \vec{1}_z \times \vec{1}_x$.

θ_0 and ψ_0 are respectively the horizontal and vertical starting angles of the gun launcher (represented by the direction of the velocity vector \vec{V}_0) with respect to ground. α_0 and β_0 are the initial pitch and yaw angles of the projectile ($\vec{1}_{x_0}$ with respect to the gun launcher).

$$\begin{bmatrix} 1_{x_{01}} \\ 1_{x_{02}} \\ 1_{x_{03}} \end{bmatrix} = \begin{bmatrix} \cos(\theta_0 + \beta_0) \cos(\psi_0 + \alpha_0) \\ \sin(\psi_0 + \alpha_0) \\ \sin(\theta_0 + \beta_0) \cos(\psi_0 + \alpha_0) \end{bmatrix}$$

$$\begin{bmatrix} 1_{y_{01}} \\ 1_{y_{02}} \\ 1_{y_{03}} \end{bmatrix} = \begin{bmatrix} -\cos(\theta_0 + \beta_0) \sin(\psi_0 + \alpha_0) \\ \cos(\psi_0 + \alpha_0) \\ -\sin(\theta_0 + \beta_0) \sin(\psi_0 + \alpha_0) \end{bmatrix} \quad \begin{bmatrix} 1_{z_{01}} \\ 1_{z_{02}} \\ 1_{z_{03}} \end{bmatrix} = \begin{bmatrix} -\sin(\theta_0 + \beta_0) \\ 0 \\ \cos(\theta_0 + \beta_0) \end{bmatrix}$$

The initial time rate of change of the projectile's orientation $\vec{1}_{x_0}$ is then given by equation 3.87, while the calculation of $\frac{d\vec{1}_x}{dt}$ is done according to formula 3.83.

$$\frac{d\vec{1}_{x_0}}{dt} = r_0 \vec{1}_{y_0} - q_0 \vec{1}_{z_0} \tag{3.87}$$

with q_0 and r_0 the initial angular velocities about $\vec{1}_y$ and $\vec{1}_z$ unit vectors¹⁶. Equation 3.87 allows to calculate the muzzle value of \vec{h}_0 (Eq.3.88), the initial angular momentum divided by the transverse moment of inertia, following equation 3.81, and by means of the expression of p_0 (Eq.3.89):

$$\vec{h}_0 = \begin{bmatrix} \frac{I_x p_0}{I_y} 1_{x_{01}} + 1_{x_{02}} \dot{1}_{x_{03}} - 1_{x_{03}} \dot{1}_{x_{02}} \\ \frac{I_x p_0}{I_y} 1_{x_{02}} - 1_{x_{01}} \dot{1}_{x_{03}} + 1_{x_{03}} \dot{1}_{x_{01}} \\ \frac{I_x p_0}{I_y} 1_{x_{03}} + 1_{x_{01}} \dot{1}_{x_{02}} - 1_{x_{02}} \dot{1}_{x_{01}} \end{bmatrix} \tag{3.88}$$

¹⁶ q_0 and r_0 are determined experimentally, by reconstruction of the trajectory at the muzzle, but this is a rather complicated process, they are most of the time neglected or filled in hypothetically to see the "worst" influence that the initial conditions may have.

$$p_0 = \frac{2\pi V_0}{T w * d} \tag{3.89}$$

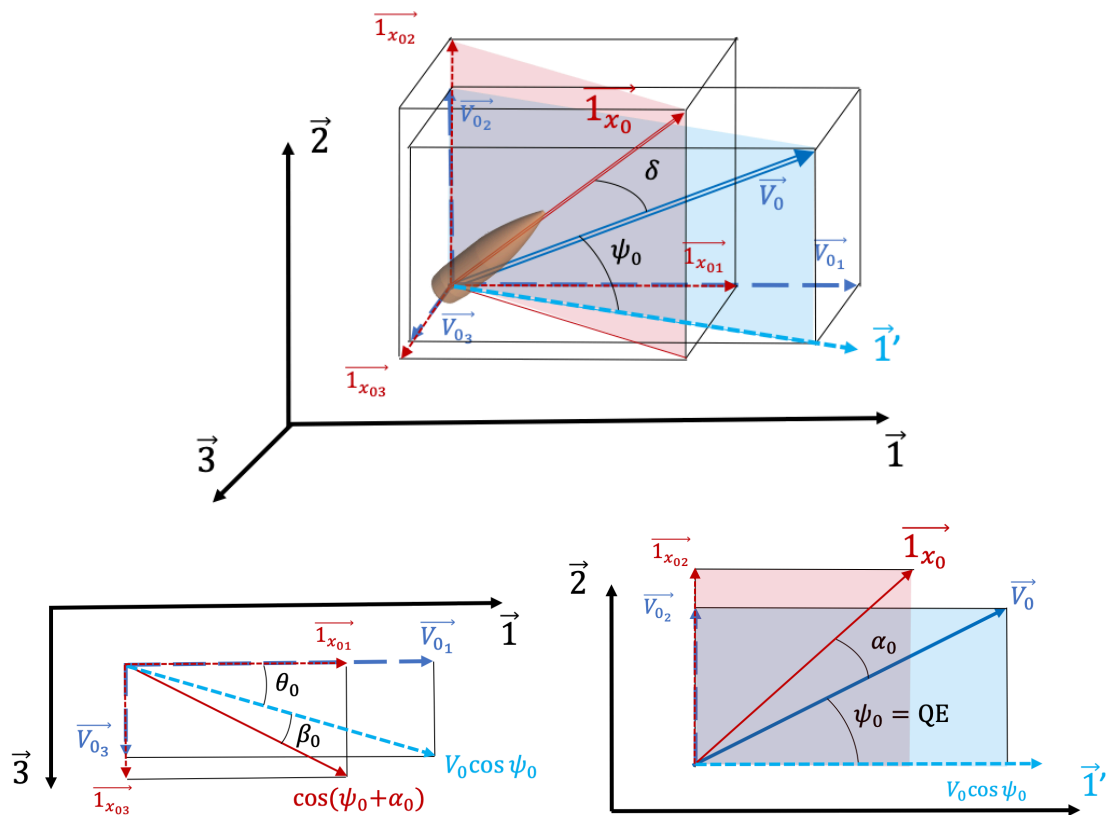


Figure 3.26: Initial Velocity and Position vectors. The colors are used to enhance the visualization of the different reference systems.

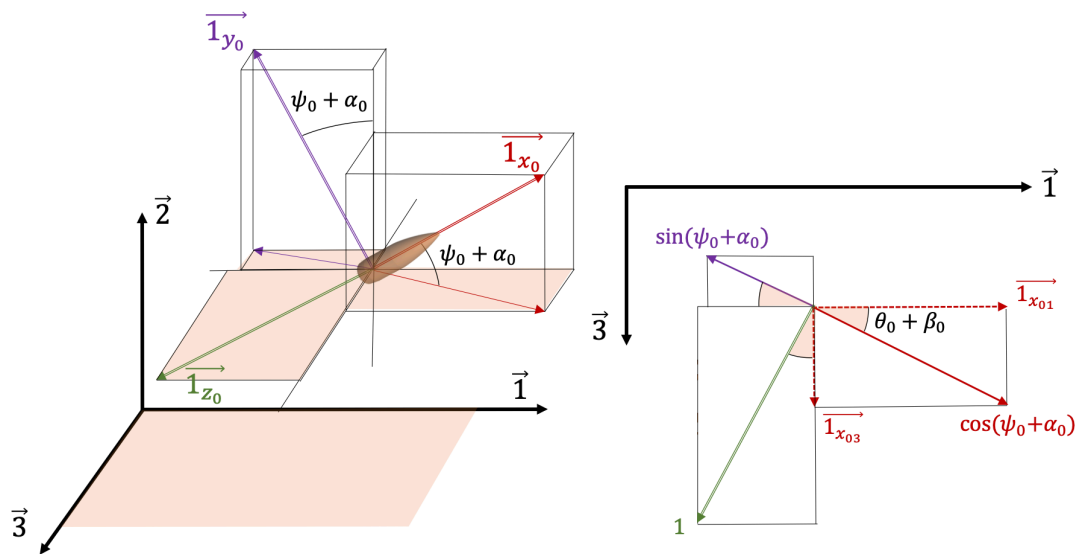


Figure 3.27: Initial position unit vector triad.

3.5 Validation of the 6-DoF models

Both 6-DoF models implemented in LabVIEW for rigid bodies (section 3.2) and symmetrical projectiles (section 3.4) have to be validated with higher fidelity results.

In his book[137], McCoy provides trajectory details for the 120mm mortar, which can be used as a basis for validation. Those trajectories were made using the Fortran HTRAJ computer program[162] developed by the Firing Tables and Ballistics Division (FTaB). FTaB is also established at Aberdeen Proving Ground (APG) in Maryland, and is part of the Armament Research, Development and Engineering Center (ARDEC). It has for mission to create firing tables[61], perform mathematical analysis of trajectories and conduct experiments in order to increase the accuracy of unguided and some guided weapon systems from the US Army inventory¹⁷. This includes small caliber infantry systems, mortars, tank fired munitions, artillery, missiles, and rockets¹⁸.

It is a chance to dispose of these data because without a reference software it is very complicated to find a source that gives both the inputs and outputs to compare with. The following validation is therefore considered to be macroscopic, since there is not sufficient material to compare the subtle details of all the tiny variations due to programming techniques and integration schemes, as it is done between referenced software (See Sec. 4)[84, 268].

On the basis of Silton's work[215, 217, 218], a qualitative comparison is also made for the 5.56mm over a distance of 100m, but in this case the initial conditions are not known, so they were approximated to obtain the same point of impact and on the basis of this, the other parameters were compared.

While table 3.1 already gave the general parameters for the firing scenario's, table 3.2 gives 9 cases for both projectiles already addressed with additional inputs, as well as two additional cases from McCoy[137] allowing an overview of Δt -convergence. The calculations were stopped in height ($Y_{Target} = Y_{Fire}$) for all cases except for case 7 where there were stopped in range ($X = 100\text{m}$), with

¹⁷<https://www.army.mil/article/215516>, 01 Feb 2021.

¹⁸<https://dodstem.us/labs/ardec-firing-tables-and-ballistics-division>, 01 Feb 2021.

a tolerance in height and in range of 10^{-6} m. The trajectory integration is carried out using a standard fourth-order Runge-Kutta scheme with a fixed Δt of 10^{-2} s for the 120 mm Mortar and 10^{-4} s for the spin-stabilized projectiles, according to figure 3.28 showing the convergence of the solution for different increment sizes as a function of the chosen integration scheme. The values have been normalized¹⁹ on the basis of the reference ranges given in [137]. We notice that a discrepancy remains between the integration schemes when the initial conditions (r_0, q_0) are non-zero. This difference still needs to be checked with another reference software.

Table 3.2: Additional inputs for control scenario's

#	Cal [mm]	MV [m/s]	$QE=\psi_0$ [$^\circ$]	p_0 [rad/s]	r_0 [rad/s]	q_0 [rad/s]
1	120	102	45	0	0.913	0
2	120	102	65	0	0.913	0
3	120	102	85	0	0.913	0
4	120	318	45	0	1.795	0
5	120	318	65	0	1.795	0
6	120	318	85	0	1.795	0
7	5.56	405	0.16	14311	75	4
8	7.62	792	0.84	16333	0	25
9	105	205	45	682	0	1.44

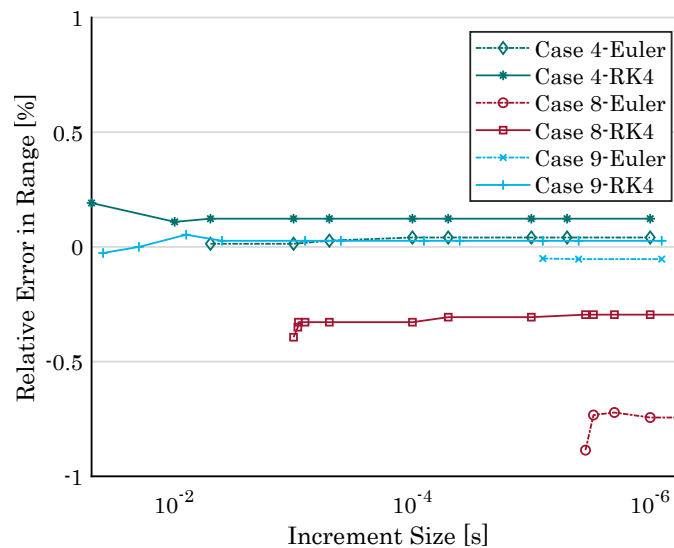


Figure 3.28: Time increment convergence for cases 4, 8 and 9 from table 3.2 and two integration schemes. The relative error is calculated on the basis of the results given by McCoy [137].

¹⁹No point means that the program did not give any solution or that the error was greater than 1%.

Table 3.3 shows the results in range, according to both models implemented in LabVIEW ($VTraj_L =$ Lieske Model - $VTraj_G =$ Generalized 6-DoF). The ranges reported by McCoy have been rounded to the meter, but the margin of error is still less than 0.5%, often even below. Figure 3.29 gives a qualitative comparison of the evolution of the pitch angle α for the two cases with the highest elevation angle and the two extreme muzzle velocities for this application. The match, both in size and frequency, is good for case 6 but shows some angle overprediction after the apogee of the trajectory for case 3, while the macroscopic trajectory parameters such as range, maximum height and flight time match perfectly. This difference in angular dynamics seems to be a recurrent problem in trajectory comparison, even for reference programs [84, 270]. This will be the subject of further analysis using the BALCO program (Chap. 4).

Table 3.3: Comparison data on the Range for the 120mm mortar.

#	R_{McCoy}	$R_{VTraj,L}$	$\%_{error}$	$R_{VTraj,G}$	$\%_{error}$
1	1010	1010.42	0.041	1010.5	0.049
2	770	766.53	0.452	766.68	0.433
3	165	164.89	0.067	165.01	0.006
4	7315	7315.4	0.005	7312.34	0.036
5	5570	5569.91	0.002	5577.81	0.140
6	1275	1275.95	0.074	1277.15	0.168

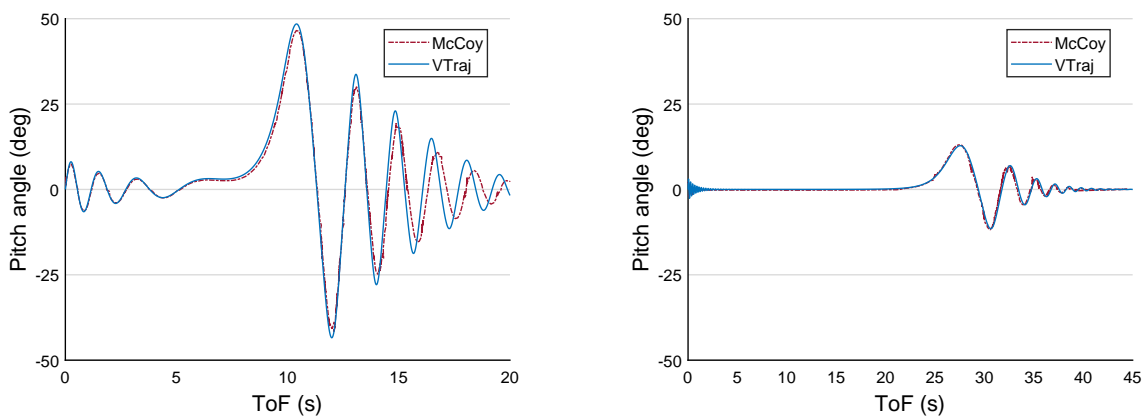


Figure 3.29: Comparison Pitch Angle in function of the Time of Flight (ToF)- Case 3 on the left - Case 6 on the right.

Figures 3.30-3.31 compare VTraj calculations with the Generalized 6-DoF model and the trajectory reconstruction from Silton's work using ARFDAS soft-

ware [217]. A distinction is therefore made in the graphs between the measurement points recorded during the firing experiments and the reconstructed 6-DoF curves from these points. Although some discrepancies may appear, the orders of magnitude and the oscillations frequencies are very close, the differences being due to the initial conditions, which are very likely not the same. It is also important to underline that what seems to be a curved trajectory on figure 3.30 is in reality a straight trajectory if we refer to the scales' ratio: this reinforces the match obtained.

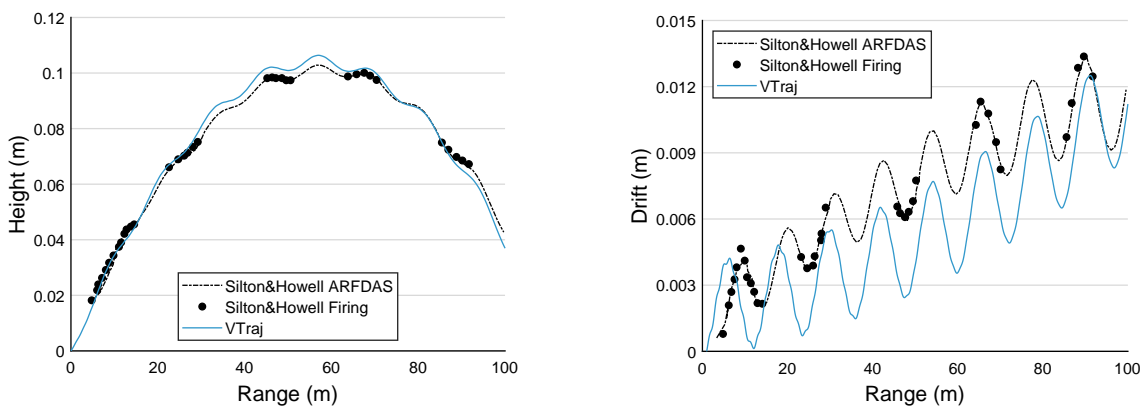


Figure 3.30: Comparison XY and XZ projections for scenario 7 [217].

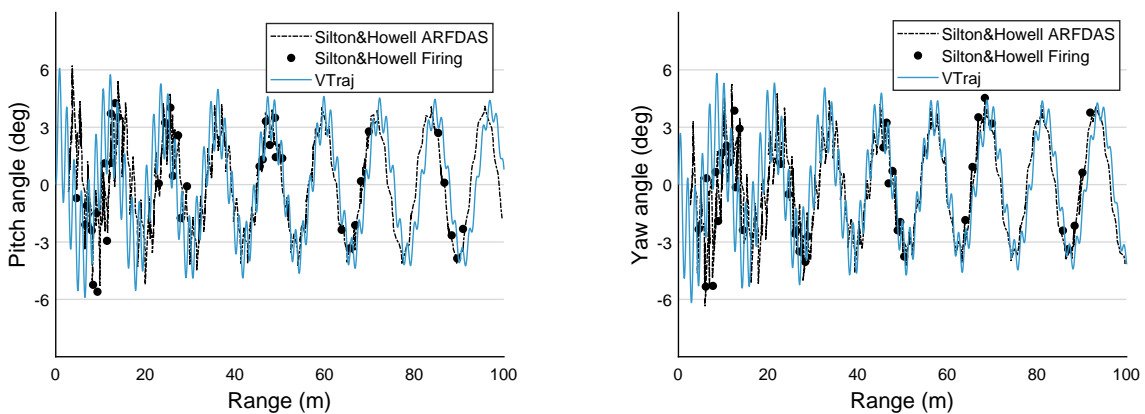


Figure 3.31: Comparison isolate Pitch (α) and Yaw (β) angles for scenario 7 [217].

These latest representations allowed to visualize the attitude of a spin-stabilized projectile in flight. The details of these movements will be discussed in the following section.

3.6 Projectile Linear Theory

This approach is not a model in its proper sense, but a strong analytical theory based on the 6-DoF equations that described the free-flight motion of a rigid spinning body under specific flight conditions. This part is addressed here because it provides a link with the following model (Sec. 3.7) and will make it easier to understand the reasons for the simplifications made there. This theory will also make it possible to address the different types of in-flight projectile stabilities, an essential step in the conception and design of new products. It is not a question here of rediscussing all the stages of this relatively complex mathematical theory, literally and figuratively, but of describing the essential steps involved in obtaining a solution that can be used for practical purposes and representation in space.

The Linear approach, from which result the epicyclic and tricyclic theories seems to have made its appearance in 1920, in Fowler's publication[79], in which the first movements of the nose of the projectile are seen in a plane perpendicular to the trajectory. The work then continued and expanded, and several sources detailed the basis of the Projectile Linear Theory in its standard version of today, such as Kent in 1937[108], Kelley & McShane in 1944[107] or Nicolaides in 1953[163]. These works provide the theoretical basis for the estimation of the required spin and they describe analytically the motion of a yawing, spinning projectile. The theory was later expanded to include a wide range of applications in terms of projectile geometric and mass properties (See also Sec. 12)[42, 98, 161, 245, 246, 255].

To be able to provide a solution to a linear differential equation, the model begins with the aeroballistic equations (Eq.3.33-3.38) and the assumptions of **rigid body, constant aerodynamic coefficients and small angles, rotation and mass symmetry, products of inertia and rates of change of inertia equal to zero**. As a reminder, the aeroballistic equations are given here:

$$\dot{u} = \frac{F_x + G_x}{m} - qw + rv \quad (3.90) \quad \dot{p} = \frac{M_x}{I_x} \quad (3.93)$$

$$\dot{v} = \frac{F_y + G_y}{m} - ru \quad (3.91) \quad \dot{q} = \frac{M_y - I_x pr}{I_T} \quad (3.94)$$

$$\dot{w} = \frac{F_z + G_z}{m} + qu \quad (3.92) \quad \dot{r} = \frac{M_z + I_x pq}{I_T} \quad (3.95)$$

The intention is to obtain an analytical solution to those equations. Therefore, a first step is to decouple the roll from the pitch and yaw equations, assuming p constant and separating in all aerodynamic expressions related to yaw and pitch, the contributions due to $q, r, \dot{\beta}, \dot{\alpha}, \beta, \alpha$ and Magnus moment resulting from combined roll rate and angle of attack.

$$m\ddot{y} + mru - F_{y\beta}\beta - F_{yT} - g \cos \psi = 0 \quad (3.96)$$

$$m\ddot{z} - mqu - F_{z\alpha}\alpha - F_{zT} = 0 \quad (3.97)$$

$$I_T\dot{q} + rpI_x - M_{y\beta}\beta - M_{yq}q - M_{y\dot{\beta}}\dot{\beta} - M_{y\dot{\beta}p}p\beta - M_{yT} = 0 \quad (3.98)$$

$$I_T\dot{r} - qpI_x - M_{z\alpha}\alpha - M_{zr}r - M_{z\dot{\alpha}}\dot{\alpha} - M_{z\dot{\alpha}p}p\alpha - M_{zT} = 0 \quad (3.99)$$

F_{yT}, F_{zT}, M_{yT} and M_{zT} are added forces and moments due to control deflection when an aerodynamic asymmetry is added (for canards for instance) [245].

As the angles are assumed to be small, $q \approx \dot{\beta}; \dot{q} \approx \ddot{\beta}; r \approx -\dot{\alpha}; \dot{r} \approx -\ddot{\alpha}$, leading to the definition of a complex angle of attack ξ , composed of the two angles α and β (Eq. 3.100). This definition allows to represent any yaw angle in a complex plane, perpendicular to the x -axis and coincident with y - and z -axis. This is somewhat like a polar representation of the movements of the projectile's nose with respect to the flight path.

$$\xi = \alpha + i\beta \quad (3.100)$$

Here again, α and β are defined positive when the nose is respectively pointing upwards and to the right, and the rotations are positive when going clockwise. The definition of complex numbers takes advantage of the assumed rotational symmetry and allows to bring together two differential equations into one (by adding up the contributions in pitch and yaw together). Moreover, this rotational symmetry also allows to equalize the coefficients with respect to y and z :

$$F_\delta \equiv F_{y\beta} = F_{z\alpha};$$

$$M_\delta \equiv M_{y\beta} = M_{z\alpha}; M_q \equiv M_{yq} = M_{zr}; M_{\dot{\alpha}} \equiv M_{y\dot{\beta}} = M_{z\dot{\alpha}}; M_{p\delta} \equiv M_{y\dot{\beta}p} = M_{z\dot{\alpha}p}$$

Before assembling the linear and angular equations together, the independent time variable is changed into a dimensionless arc-length, s (measured in calibers of travel) in order to have events independent of the size of the projectile:

$$\dot{\xi} = \frac{d\xi}{ds} \frac{ds}{dt} = \frac{V}{2d} \xi' \quad (3.101)$$

Then multiplying equations 3.97 & 3.99 by i and adding them to 3.96 & 3.98 leads to a single equation where α and β and their derivatives can be assembled as complex numbers. The problem is now posed in the complex plane, which makes it possible to find a solution dependent on a single complex angle ξ . By collecting the terms together and converting them into already defined aeroballistic forces & moments, it comes finally a linear second order differential equation (starred coefficients $C_R^* = \frac{\rho S d}{2m} C_R$):

$$\begin{aligned} \xi'' + \left[C_{L\delta}^* - C_D^* - \frac{md^2}{I_T} (C_{Mq}^* + C_{M\alpha}^*) - i \frac{I_x}{I_T} \frac{pd}{2V} \right] \xi' \\ - \left[\frac{md^2}{I_T} C_{M\delta}^* + i \frac{I_x}{I_T} \frac{pd}{2V} (C_{L\delta}^* + \frac{md^2}{I_x} C_{M_{p\delta}}^*) \right] \xi \\ = \frac{iM_T}{I_T} e^{ipt} + i \frac{I_x}{I_T} \frac{pd}{2V} \frac{gd \cos \psi}{V^2} \end{aligned} \quad (3.102)$$

3.6.1 Linearized aeroballistic equation

Equation 3.102 with complex coefficients is called the **linearized aeroballistic equation**. If the problem of asymmetric deflection is not considered, it is only a question of considering the homogeneous solution, this is called the epicyclic theory since there will be two principal solutions. It is supposed to give a good approximation to the complete motion of spinning or non-spinning projectiles for small yaw amplitudes and flat-fire trajectories. If this deflection is considered, the particular solution must also be addressed to take into account the trimming²⁰ part due to asymmetry and this becomes the tricyclic equation. Further abbreviated, equation 3.102 for projectiles leads to the short and common equation 3.103 for symmetric spin-stabilized and rolling fin-stabilized projectiles [137, 217] and 3.109 for fin-stabilized projectiles with deflection[29]:

²⁰Trim = sideways flight with a constant inclination.

**Linearized pitching and yawing motion equation
for rolling projectiles:**

$$\xi'' + (H - iP)\xi' - (M + iPT)\xi = -iPG \quad (3.103)$$

$$H = C_{L\delta}^* - C_D^* - \frac{md^2}{I_T}(C_{Mq}^* + C_{M\dot{\alpha}}^*) \quad (3.104)$$

$$P = \frac{I_x}{I_T} \frac{pd}{2V} \quad (3.105)$$

$$M = \frac{md^2}{I_T} C_{M\delta}^* \quad (3.106)$$

$$T = C_{L\delta}^* + \frac{md^2}{I_x} C_{Mp\delta}^* \quad (3.107)$$

$$G = \frac{gd \cos \psi}{V^2} \quad (3.108)$$

**Linearized pitching and yawing motion equation
for finned (non-rolling) projectiles:**

$$\xi'' + H\xi' - M\xi = i(D + G) \quad (3.109)$$

$$H = -C_{N\delta}^* - 2C_D^* - \frac{md^2}{I_T}(C_{Mq}^* + C_{M\dot{\alpha}}^*) \quad (3.110)$$

$$M = \frac{md^2}{I_T} C_{M\delta}^* \quad (3.111)$$

$$D = \frac{md^2}{I_T}(C_{mT}^* + iC_{nT}^*) \quad (3.112)$$

$$G = -\left(\frac{md^2}{I_x} C_{Mq}^* - C_D^*\right) \frac{gd \cos \psi}{V^2} \quad (3.113)$$

The homogeneous solution of equation 3.103 is given in equation 3.114 and consists of an epicycloid²¹ with two modes, called **arms**, that rotate at different **amplitudes** K and different **frequencies** ϕ . The "Fast" mode is called **nutation** and the "Slow" mode **precession** (Cfr Box 2.2). The third arm is the trim arm due to control deflection²². This arm is used to quantify the amount by which the projectile

²¹<https://www.dictionary.com> : Epicycloid = a curve generated by the motion of a point on the circumference of a circle that rolls externally, without slipping, on a fixed circle.

²²neglected for spin-stabilized symmetric projectiles

will have the tendency to trim.

$$\xi = K_F e^{i\phi_F} + K_S e^{i\phi_S} + K_T e^{i\phi_T} + i\delta_R \quad (3.114)$$

K_F and K_S are determined from the initial boundary conditions and the exponential real damping coefficients ($\lambda_{F,S}$ in Eq.3.115). The complex roots are further developed in equation 3.116 in terms of initial phase angles (ϕ_{F_0,S_0}) and turning frequencies ($\phi'_{F,S}$).

$$K_{F,S} = K_{F_0,S_0} e^{\lambda_{F,S}} \quad (3.115)$$

$$\phi_{F,S} = \phi_{F_0,S_0} + \phi'_{F,S} \quad (3.116)$$

According to the calculation underlying this development, it also comes that:

$$\lambda_{F,S} + i\phi'_{F,S} = \frac{1}{2} \left[-H + iP \pm \sqrt{4M + H^2 - P^2 + 2iP(2T - H)} \right] \quad (3.117)$$

It is then possible to further develop equation 3.117 to match the forces and moments factors with the exponents of the yawing arms [156]:

$$P = \phi'_F + \phi'_S$$

$$M = \phi'_F \phi'_S - \lambda_F \lambda_S \approx -\phi'_F \phi'_S$$

$$H = -(\lambda_F + \lambda_S)$$

$$PT = -(\phi'_F \lambda_S + \phi'_S \lambda_F)$$

Frequencies and damping exponents
(P vanishes for non-rolling projectiles):

$$\phi'_{F,S} = \frac{1}{2} \left[P \pm \sqrt{P^2 - M} \right] \quad (3.118)$$

$$\lambda_{S,F} = -\frac{1}{2} \left[H \pm \frac{P(2T - H)}{\sqrt{P^2 - M}} \right] \quad (3.119)$$

Equations 3.118 & 3.119 are the basis for the discussion on stability that will take place in chapter 5, but are also interesting to provide some important input pa-

rameters for the numerical computation of the pitch damping coefficients (Chap. 9.2.2)

Figures 3.32-3.33 give some geometrical spatial representations of the oscillating arms for spin-stabilized and finned projectiles in an undamped configuration ($\lambda_{F,S}$ being neglected). Figure 3.34 is the complex plane, perpendicular to the trajectory, which represents in two dimensions the movements of the nose of a 5.56 mm projectile: on the figure on the left, almost five nutation cycles can be seen for one precession cycle during the first 10 meter, while no nutation is to be seen if no initial perturbations are induced (right picture).

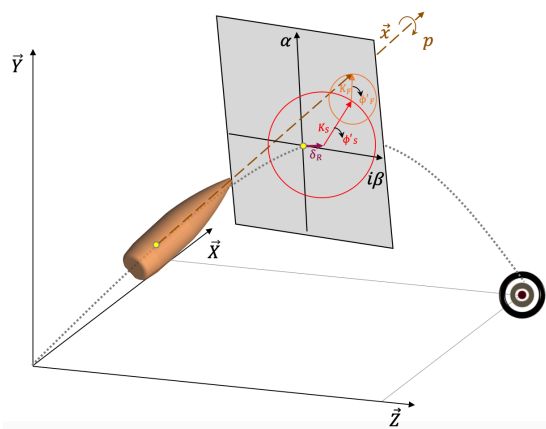


Figure 3.32: Epicyclic Pitching and Yawing Motion for non-trimming rolling projectile. According to equation 3.118, both arms K_S & K_F turn in the same direction.

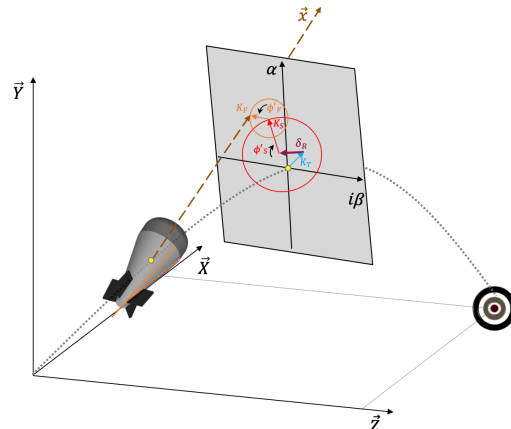


Figure 3.33: Tricyclic Pitching and Yawing Motion for a finned projectile with control deflection. According to Eq.3.118, both arms K_S & K_F turn in opposite directions.

The fact that the epicyclic arms are composed of a damping part indicates that the amplitude of the motion can decrease or increase exponentially along the trajectory. A damped solution is therefore obtained if λ_F and λ_S are both negative. Figure 3.35 illustrates for a 5.56mm projectile up to 100m at low velocity, the evolution of λ_F and λ_S as a function of the range (assuming invariant parameters to be able to apply the linear approach). Both exponents are initially negative, the nutation is quickly damped since λ_F decreases further. Besides that, the precession increases until it becomes positive, meaning that the projectile gradually loses its stability. This is due to a too low MV (405 m/s). Figure 3.35 on the right shows the λ coefficients for an almost nominal speed of 800 m/s: even if λ_S increases slightly, the stability is more guaranteed.

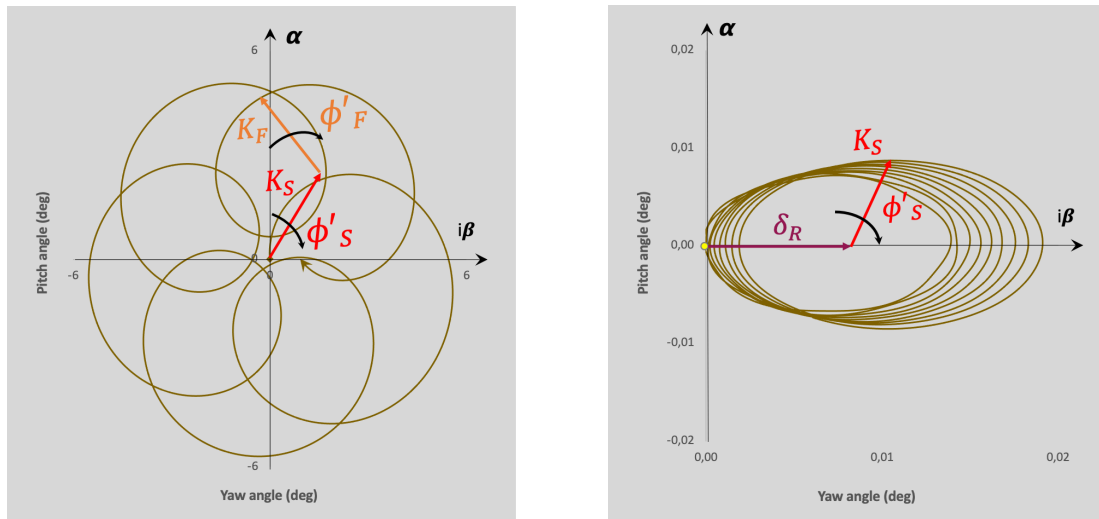


Figure 3.34: Trajectory beginning of a 5.56 mm caliber projectile - scenario 7 from table 3.2. Left : Epicyclic Pitching and Yawing Motion during the first 10 meters because of initial perturbations. Right : No initial perturbations ($q_0, r_0 = 0$), only the **precession** motion is to be seen with a slight yaw of repose δ_R from the very beginning.

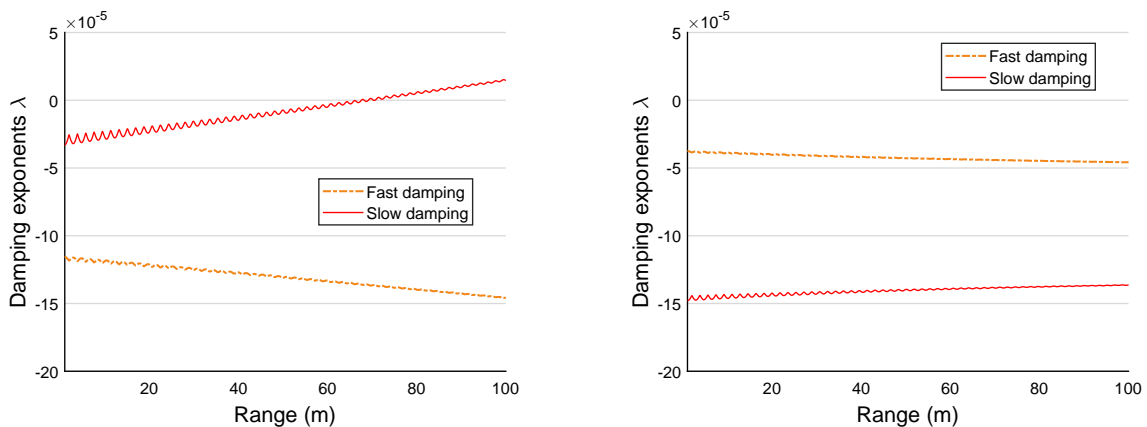


Figure 3.35: Damping exponents λ_F and λ_S as a function of the range for a 5.56 mm projectile with $MV = 405$ m/s on the left (case 7 from table 3.2) and $MV = 800$ m/s on the right.

3.6.2 Yaw of repose

There remains one term (already shown in the three previous figures) in equation 3.114 which has not yet been addressed and which is a result of the particular solution to the differential equation: δ_R . The residual equilibrium yaw, or **yaw of repose** appears when the axis of the gyroscopic stabilized projectile falls away from the trajectory as it curves downwards due to the gravity[14]. For **flat-fire trajectories** it is defined with equation 3.120 & 3.121 for both types of projectiles.

Rolling projectiles:

$$\delta_{R,spin} = \frac{PG}{M + iPT} \quad (3.120)$$

Non-rolling projectiles:

$$\delta_{R,fin} = \frac{G}{M} \quad (3.121)$$

The yaw of repose is also visible in figures 3.32 & 3.33. For right-handed grooved projectiles, it tends to move the flight-path slightly upwards and to the right. Physically, it is related to the delay that the longitudinal axis of the projectile has with the velocity vector. The latter will "fall" first due to gravity and the longitudinal axis of the projectile will follow with a slight delay because of inertia. This predominantly positive angular difference between the two axes leads to a small pitching moment pushing the nose of the projectile upwards, which will be compensated by a movement of the nose to the right, given the right-handed gyroscopic stabilization (See Box 2.2).

Conversely, for a statically stable projectile with a slight rotation to the right, the yaw of repose will point to the left since the pitching moment is reversed. A finned projectile that does not rotate will have a yaw of repose that should theoretically remain in the vertical plane (this of course implies the total absence of external disturbances).

The linear theory has proven to be a precious tool in the analysis of basic dynamic characteristics of projectiles in flight, allowing to establish stability criteria for fin- and spin-stabilized projectiles (Chap.5), and for the implementation of software allowing the extraction of projectile aerodynamic coefficients based on spark range data (Chap.6). However, the standard linear theory being limited to low launch angles, Hainz [93] and Gkritzapis [88] have more recently formulated and illustrated a modified linear theory closed-form solution, allowing rapid and accurate calculation of long-range trajectories with large pitch angles.

3.7 The Modified Point Mass Model - MPMM

Following the 6-DoF Lieske & McCoy approach in 1964 [120], Lieske & Reiter developed the equations of the Modified Point Mass Model²³ [121], by giving a more general definition of the vector yaw of repose than that given in the linearized approach. The original and relatively complex mathematical development will then be reviewed by a more direct and mathematically simpler approach by Eduard Celens in 1987 [32].

As it has been put forward with the Linear theory with some simplifications (Sec. 3.6), the differential equations of motion set out at the beginning of this chapter (Eq. 3.19 & 3.20) can be formulated as a second order equation in terms of complex variables (Eq. 3.102). If a projectile presenting a symmetry of revolution is considered, the homogeneous solution is a transient epicyclic motion, while the particular solution is a quasi steady-state yaw of repose, also called yaw of equilibrium. These solutions had been physically represented in figure 3.32 for a spin-stabilized projectile.

The Modified Point Mass Model is a model that takes advantage of the representation made in the Linear theory to postulate that **if the epicyclic pitching and yawing motion is small everywhere along the trajectory, i.e. if the projectile is correctly dynamically stabilized**, it is not necessary to distinguish all the nose movements of the projectile with precision to make an accurate trajectory prediction. For a right-hand spinning projectile, this results in a nose motion to the right, already defined as the **Yaw of Repose** in section 3.6.2. The knowledge of a "smooth" angle of attack allows the projectile to drift the right amount while being fairly accurate. This approach is also consistent for a finned projectile, but then only in the vertical XY plane. The present assumption allows a consequent simplification of the 6-DoF since the time step can then be multiplied by at least a factor of 10^3 for the most common applications.

This explains why the MPMM is the operational model by excellence, since it lightens the calculations without losing much accuracy on the target compared to a 6-DoF calculation (as long as the model has been properly fitted - Sec. 3.7.1). This model is the NATO standard 4 degrees of freedom model for spin stabilized cannon and mortar projectiles, defined in STANAG/AOP-4355 [11, 14]. It is however necessary to emphasize that this model efficiently calculates a trajec-

²³It is therefore called the Lieske's MPM Model in AOP-4355 [11].

tory but is not at all appropriate for the design phase of a barrel-projectile combination since it is not able to give a correct indication on the projectile's stability. The MPMM will then in some cases be able to give a trajectory solution when in reality the projectile will have already reversed and described another completely unpredictable trajectory.

The definition of the vector yaw of repose was already given in the previous section, but this remained within the framework of the assumptions made for the Linear theory. In order to keep the yaw angle small, the longitudinal axis of a symmetric gyroscopic stable projectile should follow the angular velocity of the vector velocity $\omega_{\vec{V}}$. This angular velocity can be described as:

$$\omega_{\vec{V}} = \frac{\vec{V} \times \dot{\vec{V}}}{V^2} \quad (3.122)$$

Then, according to the explanation given for the reaction of a gyroscope to an external torque (Box 2.2 - in this case the pitching moment (Eq. 3.46)), it is to be expected that the longitudinal axis will be placed in the plane formed by $\omega_{\vec{V}}$ and \vec{V} . The precession velocity of the axis had also been defined as :

$$\vec{\omega}_p = \frac{M}{I_x p} (\vec{1}_x \times \vec{1}_M) \quad (3.123)$$

where \vec{M} has a modulus proportional to $\sin \delta$ and is pointed along $(\vec{1}_V \times \vec{1}_x)$. If the vector yaw of repose $\vec{\delta}_R$ is now defined as:

- It has its origin at the CG;
- Its modulus $|\vec{\delta}_R| = \sin \delta$;
- It is perpendicular to \vec{V} and located in the plane $[\vec{1}_V, \vec{1}_x]$;
- It is oriented from $\vec{1}_V$ towards $\vec{1}_x$;

it can be deduced that $\vec{\delta}_R$ is oriented in the opposite direction to $\frac{\vec{V} \times \dot{\vec{V}}}{V^2}$ producing an overturning moment depending on $|\vec{\delta}_R|$. By resuming equations 3.122, 3.123 and 3.46 where ω_p "follows on average" ω_V , it comes that:

$$-\frac{\vec{V} \times \dot{\vec{V}}}{V^2} = \frac{\frac{\rho V^2}{2} \frac{\pi d^2}{4} dC_{M_\delta} \vec{\delta}_R}{I_x p} \quad (3.124)$$

$\sin \delta_R \approx \delta_R$ as the angles are assumed to be small. This leads to equation 3.127 for the yaw of repose of spin-stabilized projectiles, with the introduction of wind through $\vec{V}_W = \vec{V} - \vec{W}$.

For fin-stabilized projectiles, without lateral velocity nor side motion, and assuming small angles ($q = r = 0, w = 0, v \approx 0, u \approx V$), the axis of the projectile tends to follow directly the velocity vector and it results that:

$$\omega_{\vec{V}} = \frac{\vec{V}}{V} \quad (3.125)$$

In addition, the angular velocity of the longitudinal axis can be seen as the pitching moment on its damping:

$$\omega_{1_x} = \frac{\frac{1}{2}\rho V^2 \frac{\pi d^2}{4} d C_{M_\delta} \delta_R}{\frac{1}{2}\rho V^2 \frac{\pi d^2}{4} d (C_{M_q} + C_{M_\alpha}) * d/V} \quad (3.126)$$

By equating the two angular velocities of equations 3.125 and 3.126, we then find the vector yaw of repose for fin-stabilized projectiles in equation 3.128.

**Yaw of repose for
spin-stabilized projectiles:**

$$\delta_R = \frac{-8I_x p (\vec{V}_W \times \vec{V})}{\pi \rho d^3 V_W^4 C_{M_\delta}} \quad (3.127)$$

**Yaw of repose for
fin-stabilized projectiles:**

$$\delta_R = \frac{-d(C_{M_q} + C_{M_\alpha}) \vec{V}}{C_{M_\delta} V_W^2} \quad (3.128)$$

The use of the yaw of repose replaces the angular motion equations and the resolution of equation 3.129 allows a reliable calculation, the pitch moment & pitch damping moments being still included in the expression of the yaw of repose. δ_R being dependent on the rotation rate p , it is however also necessary to compute the axial deceleration by means of equation 3.36, which becomes 3.130 since the only angular moments around x are the spin damping moment and/or the rolling moment [137].

MPMM Equations of motion:

$$\begin{aligned} \frac{d\vec{V}}{dt} = & -\frac{\pi\rho id^2}{8m} [C_{D_0} + C_{D_{\delta^2}}(Q_D\delta_R)^2]V\vec{V} + \\ & \frac{\pi\rho f_L d^2}{8m} [C_{L_{\delta_0}} + C_{L_{\delta_3}}(\delta_R)^2]V^2\vec{\delta}_R + \\ & \frac{\pi\rho Q_M d^3}{8m} C_{N_{p\delta}} p(\vec{V} \times \vec{\delta}_R) + \vec{g} + \frac{\vec{\Lambda}}{m} \end{aligned} \quad (3.129)$$

$$\frac{dp}{dt} = -\frac{\rho S d^2 V_W}{2I_x} p C_{l_p} + \frac{\rho S d V_W^2}{2I_x} \delta_F C_{l_{\delta F}} \quad (3.130)$$

i = form factor

Q_D = yaw drag fitting factor

f_L = lift fitting factor

Q_M = Magnus force fitting factor

3.7.1 Fitting factors

Equation 3.129 contains four "new" parameters, being fitting factors or form factors.

Fitting factors are used to calibrate models, where certain phenomena have been neglected (in the case of the MPMM, precession and nutation), to "reality", i.e. to ensure that these models reproduce results as close as possible to other²⁴ trajectory information [63]. In the case of the MPMM, these fittings can be generated on the basis of a 6-DoF model or directly from the firing data. The parameters of the mean impact points of shots fired under the same conditions with the same firing elements are then considered. If no fitting is available, the factors contained in the models should be equal to one. Moreover, these factors must respect a certain margin beyond which the model to be fitted is no longer relevant regarding the application to be modeled. The method to establish fitting factors is described in AOP-65 [14].

The form factor i is a range fitting factor with the aim of modifying the drag force. It is typically a function of charge (MV) and quadrant elevation (QE).

²⁴"Other" means real or computed trajectory with higher fidelity model.

3.7.2 Validation of the code

As it is an operational model and the finality is to have the firing elements to reach a given target (indirect problem), the MPM implemented in LabVIEW was validated on the basis of the Fire Control Trajectories (FCT) 155-AM-B computed with the Battery Computer Software (BCS) version 11 by the FTaB in June 1995 [73].

The FCT 155-AM-B are valid for the 155 mm gun M185 on howitzer M109A1 firing M107 HE projectiles. Table 3.4 shows the general parameters of the firing scenario. The trajectory integration is carried out using a standard fourth-order Runge-Kutta scheme with a fixed Δt of 10^{-2} s.

Table 3.4: Firing scenario for FCT 155-AM-B.

d	0.155	m
m	43.092	kg
I_x	0.146	kgm ²
Tw	20	cal/turn
Q_D	1.2	
Meteo	ICAO	
Lat	45 North	°
Alt	0	m
Alt Target	0	m
Az Target	6400	mils

Table 3.5: Additional data as a function of the propellant charges.

Case	Charge	MV	Target Distance	f_L	i
1	M3A1 1G	207.8 m/s	3084 m	0.967	1.3378
2	M3A1 2G	235.8 m/s	3898 m	0.967	1.3161
3	M3A1 3G	275.7 m/s	5227 m	0.967	1.1819
4	M3A1 4G	315.7 m/s	6563 m	0.9076	1.1336
5	M3A1 5G	375.6 m/s	7904 m	0.9076	1.0554
6	M4A2 3W	296.7 m/s	5930 m	0.967	1.1819
7	M4A2 4W	336.7 m/s	7071 m	0.9076	1.1336
8	M4A2 5W	396.6 m/s	8309 m	0.9076	1.0554
9	M4A2 6W	473.6 m/s	9949 m	0.9076	1.0320
10	M4A2 7W	567.5 m/s	12058 m	0.9076	1.0230
11	M119A2 7R	685.6 m/s	14928 m	0.9076	0.9999

For each charge and under the scenario conditions, the firing corrections (azimuth and elevation) to reach the target located at the distances listed in table 3.5 must therefore be obtained, with the muzzle velocities (MV) corresponding to each charge. For each of the cases, fitting factors are also given.

Validation requires that the solution be included within a tolerance range for each case. FTaB recommends a tolerance of 0.05% of range when comparing the solutions generated by computers and those generated by the FTaB[73]. These solutions and tolerances translated in firing angles are listed in elevation and azimuth in tables 3.6 and 3.7 and represented in corridors in figures 3.36 and 3.37. This illustrates the "theoretical" validation of the LabVIEW program.

Table 3.6: Elevation control data.

#	QE_{FTaB}	QE_-	QE_+	QE_{VTraj}
1	440.5	438.5	442.5	440.5
2	442.0	440.5	444.0	442.3
3	444.0	442.5	445.0	444.2
4	445.0	444.0	446.0	445.6
5	446.5	445.5	447.5	447.1
6	445.0	443.5	446.0	445.1
7	446.0	445.0	447.0	446.5
8	447.0	446.0	448.0	447.3
9	447.5	446.5	448.5	448.0
10	448.0	447.0	449.0	448.7
11	448.5	447.5	450.0	449.7

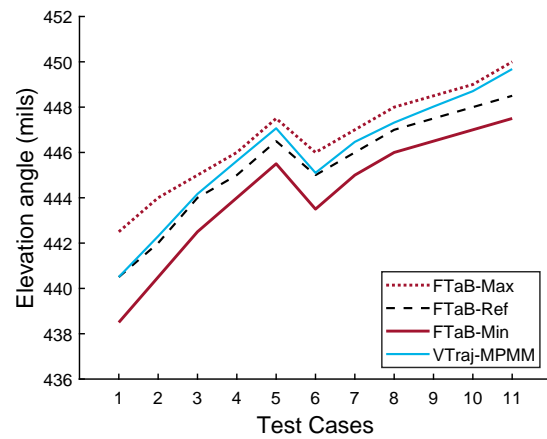


Figure 3.36: Solution VTraj included in the FTaB corridor for elevation[73].

Table 3.7: Azimuth control data.

#	Az_{FTaB}	Az_-	Az_+	Az_{VTraj}
1	6389.0	6385.5	6392.0	6388.9
2	6388.5	6385.8	6391.0	6388.5
3	6388.0	6386.2	6390.0	6388.1
4	6389.0	6387.5	6390.5	6388.9
5	6388.2	6387.0	6389.5	6388.2
6	6388.0	6386.5	6390.0	6388.1
7	6389.0	6387.5	6390.0	6388.8
8	6388.0	6386.5	6389.0	6387.9
9	6386.5	6385.0	6387.5	6386.5
10	6385.0	6383.7	6386.0	6384.9
11	6383.0	6382.0	6384.0	6383.0

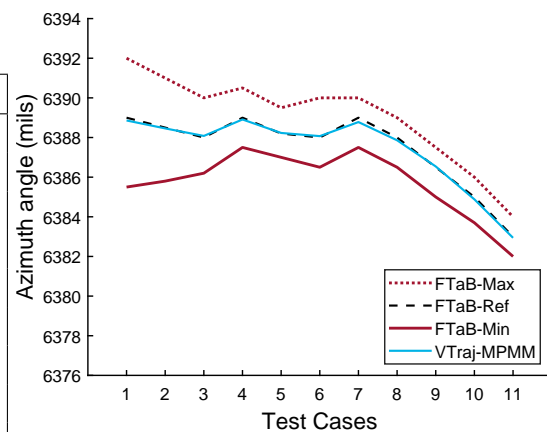


Figure 3.37: Solution VTraj included in the FTaB corridor for azimuth [73].

3.8 The Point Mass Model - PMM

The Point Mass Model is based on the principle that the main force acting on the projectile is the **drag force**, provided the projectile is flying at a low angle of attack, so all other aerodynamic interventions can be neglected. This model is then derived in assuming a zero angle of attack and therefore only considers the drag force at zero incidence. This simplifies the calculations in a non-negligible way, since only one expression defines the model and it can be solved very simply without using a complex solver. Furthermore, the C_{D_0} , which is the only aerodynamic coefficient needed, can be determined relatively simply experimentally (Box3.3).

Given the assumptions, this model is mainly used for small caliber, direct fire and preferably at short range (to avoid high angles of attack and the passage through the transonic zone given the non-linear character of the C_{D_0} in this zone). It can also be used for arrow projectiles with very high speed and flat trajectories. Outside these applications, commonly known as **Flat-Fire Trajectories**, it is not recommended to use this model. However, given the wide public confronted with small arms, this model is very widespread and is covered in any basic ballistics course[64].

The Point Mass Model is standardized in the STANAG 4355[11] as well, as 3DoF model, and can also consider a fitting factor to apply a range correction. In addition to this, as the model does not take into account the lift and consequently does not give any drift, an empirical drift can be formulated as a polynomial function of the initial elevation (QE). The Point Mass Model may also use the Spin Damping Moment Coefficient to simulate the spin rate of projectiles or submunitions for the purpose of turn counting[14, 277]. Since spin damping is not dependent on the angle of attack when the latter is small, adding a spin does not complicate the calculation with interdependent variables, it only adds one parameter.

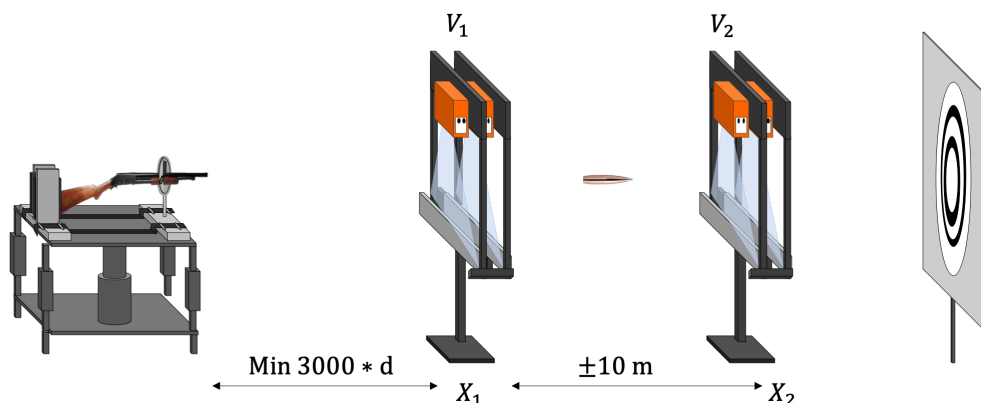
Box 3.3: C_{D_0} in the lab...

If the only force considered is the drag force at zero incidence^a, which is the force that slows down the projectile in the direction opposite to its velocity vector, it is fairly straight forward to deduce the expression of the aerodynamic coefficient as a function of this deceleration, that can be measured between two points (Eq.3.131). The representation below outlines the relatively basic setup required to measure this parameter, showing two velocity measurement bases positioned at the distances X_1 and X_2 . X_1 is significant since an anticipated measurement could still be in the phase of the initial percussion, with oscillations not yet damped, while a measurement too far away increases the risk of a projectile already falling down. The acquisition can also be done with a Doppler radar, considering two speeds at two fixed distances, this setup is of course more suitable for field measurements for larger calibers.

$$C_{D_0} = \frac{8m}{\rho\pi d^2} \frac{\ln(V_1) - \ln(V_2)}{X_2 - X_1} \quad (3.131)$$

Like any aerodynamic coefficient, C_{D_0} depends on the Mach number. It is therefore necessary to modify the quantity of powder in the cartridge case to vary its velocity and thus have enough points representative of the shape of C_{D_0} in the different velocity regimes.

^aGravity is perpendicular to the trajectory.



3.8.1 Analytical Solution with drag Modeling

As part of the U.S. Army's investigations into possible replacements for the 5.56 mm ammunition in the early 2000s, Weinacht, Newill & Conroy from ARL have proved the value of the PMM model for assessing the ballistic performance of high velocity direct-fire munitions, at the conceptual research stage when no definitive design is defined yet[262]. 3-DoF equations are usually solved numerically but with the Flat-Fire assumptions and the associated unvarying atmospheric conditions it is possible to find an analytical solution. Indeed, a drag coefficient varying with the inverse of the Mach number raised to a power "n" has been identified as a sufficient approximation. This relation is shown in equation 3.132:

$$C_D \equiv \frac{1}{Ma^n} \quad (3.132)$$

This equivalence was checked for a variety of munitions and it finally allowed to characterize the trajectories in terms of three independent parameters: the muzzle velocity, the muzzle retardation and the parameter "n" defining the shape of the drag curve in the supersonic regime[261]. This approach in the supersonic regime is illustrated in figure 3.38 for the different projectile geometries already presented in figure 3.11. Cooper, Weinacht & Newill[43] extended the approach for elevation angles up to 30° and finally presented an efficient parametrized model that can be used in engineering applications such as ammunition benchmark phase.

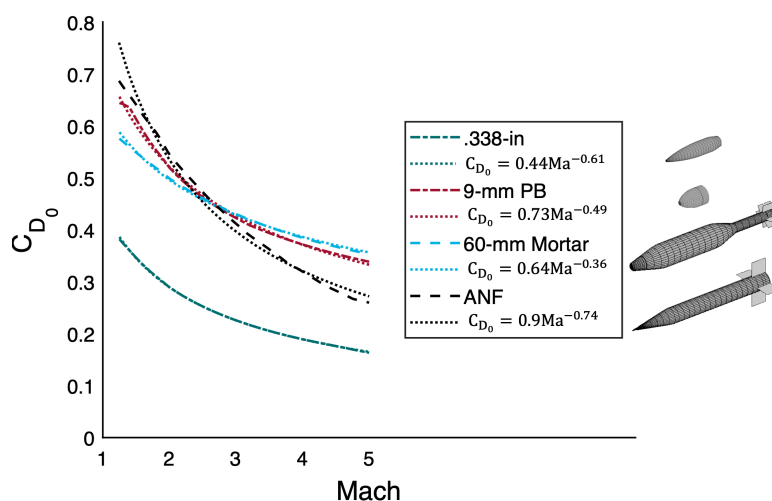


Figure 3.38: "n"-power approximation for different projectile geometries.

3.8.2 Siacci's Method vs Ballistic Coefficient

Siacci's method (well described in [137]) was implemented around 1880 for flat-fire trajectories with $QE < 15^\circ$. The method consists of referring for each trajectory, tabulated values of the range, time of flight, height and inclination, in terms of the "pseudo-velocity". This velocity is equivalent to the product of the horizontal component of true velocity and the secant of the angle of departure.

The method is based on the PMM theory, but instead of considering a zero incidence drag curve (non-linear curve) as a function on the Mach number, it is based on a single value referring to drag, called the ballistic coefficient (BC- Eq.3.133). BC is defined as the ratio between the sectional density (SD) of the projectile and its shape factor (i_x). The latter being the ratio between the real C_{D_0} coefficient of the projectile under consideration and the C_{D_0} of a standard projectile (G_x). As the method has been first extended in the United States, it does not consider the SI units but the US customary units²⁵.

$$BC = \frac{SD}{i_x} = \frac{\frac{m}{d^2} \left[\frac{lb}{in^2} \right]}{\frac{C_{D_0}}{G_x}} \quad (3.133)$$

The ballistic coefficient (BC) is then referred as the ability of the bullet to maintain velocity, in comparison to a standard projectile[124]. A high BC bullet can maintain velocity better than a low BC bullet under the same conditions, which is logically the inverse definition of the drag coefficient. Although this method has been abandoned in operational artillery environment, it is still used throughout the sporting and ammunition community[137, 261]. Indicative BC values can therefore still be found on commercially available ammunition boxes.

As confirmation, many nations have adopted for their sniper teams fire control equipment based on the Siacci method with the use of the application *Applied Ballistics*²⁶. This product line developed by Bryan Litz is essentially based on the definition of the ballistic coefficient.

²⁵1 lb = 7000 gr. \approx 0.45 kg (gr.=grain) 1 in \approx 0.3048 m.

²⁶<https://appliedballisticsllc.com/>

In the original Siacci's theory there were eight standard projectiles, but nowadays only two come up systematically in practice, called G_1 and G_7 (Fig.3.39). G_1 projectile is short, with a flat base and a tangent ogive, while G_7 projectile is more elongated, presenting a boat-tail and a secant ogive.

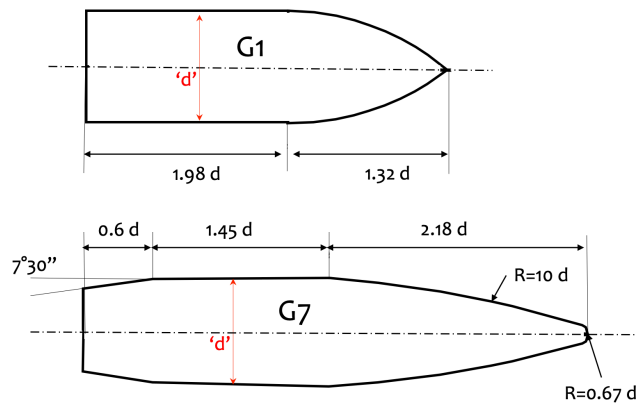


Figure 3.39: G1 vs G7 standard projectile's geometries.

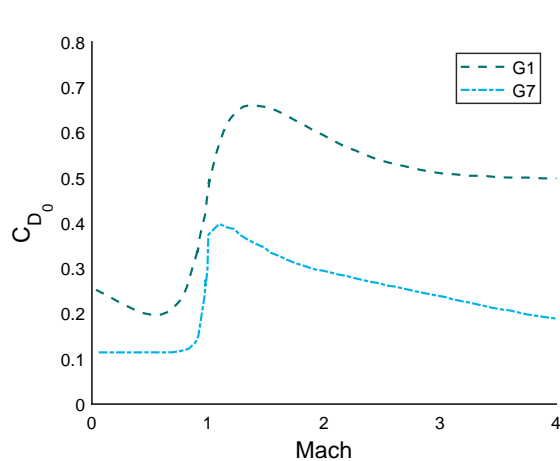


Figure 3.40: C_{D_0} coefficient shapes for G_1 and G_7 standard projectiles[137].

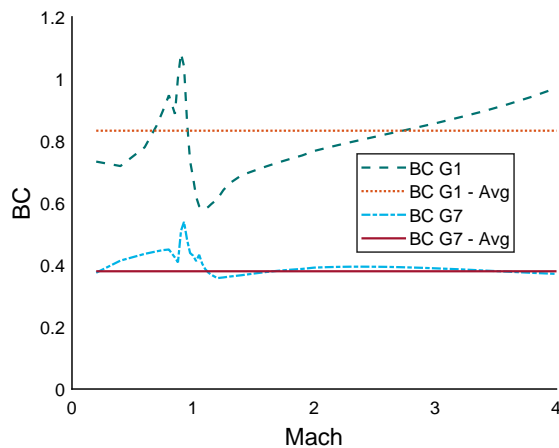


Figure 3.41: Ballistic coefficient for the .338-inch projectile, according to G_1 and G_7 .

From the way they look, one might wonder why the G_1 projectile is still in the race, as it does not look like the current precision projectiles. The reason is rather related to tradition and to the fact that the value of BC G_1 will always be higher than the BC G_7 value for the same projectile, which is interesting from a marketing point of view... From an accuracy point of view however, it is much more correct to use the G_7 projectile as a reference for long distance shooting, since the shape factor will indeed be much more constant than for the G_1 projectile whose drag curve will differ widely, as shown in figure 3.41 for a .338-inch projectile, commonly used within the sniper community.

Since this approach is used in the world of sniping, where it is necessary to cross the transonic zone with precision, corrections are applied by firing, to "calibrate" the BC at transonic and subsonic distances, this can be seen as the work with fitting factors, already discussed earlier. This calibration in the field is nevertheless tedious, but it is the price to pay to work without a complex calculation, which requires aerodynamic coefficients that are impossible to determine by a standard user.

This last point underlines in a way the interest of this present work which aims at facilitating the access to these precious data for any user, while keeping in mind of course that the calculation software will have to adapt to the available data (intermediate model between PMM and MPMM for instance).

Chapter 4

Existing software in practice

The programming behind this work is certainly not pioneering in this area, as commercial software as well as software developed by national or NATO working groups has been revising their versions for a couple of decades now. The purpose of this part is to highlight the references in the field of trajectography software, regardless of their accessibility. These programs are managed and optimized in accordance with all the proper rules and with a large set of operational functionalities, but the central architecture and the sensitive points remain essentially the same.

As with any problem confronted with simulation, whatever it may be, the problem of THE reference always arises when there is a discrepancy: *Who's telling the truth?* This was for instance recently highlighted by Eric Gagnon comparing several major codes and proposing further improvement solutions [84]. The development task is therefore not quite finished yet, and that's rather a good news, there is always room for discussion and improvement...

HTRAJ

As mentioned in the section about 6-DoF validation codes (sec.3.5), HTRAJ was developed in Fortran by the Firing Tables and Ballistics Division (FTaB), which is part of the US ARDEC (Armament Research, Development and Engineering Center), to support Army & Naval firing. HTRAJ was a national product developed before the NATO products, it was later one of the piece of software used for the quality assurance of the NABK package (See below) [10]. Document [162]

seems to give the necessary details about this code but the author could not find this reference. More recently, HTRAJ was used for the validation of the BALCO 6 DoF module [270].

ARFDAS

The **Aeroballistic Research Facility Data Analysis System** (ARFDAS) is again a set of Fortran programs used for the determination of aerodynamic coefficients from spark range experimental data and analyze of the 6-DoF ballistic trajectories reconstructed from free flights [76]. It was developed by the United States Air Force Aeroballistic Research Facility (ARF), and was then also regularly used by the Army Research Laboratory for their sessions on firing ranges [217].

PRODAS

Projectile Design and Analysis System (PRODAS) version 3 is a Commercial Software originated at General Electrics in 1972 and further developed by Arrow Tech Associates Incorporated since 1991 [55]. Arrow Tech was founded in 1987 by Bob Whyte, a former aeroballistician and ammunition development technical leader at the US ARDEC¹. Unsurprisingly, aerodynamics and flight simulation have always been at the core of Arrow Tech's activities. The company also offers various training courses in exterior ballistics to learn how to use their products [17]. The main purpose of PRODAS is to perform rapid design and evaluation on the performance of ammunition characteristics, using a 6-DoF core and semi-empirical functions for determining aerodynamic coefficients (Sec. 6.2.2). The program links several diversified analyses in a common database, so that the results of one analysis feed directly into a later analysis [250]. From the author's point of view, it is the most validated and comparative reference program used for trajectography.

¹<https://arrowtechassociates.com/aerodynamics>.

As shown in figure 4.1, the analysis possibilities of PRODAS are impressive.

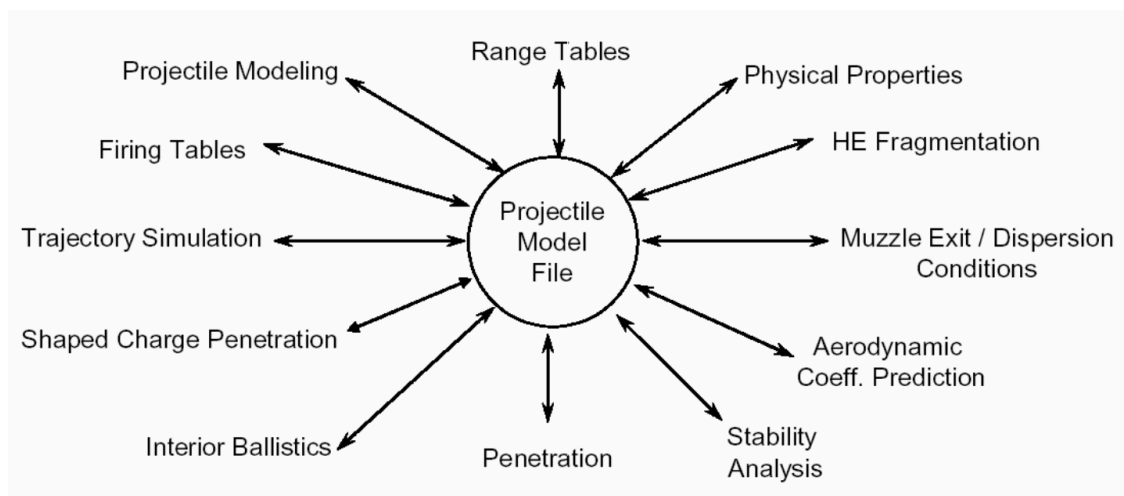


Figure 4.1: PRODAS Analysis options [16]

NABK

The **NATO Armaments Ballistic Kernel** is part of the NATO Army Armaments Group AC/225² Land Capability Group/3 (Fire Support), Sub-Group 2 (Accuracy and Ballistics) Sharable Software Suite (S4) and is the component that performs the ballistic computations intended to support indirect fire such as howitzers, rockets, and mortars [227], as illustrated in figure 4.2.

STANREC-4537[231] rules the NABK, together with **AOP-37** (4 volumes). The technology implemented in the product is primarily based on that from STANAGs 4355 [11] and 4500 [230]. This means concretely that the NABK is based on a **MPMM** calculation, and contains a large database of fitting factors for all types of ammunition supported by the software. The first formal release was NABK version 0.9 in 1998 and the current version is version 20.0 (OSCAR), implemented from the beginning in ADA programming language. *"The NABK is implemented in more than 20 countries and is used in every operational cannon artillery fire control system in service with the United States Army and Marine Corps, as well as several mortar fire control systems"*³.

²<https://diweb.hq.nato.int/naag/>

³<https://www.army.mil/article/215516>, Feb 2021.

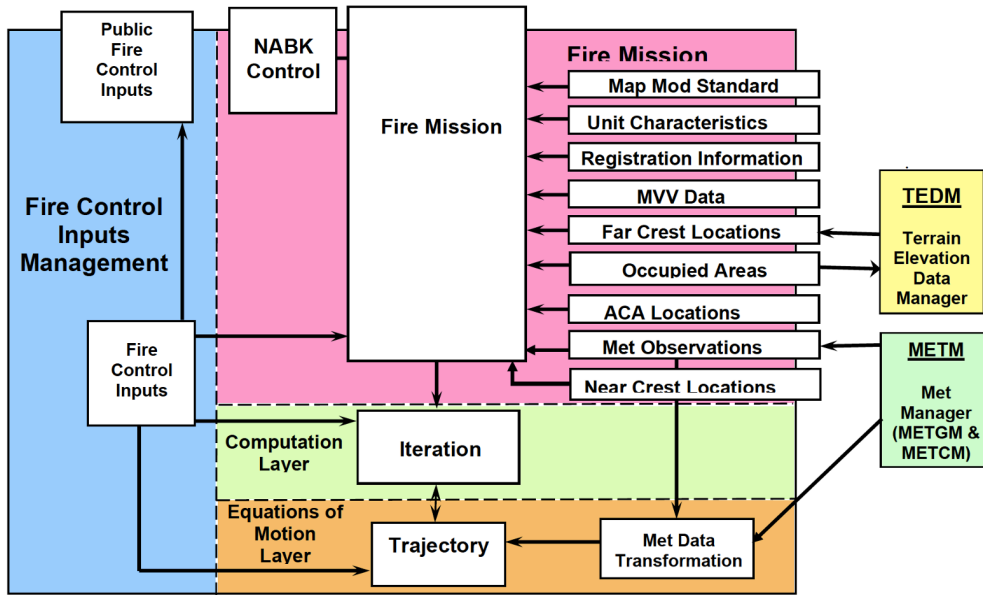


Figure 4.2: NABK Software Architecture

SABK

The **Small Arms Ballistic Kernel** is a by-product of the NABK, the first version of which was released in 2016. It was optimized to support ballistics computation for direct fire weapon systems including rifles, machine guns, and grenade launchers.

This program was first dedicated for the Canadian snipers, so that Canadian DRDC Valcartier Research Center was asked to carry out high-fidelity 6-DoF trajectory simulations for a set of relevant scenarios for the snipers, and to compare the direct fire results with those obtained with the 4-DoF NABK adapted to simulate small-arm ammunition trajectories [44].

BALCO

BALCO, abbreviation of **BALlistic COde**, is a computer code implemented under cover of the STANREC-4618 [232] and AOP-50 [270], AEP-96 [1] aimed to standardize high-fidelity 6/7-DoF trajectory models for both conventional and precision-guided projectiles. While the 6-DoF model is used to describe the motion of single rigid bodies, the 7-DoF model allows the description of a projectile which consists of two coaxial rigid bodies that can spin independently [272].

BALCO version 1.0b was first released in March 2015 for beta testing and comparison with PRODAS V3, HTRAJ [232] and DRDCSIM [84]. Reference [84] gives an overview of the comparison with PRODAS and DRDCSIM. The code is written in Fortran 2003, uses quaternions and a RK7 integration scheme. The working group is under the lead of the Franco-German Institut Saint Louis (ISL) [272] and the 1.0 version will be very soon distributed to the S4 NATO Community. It also includes a graphical interface *WinBALCO* developed by Nexter Munitions.

DRDCSIM

This piece of software was developed by the Defense Research and Development Canada— Valcartier Research Center (DRDC-VRC) in Simulink and is largely used at DRDC-VRC to study multiple types of flying vehicles, including fin and spin-stabilized projectiles. It was also use as "mediator" to understand the discrepancies between PRODAS and BALCO software[84]. The program uses also the quaternions for the coordinates rotations while PRODAS still uses Euler angles.

Chapter 5

Stabilization concepts

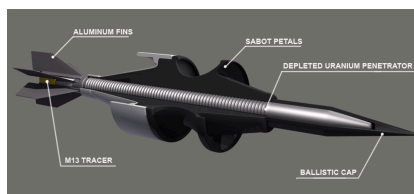
Stability has already been approached in the previous chapters. Now it is possible to quantify this stability by means of the trajectory models already described. The approach described below uses the notations and representations of Murphy [156].

Static stability is not included here since it is only based on the relative position of the center of pressure with respect to the center of gravity (Chap. 2). As a reminder, a projectile with fins has its center of pressure behind its center of gravity with respect to the nose of the projectile, which makes it a statically stable projectile. Conversely, a conventional projectile is by nature statically unstable and will need to be gyroscopically stabilized (Fig. 2.2). It is therefore precisely this spin that needs to be quantified in order to establish gyroscopic stability criteria, discussed in the next section.

Box 5.1: Why not always use fins?

The use of fins has an advantage in terms of stability, because the projectile will naturally tend to position itself correctly. Also, the design process of the grooves in the tube according to the dimensions of the projectile does not arise because a smooth barrel is used. If the projectile is provided with fins, its body is either under-calibrated (in the case of arrow projectiles - APFSDS) or the fins are hidden by the body of the projectile, as it is the case with mortar bombs. In this particular case, the projectile is loaded through the muzzle of the tube, so it does not completely seal the barrel, which results in significant losses of speed during propulsion and a lot of dispersion on the muzzle velocity. This last consequence is accepted in the case of mortar fire because it allows the use of a much simpler weapon for indirect fire (a simple smooth tube fixed on a plate), and the projectile contains an explosive charge with a much greater operating radius than kinetic energy projectiles.

Two types of 120-mm finned projectiles:



APFSDS : fins > body.



Mortar bomb : fins < body.

In the case of "arrow" firing, in contrast, we necessarily have direct firing, since the energy density at impact is crucial (See also Box. 5.2). The design of the sabots must be done for a projectile that is always finer, longer, denser and faster (but also more sensitive to bending deformations). This complexity also generates an exorbitant cost that can exceed the gain achieved by the absence of grooves. The use of sabots is also a critical aspect in terms of opening at the exit of the tube. Their interaction with the muzzle brake and their lethality at the outlet must not be overlooked. Finally, the need to use sabots is a loss in terms of kinetic energy, since they must also be accelerated, without participating to the impact.

5.1 Gyroscopic stability

In order to address gyroscopic stability, it is necessary to resume the linearized pitching and yawing motion equation for rolling projectiles (Eq.5.1) and its solutions for the arm turning rates (Eq.5.4). These are included here to ease the analysis (see section 3.6.1 for further details):

$$\xi'' + (H - iP)\xi' - (M + iPT)\xi = -iPG \quad (5.1)$$

$$\xi = K_F e^{i\phi_F} + K_S e^{i\phi_S} + K_T e^{i\phi_T} + i\delta_R \quad (5.2)$$

$$\phi_{F,S} = \phi_{F_0,S_0} + \phi'_{F,S} \quad (5.3)$$

$$\phi'_{F,S} = \frac{1}{2} \left[P \pm \sqrt{P^2 - M} \right] \quad (5.4)$$

If $(P^2 - M)$ is positive in equation 5.4, then the exponents for the fast and slow arms are pure imaginary, meaning that their lengths remain fixed. Conversely, if $(P^2 - M)$ is negative, then the exponents will have a real part and the slow arm will tend to grow exponentially. For that reason, it is necessary to fix $(P^2 - M) > 0$ to avoid this trouble. By developing P and M respectively, this condition is reformulated to establish a gyroscopic stability criterion (Eq.5.5)[246]:

Gyroscopic Stability Condition:

$$S_g = \frac{P^2}{M} = \frac{2I_x^2 p^2}{\pi I_T d^3 \rho V^2 C_{M\delta}} > 1 \quad (5.5)$$

In most cases, the translation velocity slows down faster than the rotation velocity, and this is especially true for curved trajectories. This implies that the S_g factor will tend to increase downrange, so it is at the muzzle exit that this condition is the most constraining. For fin-stabilized projectiles, M is negative anyway and therefore $(P^2 - M) > 0$ is respected in any case. This proves that they are statically stable with or without rotation. This formula also shows that if the length of a projectile increases (I_T will increase), while it is not possible to increase the spin rate p accordingly, the ratio $S_g > 1$ will become impossible to maintain, hence the need to adopt a fin-stabilized projectile (See Box 5.2).

5.2 Dynamic stability

If the damping is now considered, it is necessary to have both damping exponents (Eq.5.6) negative during the flight in order to damp the oscillations and achieve stability. This was already illustrated for a 5.56 mm projectile in section 3.6.

$$\lambda_{S,F} = -\frac{1}{2} \left[H \pm \frac{P(2T - H)}{\sqrt{P^2 - M}} \right] \quad (5.6)$$

$$\left[H \pm \frac{P(2T - H)}{\sqrt{P^2 - M}} \right] > 0 \quad (5.7)$$

If a new perturbation appears, one of the damping exponent could become positive, but for a limited time. It is therefore necessary to minimize these slots by considering that they must be negative. For finned projectiles, this only implies that $H > 0$ (P being zero or negligible). As for these projectiles ($C_{M_q}^* + C_{M_{\dot{\alpha}}}^*$) is generally negative and C_D, C_L are positive, this leads anyway to a positive H . For spin-stabilized projectiles, it is necessary to define a new criterion to ensure negative damping exponents, reason why S_d , is defined as dynamic stability factor [156] as:

$$S_d = \frac{2T}{H} \quad (5.8)$$

Substituting S_d in inequation 5.7 leads to $H > 0$ and:

$$\left[\frac{P^2(S_d - 1)^2}{P^2 - M} \right] < 1 \Rightarrow \frac{M}{P^2} < S_d(2 - S_d)$$

Linking the latter expression with the coefficient of gyroscopic stability gives the final conditions:

Dynamic Stability Conditions:

$$H > 0 \quad (5.9)$$

$$S_g > \frac{1}{S_d(2 - S_d)} \quad (5.10)$$

The second relation expresses that for values of S_d lower than 0 or higher than 2, it is not possible to dynamically stabilize a statically unstable projectile, regardless of

the induced rotation. On the other hand, a statically stable projectile can be made dynamically unstable if too much spin is transmitted. Equation 5.10 is illustrated in figure 5.1 for S_d values between 0 and 2 [137, 156].

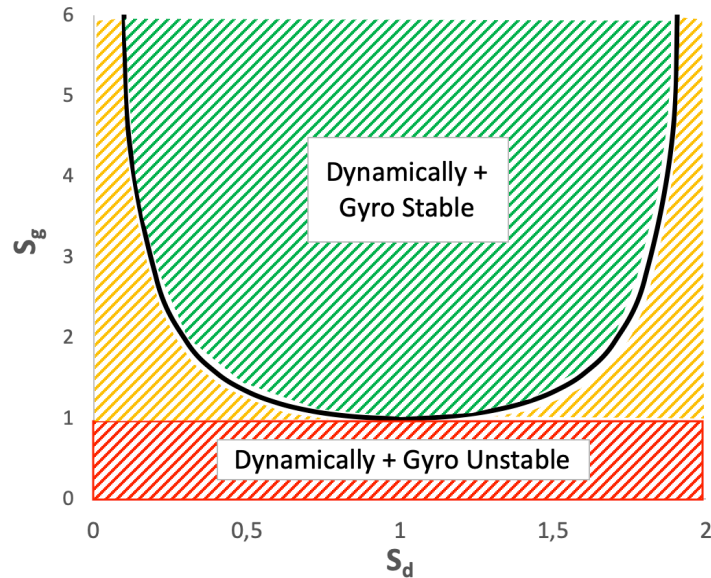


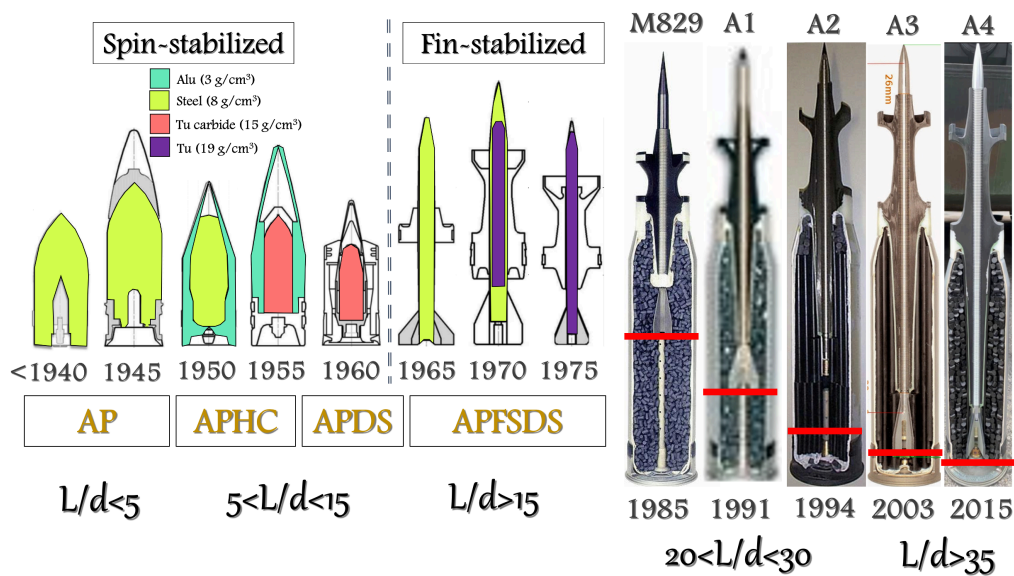
Figure 5.1: Gyroscopic versus Dynamic Stability Criterion. The orange part implies gyroscopic stability but not dynamic stability.

It allows to understand that a gyroscopically stable projectile is not necessarily dynamically stable. This is why it is not enough in the design phase to be satisfied with a S_g close to one, it is better to take a safety margin to consider the dynamic properties.

Box 5.2: Evolution of Armour Piercing...

The requirements of terminal ballistics have given external ballistics a hard time in terms of stability [116]. Indeed, the development of the APFSDS as we know it today (Box 5.1) went through several crucial and determining stages in terms of calculation. The Armour Piercing (AP), designed as its name suggests to pierce armor, was initially a gyroscopically stabilized projectile, composed of steel with a L/d ratio <5 , a mass of less than one kilogram and an impact velocity around 700m/s. The energy density being too low, it was first a question of changing the core into tungsten carbide (hence the name AP Hard Core - APHC). This being not yet sufficient, the caliber was reduced and the length of the projectile increased, bringing out the first sub-calibrated projectiles using sabots but still gyroscopically stabilized (AP Discarding Sabot - APDS). At some point in the development, the rotation that had to be induced to the projectile became impossible to implement in practice (I_T & V being in the denominator in equation 5.5), it was then time to change the stabilization mode.

As an example, the right part of the illustration below shows the evolution of the 120-mm M829 ammunition with its four upgrades. This ammunition is used among others by the ABRAMS tank and because the weapon did not change, it is the composition and the arrangement of the arrow inside the casing which had to be optimized. The latest version of the arrow now have a mass of 10kg with ultra-light composite sabots and impact velocities exceeding 1400m/s.



5.3 Overstabilization

In terms of development, the reasoning below makes also possible, **provided that the necessary coefficients are available**, to estimate the minimum spin to be induced to a projectile to ensure gyroscopic and dynamic stabilities:

$$P^2 > \frac{M}{S_d(2 - S_d)} \quad (5.11)$$

However it is also necessary to keep in mind the expression of the precession velocity ω_p which depends on the spin rate p :

$$\omega_p = \frac{\tau}{I_x p} \quad (5.12)$$

In the expression 5.12, τ is typically the pitching moment due to air resistance, but it can be any disturbing torque, which the gyroscopic effect has to deal with. Now if p is too large, ω_p will be very small and the projectile will be like "frozen", it will no longer be able to follow the curvature of the trajectory as it should, it is said to be overstabilized[63]. This will result in the projectile landing on its base and not on its nose as it should (Fig.5.2).

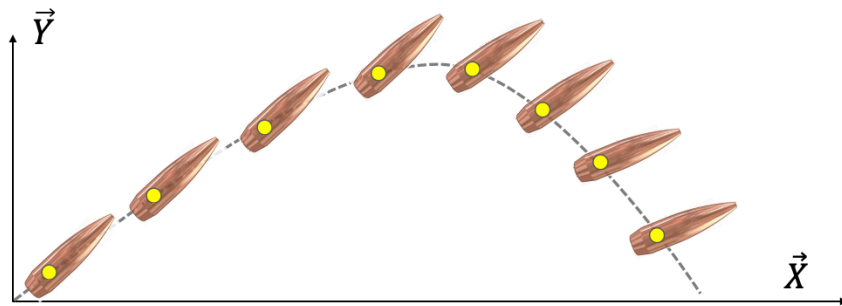


Figure 5.2: Representation of an overstabilized projectile. This makes it actually a better gyroscope since it is less sensitive to perturbations.

Chapter 6

Coefficient collection process

All the concepts considered so far make the reader aware of the importance of aerodynamic coefficients, both in the preliminary design phase to evaluate the potential stability of a projectile configuration, and also during the operational phase, to calculate a trajectory with precision and provide the right firing elements, whether with a very complete 6-DoF model or with a lighter but almost as powerful MPMM model to calculate a drift, without having to carry out a whole series of very costly experiments (only a few tests can be necessary for fitting and validation).

It is in this context that this section lists the techniques used to date for the acquisition of these valued coefficients. This is the logical link to consider the parts that will follow and focus more particularly on one of these methods, which is the determination by numerical simulation. This method certainly requires less effort in terms of equipment and practical implementation, but more technical background in terms of fluid mechanics.

Aerodynamic coefficients are mainly function of the nondimensional flight velocity: the Mach number (Ma). They also exhibit some dependence on the Reynolds number (Re) but the effects are implicitly included in the coefficient variation with Mach number (See Box 7.2). As officially mentioned in AOP-65[14], specifically in Annex G, aerodynamic coefficients are dimensionless and given in the form of consecutive polynomials of fourth degree or less defined over ranges of velocity. Each coefficient should then have the form :

$$C_i = a_{0,i} + a_{1,i}Ma + a_{2,i}Ma^2 + a_{3,i}Ma^3 + a_{4,i}Ma^4$$

The series of polynomials must be continuous and, for third or fourth degree polynomials, preferably differentiable at connecting breakpoints (using spline functions). A recent study of Rabbath & Corriveau (DRDC Valcartier)[181] mentioned there were very few published papers and reports that study the methods to generate such piecewise polynomial functions [193]. It makes a comparison of Piecewise Cubic Hermite Interpolating Polynomial (PCHIP), cubic splines, and piecewise linear functions to approximate the aerodynamics of a generic small arms projectile, in order to show the impact of the chosen polynomial functions on flight trajectory predictions obtained with 6-DoF simulations.

The method for aerodynamic coefficients determination depends of course on the available equipment. Below are listed most of the methods used in practice [14].

6.1 Experimental measuring techniques

6.1.1 Full scale firings

This method was the most widespread and the preferred one for long and high trajectories (artillery) when simulation techniques were less available [35, 157]. It includes principally the use of impact measurements, muzzle velocimeter, doppler radar, optical instrumentation and yaw measuring systems as yaw cards (Fig. 6.1)[41, 52, 176], but also a software package allowing the reconstruction of the trajectories for the extraction of the coefficients (such as ARFDAS piece of software [76]).

In France, the Direction Générale de l'Armement Techniques terrestres (DGA Tt) carries out firing tests for the company Nexter Munitions and has a large firing range at Bourges where techniques for identifying aerodynamic coefficients from measurements taken in flight have been developed. Magnetometry is one of them and has been developed by Institut Saint-Louis (ISL). It consists in placing three magnetic sensors in a very precise orientation in a highly integrated electronic system in the projectile. The sensors measure the earth's magnetic field locally, from which information about the projectile's behavior in flight can be deduced [52].



Figure 6.1: Yaw cards installed on the shooting range of Bourges (FRA) consisting of wooden posts between which are stretched sheets of kerosene, paper or cardboard, to disrupt the flight as little as possible [41, 52].

6.1.2 Aeroballistic Ranges (or Spark Ranges)

This method consists of taking multiple sequences of shadow photographs. In each position, two orthogonal cameras simultaneously make a recording of the velocity and the orientation of the projectile in flight. By means of image processing and a computer algorithm, the angles are calculated automatically and allow to extract the aerodynamic coefficients for small to medium yaw angles, depending on the facilities. Murphy already published in 1954 methods for extracting non-linear coefficients by means of free-flight tests in spark ranges[157]. Since then, dozens of articles have been published for all kinds of projectiles, a good number of them from Arrow Tech and its researchers, within the framework of the development of the PRODAS software¹.

TNO Science and Industry (NDL) has developed for instance such a Projectile Orientation Measurement (POM) device [36] for their ranges where it is possible to fire small and medium caliber, from test weapons but also from vehicles.

ARL (USA) have access to different firing ranges with for the biggest ones, the possibility to use up to fifty stations over a few hundred meters, for small to large caliber projectiles [189, 273] and for different velocity regimes [189]. Siltou & Howell's work [217], for instance, which enabled the acquisition of the aerodynamic coefficients of the 5.56 mm ammunition, has been carried out in a 100 meter indoor range with 39 dual-plane, direct-image spark shadowgraph stations with the first station at 1.8 meter from the muzzle of the gun[217].

¹A list with those publications can be found on their website www.PRODAS.com.

Free-flight experiments are also conducted with asymmetric maneuvering flight bodies to investigate nonlinear aerodynamic models and improve guided projectile configurations [81]. The results are then compared with wind tunnels experiments, computational fluid dynamics and onboard sensor techniques [26, 80].

For their part, DRDC Valcartier (CAN - Fig.6.2) is equipped with a 250 m instrumented firing tunnel capable of firing from 5.56 mm to 155 mm up to Mach 7 with temperature and humidity controlled conditions. In addition to the conventional devices found in shooting laboratories, they have 54 orthogonal indirect shadowgraphs (108 cameras) and 4 stations for Schlieren flow-visualization[45, 50, 62].



Figure 6.2: DRDC Valcartier Aeroballistics Range [62].

6.1.3 Wind Tunnels

This system is less specific to ballistics and more complicated to set up with high spin rates but it nevertheless allows to be used in very specific ranges and in very well controlled conditions. While steady forces and moments measurements are perfectly mastered today, dynamic measurements are still a real challenge. However, these last years have seen the appearance of new combined techniques, such as for instance stereovision techniques with high-speed camera's (Fig. 6.3), used by the Franco-German institute ISL [134], and their three-axis freely rotating test bench (MiRo) [155]. As in the spark ranges, the projectile is captured stereoscopically and its attitude is reconstructed a posteriori using image processing and

6-DoF codes. Their goal with the MiRo platform is to be able to characterize all the aerodynamic coefficients, including for an artillery shell [155]. ISL research center is furthermore equipped with aerodynamic testing facilities for the complete range of flow velocities from Mach 0.1 up to Mach 15², including ISL's Shock Tube Laboratory [271].



Figure 6.3: ISL's trisonic blow down wind tunnel with high speed camera's for stereovision-technique[134, 155].

At the Von Karman Institute (BEL), which has huge wind tunnel facilities, developments are underway to also determine experimentally pitch damping coefficients of slender bodies [112]. The latter are instrumented in a way that they can oscillate about the same location as in free flight, i.e. their CG (Fig. 6.4). As for CFD techniques (Sec. 9.2.2), a forced oscillation is generated in order to record the response and extract the coefficients.

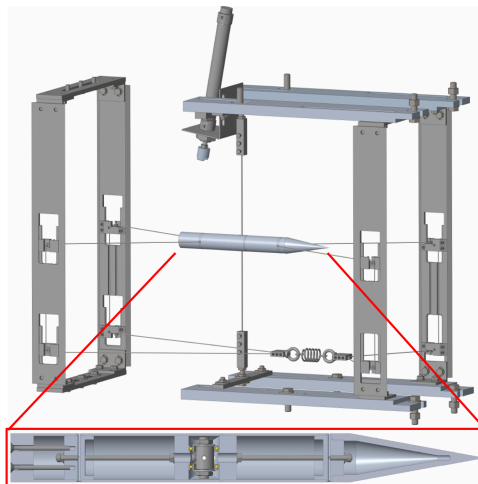


Figure 6.4: CAD model of the semi-free oscillation test bench with instrumented projectile, to use within the VKI S-1 Supersonic-Transonic wind tunnel [112].

²<https://www.isl.eu/en/flight-techniques-for-projectiles>

6.2 Software simulation techniques

6.2.1 Computational Fluid Dynamic Codes

This technique will be the subject of the next part of this work.

6.2.2 Semi-Empirical Interpolation Codes

This includes interpolating among simplified theory or tabulated aerodynamic data for typical projectile designs and shapes[12]. Component-build-up techniques consist in predicting an aerodynamic coefficient for a projectile by summing up aerodynamic properties calculated for various parts of the projectile, such as nose, base or fins[210]. In terms of codes, the following ones can be identified :

- **McDrag**

The McDrag Code is once again a work of Robert McCoy, available in FORTRAN language in its totality, with a detailed explanation of the calculations[136]. This code is suitable for determining the zero-yaw drag coefficient for spin-stabilized projectiles, from the given values of certain size and shape parameters. The results are valid over a Mach number range from 0.5 to 5 and a projectile diameter range from 4 to 400 millimeters. The code estimates drag coefficient to within 3% error at supersonic speeds, 11% error at transonic speeds, and 6% error at subsonic speeds.

- **SPINNER 72 ⇒ SPINNER 2004**

Spinner is the predictive code contained within PRODAS design program developed by Arrow Tech. It computes all the aerodynamic coefficients of Spin-Stabilized Projectiles based on projectile geometry[214]. The implementation of this code began in 1967 and most of the software was already developed in 1973. Subsequently the various upgrades involved improvements to the models for better prediction of Magnus and Spin Decay. The Spinner 98 version is the one implemented in the PRODAS v3 version which is the most widespread, but a new version, Spinner 2004, has appeared with a larger database of projectiles³ and a better quantification of the calculation

³According to Arrow Tech itself, the empirical database included in Spinner 2004 contains all of the ballistic shapes tested within the North American Spark Ranges since 1938.

uncertainty thanks to a more in-depth statistical analysis.

Aerodynamic Coefficient	Wind Tunnel	Spark Range	SPINNER-98
Axial Force	5-10	0-2	3-5
Normal Force	3-7	4-8	6-10
Magnus Force	Large	25	33
Pitching Moment	5-10	0-3	3-6
Damping Moment	Large	10-20	15-25
Magnus Moment	Large	10-20	15-25
Spin Deceleration	Large	5-10	10-15

Figure 6.5: Expected Aerodynamic Coefficient Percent Errors from PRODAS Program [16] par rapport aux différentes.

It is to be noted that no CFD code is implemented in the PRODAS software for the prediction of aerodynamic coefficients. The results are based on wind tunnel tests, free-flight tests and semi-empirical codes. The margins of error for these three techniques are shown in figure 6.5, which comes from their commercial advertising. The error percentage with the new Spinner 2004 version remains more or less the same.

- **Missile Datcom**

Besides the ARDEC work (US Army) and their very close contribution to the industry Arrow Tech, Missile Datcom is a development of the US Air Force. As its name suggests, this program provides an aerodynamic design tool to predict aerodynamic coefficients of conventional missile configurations, i.e. axisymmetric or elliptically-shaped bodies with one to nine sets of fins that can be operated independently, with or without airbreathing propulsion system[191].

- **AP72 ⇒ AP09**

In addition to the Army and the Air Force, the **AeroPrediction Codes** serie was developed in the early 1970s by the Naval Surface Warfare Center in Virginia, in order to also have a code for predicting aerodynamic coefficients for guided and unguided projectiles. As depicted in figure 6.6, the upgrades were aimed at increasing the range of Mach and angles of attack, as well as the number of possible fins and span configurations. It is only from the AP02 version that trajectory models are also implemented to generate range in a timely and cost effective manner[149, 150].

VERSION	WEAPONS	AERODYNAMICS	MACH NO.	FLIGHT CONDITIONS					NONLINEAR DISTRIBUTED LOADS AVAILABLE	COMPUTERS	EMERGING PROJECTILE NEEDS
				REAL GAS AVAILABLE	AOA RANGE	ROLL	TRAJECTORY AVAILABLE				
1972	AXISYMMETRIC UNGUIDED PROJECTILES	STATIC ONLY	0-3	NO	0-15°	$\Phi=0^\circ$	NO	NO	CDC	NO	
1974	AXISYMMETRIC UNGUIDED PROJECTILES, ROCKETS, MISSILES	SAME	0-3	NO	SAME	SAME	NO	NO	CDC	NO	
1977	SAME	STATIC AND DYNAMIC	0-3	NO	SAME	SAME	NO	NO	CDC, IBM	NO	
1981	SAME	SAME	0-8	NO	0-15° (LIMITED CONF AT HIGHER α)	SAME	NO	NO	CDC, IBM, VAX	NO	
1993	SAME	SAME	0-20	YES	0-30°	SAME	NO	NO	CDC, IBM, VAX SILICON GRAPHICS	NO	
1995	SAME	SAME	SAME	YES	0-90°	SAME	NO	NO	INTERACTIVE PC	NO	
1998	AXISYMMETRIC & ASYMMETRIC MISSILES, ROCKETS	SAME	SAME	YES	SAME	$\Phi=0^\circ, 45^\circ$	NO	YES	INTERACTIVE PC, WINDOWS 98 ONLY	NO	
2002	SAME PLUS MULTI-FIN	SAME	SAME	YES	SAME	SAME	YES	YES	IMPROVED INTERACTIVE PC, WINDOWS 98, 2000 & NT	YES	

Figure 6.6: Evolution of AeroPrediction Code with major new added capabilities[149].

Frank G. Moore, promoter of the AP02[150] and AP05[151] versions, published a book in 2000[148] in which he retraces 30 years of experience with empirical codes to predict aerodynamics with all kinds of configurations considered so far, allowing engineers to see the pros and cons of each approach, for both linearized and nonlinear methods.

The major improvement of the AP09 version, which is the latest version found by the author, is the development of new methods to predict nonlinear roll and pitch damping aerodynamics[152].

- **MISSILE**

The MISSILE code was developed by ONERA (FRA) in the 1990s to quickly estimate the aerodynamic characteristics of missiles from Mach 0 to Mach 10, for incidences up to 40°, steering angles of the control surfaces of $\pm 30^\circ$ and any roll angles⁴. The methodology combines semi-empirical and theoretical methods as well as correlations from missiles databases [52, 169].

- **AerfoFI**

This program has been first produced for the Finnish Army Material Command Headquarters in 2008 and was then made available to NATO members, participating to the NAAG AC/225 LCG/3 SG/2, in the framework of the Sharable Software Suite, together with the NABK. AeroFI is written in

⁴ONERA also has three important 6-DoF wind tunnels for all speed ranges: (<https://www.onera.fr/fr/windtunnel/testing-capabilities>)

Fortran77 and supplied on a CD without encrypted keys, unlike other NATO software from the S4 Suite that require the tracking of codes and decryption keys in order to be upgraded[13, 210].

The primary use of the AeroFI program was to create the aerodynamic input data for firing table computations, but it can also be used at a projectile preliminary design phase. The methods are mainly based on data available in open literature, but unlike previous software, CFD computations are also implemented to complement some of the predictions.

In 2014 appeared the STANAG-4655[12], intended to facilitate the exchange of projectiles aerodynamics data. It includes data and methods for body aerodynamics, fin aerodynamics and generalized yaw aerodynamics. It is based on, among others, methods published in the context of the development of the three software packages mentioned above (AP & Spinner series and Missile Datcom) and AeroFI technical report. All of the programs listed above include a large number of references concerning methods that enable to predict or retrieve the aerodynamic coefficients of very particular configurations. These references are not included in this work but are for the most part easy to find.

6.3 Conclusion on Part I

The choice of using one or another trajectory model is justified by the final purpose: do we need it as a user, or as a designer? Based on the answer to this question, two types of approaches can be considered.

On the one hand, the user can choose between the Point-Mass Trajectory (PMM), requiring only the drag vs Mach number, or the Modified Point Mass trajectory, which considers in addition to the mass point, a longitudinal axis and the rotation around this axis. The simplest model allows the user to determine mainly the gravity drop, the velocity decay and the wind drift, which already makes it interesting for small arms in supersonic regime and APFSDS, while the more complex one is able to determine the drift of the projectile as well as a the global impact angle (no distinction of directions yet), for any larger trajectory, independently of the speed regime and provided that the weapon-munition system is well designed.

On the other hand, the second approach, more benchmark- and design-oriented, can also be subdivided into two layers. The first one is the gyroscopic stability analysis for spin-stabilized projectiles, requiring in addition to the drag, the pitch moment, for the evaluation of the stability factor at short and long range. The last layer available with the current means, is the dynamic analysis, requiring the complete set of static and dynamic aerodynamics, in order to feed the complete 6-DoF model for any type of rigid body, allowing also the computations of trim angles for asymmetric configurations.

All these tools already exist on the market and some of them are standardized and documented through NATO groups, this has therefore been the subject of a separate chapter. However, the mastery of these tools remains a delicate issue, which is why their implementation, with supporting documentation and references, has been extensively discussed in the first chapters.

The last chapter of this first part put forward the current techniques to determine the aerodynamic coefficients, mainly experimental, in order to make the link with the second part of this thesis which approaches in particular the numerical techniques of determination by means of Computational Fluid Dynamics.

Part II

CFD Methodology

As it was put forward in the preceding part, the most expensive aspect in external ballistics is not so much the trajectory calculations as such but the input data to get good calculations. Chapter 6 highlighted the efforts already made to estimate the various aerodynamic coefficients that are essential to flight dynamics, by means of experimental and semi-empirical methods. However, live firing and wind tunnel tests are time consuming, difficult to perform and very expensive, in terms of installation, number of tests or even in terms of projectiles when the caliber and/or the complexity increases. And even if these techniques are available, the benefit of cross-checking them with a simulation method is no longer questionable. Semi-empirical codes have on the other hand a low computational cost, but provide reliable results only in a limited range of flow conditions and geometries, and are especially reliable for the acquisition of static coefficients. Dynamic derivatives prediction requires the ability to calculate the aerodynamic response to prescribed motions as a function of time.

The last decades have though seen, with the emergence of numerical simulation, and Computational Fluid Dynamics (CFD) in particular, a good number of methods to facilitate the work of ballistics experts.

"CFD is a science that, with the help of digital computers, became a tool for analyzing fluid-flow problems and producing quantitative predictions of phenomena, based on the conservation laws (conservation of mass, momentum, and energy) governing fluid motion"[113].

CFD has the capability to complement experimental testing techniques for obtaining these aerodynamic parameters with the ability to separate physical effects from each other, which is not so obvious with flight test data. The practical limitations and kinematic constraints of wind tunnel testing, such as

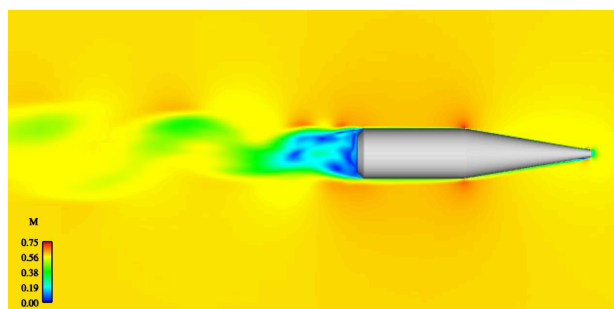


Figure 6.7: Mach number contours on pitch plane at $Ma = 0.6$ with a time-accurate Detached Eddy Simulation (DES) model [55].

motion and model support interference effects, are no longer part of the problem. Results that can be generated by CFD using commercial software are moreover truly fascinating: everything is quantified, anything can be easily presented in color and graphics (Fig. 6.7), requiring little or even no post-processing if the routines are well prepared and automated.

Despite this, the traps are omnipresent with CFD, and the error sources numerous. As with RBD, CFD simulation is also based on discretization over time, with the implicit shortcomings already expressed in the previous part (model, solver code, integration schemes, etc). But in addition to this, other sources of error are added: space discretization, instabilities, transition, turbulence modeling... making predictions more or less accurate depending on the effort invested in the initial modeling.

Even if CFD has increased in importance and in accuracy over the last decades, one must always remain cautious when interpreting the results, because much more than for a trajectory that will "crash" if the projectile is not stable enough, CFD can provide a solution to a poorly posed problem. The problems of "*Who's telling the truth?*" and uncertainty quantification are more present than ever.

In order to detail all the technical specifications of CFD, the following chapter will first outline the important theoretical aspects of fluid properties and subsequently the CFD approaches for the interaction of air with any wall. This will be followed by a whole methodology to find a complete set of static and dynamic aerodynamic coefficients. Different precise and up-to-date applications will then be contextualized thanks to these approaches.

Chapter 7

Fluid Properties and Governing Equations

The problem we are faced with, and which we want to define by means of models, is the study of air flow around a projectile in motion. As the projectile moves through air, the gas molecules near the walls are disturbed and move around. Aerodynamic forces are generated between the air and the projectile, and the magnitude of these forces depend on many factors associated with the projectile and the air characteristics, which may vary as the projectile evolves along its trajectory.

In order to compute all the forces exerted on the projectile during its trajectory and then extract the aerodynamic coefficients, it will then be necessary to identify the different behaviors to enable possible simplifications and ease the calculations while remaining within an acceptable range of validity.

7.1 Conservation Laws & Navier-Stokes Equations

Air is known as a **Newtonian fluid**, meaning that the shear force needed to deform the fluid is proportional to the velocity gradient. This implies that shear stresses (tensor $\bar{\tau}$) and strain rates have an isotropic¹ relationship, with a proportionality factor μ , called the **dynamic viscosity coefficient**[27, 183]. This coefficient is a characteristic of the fluid and depends on the temperature.

To model the air in motion in three dimensions, one of the methods is to use the Navier-Stokes (NS) equations, which are the basic governing equations

¹There is no preferred orientation in the fluid.

for a compressible, Newtonian, heat conducting fluid and which rely on the conservation laws. Conservation of mass (= continuity equation), momentum, and energy have to be concurrently satisfied and consist in five differential equations containing next to the velocity components of the fluid, unknown thermodynamic variables: ρ being the air density, p the static pressure, e the specific internal energy and T the static temperature. Relations between these thermodynamic variables can be obtained through the equations of state (Box 7.1).

1. **Mass Conservation.** This first law ensures that mass is neither created nor destroyed. Thus, individual fluid particles may be tracked within a flow field because they will not disappear and new elements will not spontaneously appear. Equation 7.2 states that the rate of increase of mass in a fluid element is equivalent to the net rate of flow of mass into this fluid element[113].
2. **Momentum Conservation.** The momentum conservation law is developed from Newton's second law: the rate of increase of momentum of a fluid particle is equivalent to the sum of forces applied on this fluid particle[247].
Among the forces, a distinction must then be made between the distant, or volume forces, and the contact, or surface forces, including all the effects related to the viscosity of the fluid through the shear stress tensor $\bar{\tau}$ [129]. The momentum conservation logically gives rise to three equations for the three dimensions in space (Eq. 7.3).
3. **Energy Conservation.** This third statement comes from the first law of thermodynamics which implies that the rate of change of energy of a fluid particle is equal to the rate of work done on the particle plus the rate of heat added to the fluid particle (Eq. 7.4 [247]).

The **total energy** per unit mass e_0 is a state of the matter and is defined as the sum of the **internal energy** per unit mass e and the kinetic energy per unit mass².

The heat flux vector \vec{q} due to thermal conduction can be expressed following **Fourier's law** which relates the heat flux to the absolute temperature gradient³(Eq. 7.1).

$$\vec{q} = -k\vec{\nabla}T \quad (7.1)$$

with k the **thermal conductivity**, which is also a characteristic of the fluid.

²A third contribution is the potential energy, but is often neglected for gases

³Absolute temperature = static temperature relative to absolute zero.

Finally, equations 7.2-7.4 taken together become a nonlinear, incompletely parabolic partial differential equation system with five equations and seven unknowns, considering only the four thermodynamic variables and the three velocity components (volume heat sources being neglected since we are dealing here with a non-reacting flow).

Time-dependent three-dimensional Navier-Stokes Equations for a Newtonian Compressible Flow [128]:

$$\frac{\partial \rho}{\partial t} + \frac{\partial(\rho u_j)}{\partial x_j} = 0 \quad (7.2)$$

$$\frac{\partial(\rho u_i)}{\partial t} + \frac{\partial(\rho u_i u_j)}{\partial x_j} = \frac{\partial}{\partial x_j} [-p\delta_{ij} + \tau_{ij}] + \rho g_i, \quad i=1,2,3 \quad (7.3)$$

$$\frac{\partial(\rho e_0)}{\partial t} + \frac{\partial(\rho u_j e_0)}{\partial x_j} = \frac{\partial}{\partial x_j} [-u_j p + u_i \tau_{ij} - \dot{q}_j] + \rho g_i u_i \quad (7.4)$$

with u_i the total velocity of the flow, δ_{ij} the kronecker symbol and τ_{ij} the deviatoric stress tensor, that is expressed in terms of gradients of velocity components [183, 212]:

$$\tau_{ij} = \mu \left(\frac{\partial u_i}{\partial x_j} + \frac{\partial u_j}{\partial x_i} \right) - \frac{2}{3} \mu \delta_{ij} \frac{\partial u_k}{\partial x_k} \quad (7.5)$$

Various simplifications of these equations can be applied, depending on which effects are deemed less or no significant. In addition to this, different equations of state can be added, to close the system. However, it will only be possible to solve this system as it is, under certain conditions of laminarity, which generally correspond to a low Reynolds number (See Box 7.2). Otherwise, for large Reynolds numbers, the flows present some velocity fluctuations, called turbulence, particularly in the vicinity of the projectile's walls. These fluctuations are often inherent to the flow itself. When the flow is decomposed in an average and a fluctuating part, as it will be done in section 7.4.2, these fluctuations result in an additional stress on the average flow: the so-called **Reynolds stresses**. The subject of turbulence still generates a lot of research attention over the last decades.

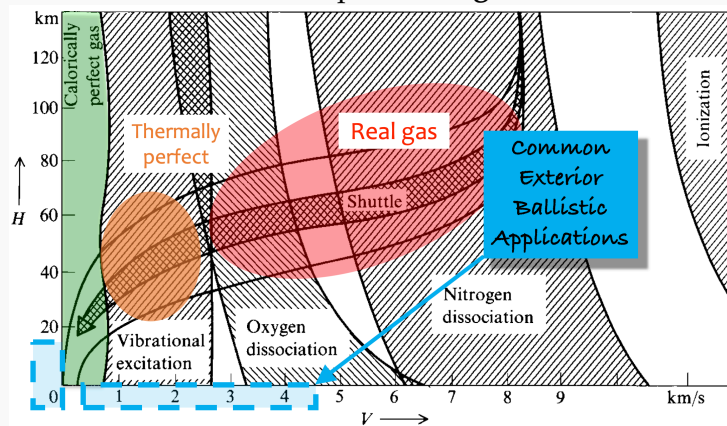
Box 7.1: Perfect or Imperfect gas?

In ballistic applications, thermodynamics should be borne in mind for the role it plays in high speed flight. For gas at low speeds, intermolecular forces are negligible and the gas is said to be **calorically perfect**: the ratio of the specific heat capacities γ is a numerical constant equal to 1.4. Perfect gas obeys in particular three equations of state: the **ideal gas law** (Eq. 7.6) where R is again the specific gas constant for dry air ($=287.085 \text{ J}/(\text{kgK})$), and two equations which link the absolute temperature change with the change of specific internal energy or enthalpy (Eq. 7.7-7.8)ⁱ [125].

$$p = \rho RT \quad (7.6)$$

$$de = c_V dT \quad (7.7) \quad dh = c_p dT \quad (7.8)$$

As the flight Mach number increases, some of the kinetic energy of the moving projectile is converted into heat. The excitation of the vibrational modes of the diatomic nitrogen and oxygen of the atmosphere will result in changes of the specific heat capacity with temperature, and the gas is said to be **calorically imperfect**. As shown in the figure below from Anderson [5], when the velocity exceeds Mach 3, the gas is first considered as **thermally perfect** and ideal-gas law is still validⁱⁱ but when dissociation and ionization take place, **real gas** models have to be considered.



Mathematical models allow to account for real gas effects and the limit at which it is necessary to switch to real gas equations of state is estimated on the basis of the following relations [6]:

$$T/T_c < 2 \quad \text{and} \quad p/p_c > 1$$

where T_c and p_c are the critical temperature and pressure of air.

Fortunately, although unguided ballistic applications are at the limit of having to consider real gas conditions, their effects are still negligible [89]. This will be confirmed for the fastest calculations in the next chapter 8.5.2. Other applications such as re-entry vehicles at high hypersonic velocities must, however, consider real-gas Navier-Stokes computations in order to match experimental results [99, 275].

ⁱ c_p and c_V are the specific heat at constant pressure and volume respectively [J/kg.K].

ⁱⁱIt is however necessary to consider heat capacities depending on the temperature.

7.2 Inviscid Flow

The inviscid assumption is used when the time scales for diffusion⁴ are much larger than the time scales for convection⁵, i.e. when viscous effects can be neglected. This can be verified using the Reynolds number (Box 7.2). Even at high velocity, and therefore at high Reynolds number, the viscous effects will only have to be considered in the boundary layer that has formed at the wall of the projectile and the flow outside can be considered as inviscid.

The governing equations for an inviscid flow, also known as **Euler equations**, are obtained by discarding the viscous terms and heat flux (Fourier term) in the energy equation from the Navier-Stokes equations 7.2-7.4. When resources did not allow to solve the complete system of NS equations, Euler's methods still allowed to compute shocks, with results that matched experimental measurements, as demonstrated by Park, Kim & Kwon [172] and Oktay & Akay [168] who computed some dynamic derivatives for finned configurations. The exterior inviscid flow is dominated by the pressure distribution on the projectile since the boundary layer transmits the pressure to the wall without change⁶. This explains why inviscid methods such as Euler gave good results as long as phenomena such as separation, transition and turbulence do not play an important role. The next chapter will distinguish between coefficients that can be approximated under the inviscid hypothesis and those where this is not possible at all.

7.2.1 Incompressible Inviscid Flow

If the density variation of a fluid element contained in an inviscid flow remains small during its motion, then the flow can be considered as incompressible. Only pressure and velocity are the unknowns to be found, typically defined by solving the continuity and momentum equations (Eq. 7.2-7.3). Compressible flows can be generally considered as incompressible for steady flows with $Ma < 0.3$, meaning that for ballistic applications, only some less lethal projectiles can be studied under this assumption, with typical velocities below 100 m/s [24]. If the flow is inviscid, steady and incompressible, this leads to much more simplified NS equations.

⁴Diffusion is the contribution present in fluids at rest, due to the macroscopic effect of the molecular thermal agitation[95]

⁵Convection refers to the amount of energy transported by the large displacement of the fluid.

⁶From Prandtl's boundary layer equations, the wall-normal pressure gradient is zero ($\partial p / \partial y \approx 0$).

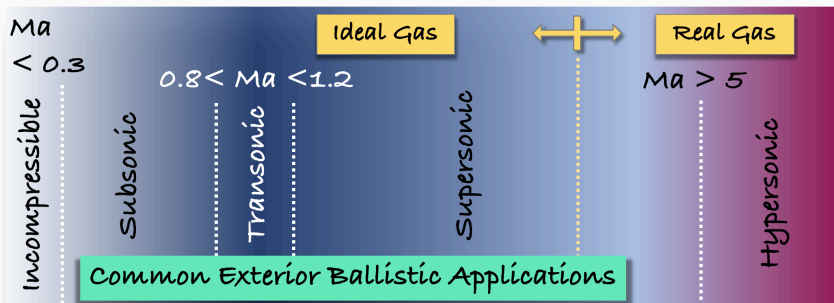
Box 7.2: Key Parameters...

Physically meaningful dimensionless parameters allow to identify the most prominent physical effects in the fluid.

1. **Mach Number:** Already mentioned numerous times in the first part, **compressible flows are categorized according to the Mach Number** (Ma), being the local flow-velocity, divided by the local speed of sound (Eq.7.9). The speed of sound c is the speed of transmission for a small isentropic disturbance in a gas, given in equation 7.10 for an **ideal gas**:

$$Ma \equiv \frac{V}{c} \quad (7.9)$$

$$c = \sqrt{\gamma RT} = \sqrt{\gamma \frac{p}{\rho}} \quad (7.10)$$



2. **Reynolds Number (Re):** It allows to characterize the state of the flow, whether it is laminar or turbulent. It is defined as the ratio between the inertial and the viscous forces (Eq.7.11). In ballistic applications, as the relative air velocity with respect to the projectile is generally very high, the Reynolds number is also high, resulting in turbulent boundary layers along most of the projectile's body.

$$Re = \frac{\rho V L}{\mu} = \frac{V L}{\nu} \quad (7.11)$$

L [m] is the reference length of the body under study^a. The **kinematic viscosity** ν is commonly defined as the **dynamic viscosity** μ [N.s/m²] divided by the air density ρ . The kinematic viscosity can then be seen as the diffusion coefficient[95].

3. **Prandtl Number (Pr):** This number is defined as the ratio of momentum diffusivity to thermal diffusivity. The ratio of the velocity boundary layer thickness to the thermal boundary layer thickness is 1 when $Pr = 1$ ⁱⁱ (Eq. 7.12).

$$Pr = \frac{\mu c_p}{k} \quad (7.12)$$

As air has a Prandtl number $Pr < 0.75$ for positive temperature, it means that heat diffuses more quickly than momentum.

^a Re is thus very low at the tip of the projectile and increases as we get closer to the base.

ⁱⁱ c_p = specific heat at constant pressure [J/kg · K] - k = thermal conductivity [W/m · K].

7.2.2 Compressible Inviscid Flow

If the flow speed is high, the flow kinetic energy becomes important, with air density ρ that cannot be considered as constant. Therefore, the energy equation has to be solved with an equation of state for the gas to link density and pressure, in most cases provided by the ideal gas law (Box 7.1).

Supersonic flows should allow the solution of discontinuous flows, such as shock wave compression, with correct relations between the upstream and downstream flow properties across the discontinuities. The transonic flows, that contain both subsonic and supersonic flow regions, require special attention in pressure-based solver for the calculation of the density from the velocity fields, so that the non-linearity of the flow field is preserved [6]. One application in particular will address this topic (Sec. 11).

7.3 Viscous Flow

Viscosity is an important fluid property governing the interaction between a fluid and a solid wall.

"In 1904, a little known physicist - Ludwig Prandtl - revolutionized fluid dynamics with his notion that the effects of friction are experienced only very near an object moving through a fluid" [4]. This "very near" zone around the projectile is called the **Boundary Layer** (BL). In this region, the velocity components will be zero at the wall and will change drastically over a very short distance normal to the surface of the projectile, to become equal to the free-stream velocity components infinitely far from the wall. At the outer border of this boundary layer, the velocity is equal to the exterior velocity which is that of the inviscid flow circumventing the projectile. According to **Newton's law of viscosity**, these very large velocity gradients in the wall normal direction y^7 generate large strain rates. As a result, skin-friction drag is clearly significant. The flow dynamics in this rather small region have macroscopic effects on the overall flow field and consequently on the aerodynamic performance of a given projectile. In order to calculate the net forces on these projectiles, viscous flow equations have to be used.

The boundary layer with a variable thickness $\delta(x)$ can be classified as **laminar** or **turbulent**, with an intermediate zone called **transition**. These three regions, which are in practice not so easily split up, are schematized in figure 7.1 and further detailed in the following paragraphs.

⁷A new local wall-bounded coordinate system is defined according to figure 7.1 with its origin at the tip of the nose, x tangent to the wall surface and y perpendicular to it.

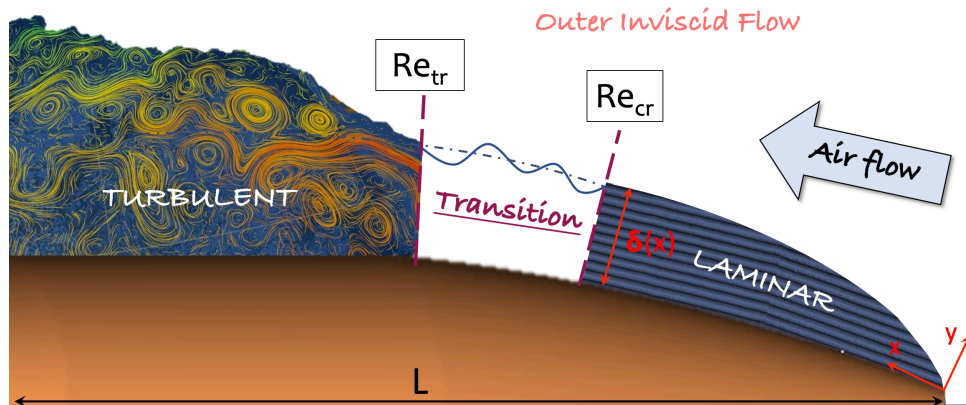


Figure 7.1: Schematic development of the boundary layer along the nose of a projectile, with an imperfectly defined transition zone. L is the total length of the projectile facing air. The laminar zone has been stretched for clarity, but it is in fact hardly perceptible in reality.

The boundary-layer over streamlined bodies has been the subject of intense research in order to analyze the flow pattern and to quantify the surface pressure distribution. Moreover, spinning projectiles have a specific swirling pattern, giving rise to phenomena such as Magnus, already described in section 3.2.2, when the directional flow pattern interacts with the free stream flow at certain yaw angles [38]. The parameters affecting the BL thickness and flow characteristics, such as Mach number, Reynolds number, surface roughness, spin rate or projectile geometry, will also affect the Magnus force and moment.

7.3.1 Laminar BL

In a laminar boundary layer, the fluid sticks to the projectile's surface and follows its curvature, with the streamlines mostly parallel to each other. The flow associated with low downstream **distance-based Reynolds number** Re_x , is then characterized by order, stability and predictability. The fluid layers exchange momentum by diffusion (viscous shear) and no particle motion occurs in the perpendicular direction to the parallel flow layers [211]. The streamwise pressure gradient governs the transport of momentum along the wall.

7.3.2 Transition

Transition refers to the process that brings an initially developing boundary layer from the laminar to the turbulent state. Transition occurs when Re_x is larger than some critical value, Re_{cr} , that depends on fluctuations in the free stream above the boundary layer and on the surface shape, curvature, roughness, vibrations,

and pressure gradient. Generally, Re_{cr} decreases when the surface roughness or free-stream fluctuation levels increase, but it is still a highly variable parameter, which is very difficult to predict [113].

7.3.3 Turbulent BL

"Turbulence is an enigmatic state of fluid flow that may be simultaneously beneficial and problematic"[113]. Turbulent flows have unsteady velocity fluctuations and are simultaneously dissipative, vortical, and nonlinear:

1. Turbulence is **dissipative**: Turbulent kinetic energy is produced at large scales (L -dimension) from the mean flow, then transferred to the intermediate scales and finally dissipated at small scales (η -dimension) through heat. This exchange is also called **mixing**. Consequently, energy is needed to sustain this turbulence [239].

The mixing of particles with higher and lower momentum that occurs in the turbulent BL leads to higher average kinetic energy levels compared to the laminar counterpart. This implies that turbulent BL is considerably more resistant to separation (Sec. 7.3.4) [211].

This property is important because it explains why BL transition is artificially promoted and why a compromise has to be reached in the design of current long-range projectiles: thanks to their boat-tail, a turbulent boundary layer is more likely to be maintained. This one will be more energy consuming and will cause more drag, but it will avoid the premature separation associated with wake drag increase and with a stronger turbulence zone generating instabilities for the projectile flight [53].

2. Turbulence is tri-dimensional and **vortical** [51]: The rotational of the velocity, called vorticity, exhibits strong random fluctuations, evolving with time, which prevent any reproducible representation and require a statistical description.
3. Turbulence is **nonlinear**: Between the various fluctuation scales, some interactions correspond to a phenomenon of energy transfer due to the nonlinear terms. Additional equations will be needed to bring closure to the Navier-Stokes equations (Eq. 7.2-7.4).

7.3.4 Separation

Separation occurs when a significant adverse pressure gradient appears along the streamwise direction: this pressure increase cannot be overcome by the low momentum particles and the flow leaves the wall. The BL **separates** from the surface and trails downstream.

The separation point at which the reverse flow meets the forward flow, is a local stagnation point and characterized by the absence of shear stress at the wall ($\tau|_{y=0} = 0\text{Pa}$). The separate low energy flow region forms in the wake behind the body, and the term "dead air" is commonly used [4]. Because of the radical change in pressure distribution over the surface, separation results in increased wake drag and reduced lift [211], which is definitely not a favorable phenomenon for the projectile's flight.

As both processes of transition and separation may significantly affect the aerodynamic performances, many specific applications are the subject of much attention in the last few years, both numerically and experimentally, precisely to feed and improve the calibration of existing turbulence models. Besides all types of airfoils for aircraft [141] or missiles, we can think of wind turbine blades [60] or even UAV's in their entirety [254].

7.4 Turbulence modeling

7.4.1 Available CFD methods

To simulate turbulent flows, the four methods below are usable, listed from the most demanding in terms of calculation but most accurate, to the most "popular" one [130, 239]:

1. **Direct Numerical Simulation (DNS)**: The NS equations are numerically solved without any turbulence model. The whole scale range of turbulence are fully resolved with a statistical treatment of the data, from the smallest dissipating scales η , up to the larger scales L containing most kinetic energy. This method is currently only conceivable for low Re and simple configurations on supercomputers, given the considerable refinement needed for the mesh.

Various studies established laws for determining the number of mesh points required based on the Reynolds number. According to Choi & Moin [37], the number of meshing points should be scaled with $Re^{37/14}$. For a simula-

tion of a small caliber ($L \approx 2\text{cm}$) at Mach 3, this would amount to a mesh size of the order of $1.5 \cdot 10^{16}$ grid points⁸, making the process not achievable with the current means.

2. **Large Eddy Simulation (LES)**: This method is based on the principle of self similarity which assumes that large eddies of the flow are dependent on the geometry while the smaller scales are more universal. All scales above a cut-off length scale are therefore accurately resolved while the rest is modeled. Supercomputers can solve large Re with this method for simple geometries.

Depending whether the wall is modeled or resolved, Choi & Moin [37] estimate the total number of grid points for the entire computational domain to scale with $Re^{2/7}$ to $Re^{13/7}$, meaning for the latter $2 \cdot 10^{11}$ points for a small caliber projectile at Mach 3. This remains an order of magnitude that is far too demanding for conventional calculation means.

3. **Reynolds Averaged Navier-Stokes (RANS)**: This method is fully based on a statistical approach, which models the huge amount of chaos-related data from irregular motions into reproducible, ordered and regular data, suitable for engineering. All scales are modeled and turbulence statistics are computed by a predefined model.
4. **Detached Eddy Simulation (DES)**: This is an hybrid RANS-LES approach where RANS is used in attached boundary layers (where the calibration of the models is more accurate) and switches to LES calculation in the separated regions.
5. **Zonal Detached Eddy Simulation (ZDES)**: This a derived method of DES simulation, particularly adapted when the flow separation is clearly predetermined by the studied geometry. The user can then choose the zones in which he will work in DES or in RANS and adapt the mesh refinement by subdomain treated, according to the approach he will have chosen [122]. In the case of projectiles, where the separation appears systematically around the base of the projectile, the ZDES approach has been regularly used to study the behavior of the fluid in the wake region more specifically [224]

With RANS computations, only the grid near the wall can be demanding in terms of memory usage, but the macro-values such as the aerodynamic coefficients expected in this research are computed with satisfactory accuracy. DeSpirito & Heavey [55], DeSpirito & Sifton [58, 59], DeSpirito [53] and Simon et al.[222–224], among others, compared DES and RANS for differ-

⁸Reynolds number above one million.

ent spinning canonical configurations in all velocity regimes and the added value of the DES for the determination of the aerodynamic coefficients compared to the requested cost, is not particularly significant, except possibly for the Magnus effects, because of the non-linearity with respect to the speed and the yaw angle [55].

7.4.2 RANS Modeling

Turbulent NS Equations

The Reynolds Averaged Navier-Stokes approach for a compressible unsteady viscous flow actually includes two averaging approaches: Reynolds and Favre averaging [128, 274]. The first consists in splitting the scalar parameters as ρ and p into a sum of their mean value over time $\bar{\rho}(x, t)$ and their fluctuating part $\rho'(x, t)$ (Eq. 7.13). Favre averaging takes a similar approach for the other quantities, but this time averaged over densities. This is applied to the instantaneous velocity $u_i(x, t)$, which is also separated into a mean part $\tilde{u}_i(x, t)$ and a fluctuating part $u_i''(x, t)$ (Eq. 7.14).

$$\rho(x, t) = \bar{\rho}(x, t) + \rho'(x, t) \quad (7.13)$$

$$u_i(x, t) = \tilde{u}_i(x, t) + u_i''(x, t) \quad (7.14)$$

Equations 7.2-7.4 are then written as follows (gravity left aside) :

RANS Equations [128]:

$$\frac{\partial \bar{\rho}}{\partial t} + \frac{\partial(\bar{\rho}\tilde{u}_j)}{\partial x_j} = 0 \quad (7.15)$$

$$\frac{\partial(\bar{\rho}\tilde{u}_i)}{\partial t} + \frac{\partial(\bar{\rho}\tilde{u}_i\tilde{u}_j)}{\partial x_j} = -\frac{\partial \bar{p}}{\partial x_i} - \frac{\partial \overline{\rho u_i'' u_j''}}{\partial x_j} + \frac{\partial \bar{\tau}_{ij}}{\partial x_j}, \quad i=1,2,3 \quad (7.16)$$

$$\begin{aligned} \frac{\partial(\bar{\rho}\tilde{e}_0)}{\partial t} + \frac{\partial(\bar{\rho}\tilde{u}_j\tilde{e}_0)}{\partial x_j} = & \frac{\partial}{\partial x_j} [-\tilde{u}_j\bar{p} - \overline{\rho u_j'' h''} + \bar{\tau}_{ij}'' u_i'' - 1/2 \overline{\rho u_j'' u_i'' u_i''}] \\ & + \frac{\partial}{\partial x_j} [\tilde{u}_i(\bar{\tau}_{ij} - \overline{\rho u_i'' u_j''})] \end{aligned} \quad (7.17)$$

The non-linear term $-\overline{\rho u_i'' u_j''}$ shown in color and already defined as a turbulence related variable, are the **Reynolds stresses**. This term must be modeled in order

to close the momentum equations 7.16, as well as the new extra terms present in the energy equation 7.17.

The Boussinesq assumption

One method of bringing closure to the problem is to use the Boussinesq hypothesis (also called the Turbulent or Eddy viscosity hypothesis), based on the definition of a turbulent viscosity μ_t , which relates the Reynolds-stress components to the mean velocity gradients (In this case, k is the Turbulent Kinetic Energy (TKE)):

$$-\overline{\rho u_i'' u_j''} = \mu_t \left(\frac{\partial u_i}{\partial x_j} + \frac{\partial u_j}{\partial x_i} \right) - \frac{2}{3} \left(\rho k + \mu_t \frac{\partial u_k}{\partial x_k} \right) \delta_{ij} \quad (7.18)$$

The computational cost associated with the computation of the turbulent viscosity μ_t , constitutes the main advantage of this assumption. The main disadvantage of the Boussinesq hypothesis is that it assumes μ_t as an isotropic scalar quantity, which is not completely true. However the assumption of an isotropic turbulent viscosity is good enough for shear flows dominated by only one of the turbulent shear stress components, which is the case for the present problem. The models presented below are all based on this assumption.

Inner layer velocity profile

Even in the turbulent boundary layer, the mean velocity profile near the wall follows a universal profile in wall units. This profile is shown in figure 7.2, with non-dimensional coordinates u^+ , y^+ defined in equations 7.21-7.22, based on the definition of the wall shear stress τ_w ⁹ and friction velocity u_τ (Eq. 7.19-7.20).

$$C_f = \frac{\tau_w}{\frac{1}{2}\rho V^2} \quad (7.19) \quad u^+ = \frac{V}{u_\tau} \quad (7.21)$$

$$u_\tau = \sqrt{\frac{\tau_w}{\rho}} \quad (7.20) \quad y^+ = \frac{y u_\tau}{\mu} \quad (7.22)$$

In the viscous sub-layer with dominant viscous stresses, $u^+ = y^+$, whereas in the log-layer, also called law of the wall:

$$u^+ = \frac{1}{\kappa} \ln y^+ + B \quad (7.23)$$

⁹ C_f is the skin friction coefficient.

with κ and B being two constants empirically defined. Models based on the Boussinesq assumption are constructed to follow the velocity profile in this log-layer in particular and require specific spatial discretization features for this purpose.

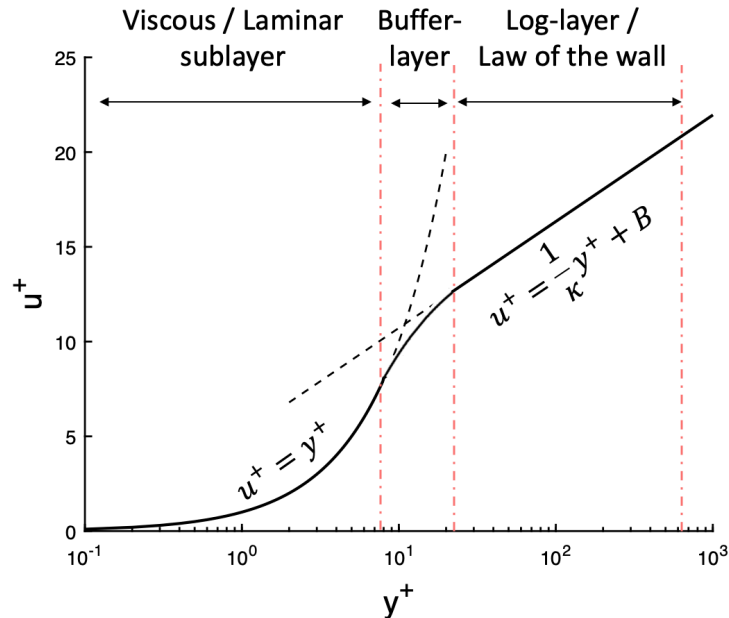


Figure 7.2: Schematic velocity profile in the inner layer of a turbulent BL.

7.4.3 Choice of the RANS Models with ANSYS Fluent

In the case of an external wall-bounded flow with boundary layer subjected to adverse pressure gradients, different models implemented in FLUENT and explained in the FLUENT user's manual [6] could give some general good approximation. However, Ansys Fluent recommends some transition models in particular, and gives a comparison of these models for Laminar-Turbulent Transition Cases [85]. Three models are presented but two of them seem to perform better on a multitude of transition cases because of their link with the Shear Stress Transport model (SST). These are the **Transition SST model** ($\gamma - \theta$ SST-model / SST-T4) and the **Intermittency Transition Model** (γ SST-model / SST-T3).

For the first calculations that will be carried out, three variants based on the given recommendations will be adopted - The latest developments integrated in Fluent to manage the transition are confronted to a standard Shear-Stress Transport $k - \omega$ model because this standard version is still widely used in many recent researches focusing on aerodynamic coefficients [30, 110, 114, 142, 279]. It was therefore interesting to perceive the added value of the transition models modifications.

1. The **SST $k - \omega$ model** (SST - T2) is based on the $k - \omega$ model formulated by Wilcox [274], with two transport equations allowing to solve the turbulent kinetic energy, k , and the specific dissipation rate, ω ¹⁰.

The standard $k - \omega$ model in ANSYS Fluent is applicable for both wall-bounded and free-shear flows but presents some strong sensitivity to free-stream and overpredicts the eddy viscosity. This model has been modified over the years in Fluent by addition of production terms to both equations. The goal was to improve the accuracy for predicting free shear flows, which is naturally very interesting for the study of the projectile wake.

The SST-model was developed by Menter [139] to effectively blend the robust and accurate formulation of the $k-\omega$ model in the near-wall region with the freestream independence of the $k-\epsilon$ model [117] in the far field (ϵ being the dissipation rate). To overcome the overprediction of the eddy viscosity in the $k-\omega$ models, the SST-model accounts for the transport of the turbulence shear stress in the definition of the turbulent viscosity. It makes use of a limiter in the formulation of the eddy-viscosity to avoid this overprediction. Even before the models presented below appeared, this model had already been refined for problems presenting for instance adverse pressure gradient or transonic shock waves [6]. This model belongs to the low Reynolds models, unlike the other two which are categorized as correlation models [254]. To use this model it is necessary to activate the $k - \omega$ model (2 eqn), then choose the Model SST (Fig. 7.3).

2. The **Intermittency Transition Model** (γ SST-model / SST-T3)[Menter2004, 251] is the more recent in-house development effort from ANSYS regarding transition models. The γ -SST transition model solves an additional transport equation for the turbulent intermittency. Like other engineering transition models, this model is best applicable to wall-bounded flows and not to transition in free shear flows. It will predict free shear flows as fully turbulent. To use this model it is necessary to additionally activate the transition equation for the intermittency γ (Fig. 7.3). Furthermore, the Intermittency Transition Model is the only one accounting for crossflow instability [211], which may be useful given the spinning motion with yaw angle and the possibility of further simulations of asymmetric bodies.

¹⁰The specific dissipation rate ω is the dissipation rate ϵ (the rate at which specific turbulent kinetic energy is converted into specific internal energy) divided by k .

3. The **Transition SST model** ($\gamma - \theta$ SST-model / SST-T4), also regularly appearing as $\gamma - Re_\theta$ correlation transition model [115, 140], solves again one additional transport equation for the transition onset criteria, in terms of momentum-thickness Reynolds number Re_θ . It is thus computationally more expansive than the previous one, hence the interest in comparing the efficiency of these two models for the first simulations.

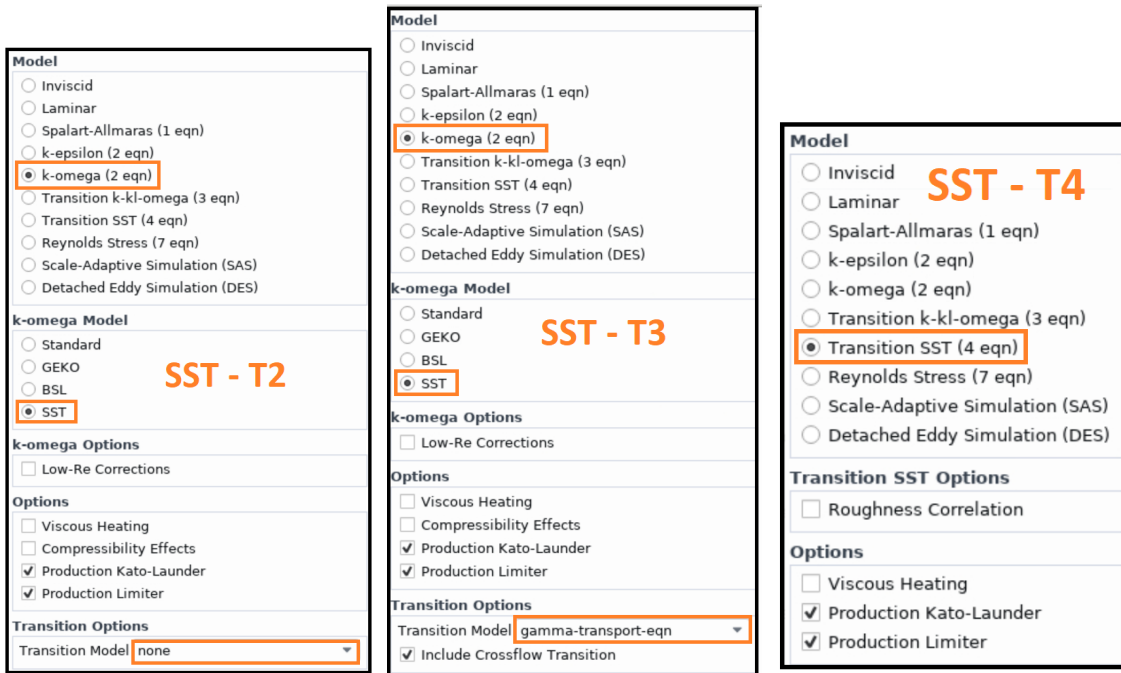


Figure 7.3: Three SST models' activation.

As shown in figure 7.3, the three model configurations consider a Kato-Launder limiter [105], to avoid predicting transition significantly upstream [60] because of the excessive generation of kinetic energy in stagnation regions [6].

The curvature correction is also enabled for the cases where high spin rates are considered, to account for the deficiencies of the SST formulation to model flows with high swirl patterns [85].

7.5 BL-research for projectiles so far...

Although the effects of drift have already been observed in the 17th century on a sphere [237], reports studying the boundary layer on Slender Bodies of Revolution appeared in the 1950s [133]. The Magnus effect is known to affect the trajectory at small yaw angles, but no satisfactory theory was yet presented. The effect of the boundary-layer displacement thickness was however analytically and experimentally analyzed in the laminar boundary layer on a cylindrical portion of a slender body of revolution at small angle of attack.

In the 1970s, Sturek [233] and Jacobson [101] studied the boundary layer experimentally and attempted to quantify the Magnus effect using optical systems and Strain-Gage Balance Measurements in windtunnels and spark-ranges. More experimental data on the transition in supersonic regime are then provided. Some time later, numerical methods appeared [104], to solve the laminar/turbulent boundary layer equations with the influence of asymmetric transition, and several contributions to the Magnus effects are considered. Important variables in the flow field are identified by considering variations of spin rate, Mach number, angle of attack and length of the body.

The boundary layer on spinning slender bodies of revolution at angle of yaw with discontinuities in surface curvature [234], is then further studied both experimentally and numerically with steady-state methods, and through the different velocity regimes: supersonic [235], subsonic [192], and transonic of course [145, 164, 166], since this area has always been the sensitive part of the spectrum.

The next step was to consider finned projectiles & missiles boundary layers [175], and the interaction that can have the asymmetric boundary layer-wake of the body and the fins as well as the spin induced modifications of the local incidences and the flow topology around the fins [31]. All kinds of investigations are then carried out in the field of fins, which are sealed to canted fins and canards controls [142, 205], but also to the interaction of the already perturbed boundary layer with nozzle jets [204]. What emerges from all these last works is the need for unsteady calculations (URANS) to provide increased accuracy in trajectory calculations, or even the transition to RANS/LES methods to accurately dissociate all the different interactions in the boundary layer and especially in the wake of the projectile [38, 53]. Still, Magnus effect aside, the RANS steady methods have proven to give excellent estimates of the total coefficients at low angles, which are ultimately a global measure of the pressure and viscous profiles.

Chapter 8

Computational Fluid Dynamics

The numerical simulations carried out as part of this research were performed using Ansys Fluent software[6], as well as Design Modeller[8] and ICEM CFD[7] components for the CAD and meshing setups, in the Workbench environment[9].

Again, to facilitate and lighten the explanations given in this chapter, concrete studies will be presented as the headings progress. For this purpose, two spin-stabilized geometries and one finned configuration are used, given the complementary results provided in the references using experimental methods or higher fidelity calculations (LES-ZDES). Not all steps will be shown for all geometries but the same procedure is applied for all of them.

1. The first geometry is the Secant-Ogive Cylindrical Boat-Tail (**SOCBT** - Fig. 8.1) configuration, already widely studied with CFD [195, 196, 206, 225, 236, 238, 266], and in particular for the comparison of the RANS and (Z-)DES approaches [222–224]. The focus will be put on the behavior of the flow around the projectile and in the wake region, according to available experimental data [106, 184]. The experimental data allows gain insight into the physics of the flows. Some static and Magnus coefficients were also investigated for this configuration in supersonic windtunnel by Nietubicz & Opalka [165].
2. The second geometry is the sub-cal¹ of the 25-mm M910 TPDS-T projectile, called **Spinner** (Fig. 8.2). This projectile is a training projectile developed in the 1970s for the American armed forces and was in particular extensively studied by DeSpirito, Plostins & Silton [55, 56, 58, 59, 178, 179] and then also

¹A sub-caliber projectile has a smaller caliber compared to the internal tube caliber from which it is fired. Either sabots or a thinner tube are used within the original tube.

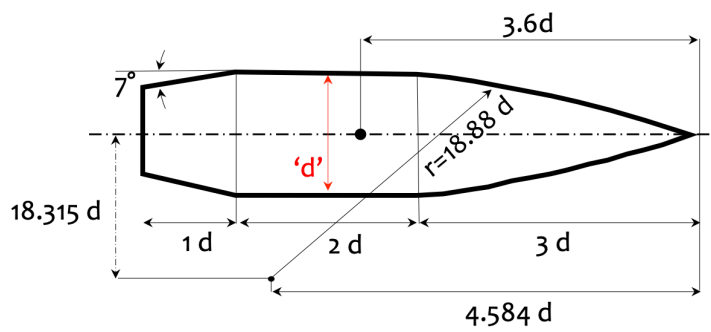


Figure 8.1: SOCBT configuration dimensions ($d = 0.0572\text{m}$).

used as a validation case for the AeroFI program [210] for the determination of some coefficients. Through the different references it is possible to find the complete set of coefficients.

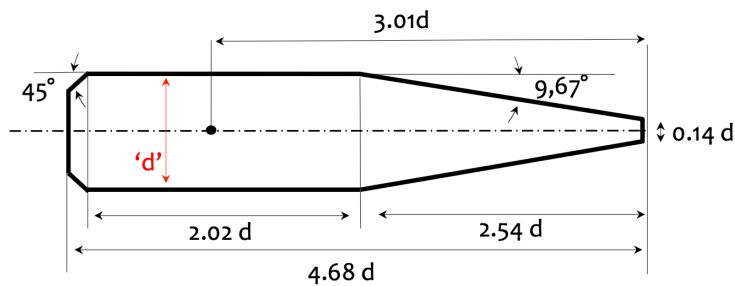


Figure 8.2: Spinner configuration dimensions ($d = 0.0162\text{m}$).

- To complete the panel of configurations, the U.S. **Army-Navy Basic Finner (ANF)** missile (Fig. 8.3) was chosen for its non-rolling behavior and data availability. This model is a symmetric, cruciform-finned, homogeneous aluminum alloy projectile and experimental data were obtained from free-flight tests conducted at DRDC-Valcartier Aeroballistic Range (Sec. 6.1.2)[69–71] and from wind-tunnel tests [269]. This configuration has also been largely used for the validation of CFD methods [21, 22, 87, 126, 201, 208, 228], with even variants featuring canards controls [205] and nozzle jets [204]. In the present work, this configuration is mainly used for the validation of the **dynamic stability**, where no roll is involved in the calculations.

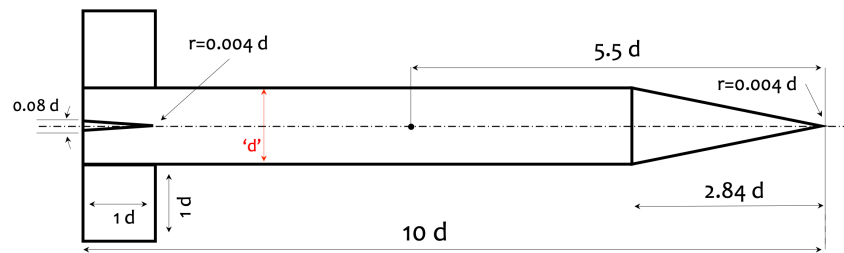


Figure 8.3: ANF configuration dimensions ($d = 0.03\text{m}$).

8.1 Discretization of the equations & Solver settings

Many numerical approaches to supersonic and hypersonic flow problems, employed density-based coupled formulations where the governing equations are solved simultaneously as a set of equations [89, 114]. Density is used as a primary variable found from the continuity equation, and then pressure is deduced from it using an equation of state. Density-based techniques are found to be efficient when used for transonic or supersonic flows, but require modifications such as preconditioning [267] in low Mach number flows, which can also alter convergence [89, 114]. As low Mach number regions are also found even at supersonic velocities in wakes behind bodies and inside boundary layers, a more recent alternative to the density-based approach is the coupled² pressure-based method which gives good results in all speed regimes for wall-bounded external flows, with an improved rate of solution convergence. It is thanks to the coupling that the pressure-based solver is able to solve supersonic or even hypersonic problems [114].

Together with the pressure-based coupled double-precision solver, a Green-Gauss Node-Based gradient reconstruction is used in this work [6, 85]. Second order discretization schemes for all variables are used, even if in some cases they come with difficulties to converge (heavier mesh or with more pronounced stagnation regions). In those particular cases, a first part of the calculation was done with a first order discretization for the turbulent quantities such as k and ω , to initiate convergence more easily. High order term relaxation option was anyway always activated to help convergence [6].

²The coupled system of equations includes the pressure-based continuity equation and the momentum equations [6].

8.2 Temporal discretization

Three types of calculations are performed:

1. **Steady-state calculation:** Calculations used to check the convergence of the meshes, the validity of the solver parameters used and as a base calculation to initiate the transient calculations. These calculations are run until convergence is achieved (depending on the type of calculation).
2. **Sweep calculation:** The purpose of these calculations is to rapidly obtain entire curves of coefficients as a function of the Mach number. It is also called quasi-static approach because once a configuration has converged for some fixed parameters (steady-state solution), it is used as initial condition for successive steady calculations where each increment in Mach number is implemented as a fictitious timestep and represents a point of the desired coefficient curve. The AoA-sweep method has been presented by Silton [220] at subsonic speed for a complex finned geometry at angles of attack ranging from -14° to 14° . It has recently been generalised in the supersonic domain by Sahu & Fresconi [204] for the ANF geometry with canards and a nozzle in the back of the projectile.

As the coefficients are dependent on both the Mach number and the yaw angle, two complementary approaches have been used in this work where each time one of the two parameters is fixed. When the angle of attack is fixed, the speed varies from Mach 4.5 to Mach 0.5, in steps of 0.01 Mach, which gives 400 global iterations (N) with 30 inner iterations (i) to reduce the normalized residuals by a factor of about 10^{-2} between each step, when started from a converged solution. We will therefore use the term **Machstep** hereafter for this type of sweep method. When the velocity is set, the angle is varied between -15° and 15° in steps of 0.1° . The calculation is repeated for several velocities, which finally allows to deduce both linear and quadratic or third-order coefficients. The choice of the parameters Δt (velocity and angle increments), N and i has been the subject of sensitivity studies with respect to steady-state calculations and will be discussed in section 9.1 for two distinctive geometries (ANF and Spinner).

The interest of this method compared to the traditional steady-state calculation will be further emphasized in chapter 11 dealing with long-distance

shooting, where the flight has to start at largely supersonic speeds and then crosses the transonic zone full of perturbations. A detailed knowledge of the variations of coefficients in this zone is thus desired in order to limit the calculation errors. This method will also be largely used in chapter 12 to determine the coefficients of a small caliber projectile with a mass unbalance.

3. **Forced Oscillation calculation:** These calculations were used for the determination of the pitch damping forces and moments. The method and the parameters choice will be detailed in section 9.2.2.

A **first order implicit transient formulation** was used for the sweep calculations and calculations with forced oscillation.

8.3 Spatial Considerations

Spatial definition consists of two important steps: **Domain Definition** and **Spatial Discretization**. The first step consists in importing the geometry to be studied, "the projectile", and defining the geometry and dimensions of the flow domain to be simulated around this projectile. The second step, also called **meshing** consists in dividing the flow domain into smaller subdomains, in order to solve the Navier-Stokes equations inside each of these subdomains, called cells or elements.

8.3.1 Domain Definition

Any self-respecting approach that studies fluids numerically in different speed regimes considers in principle different domain sizes. While a supersonic definition requires very fine cells to capture all the shocks that develop near the walls, but a spatially restricted domain in front of the object under study (Fig. 8.4), a subsonic definition can afford coarser cells but the domain must be larger because of the propagation of disturbances upstream against the flow direction, which requires more care in the choice of the inflow and outflow boundary conditions [58, 218]. As this approach aims to define the aerodynamic coefficients in the different regimes but also in the transition between these regimes and with as little processing as possible, the idea was to use a trade-off approach. A large domain will therefore be used, with sufficiently fine cells for the definition of shocks in the boundary layer. The mesh is therefore heavier, but it allows to reduce the number of manipulations to define a set of coefficients.

The dimensions of the global domain were first taken on the basis of the most commonly found dimensions of a subsonic mesh, i.e. about $15L$ in front of and behind the projectile (Fig. 8.5). However, these dimensions have been verified according to the type of projectile (L/d ratio and/or presence of fins).

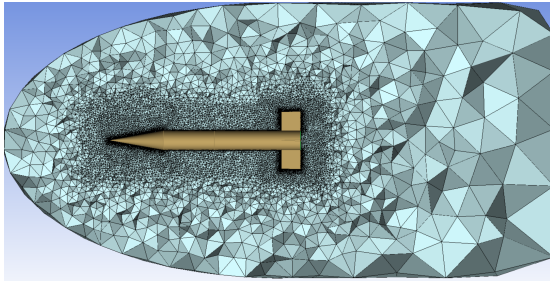


Figure 8.4: Computational domain for supersonic case (unstructured mesh).

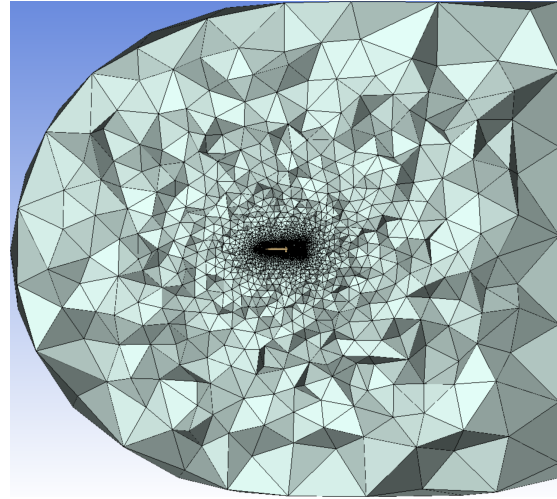


Figure 8.5: Trade-off domain for supersonic to subsonic calculations (unstructured mesh).

8.3.2 Spatial Discretization

Clearly, the smaller the cells, the closer the prediction will be to reality, at the cost of an inevitably heavier calculation. Special consideration must then be devoted to ensure smooth transition between these smaller cells in order to give a correct overall view of the fluid's behavior in the complete domain. If the mesh is well designed, this effort is however carried out by the calculation software itself. Again, several mesh classifications have to be made and will depend on the "time phasing" of the calculation process.

- Depending on the symmetry of the configuration, a 2D axisymmetric approach can be first considered. If the flow around the projectile without angle of attack is to be simulated, typically to calculate the zero-yaw drag coefficient or the roll moment, a 2D axisymmetric mesh is conceivable, whether the projectile rotates on itself or not. On the other hand, for a finned configuration or a flying projectile with an angle of attack, a 3D mesh has to be used in order to take into account all the asymmetries of the flow and the induced unsteady effects.

- Another distinction is based upon the connectivity of the mesh cells, by discerning structured meshes from unstructured meshes. A structured mesh is characterized by regular connectivity between quadrilaterals or triangles, while an unstructured mesh admits almost any possible shape of triangle element in 2D, or tetrahedral/polyhedral elements in 3D. Although a structured mesh is much more complicated to implement, it allows to reduce the memory space requirements needed to define the neighborhood relationships and the size parameters are easier to visualize (for instance, for mesh convergence). For an unstructured mesh the memory space requirements will be substantially larger since the neighborhood connectivity must be explicitly stored. However, in the case of simple geometries like axisymmetric projectiles, the mesh can also be implemented almost automatically on the basis of a few parameters, without excessive manual intervention as it is the case with a structured approach. Several studies have compared the results obtained with structured and unstructured meshes for complex geometries [94, 207] and while it is apparent that the velocity and pressure contours at the rear of the projectile appear more diffuse for unstructured meshes, the pressure profiles at the wall are equivalent.

Mesh requirements for turbulence modeling

The following recommendations are certainly required for the transition models presented in the previous section [6, 85]:

- The mesh resolution needs a y^+ lower or equal to 1 (See box 8.1);
- Hexahedral meshes in the near-wall regions are the most economical. For unstructured meshes, prismatic elements are used near the walls.
- Gradual expansion of the mesh in the wall normal directions should occur with an expansion ratio ideally of 1.15 or less. Values of 1.2 can be used as absolute maximum.
- The aspect ratio for the near-wall cells can be high, however, it is advisable to keep it below 200.

In this study, a 2D structured mesh is first used to ensure the validity of the configuration parameters, based on the values of drag coefficients and spin damping moment. Then, the implementation of a 3D unstructured mesh is per-

formed with the results obtained in 2D as confirmation support. The emphasis is clearly put on the sensitivity of the boundary layer grid (y^+ value and longitudinal spacing) in order to capture the flow interaction with the wall.

2D Mesh convergence

Just as it was done for the convergence of the trajectory's time step in section 3.5, the first step is to determine what is the optimal mesh size at the wall, knowing that the growth of these cells must also follow a certain aspect ratio.

The convergence study presented here is for the SOCBT geometry in 2D Axisymmetric (no angle of attack). A first grid was made on the basis of the y^+ estimate, as a "First Guess" (box 8.1), then other finer and coarser meshes were derived to better reflect the error generated by the spatial discretization. The calculations for this analysis have been performed at Mach 0.96 and Mach 3, for the three transition models discussed in section 7.4.3 (Fig. 7.3).

Box 8.1: First Guess mesh thanks to y^+ ...

The **non dimensional wall adjacent grid height** y^+ is of major importance to capture the effects in the boundary layer, and in particular to guarantee a satisfactory resolution of the **Viscous Sublayer** with $y^+ < 1$ (Fig. 7.2) and meet the requirement of the turbulence model of section 7.4.3. This value being dependent on the viscous conditions of the flow, an iterative process should a priori be considered to optimize the grid in the boundary layer. However, based on a first rough estimate of the wall shear stress τ_w (Eq. 7.19), it is possible to deduce a good order of magnitude for the first **cell wall distance** Δy :

$$\begin{aligned} \tau_w &= \frac{1}{2} C_f \rho V^2 & \Delta y &= \frac{y^+ \mu}{\rho u_\tau} & (8.1) \\ u_\tau &= \sqrt{\frac{\tau_w}{\rho}} \end{aligned}$$

and C_f which has been empirically estimated for external flows at $0.058 Re^{-0.2}$ *

$$Re = \frac{\rho V L}{\mu}$$

*<https://www.computationalfluidynamics.com.au/>

Grid characteristics are shown in table 8.1 for five meshes. This table includes the total number of elements, the **area-weighted average** h , which is a representative grid size, but also the averaged y^+ and the averaged cell wall distance Δy . The values of y^+ along the walls of the projectile are given for the five meshes in figure 8.6. Figures 8.7-8.9 show the 2D domains, with the coarser, the intermediate and the finer mesh, together with a zoom on the projectile and its boundary layer.

Table 8.1: Grid characteristics for the SOCBT configuration in 2D axisymmetric

Mesh	Nb Elements	h (m ²)	Avg y^+	Avg Δy (m)
1	2485	$2.68E^{-04}$	2.059	$2.06E^{-06}$
2	39880	$6.54E^{-05}$	0.6336	$5.91E^{-07}$
3	159520	$3.25E^{-05}$	0.3293	$3.04E^{-07}$
4	638080	$1.62E^{-05}$	0.1681	$1.54E^{-07}$
5	1434960	$1.08E^{-05}$	0.1118	$1.03E^{-07}$

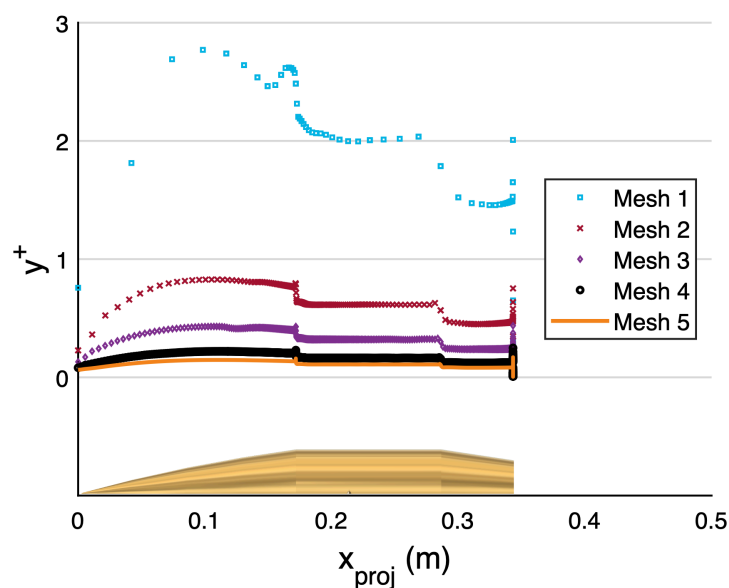


Figure 8.6: y^+ values along the 2D-axisymmetric body for the five meshes detailed in table 8.1.

The key variables available in 2D-Axisymmetric with swirl motion, C_{D_0} and C_{l_p} (sec. 9.1.1), are shown in figure 8.10 as a function of h . Thanks to these values, a Grid Convergence Index (GCI) is computed and shown for the SST-T3 model in table 8.2, to provide an estimation of the uncertainty due to discretization [33].

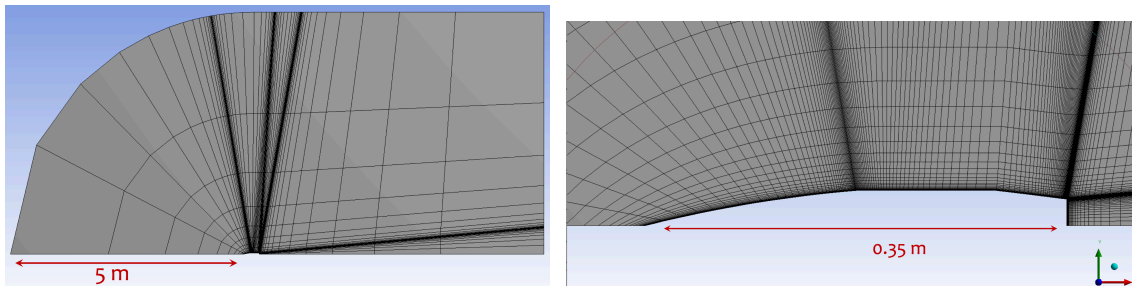


Figure 8.7: 2D axisymmetric structured **mesh 1** from table 8.1 with zoom around the projectile and its boundary layer.

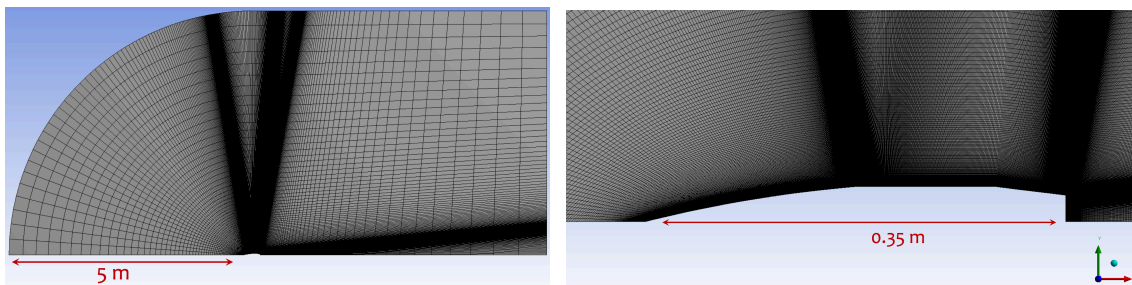


Figure 8.8: 2D axisymmetric structured **mesh 3** from table 8.1 with zoom around the projectile and its boundary layer.

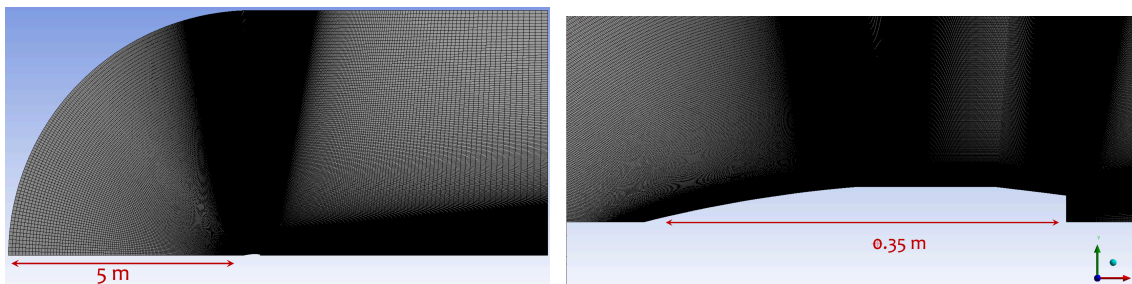


Figure 8.9: 2D axisymmetric structured **mesh 5** from table 8.1 with zoom around the projectile and its boundary layer.

The horizontal dotted line in figure 8.10 corresponds to the extrapolated value of the considered coefficient thanks to this convergence analysis (for the SST-T3 turbulence model). The last line of the table provides the estimated value given by the semi-empirical AeroFI code [210].

Each stationary case was considered as converged when a minimum of three orders of magnitude decrease in the normalized residuals was achieved, but also when the C_{lp} value remained constant for at least 200 iterations, which often happened well after the convergence of the residuals and C_{D0} .

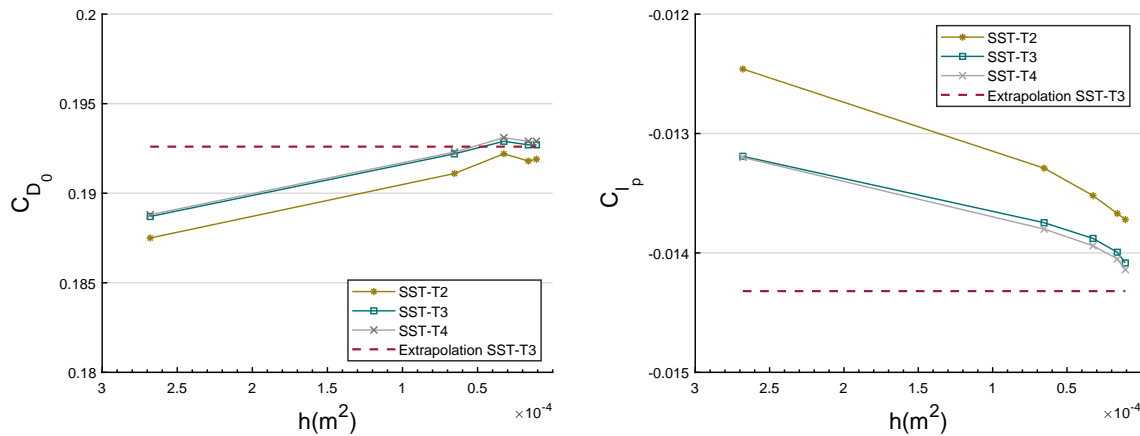


Figure 8.10: Grid convergence according to C_{D_0} and C_{l_p} as a function of the area-weighted average h .

Table 8.2: Grid Convergence Index [33] for the SST-T3 Model.

Ratio	Extrapolated C_{D_0}	GCI (%) C_{D_0}	Extrapolated C_{l_p}	GCI (%) C_{l_p}
1-2	0.1943	1.34	-0.0141	3.19
2-3	0.1943	0.81	-0.0141	1.98
3-4	0.1925	0.12	-0.0139	0.36
4-5	0.1926	0.066	-0.0143	0.99
Ref [210]	0.19	-	-0.015	-

It is immediately apparent that the percentage error related to the mesh is systematically greater for the spin damping moment than for the drag, regardless of the turbulence model used. It can also be seen that C_{D_0} is already well estimated for the third mesh, whereas C_{l_p} is still not really converged at the fifth mesh while y^+ is everywhere lower than 0.1. Other meshes were therefore made by adapting the aspect ratio and doubling the number of longitudinal subdivisions while keeping the same number of radial subdivisions, but the results do not give a better solution. They remain in the wake of the nominal results, proving in some way the limits of 2D-RANS modeling: the estimation is satisfactory but not completely converged. This is because the viscous contribution for spin damping is dominant whereas it is clearly a second order contribution for the drag (Fig. 8.11). This viscous contribution is much more complicated to capture, as explained in the previous chapter. This can be seen in the graphs representing the pressure and wall shear stress coefficients (Fig. 8.12): all turbulence models and all meshes return equivalent curves for the pressure (confirmed with experimental results from Reklis & Sturek [184] in the supersonic domain and from Kayser & Whiton [106] in the transonic domain), but discrepancies appear between meshes and between turbulence models for the skin friction coefficient.

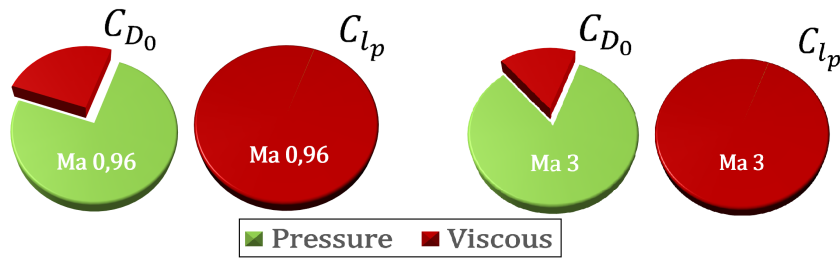


Figure 8.11: Ratio of pressure and viscous contributions at different speeds. The viscous relative contribution for drag increases as the speed decreases.

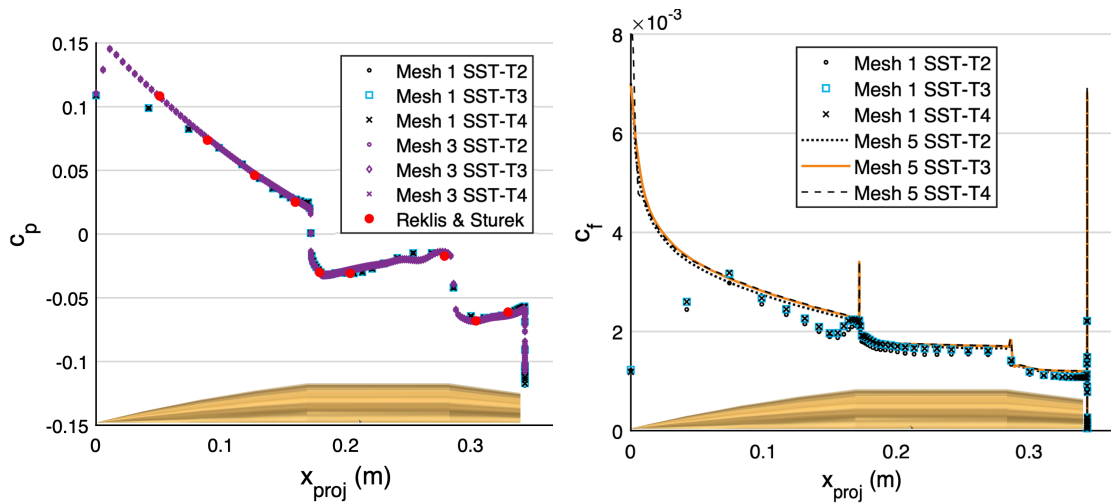


Figure 8.12: Pressure C_p and skin friction C_f coefficients at Mach 3 and 0° AoA for different 2D Axi-meshes and SST models. Experimental data from Reklis & Sturek [184].

A difference can be observed between the SST T2 model and the two other models considering an equation for intermittency in figures 8.10 and in figures 8.12 on the right. Considering the reference value given by the semi-empirical code, the SST-T2 model underestimates more the viscous contribution. The reference values for C_{D_0} and C_{l_p} being not as accurate, only numerical considerations can be used to differentiate both turbulence models SST T3 and T4, and at this stage, only the convergence speed really allows to differentiate these two models between them. For this reason, only the SST-T3 model will be used in the following developments.

Finally, in a more global way, it is necessary to pay attention to the reference variable to be considered for the convergence analysis. The drag coefficient is a readily available data, but its correct determination does not imply a successful calculation, since the coefficients that are more dependent on the phenomena in the boundary layer will probably be more poorly approximated. This observation is therefore more significant for spin-stabilized projectiles.

2D versus 3D transition

A direct and obvious approach would be to work with an extrusion of the 2D mesh to get a 3D mesh. But two issues seem to arise directly: firstly, it will still not be possible to represent finned projectiles in this way. Secondly, even for an axisymmetric projectile it will still be necessary to manually rework the area upstream of the nose to keep hexahedral elements in the alignment of the stagnation point. Figure 8.13 shows a 2D-extrusion done with ICEM CFD [7] and the problematic area in color with elements whose quality³ should be between zero and one and which becomes negative.

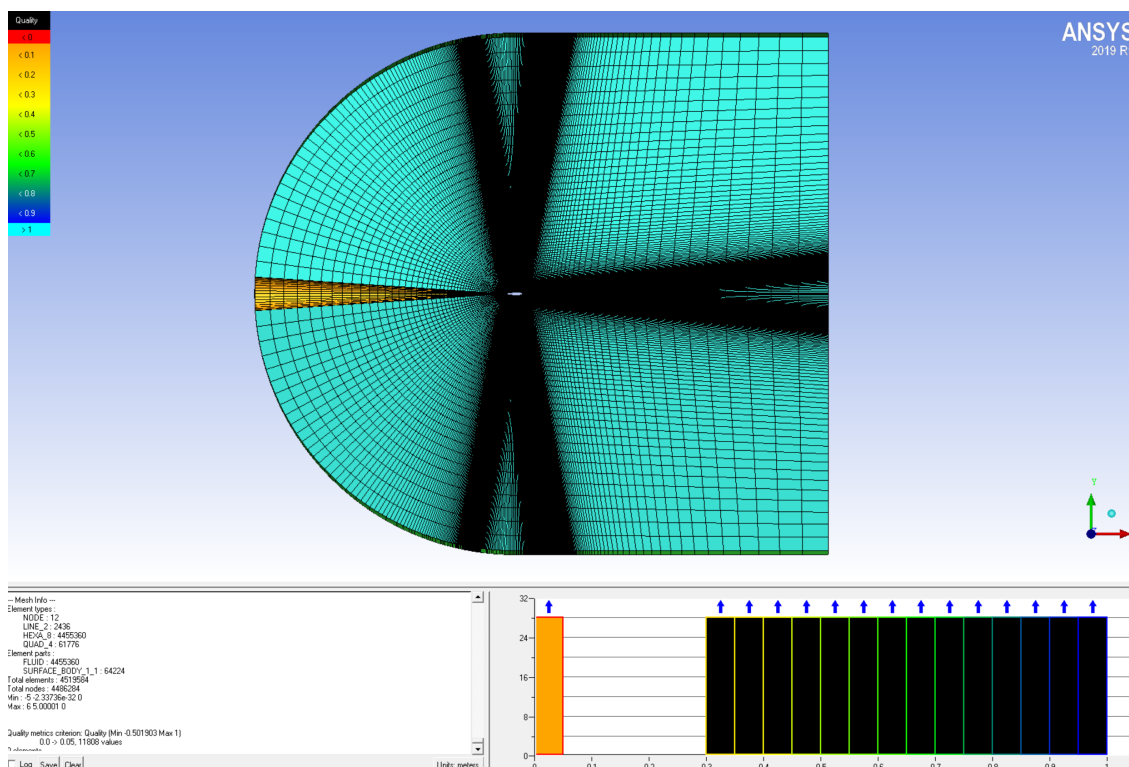


Figure 8.13: 2D-extrusion of a structured mesh, with negative quality zone upstream of the nose.

These two elements lead to the definition of a more systematic, unstructured method that should be valid for any configuration. An overview of the 3D unstructured mesh method used in ICEM CFD is given here:

- The geometry of the projectile with its domain is imported from Design Modeler to ICEM CFD ⁴.

³"The attributes associated with mesh quality in Ansys Fluent are node point distribution, smoothness, and skewness." [6]

⁴with or without the Workbench environment.

- *Part Mesh Setup* is used to configure the boundary layer: height of the first layer, maximum volume at the wall, BL growth and number of prims layers. Density boxes are also used to refine some specific parts, such as the ogive's tip (meplat) or the fins if there are any (Fig. 8.14).
- A first volume mesh is generated with *Robust (Octree)* method, in order to provide an adequate surface mesh.
- The volumes are deleted and a second volume mesh (tetrahedral dominant) is generated starting from the surface mesh, using the *Quick (Delaunay)* method, with the creation of the prism layers for the boundaries with the walls.

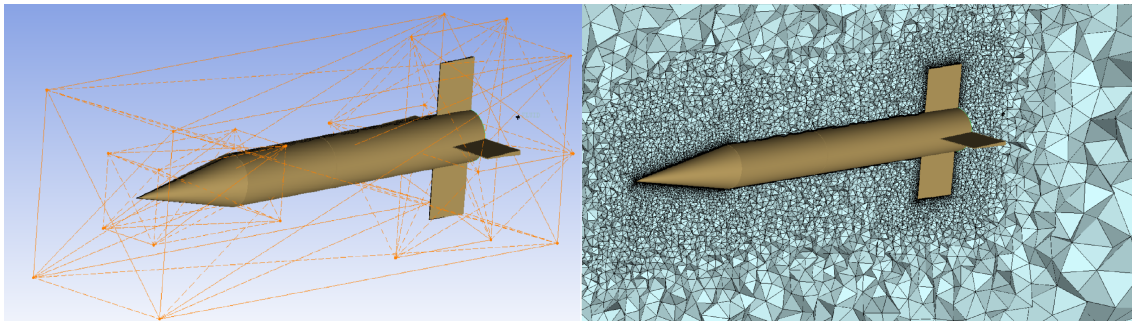


Figure 8.14: 3D unstructured mesh (left) with density boxes (right).

Prismatic Boundary Layer

The determination of the number of layers could be done in 2D to save computation time, but the assessment of the optimal number of layers must also take into account the rotation of the projectile and possible angles of attack. The analysis is once more carried out here for the SOCBT configuration. This is achieved at Mach 3 and Mach 0.96, first at 0° and then for an angle of attack of 10° , where experimental data are available [106, 184].

Five meshes with a boundary layer comprising 10, 25, 40 and 50 and 70 prism layers⁵ were used (Fig. 8.15), with the same initial wall distance (between $4E^{-7}$ and $8E^{-7}$ m) and growth factor (1.1), according to the mesh requirements for the γ -SST model (SST-T3). Together with the pressure and shear friction coefficient profiles, static coefficients and spin damping moments are compared to assess convergence and justify the methodology.

⁵Beyond 70 layers for this geometry, the quality of the outside of the boundary layer is compromised.

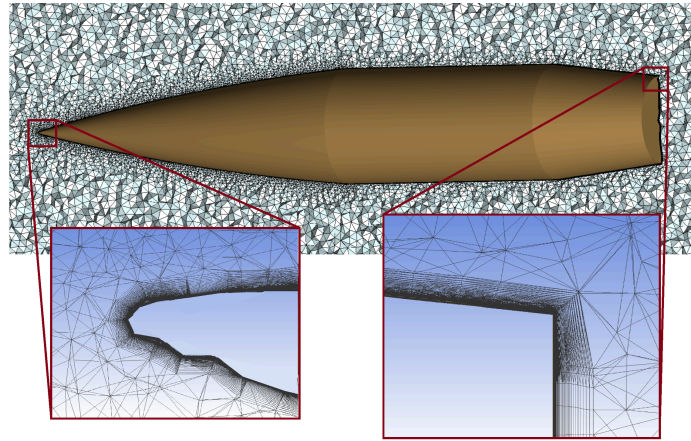


Figure 8.15: Unstructured mesh with a 50-layers prismatic boundary layer. Zoom represented with "cut plane" from ICEM CFD [7] giving a partial 3D representation of the different layers (it can give the impression of non-smooth geometry, but it is obviously smooth).

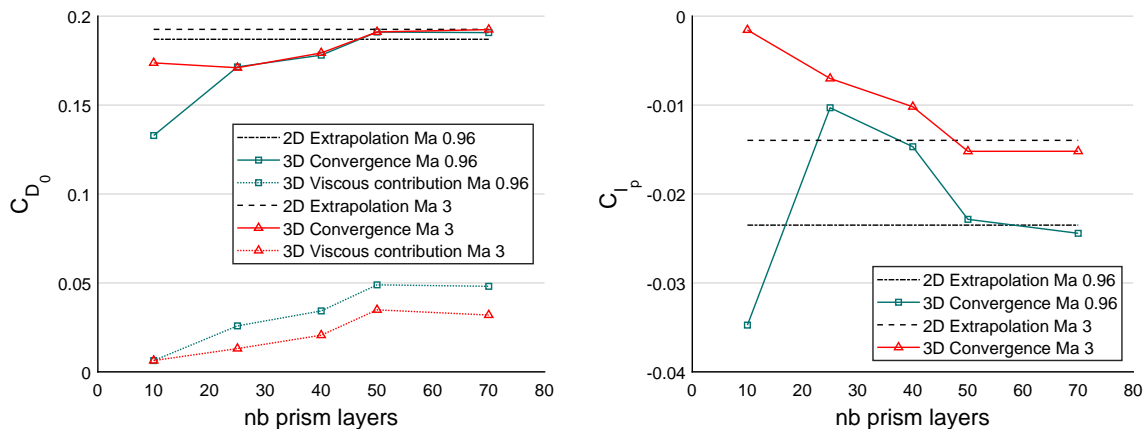


Figure 8.16: Grid convergence according to C_{D_0} and C_{l_p} as a function of the number of prism layers at the wall for a transonic and a supersonic velocity.

Figure 8.16 gives the convergence of the number of layers for the zero-yaw drag coefficient C_{D_0} and the spin-damping coefficient moment C_{l_p} for a supersonic and transonic velocity. From fifty layers, convergence seems to be reached, both for the drag and for the spin damping, which is as expected from the *GCI*-analysis (Tab. 8.37) higher than with the 2D calculations.

As the transonic zone is a sensitive zone including both subsonic and supersonic zones, but which is nevertheless necessary to cross for some applications (Sec. 11), the profiles of C_p and C_f are shown here at 10° AoA for this region. Figures 8.17-8.20 first show a comparison of what the different meshes give at Mach 0.96, while figures 8.21-8.24 compare for a 50-prism layers mesh (Fig. 8.15) the results obtained at different transonic velocities.

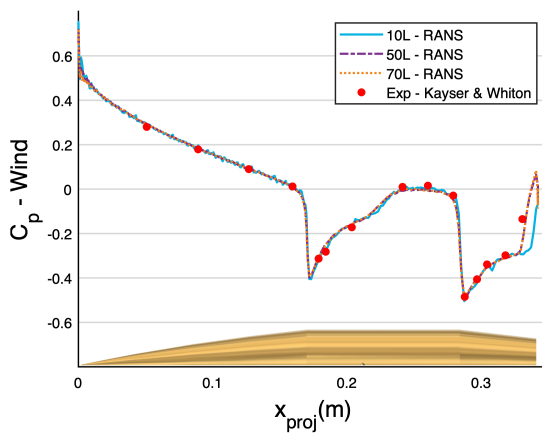


Figure 8.17: Pressure Coefficient on the windward side of the SOCBT configuration at Ma 0.96 and 10° AoA for three different meshes. Experimental data from [106].

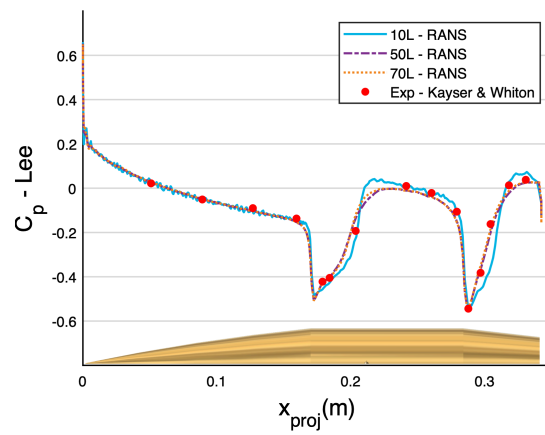


Figure 8.18: Pressure Coefficient on the leeward side of the SOCBT configuration at Ma 0.96 and 10° AoA for three different meshes. Experimental data from [106].

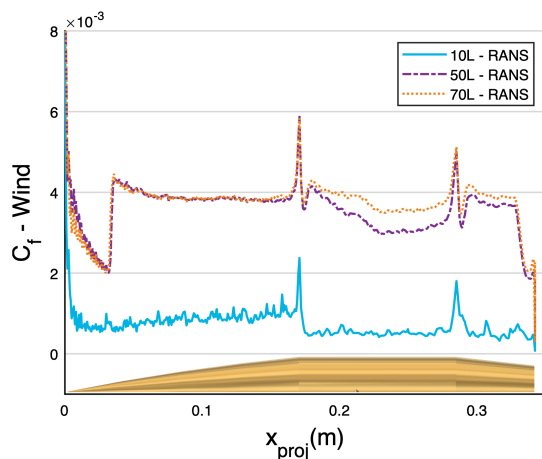


Figure 8.19: Skin friction Coefficient on the windward side of the SOCBT configuration at Mach 0.96 and 10° AoA for three different meshes.

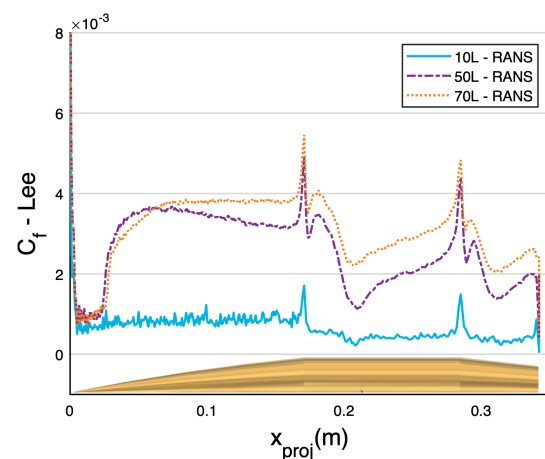


Figure 8.20: Skin friction Coefficient on the leeward side of the SOCBT configuration at Mach 0.96 and 10° AoA for three different meshes.

From the C_p -curves in figures 8.17-8.18 with the two compression gradients, it is to be seen that the flow exhibits a strong acceleration on the body, leading to the appearance of two shocks after the junctions ogive-cylinder and cylinder-boat-tail. At the junctions, the fluid expands and the pressure decreases, but given the acceleration of the fluid on the body, a supersonic shock appears a little after this junction and therefore a sudden increase in pressure follows.

It is interesting to see that again the pressure profile is well captured by all meshes, even with a reduced prismatic layer, but that on the other hand the viscous pro-

file is completely missed if the number of layers is not sufficient, even when the condition $y^+ = 1$ is satisfied. This element is therefore of major importance for the 3D implementation of unstructured meshes.

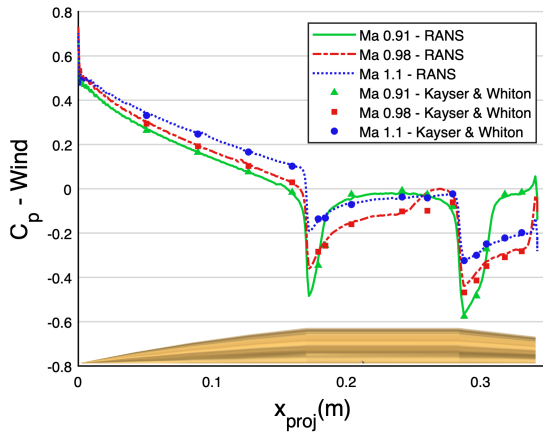


Figure 8.21: Pressure Coefficient on the windward side of the SOCBT configuration at 10° AoA for three different transonic velocities. Experimental data from [106].

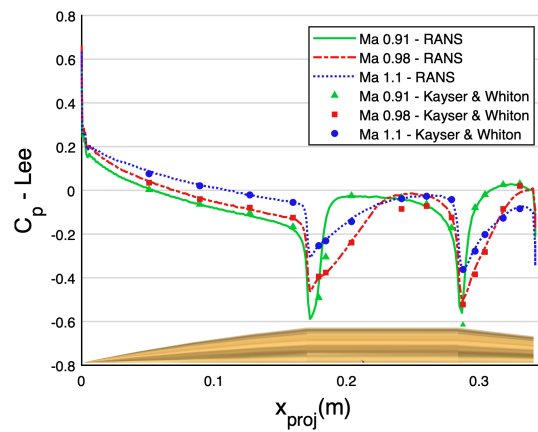


Figure 8.22: Pressure Coefficient on the leeward side of the SOCBT configuration at 10° AoA for three different transonic velocities. Experimental data from [106].

The RANS-simulations match well with the experimental data for all velocities, and even if the C_p -curves are not the best way to compare turbulence modeling, it confirms that RANS modeling gives accurate results for the calculation of the main pressure and velocity fields around the projectile. As it is known that the weaker the shock, the deeper it penetrates into the boundary layer, it makes sense that the inverted peaks (pressure gradients) are stronger at Mach 0.91 than at Mach 1.1.

Although no skin friction reference was found for the SOCBT geometry, the C_f -curves (Fig.8.23-8.24) were also added for the additional information it can provide on transition. It appears here that the flow does not separate at any time from the wall given the C_f -values always positive. Consecutive to the strong acceleration along the wall paired with the expansion at both geometrical discontinuities (intersection of arc and cylinder, and junction with boat tail), the skin friction increases drastically beyond the levels encountered in supersonic flow before reducing along with the deceleration of the shock interacting in the upper region of the boundary layer. This increase in skin friction is also greater at lower transonic velocities, but it occurs later with respect to the tip of the nose cone.

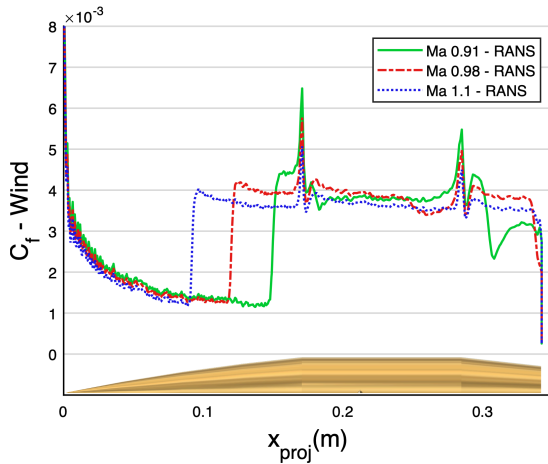


Figure 8.23: Skin friction Coefficient on the windward side of the SOCBT configuration at 10° AoA for three different transonic velocities.

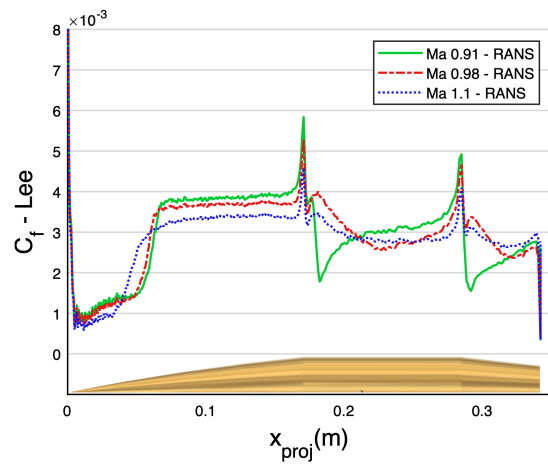


Figure 8.24: Skin friction Coefficient on the leeward side of the SOCBT configuration at 10° AoA for three different transonic velocities.

Figures 8.25-8.30 show the Mach and density gradient contours at the three transonic velocities for which the C_p and C_f profiles have been given. On a velocity difference of 30 m/s, the fluid behavior changes drastically on the asymmetric profile and the stronger density zones materializing the shocks, are again more visible on the contours at Ma 0.91 than at Ma 1.1, even if the propagation of these shocks is not yet pronounced outside the boundary layer.

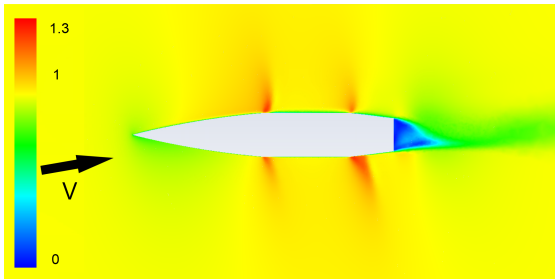


Figure 8.25: Mach contour in the xy plane for a flight speed of Mach 0.91 and 10° AoA.

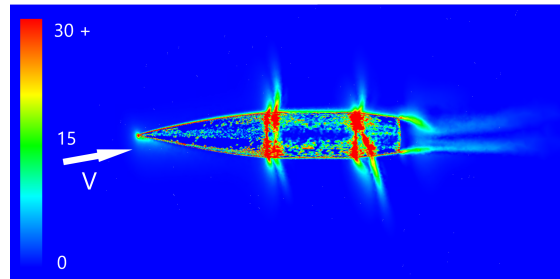


Figure 8.26: $\nabla\rho$ contour in the xy plane for a flight speed of Mach 0.91 and 10° AoA.

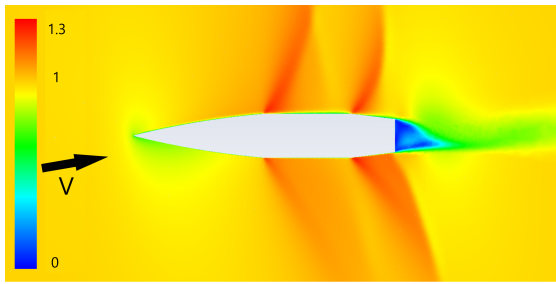


Figure 8.27: Mach contour in the xy plane for a flight speed of Mach 0.98 and 10° AoA.

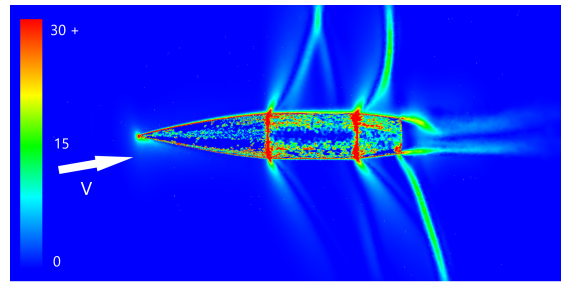


Figure 8.28: $\nabla\rho$ contour in the xy plane for a flight speed of Mach 0.98 and 10° AoA.

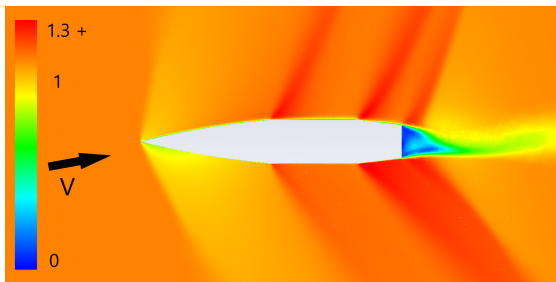


Figure 8.29: Mach contour in the xy plane for a flight speed of Mach 1.1 and 10° AoA.

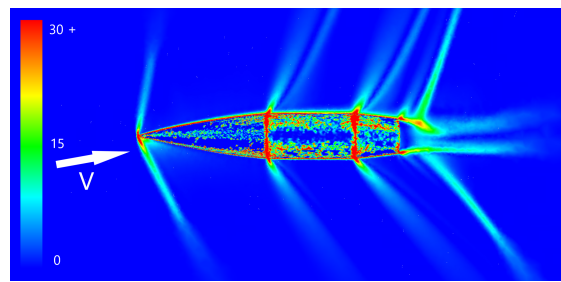


Figure 8.30: $\nabla\rho$ contour in the xy plane for a flight speed of Mach 1.1 and 10° AoA.

At the end, the mesh used for the steady and unsteady RANS simulations of the full projectile in free-air consists of about 3 million elements⁶, with a prismatic boundary layer mesh comprising between 50 and 70 layers resulting in an average value for y^+ smaller than one. As this mesh is optimised in the different "critical" velocity regimes, the order of magnitude of the number of elements should remain equivalent for any equivalent geometry. For a larger projectile with fins (ANF for instance), about 6 million elements are needed.

⁶For an optimized mesh to compute the aerodynamic coefficients. The mesh used for the contours of figures 8.27-8.30 has been refined outside the boundary layer to better visualize the density gradients.

8.4 Initial and Boundary conditions

Another important requirement when solving differential equations are the initial and boundary conditions. Just as it is necessary to know the initial conditions for a trajectory calculation, such as the velocity or the spin of the projectile at the muzzle of the tube, its inclination, the ambient air pressure and temperature, etc... the accurate definition of the initial and boundary conditions of the calculation domain is a crucial point of the flow simulation.

When using **ideal-gas properties**, following conditions are applied on the different zones defined as in figure 8.31-8.32:

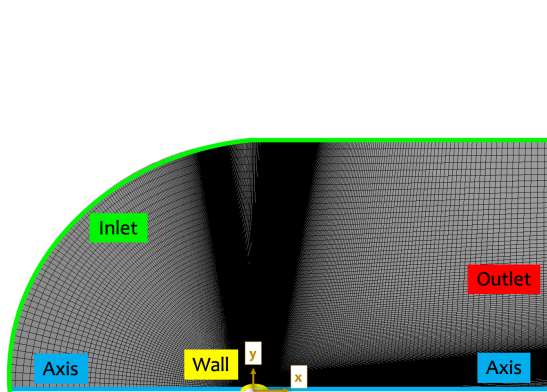


Figure 8.31: Boundary Conditions in 2D.

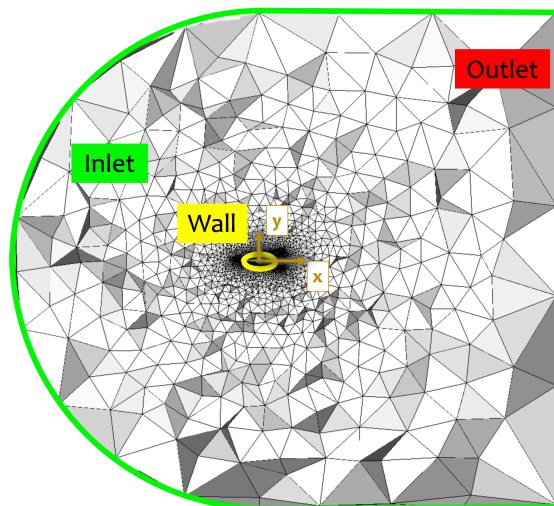


Figure 8.32: Boundary Conditions in 3D.

- **Axis:** This part appears only in 2D and is simply defined as "axis" for the Axisymmetric condition (with or without swirl);
- **Inlet:** Pressure-far-field conditions are applied together with the desired Mach velocity and angle of attack.
 - By default, the gauge pressure is set to 101325 Pa and the temperature to 288 K, unless the calculation has to be aligned with experimental conditions where pressure and temperature have to be adapted.
 - If a variable velocity is to be simulated, a *named-expression*⁷ is used to express the velocity as a function of time.

⁷The *named-expression* in Fluent are user-defined functions allowing the dependence of certain parameters with respect to others, such as the axial velocity as a function of the speed, the speed or the AoA as a function of the time, etc...

- If a variable angle of attack is to be simulated, a *named-expression* is used to express the orientation as a function of time with a sinusoidal function.
- Intermittency was set to 1, turbulent viscosity to 5% and the turbulent viscosity ratio set to 10^8 .
- **Outlet:** Pressure-outlet conditions are applied, where the gauge pressure is set to 101325 Pa by default.
- **Projectile:** Walls are defined with an adiabatic no-slip condition. If a spin is to be simulated, a *named-expression* is used to express the rotation rate in [rad/s] around the "x-axis". This spin angular rate is expressed as a function of the Mach number, to keep a constant ratio $pd/2V$.

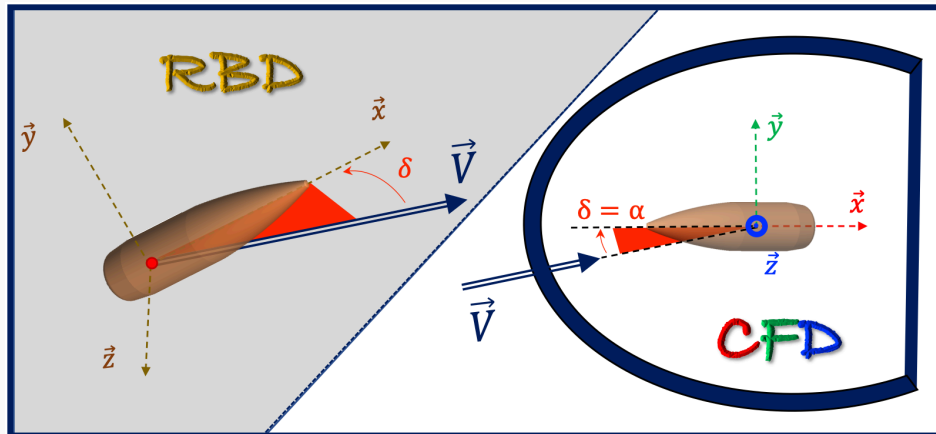
For **real-gas** simulations in Ansys Fluent [6], the **pressure-far-field** condition imposed at the inlet has to be changed to **pressure-inlet** condition where total pressure and temperature p_0, T_0 as well as the static pressure and temperature p and T have to be derived from the Mach velocity and γ using isentropic relations for compressible fluids:

$$\frac{p_0}{p} = \left(\frac{T_0}{T}\right)^{\left(\frac{\gamma}{\gamma-1}\right)} = \left(1 + \frac{\gamma-1}{2}Ma^2\right)^{\left(\frac{\gamma}{\gamma-1}\right)} \quad (8.2)$$

As for ideal-gas, Fluent uses the isenthalpic and isentropic relationships in iterative process to get the stagnation pressure. The heat capacity c_p is however function of temperature for the real gas models (Fig. 8.37).

⁸Other values were taken (lower turbulent viscosity down to 2 and higher turbulent viscosity ratio up to 50) to see the influence on the results and no significant difference was observed for the applications here.

Box 8.2: RBD vs CFD Axis system...



For the implementation of the numerical simulations, the body reference frame defined in section 3.2.1 (Fig. 3.4) and represented in the left part of the figure above, is somewhat revised in order to facilitate the consideration of variable velocities and yaw angle at the inlet of the fluid calculation domain. Indeed, it is no longer the projectile that moves relative to the air but the airflow that moves relative to a fixed projectile, as in a wind tunnel. The velocity vector is therefore always defined in the same sense as the projectile longitudinal \vec{x} -vector, but the projectile is returned to "face" the flow. Moreover, the yaw angle δ , which in RBD had a horizontal and a vertical component, is reduced to the vertical angle of attack α in CFD, to facilitate the extraction of aerodynamic coefficients depending on an inclination angle.

8.5 Physical properties

8.5.1 Callorically Perfect gas

"Air" has to be defined in the Fluid Materials dialog box, with the following characteristics:

- Density = ideal-gas;
- Constant c_p ($=1006.43\text{J}/(\text{kgK})$), **thermal conductivity coefficient** k ($=0.0242\text{W}/(\text{mK})$) and molecular mass ($=28.966\text{ kg}/\text{kmol}$);
- **Dynamic viscosity coefficient** μ according to default **Sutherland law** with three coefficients⁹.

8.5.2 Thermally Perfect gas

Although flow modeling with real-gas flow is much more complex and challenging than with ideal-gas flow, Fluent allows to take into account an equation of state (EOS) for real gas in a rather direct way thanks to the NIST model [6] or by considering a cubic EOS [6]. The first solution is however not applicable because the NIST properties are defined in Fluent within a specific range, in which the computational conditions of this work are not included. The cubic EOS of Soave-Redlich-Kwong was then used as initial approach, given its proven ability to accurately reproduce pressures of pure compounds, with a temperature dependent term [226].

The calculations performed in the next chapters will always consider the ideal-gas law, even at velocities higher than Mach 3. However a verification calculation was performed at Mach 4.5 for the Spinner configuration with the real gas conditions. The convergence is definitely more complex to reach but the results obtained correspond to the solutions in ideal conditions. Figures 8.33-8.34 represent the Mach contours in the longitudinal plane of the projectile and no noticeable difference appears between the two simulations. The C_p and C_f profiles (Fig. 8.35-8.36) show a small difference on the ogive, near the stagnation point, but this difference does not imply a significant deviation in the value of the aerodynamic coefficients. Further investigations should nevertheless be carried out for higher speeds and configurations with more stagnation zones. However,

⁹www.cfd-online.com/Wiki/Sutherland's_law

given the deviation of less than 0.07% at Mach 4.5 in the values of c_p obtained and plotted in figure 8.37, it seems undeniable that the error associated with the use of the perfect gas law is for this configuration less than other errors of numerical order.

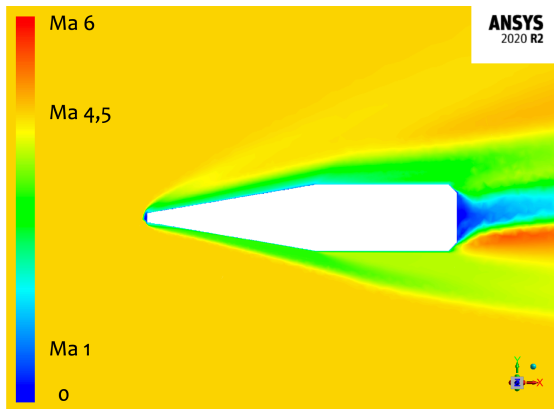


Figure 8.33: Mach contours around the Spinner configuration in the xy plane in **ideal gas** conditions - Ma 4.5 - 10° AoA.

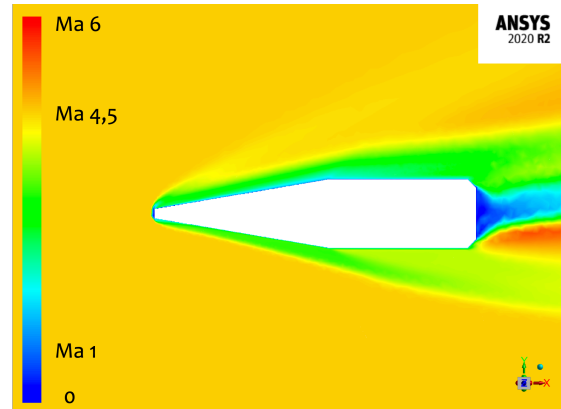


Figure 8.34: Mach contours around the Spinner configuration in the xy plane in **real gas** conditions - Ma 4.5 - 10° AoA.

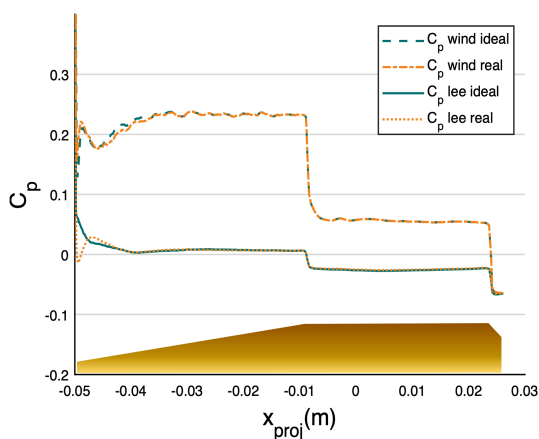


Figure 8.35: Pressure coefficient comparison in ideal and real gas conditions - Ma 4.5 - 10° AoA.

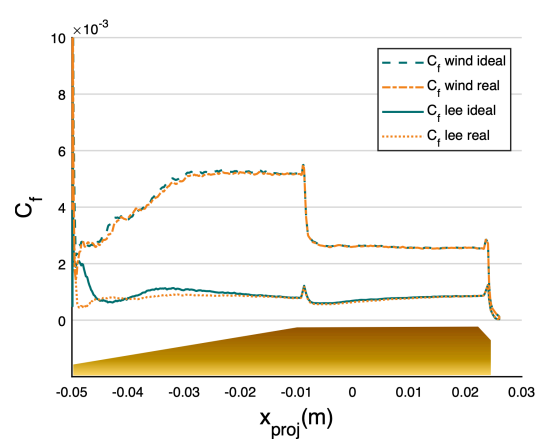


Figure 8.36: Skin friction coefficient comparison in ideal and real gas conditions - Ma 4.5 - 10° AoA.

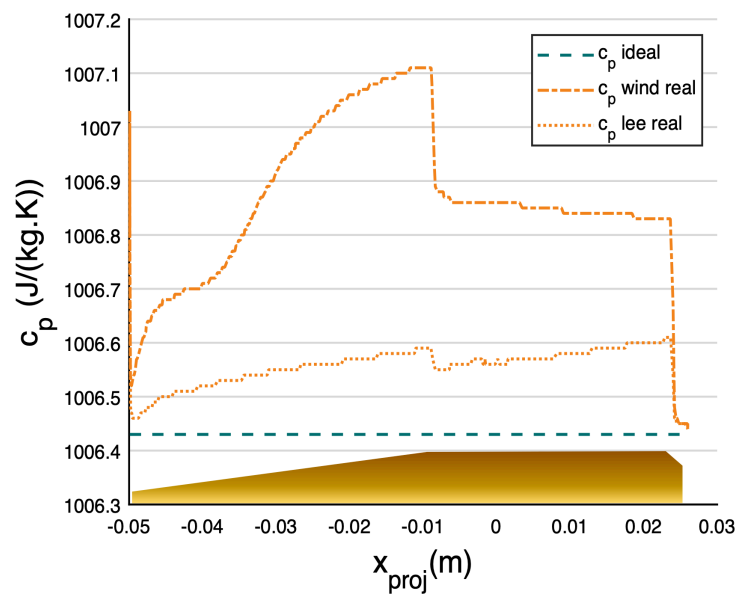


Figure 8.37: Variable heat capacity with the cubic EOS van Soave-Redlich-Kwong [226].

8.6 Digression on Uncertainty Quantification

While measurement uncertainty is an almost automatic step in the presentation of experimental results, the quantification of uncertainty (UQ) is far less obvious for numerical methods and turbulence modeling in particular [194, 276], and the concept has actually only appeared at the beginning of this century. *"UQ is a way to understand and to quantify the reliability of analysis predictions"*¹⁰. Rather than just stating that an aerodynamic coefficient has a fixed value with two digits after the decimal point, it is about working with confidence intervals. These are the results of a whole process composed of three phases.

First, potential sources of uncertainties must be defined. Then, numerical methods must be developed to propagate these uncertainties through the calculation models¹¹, after which a qualification of the results is observed, to define in a relevant way these famous corridors in which the reality should in principle be found.

Regarding the type of uncertainty in CFD, it is also necessary to realize that two types coexist: aleatory errors and epistemic errors [90]. The first are directly related to the variability of the physical input parameters, while the sec-

¹⁰<https://aerospaceamerica.aiaa.org/departments/why-were-not-there-yet-on-cfd>.

¹¹Monte Carlo [180], Polynomial Chaos [138], Latin Hypercube [68] are some examples of these methods applied for turbulent flows.

ond are related to the modeling parameters, which are intrinsically related to the limits of our knowledge. This chapter has introduced the methods of approaching turbulence, with in particular models based on the eddy-viscosity hypothesis, but it is clear that both the constants introduced in the models on the basis of empirical results, as well as the equations of the models themselves, are potentially sources of error, but in this particular case, it is much more difficult to identify on which side the truth lies. Turbulence is therefore the main reason why CFD UQ is still in its early stages: the UQ process is computationally extremely expensive and grows exponentially with the dimensionality of uncertain input parameters, since instead of running a single simulation with fixed boundary conditions or turbulence models, a large number of calculations are required to really get the statistical insight into the simulation certainty. Creating efficient systematic UQ methods is certainly an important research topic today.

Chapter 9

Aerodynamic coefficients extraction

While accurate results with cost-effective steady-state methods can be found in all common flight regimes [219], more advanced techniques, called CFD/RBD algorithms or **Virtual Fly-Out**, were also developed on high performance computing platforms and combined simultaneously a rigid **6/7-DoF** flight dynamic model with a three-dimensional time-accurate CFD simulation [24]. The RBD equations are integrated forward in time, where aerodynamic forces and moments that drive motion of the projectile are computed using the CFD algorithms [46, 47, 92, 111, 147]. The real-time feedback loop provided by the coupled analysis is an asset allowing to take instantaneously into account the changes of the parameters in flight and to conduct an effective disturbance analysis.

Alternatively, an uncoupled scheme determines the aerodynamic coefficients via CFD with respect to all possible flight conditions (mainly inclination and speed) and then uses them in the RBD 6-DoF solver, directly or as a lookup table. The coupled technique is among others presented by Sahu et al. [197, 201, 203, 209] for different configurations of fin-stabilized projectiles, with low roll rates, but also for spin-stabilized projectiles [200, 260], despite the very high rotation rates requiring very small time steps, as shown in section 3.5. The coupling methodology, although complex to set up, represents a significant advance for the time-dependent predictive capability required for the development of advanced maneuvering munitions [167, 202, 204]. From an operational point of view, this type of ammunition for remotely operated firing systems is the intermediate category between the conventional projectile and the missile (Box 9.1).

The methodology presented in this chapter provides the red thread based on quasi-static techniques to be able to express the complete set of coefficients with as little external manipulation as possible, keeping in mind a future automation, like the code implemented in the Virtual Fly-out. Each coefficient is nevertheless addressed separately in order to discuss the points of attention and to demonstrate the relevance of the numerical method using experimental data.

9.1 Static aerodynamic coefficients

9.1.1 Zero-yaw computations

As the **drag coefficient** (C_D) is the only coefficient to have a component independent of the yaw angle δ , a separate calculation at zero angle of attack must be solved over the entire speed range to determine it. The Zero Yaw Drag coefficient C_{D_0} is both the most important and the easiest to determine, both numerically [30] and experimentally (Box 3.3), but since it is omnipresent, it should be determined with the greatest care. To be noted that previous section showed a non-negligible contribution of viscosity involved in the overall calculation (Fig. 8.11).

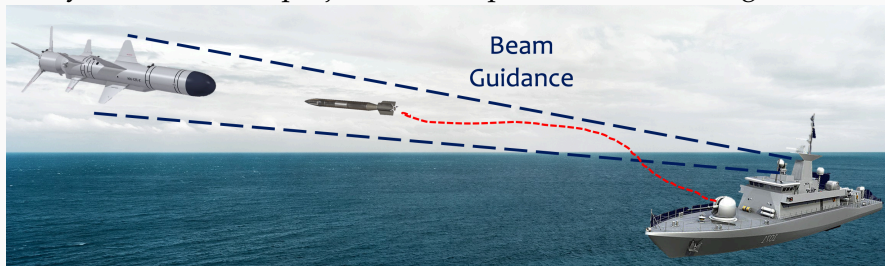
During this same calculation, it is also possible to determine the **spin damping coefficient** (C_{l_p}) if the projectile is spin-stabilized or the rolling moment coefficient $C_{l_{\delta F}}$ if the latter is set in rotation by its fins. These coefficients can be considered as independent of the yaw angle when the latter remains small. This behavior has been verified up to angles of attack of 15° for a spin-stabilized projectile (Sec. 12) and Bhagwandin [22] shows also constant values up to 10° for different finned projectiles put in rotation. Beyond approximately 15° ¹, it becomes then necessary to take into account a component depending on the angle of attack. Although it is a damping moment coefficient, and therefore transient by definition, the C_{l_p} can be determined in the same way as the static coefficients. Indeed, unsteady methods for determining roll damping are discussed for complex missile configurations [22, 228, 265] and for rotationally symmetric configurations, the results are similar to steady-state solutions. It is however important to vary the rotation velocity in proportion to the forward velocity, i.e. to keep the adimensional angular velocity $\frac{pd}{2V}$ constant².

¹Exact value depending on the geometry.

²Even if in flight this ratio tends to increase slightly because the forward velocity decreases faster than the rotation velocity.

Box 9.1: Missiles vs guided projectiles...

The main distinction on the velocity evolution between a missile and a projectile, is that the former is self-propelled. Projectiles, for their part, are fired by a cannon and solely rely on their initial kinetic energy to reach their target. They are consequently cheaper than missiles. Throughout most of warfare, ammunition was unguided and had conventional ballistic trajectories. However, recent technological breakthroughs in miniaturized guidance technology have enabled them to perform maneuvers [34]. Projectiles are therefore catching up to missiles, which have had guidance capabilities ever since the second world war. Because of their limited size, it is currently only possible to guide them through control guidance (the bullet is guided through electromagnetic radiation emitted from a friendly control point), as part of the technology is located outside of the projectile, requiring less space and complexity within it. Small fins, canards or nozzles placed judiciously on the body then allow the projectile to adapt its direction in flight.



If projectiles are fired with enough muzzle velocity, they can cover distances similar to those of medium range missiles. However, their advantage lies not with their maximal range, but rather their minimal range. Because they are fired from a barrel, they have a sufficient initial velocity to be effective almost instantaneously. Missiles, on the other hand, require a certain time until they reach their effective speed and hence are only effective after a certain distance. The development of these guided rounds falls mainly within the scope of artillery and naval defense* and in particular in the last ship defense layer (Close-In Weapon Systems) against high performance maneuvering target which succeeded in penetrating the outer ship defense layer, typically against anti-ship missile with high terminal maneuver capability. It is therefore not developed to replace missiles, but rather to complement them.

The DART (Driven Ammunition Reduced Time of flight) is an example of development project, which is a smart accessorizing of the classic 76-mm ammunition [34]. In terms of caliber, Lockheed Martin and Raytheon have lead the way with the EXACTO (Extreme Accuracy Tasked Ordnance) project and the development of a sniper rifle firing 12.7mm caliber smart projectiles capable of accurately tracking a moving target†.

*<http://ukarmedforcescommentary.blogspot.com/>

†www.maritime-executive.com.

Spin-stabilized Spinner Configuration

The experimental results of ARL (BRL-MR-3886) [179] as well as the results given by the semi-empirical programs AeroFI [210] and/or PRODAS [16] were compared with the numerical results obtained for the Spinner configuration. Some DES calculation points from DeSpirito & Heavey [55] were also added when available.

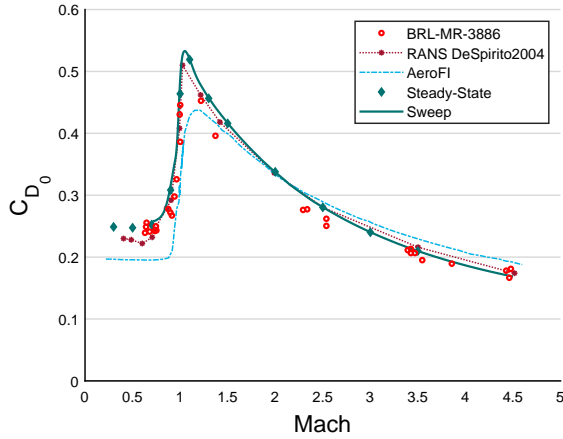


Figure 9.1: Zero-Yaw drag coefficient for the Spinner [16, 55, 179, 210].

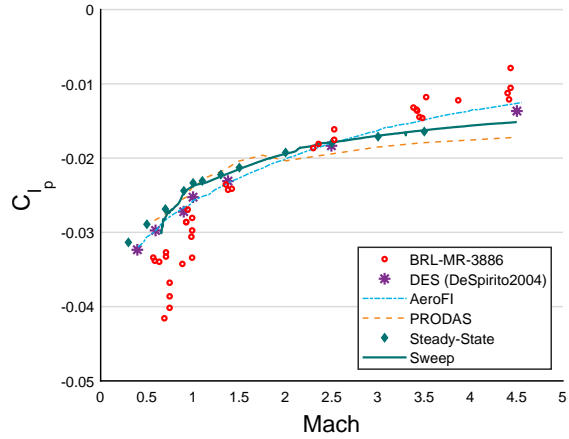


Figure 9.2: Spin damping coefficient for the Spinner [16, 55, 179, 210].

Figures 9.1-9.2 show the results for respectively C_{D_0} and C_{l_p} with the Sweep methodology ("Sweep") as well as the Steady-State calculations (Sec. 8.2), where each point corresponds to a separate calculation in which complete convergence was achieved (i.e. residuals, drag, spin)³. Both types of results blend well and correspond with the experimental results and the DES points.

Beside the mesh convergence analysis, a sensitivity analysis was also necessary to chose the right "Sweep"-computations parameters, namely the timestep Δt and the number of inner iterations per timestep i . As the spin is the more sensitive to convergence because of viscosity, the sensitivity computations were done for this coefficient. Calculations have been performed with Machsteps ranging from 0.001s to 0.05s and a number of inner iterations per Machstep ranging from 25 to 100. The results show no difference over 40 inner iterations and below 0.05s up to Mach 0.7, which is sufficient to correctly capture the changes in the transonic zone.

³CPU time needed for one sweep computation in the whole Mach range = 26-20:08:00, running on 80 cores. CPU time needed for 11 SS points (1000i each) = 86-00:49:04, running on 80 cores (3D mesh \approx 3Mo elements).

Fin-stabilized ANF Configuration

The obtained Sweep and Steady-State RANS results for the ANF configuration are compared with the semi-empirical code AeroFI [210] and Aeroballistic Free Flight Range (FF) and Wind Tunnel (WT) experiments conducted at DRDC Valcartier and reported by Dupuis [69].

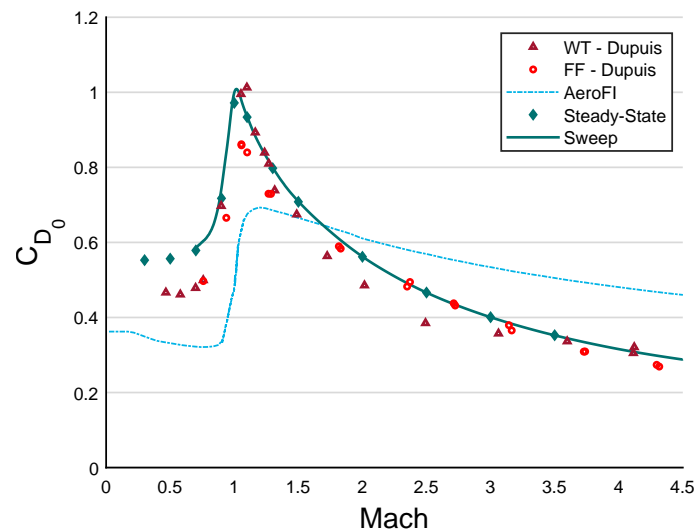


Figure 9.3: Zero-Yaw drag coefficient for the ANF configuration [69, 210].

As mentioned earlier, the AeroFI drag curve in figure 9.3 diverges quite a lot from the other results, both in magnitude and in shape, a trend that is less obvious with the other coefficients. On the other hand, the RANS calculations are satisfactory compared to the two series of tests which themselves show slightly different trends depending on the speed regime.

The significant higher drag curve with respect to the drag-curve presented in figure 9.1 is one of the benefit to further develop spin-stabilized maneuvering munition instead of fin-stabilized: the reduced drag can allow larger height of flight and hence larger ranges. This comes also with a second asset: a second life can be given to current stocks of unguided shells, which can be retrofitted with a low-cost guidance fuse, and this is less expensive than developing whole new projectiles [242].

9.1.2 Small angle computations

Lift and Pitch Moment Coefficient C_{L_δ} & C_{M_δ} .

Given the observed linearity of the effects related to the occurrence of small angles of attack (around 5 degrees but strongly depending on the application), the so-called stability derivatives can be found with small angle computations. These are defined as the first-order coefficients of a Taylor series expansion of the **normal** or **lift** force and **pitch** moment. The slope with respect to angle-of-attack will be therefore computed⁴. The same calculations have been performed with the same parameters as in the previous section, but with an angle of 3° . According to box 8.2, it is therefore necessary to take out from the simulations the coefficients of force C_y and moment C_z and to divide them by the sine of the angle at which the simulation was done, to deduce C_{L_δ} (Eq. 3.44) and C_{M_δ} (Eq. 3.47) respectively.

Spin-stabilized Spinner Configuration

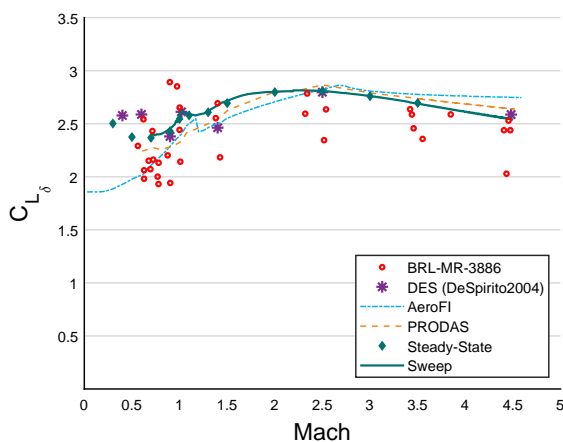


Figure 9.4: Lift coefficient derivative computed for the Spinner configuration and $\delta = 3^\circ$ [16, 55, 179, 210].

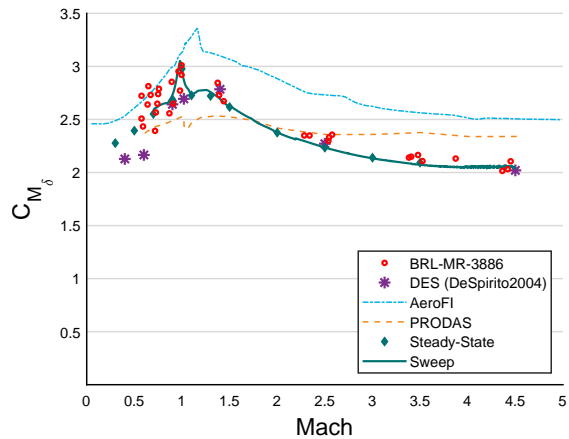


Figure 9.5: Pitch moment coefficient derivative computed for the Spinner configuration and for $\delta = 3^\circ$ [16, 55, 179, 210].

Figures 9.4-9.5 represent again the results obtained with steady-state and sweep calculations, which are compared with the experimental results of ARL (BRL) [179], DES calculations [55] and semi-empirical methods AeroFI [210] and PRODAS [16]. For the lift, all computational means tend to overestimate the values with respect to the experimental cloud, while the pitch is well captured by numerical approaches. As for the spin, the validity of the RANS calculation seems

⁴Since the coefficients C_{L_0} and C_{M_0} are zero for projectiles with a rotational symmetry and C_L and C_M vary linearly at low incidence [23]

even to be confirmed compared with the DES calculation.

Fin-stabilized ANF Configuration

As for the drag, when the projectile is provided with fins, the larger surface area subjected to lift translates directly into a much higher lift coefficient, as shown in figure 9.6. In terms of pitch, the stabilization mode is clearly distinguishable by the negative pitching moment coefficient, as presented in figure 9.7, with a minimum peak value in the transonic zone. Also because of the fins, the orders of magnitude of both lift and pitch are significantly larger than for the spinner configuration. The RANS results are compared with Wind-Tunnel (WT) and Free-Flight (FF) tests [69] and the semi-empirical code AeroFI [210].

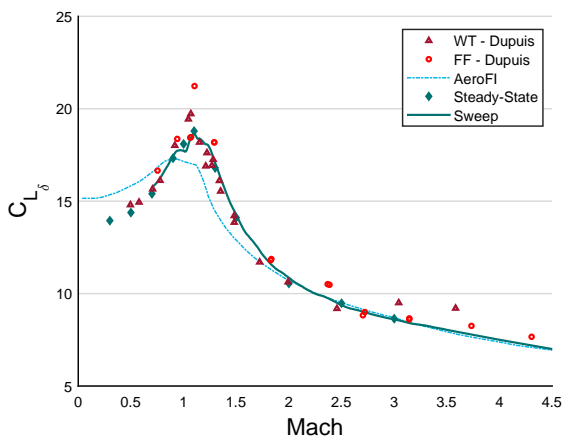


Figure 9.6: Lift coefficient derivative computed for the ANF configuration and for $\delta = 1^\circ$ [69, 210].

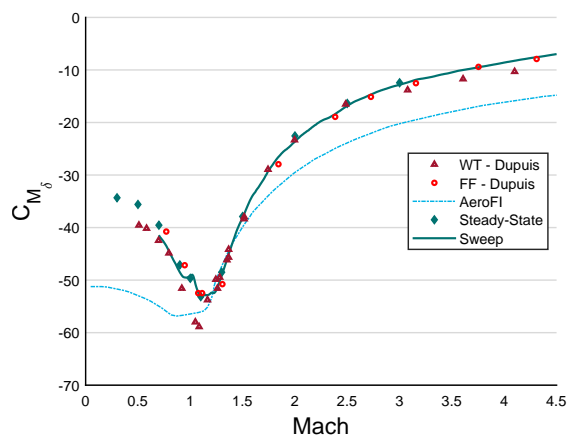


Figure 9.7: Pitch moment coefficient derivative computed for the ANF configuration and for $\delta = 1^\circ$ [69, 210].

9.1.3 Curved trajectory

All the coefficients determined so far are sufficient when dealing with flat fire trajectories (small arms, APFSDS). However, if the flight is more curved (howitzer, artillery, mortar...), the higher order derivative coefficients are also needed to account for the changing surface presented to the air. To do this, sweep computations were done by varying the yaw angle from -15 to 15° ⁵ by steps of 0.15° , for constant Mach number (Fig. 9.8-9.9). While the drag-points are quadrati-

⁵Calculations were done for positive and negative angles to verify numerically the symmetry of the drag with respect to the y-axis and the anti-symmetry of the lift and pitch with respect to the origin.

cally interpolated with linear terms that are negligible, the lift and pitch-points are interpolated with a cubic function with negligible independent and quadratic terms. This technique provides finally the quadratic drag coefficient as well as the third order lift and pitch moment coefficient derivatives. Only four velocities are presented in figures 9.8-9.9 for the **Spinner** configuration to lighten the representation but the same interpolations were done for all the point velocities shown in figures 9.10-9.11.

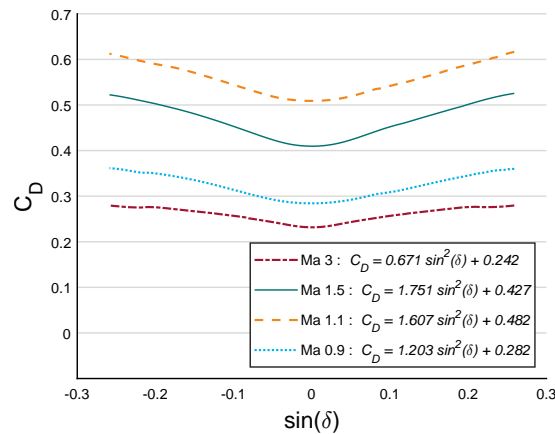


Figure 9.8: Evolution of the drag coefficient with respect to the yaw angle δ for the Spinner configuration.

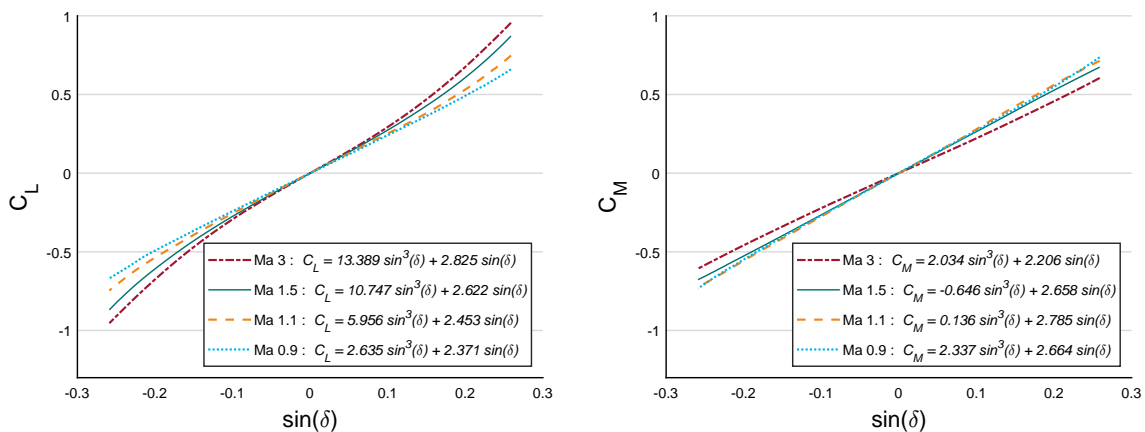


Figure 9.9: Evolution of the lift and pitch moment coefficients with respect to the yaw angle δ for the Spinner configuration.

In terms of drag, the correction to be made to take into account the angle of attack is much more important in the transonic zone, whereas for the lift this correction is more important in the supersonic domain. The pitch correction is minimal, and this could already be seen in figure 9.9 on the right where despite the use of a cubic interpolation, the curve looked quite linear.

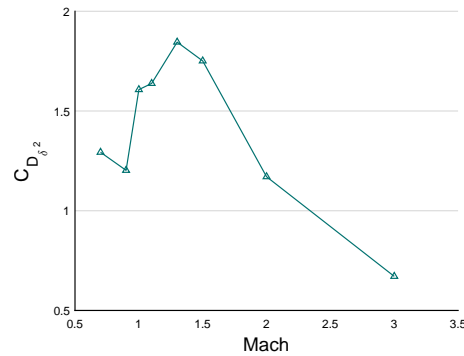


Figure 9.10: Quadratic Drag coefficient with respect to the Mach number for the Spinner configuration.

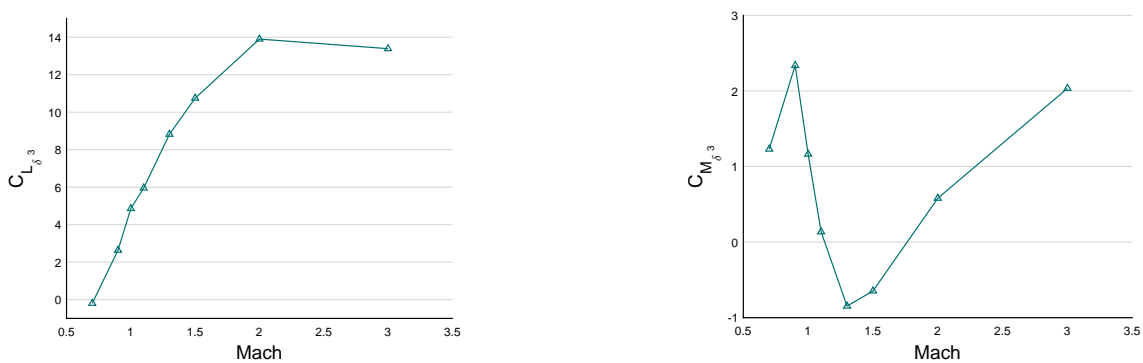


Figure 9.11: Cubic Lift (on the left) and Pitch moment (on the right) coefficients with respect to the Mach number for the Spinner configuration.

9.2 Dynamic aerodynamic coefficients

9.2.1 Magnus coefficients

Magnus moment coefficient $C_{M_{p\delta}}$ is shown in Figure 9.12 for the Spinner configuration, together with the same references already mentioned [16, 55, 179, 210]. As for the 5.56 mm projectile already discussed in section 3.2.2, this coefficient depends on the velocity but also on the yaw angle and if we want to be perfectly accurate, no simplification related to the linearity is possible as for the calculation of the lift or the pitch at small angles. Nevertheless, for classical spin-stabilized projectiles at relatively small angles ($\delta < 10^\circ$), the curve shape shows similarities in that the values are positive for largely supersonic velocities and at some point become negative as the velocity decreases. This is due to the combination of velocity components evolving in the boundary layer, which are dependent on both the linear and rotational velocity of the projectile about its longitudinal axis. As opposite flows interact with the attached boundary layer, the vortical structures of the turbulent flow is subject to significant variations [31, 38]. Figure 9.12 shows

therefore better results for the DES calculation than for the other methods in the transonic and subsonic range, indicating a need for greater accuracy in turbulence modeling and thus setting the limit of steady-RANS techniques to quantify the Magnus effect [31]. Moreover, DeSpirito & Sifton [57] compared with steady-state RANS and time-accurate RANS/LES simulations the flow around three spin-stabilized projectiles (including the Spinner projectile). While no difference was found between the RANS and RANS/LES simulations in the near-body flow field, RANS/LES simulations improved the Magnus moment prediction for projectiles with rounded or chamfered bases, thanks to the resolution of the turbulent eddies in the projectile wake. This demonstrates that the rear part of the projectile has the largest effect on the Magnus moment.

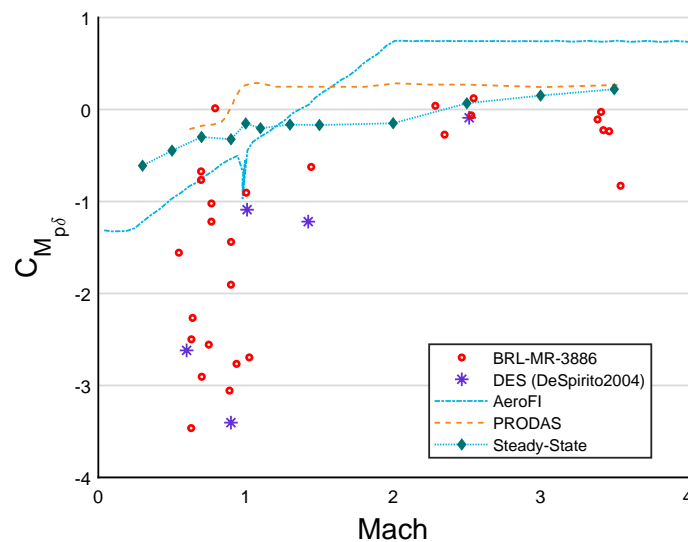


Figure 9.12: Magnus Moment Coefficient computed for a yaw angle of 3° [16, 55, 179, 210].

Also, the parameters affecting the thickness of the boundary layer, also affect the magnitude of the Magnus effect. This includes, in addition to velocities and inclination, the Reynolds number, but also the surface roughness, which must be rigorously quantified by changing the type of surface considered in the simulations. Surface roughness and the rifling grooves on the projectile's jacket were not investigated in this work, but it should be examined once the turbulence modeling will be further optimized (with optimized meshes and/or ZDES methods to better quantify the effects that these asperities can have in the boundary layer).

Chughtai et al. [38] conducted an extensive study on the Magnus effect and list the projectiles already studied by different methods (numerical and empirical), to extract the Magnus coefficients. The way the changes in Magnus force and moment can affect the trajectories was also investigated and showed an increase in precession and nutation frequencies that are significant in the transonic domain, reinforcing the need to take these effects into account for the stability analysis in the development phase of a new ammunition.

The Magnus effect over finned projectiles at larger yaw angles was also investigated by several authors [22, 142, 175]. The high rotation rate is not the most problematic, but the geometry itself, due to the fins or canards, which generate asymmetric distortions in the boundary layer and variations in the eddy structure.

9.2.2 Pitch Damping coefficients

Contrary to most of the coefficients determined so far where it was possible to have a relatively reliable reference with semi-empirical codes, the determination of the **pitch damping** coefficients poses more problems for these codes which are not always able to consider all the geometrical complexities [260].

Additionally, the results obtained by firing or virtual fly-out (RBD/CFD coupling) show a certain dependence between non-linear Magnus and Pitch-damping effects, which makes the decoupled simulation (computationally analog to a wind tunnel) interesting to, once again, make a good distinction between the different dynamic phenomena. It is important to note that some experimental results used as validation references must be considered with caution because the independence of Magnus and pitch damping are not guaranteed. This is notably the case in McCoy's work [137] which shows positive values of pitch damping coefficients for spin-stabilized projectiles, but which are in fact rather negative [218].

Two techniques are regularly used to determine pitch damping derivatives:

1. **Coning Motion:** This method is the earliest and allows the determination of dynamic derivatives in steady flows for rotationally symmetric geometries. In the literature, Weinacht describes this approach for small calibers [260] as well as for finned and standard projectiles with a high L/d ratio [256–258, 263, 264, 266]. This technique is also described by other authors, considering viscous or inviscid NS equations [119, 172–174].

2. **Planar Pitching Motion:** This second approach requires unsteady flow simulation but allows to compute the coefficients for non-axisymmetric geometries. For this reason, it is this technique that is presented hereafter, with a perspective of being able to work later with configurations that do not necessarily present a symmetry of revolution. This technique is also widely used in aeronautics, for the dynamic stability of all kinds of aircraft [28, 49, 118, 141]. The ANF and ANSR⁶ configurations are the most documented on the subject [21, 168] and these data will be used as validation data for the subsequent work, in the same way that they are often used as a mean of validation for completely other configurations [87, 244].

Planar Pitching Motion Technique

The transient planar pitching method consists in imposing a small-amplitude oscillation to the flow direction about a mean angle of attack α_0 . This time-dependent motion reproduces the harmonic oscillation of the projectile about its center of gravity in rectilinear flight [21]. On the basis of the projectile's pitching response, it is possible to deduce a damping over time due to the hysteresis motion. Based on the time history of the computed angle and force or moment (Fig. 9.13), the phase delay φ and amplitude C_{M_A} are quantified to determine the pitch damping force and moment coefficients.

The forced oscillation is defined by a sinusoidal function (Eq.9.1):

$$\alpha(t) = \alpha_0 + A \sin(\omega t) \quad (9.1)$$

where A is the **amplitude of the forced oscillation**, ω is the **angular velocity of the forced oscillation**, and α is the pitch angle relative to the body-fixed reference frame at time t . The amplitude A should be chosen so as to remain in the zone where the lift and pitch coefficients behave linearly with respect to the angle of attack.

During this forced oscillation pitch motion, the lift force and pitching moment can be developed in a Taylor expansion:

$$C_N(t) = C_{N_0} + C_{N_\alpha}(\alpha - \alpha_0) + C_{N_{\dot{\alpha}}} \frac{\dot{\alpha}d}{2V} + C_{N_q} \frac{q_t d}{2V} \quad (9.2)$$

$$C_M(t) = C_{M_0} + C_{M_\alpha}(\alpha - \alpha_0) + C_{M_{\dot{\alpha}}} \frac{\dot{\alpha}d}{2V} + C_{M_q} \frac{q_t d}{2V} \quad (9.3)$$

⁶ANSR = equivalent to the ANF body without the fins.

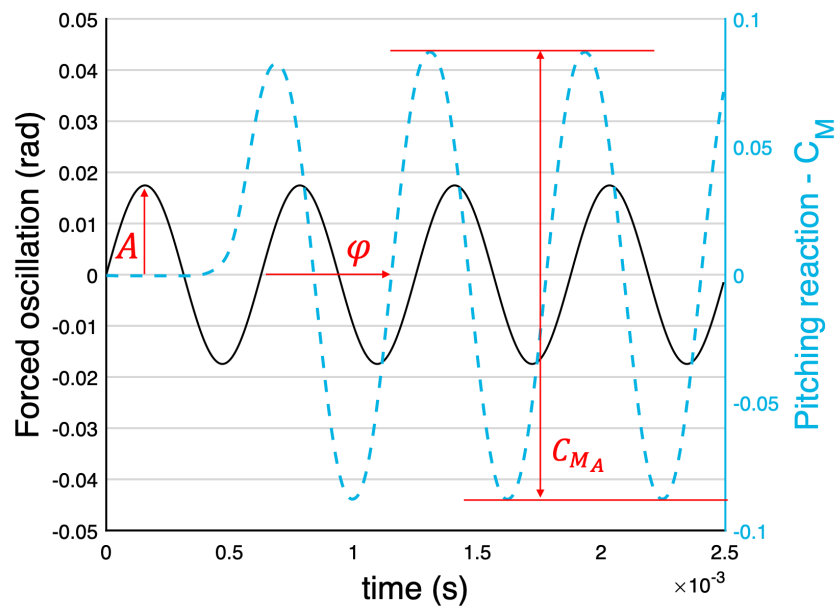


Figure 9.13: Pitching reaction (in blue) of a spin-stabilized projectile following a forced oscillation α in the vertical plane (in black). The same time-history is found for the lift.

where C_{N_0} & C_{M_0} are the static normal force (F_N in Fig. 9.14) and pitching moment coefficients at the mean angle of attack α_0 and C_{N_α} & C_{M_α} the curve slopes (Sec. 9.1.2).

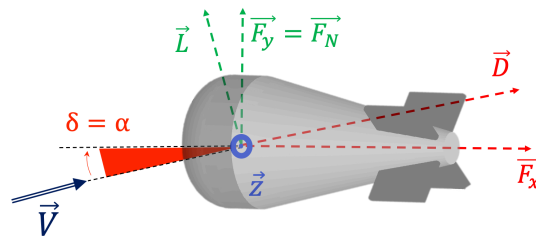


Figure 9.14: Schematic representation of axial/normal forces vs Drag/Lift.

Considering small amplitudes, the pitch rate q_t and angle of attack rate $\dot{\alpha}$ are considered to be the same:

$$q_t = \dot{\alpha} = A\omega \cos \omega t \tag{9.4}$$

Similarly to the spin damping coefficient determination, an adimensional angular velocity is used, here called the **reduced pitch frequency** k (Eq.9.5). This reduced frequency allows again to work in all speed regimes with the same ratio between angular and linear velocities.

$$k = \frac{\omega d}{2V} \quad (9.5)$$

Therefore, using 9.1, 9.4 and 9.5:

$$C_N(t) = C_{N_0} + C_{N_\alpha}(\alpha - \alpha_0) + (C_{N_{\dot{\alpha}}} + C_{N_q}) \frac{q_t k}{\omega} \quad (9.6)$$

$$C_N(t) = C_{N_0} + C_{N_\alpha} \alpha \sin(\omega t) + (C_{N_{\dot{\alpha}}} + C_{N_q}) k A \cos(\omega t) \quad (9.7)$$

and

$$C_M(t) = C_{M_0} + C_{M_\alpha}(\alpha - \alpha_0) + (C_{M_{\dot{\alpha}}} + C_{M_q}) \frac{q_t k}{\omega} \quad (9.8)$$

$$C_M(t) = C_{M_0} + C_{M_\alpha} \alpha \sin(\omega t) + (C_{M_{\dot{\alpha}}} + C_{M_q}) k A \cos(\omega t) \quad (9.9)$$

From the representation in figure 9.13, it can be assumed that

$$C_N(t) = \frac{C_{N_A}}{2} \sin(\omega t - \varphi) = C_{N_A} \sin(\omega t) \cos(\varphi) - C_{N_A} \cos(\omega t) \sin(\varphi) \quad (9.10)$$

$$C_M(t) = \frac{C_{M_A}}{2} \sin(\omega t - \varphi) = C_{M_A} \sin(\omega t) \cos(\varphi) - C_{M_A} \cos(\omega t) \sin(\varphi) \quad (9.11)$$

Then, from 9.7-9.10 and 9.9-9.11 respectively, the different coefficients of interest can be deduced:

$$C_{N_\alpha} = \frac{C_{N_A}}{2A} \cos(\varphi) \quad (9.12) \quad C_{M_\alpha} = \frac{C_{M_A}}{2A} \cos(\varphi) \quad (9.14)$$

$$C_{N_{\dot{\alpha}}} + C_{N_q} = -\frac{C_{N_A}}{2kA} \sin(\varphi) \quad (9.13) \quad C_{M_{\dot{\alpha}}} + C_{M_q} = -\frac{C_{M_A}}{2kA} \sin(\varphi) \quad (9.15)$$

A more intuitive determination technique is to consider figure 9.15 which schematizes the lift force or pitching moment history as a function of the angle of attack. The angular velocity q_t reaches two extremes when the curve passes through $\alpha = \alpha_0$, materialized by the points $C(-)$ and $C(+)$.

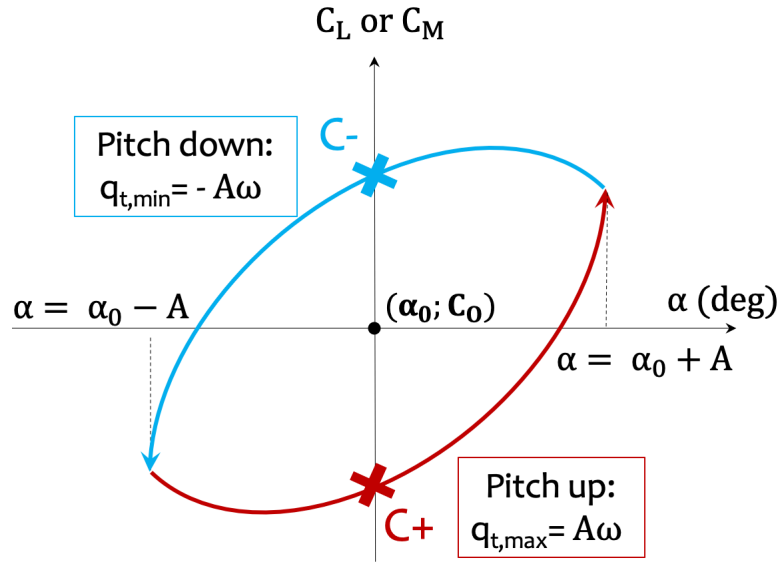


Figure 9.15: Schematic of a pitch hysteresis loop, used to identify the pitch damping coefficients from points of maximum and minimum pitch rate.

Starting from 9.6 & 9.8 and on the basis of figure 9.15, it follows that:

$$(C_{N_{\dot{\alpha}}} + C_{N_q}) = \frac{C_N(t) - C_{N_0} - C_{N_{\alpha}}(\alpha - \alpha_0)}{\frac{q_t k}{\omega}} \quad (9.16)$$

$$(C_{N_{\dot{\alpha}}} + C_{N_q}) = \frac{C_{N(q_{max})} - C_{N(q_{min})}}{(q_{max} - q_{min}) \frac{k}{\omega}} \quad (9.17)$$

$$(C_{N_{\dot{\alpha}}} + C_{N_q}) = \frac{C_N(+)-C_N(-)}{2kA} \quad (9.18)$$

and

$$(C_{M_{\dot{\alpha}}} + C_{M_q}) = \frac{C_M(t) - C_{M_0} - C_{M_{\alpha}}(\alpha - \alpha_0)}{\frac{q_t k}{\omega}} \quad (9.19)$$

$$(C_{M_{\dot{\alpha}}} + C_{M_q}) = \frac{C_{M(q_{max})} - C_{M(q_{min})}}{(q_{max} - q_{min}) \frac{k}{\omega}} \quad (9.20)$$

$$(C_{M_{\dot{\alpha}}} + C_{M_q}) = \frac{C_M(+)-C_M(-)}{2kA} \quad (9.21)$$

A way to determine the necessary inputs ω (angular rate of the forced oscillation) and then k (reduced frequency), is to refer to the linear approach (Sec. 3.6) and in particular to the definition of the natural turning frequencies $\phi'_{F,S}$ (Eq. 3.118⁷) which have to be used with or without "longitudinal angular rate" p depending on the type of stabilization.

⁷Equation 3.118 is given without dimensions, it is needed to multiply by $2V/d$ to pass in rad/s.

- For fin-stabilized projectiles, this gives:

$$q_t = \sqrt{\frac{M}{I_y}} = \sqrt{\frac{\rho V^2 d S C_{M\delta}}{2I_y}} \quad (9.22)$$

- For spin-stabilized projectiles and considering the precession motion, this gives:

$$q_t = \frac{1}{2} \left(\frac{I_x}{I_T} p - \sqrt{\frac{I_x^2}{I_T^2} p^2 - \frac{\rho V^2 d S C_{M\delta}}{2I_y}} \right) \quad (9.23)$$

Given the dependence on the non-linear term $C_{M\delta}$ in equations 9.22-9.23, it follows that the estimate of k can greatly vary when $C_{M\delta}$ changes in a significant way in the different speed regimes (i.e. especially for finned projectiles), which is in contradiction with most studies that rely on only one value for the whole velocity range. Table 9.2.2 refers to the final input data used for the projectiles discussed in this work⁸. The values are roundings of estimates made on the basis of a **Mach number of 0.88**⁹. A sensitivity study was however systematically performed on the parameters A and k , given the important dependence that the damping can have with respect to the input angular velocity.

Table 9.2.2: Necessary characteristic values to estimate the reduced input angular rate k . The amplitude of the forced oscillation $A = 1^\circ$.

	I_x [kg.m ²]	I_T [kg.m ²]	p [rad/s]	q_t [rad/s]	ω [rad/s]	k
Spinner	$2.16E^{-6}$	$1.47E^{-5}$	3150	90	5150	0.1
ANF	$7.2E^{-4}$	$4.86E^{-3}$	0	98	5595	0.3
5.56-mm	$1.46E^{-8}$	$1.14E^{-7}$	10500	130	7400	0.07
Cal.12 (Chap. 10)	$2.59E^{-5}$	$3.01E^{-4}$	0	13	765	0.07
.338-in (Chap. 11)	$1.4E^{-7}$	$1.98E^{-6}$	7940	86	4950	0.07
9-mm (Chap. 12)	$6.20E^{-8}$	$1.15E^{-7}$	7400	34	1970	0.03

⁸Using equation 9.4, $\omega = q_t/A$

⁹Except for the non-lethal 12-gauge projectile where the analysis was only held at 0.3 Mach and lower.

For the unsteady calculation, the **numerical integration timestep** Δt is determined as a function of the **number of global iterations per oscillation cycle** N , according to equation 9.24¹⁰. The parameter N , as well as the **number of inner iterations per global iteration** i must also be subject to sensitivity analysis to see their effect on the final results.

$$\Delta t = \frac{\pi d}{NVk} \quad (9.24)$$

For the determination of the second order pitch damping coefficients, depending on the angle of attack, the same procedure as in section 9.1.3 is used, where it is necessary to first determine for each speed the curve of the coefficients as a function of the angle of attack (α_0 of equation 9.1) to then interpolate the result quadratically, which will give respectively the coefficients $(C_{M\dot{\alpha}} + C_{M_q})_0$ and $(C_{M\dot{\alpha}} + C_{M_q})_{\delta^2}$.

Spin-stabilized Spinner Configuration

The complete procedure for retrieving the pitch damping coefficients is given below for the Spinner configuration for which experimental data were available, namely for the determination of $(C_{M\dot{\alpha}} + C_{M_q})$.

Before the determination itself, the sensitivity is first evaluated on the parameters A (Fig. 9.16), N (Fig. 9.17) and k (Fig.9.18). The history of the pitching moment is shown on the left as a function of time, and once the response to the oscillation is regular, one complete oscillation (red box from the left chart) is plotted on the right as a function of the amplitude A to illustrate the hysteresis phenomenon.

The results of this sensitivity analysis are summarized in figure 9.19 for the three parameters analyzed and their four respective values taken into account, case 2 being the one whose parameters are listed in table 9.2.2. It appears from this graph that the amplitude of the forced oscillation A and the number of global iterations per oscillation have a minimal influence compared to the oscillation frequency.

¹⁰ Assuming that an oscillation period is $T = 2\pi/\omega$.

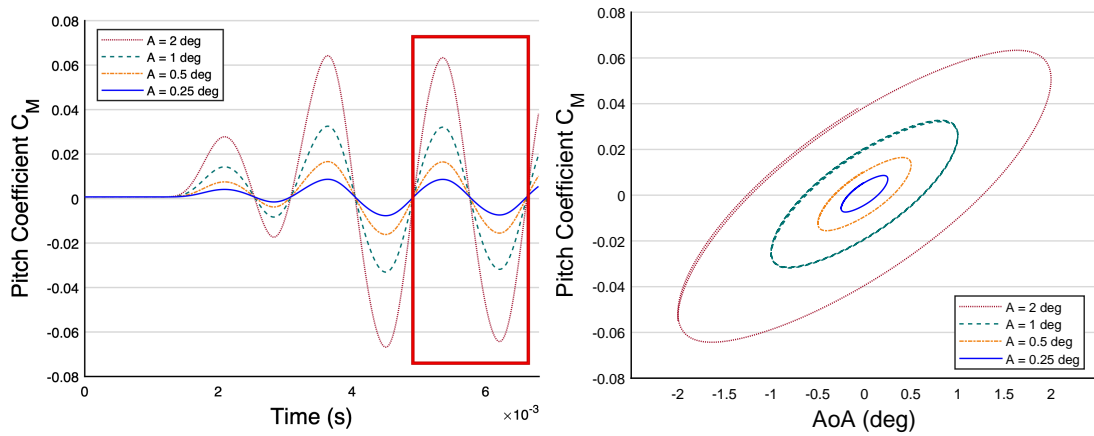


Figure 9.16: Pitch moment history as a function of time (on the left) and of the Angle of Attack (on the right) for different forced oscillations amplitudes A .

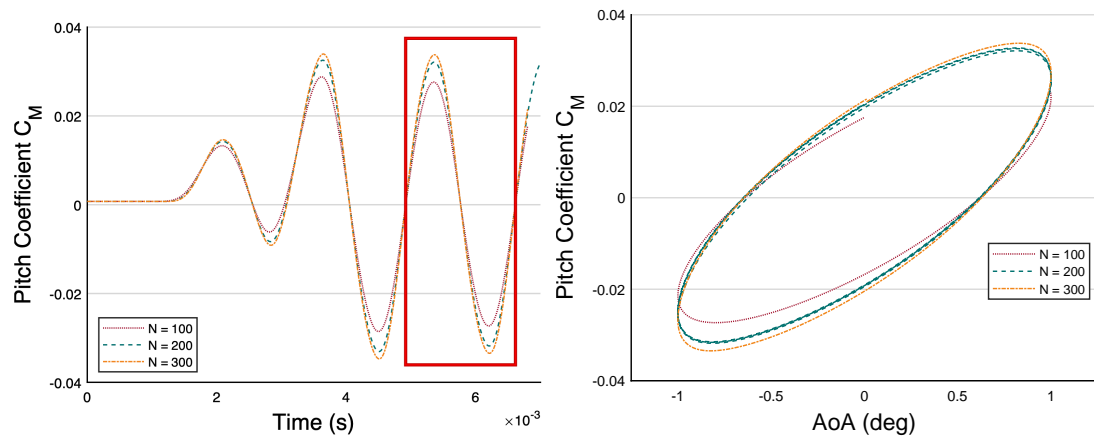


Figure 9.17: Pitch moment history as a function of time (on the left) and of the Angle of Attack (on the right) for different amounts of time-steps per period of oscillation N .

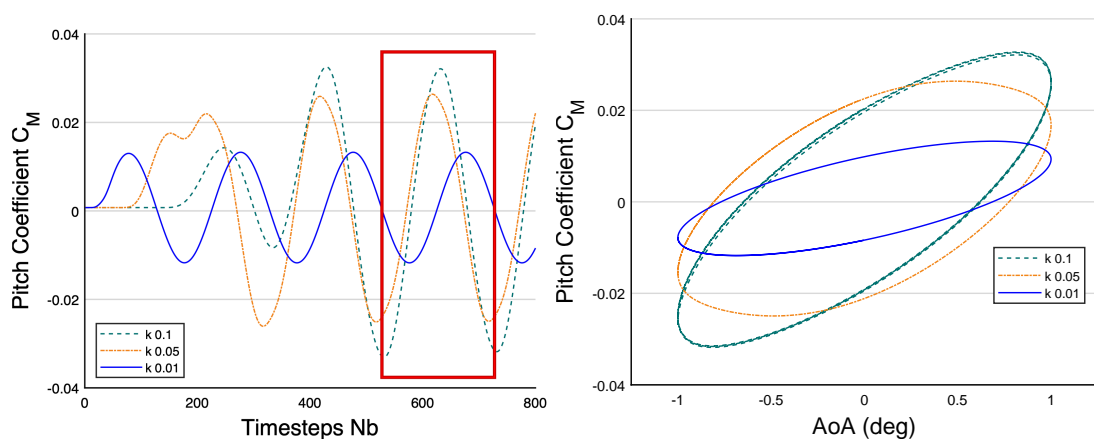


Figure 9.18: Pitch moment history as a function of time (on the left) and of the Angle of Attack (on the right) for different reduced pitch frequencies k .

The results for $(C_{M_{\dot{\alpha}}} + C_{M_q})$ which are shown in figure 9.20¹¹ and that fit well with the experimental cloud for the entire velocity spectrum, are therefore strongly related to the initial estimate of the initial reduced pitch frequency. The reference with the other presented results from DeSpirito [59], does not indicate which reduced frequency input was used, but the results remain in the same order of magnitude anyway.

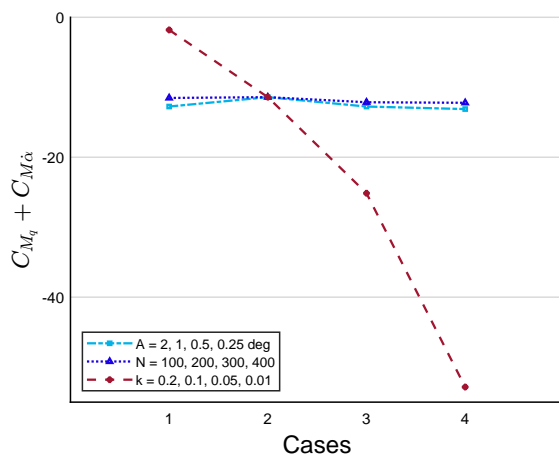


Figure 9.19: Influence of the different inputs parameters for the determination of the pitch damping moment.

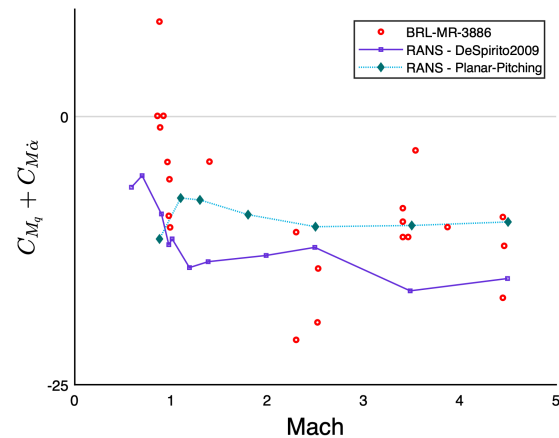


Figure 9.20: Pitch Damping Moment Coefficient as a function of the Mach number. Experimental data from [178] - CFD RANS results from [59].

Fin-stabilized ANF Configuration

The sensitivity analysis for the ANF configuration for the parameters k , A and N was found to give the same conclusions as for the Spinner configuration: As long as the amplitude remains in the linearity zone of the pitch coefficient, the results are equivalent, and from $N = 200$, the solution has stabilized. The dependence on k is also still present. As shown in figure 9.21 where the results for two different k are presented, the orders of magnitude remain equivalent and the computations follow the trends of the experimental results, but with a rather poor accuracy for some velocities. However, this k -sensitivity is physically quite logical, it means that the more the perturbation is important, the more the system has difficulty to react (negative values closer to 0), while if the perturbation is reduced (k decreases), the reaction is amplified (more negative coefficient).

¹¹CPU time needed for the 7 computation points ($N=800$ each) = 350-02:44:00, running on 80 cores (3D mesh = 3Mo elements).

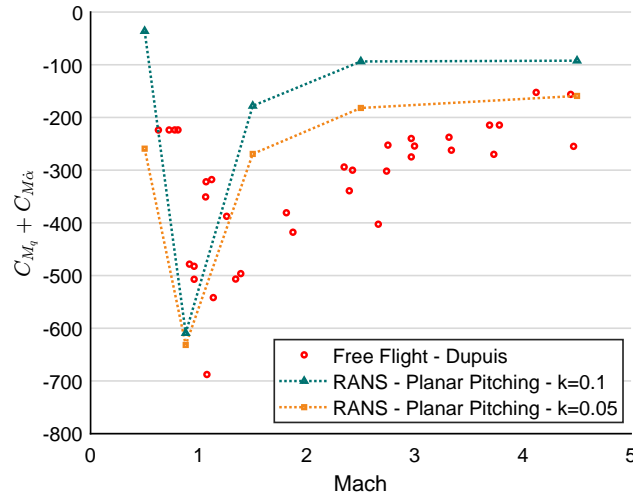


Figure 9.21: Pitch Damping Moment Coefficient as a function of the Mach number for the ANF. Experimental data from [69].

A good number of articles dealing with the damping coefficients in ballistics and with the ANF projectile in particular [21, 87, 208] seem to insensitively always use the same value of k (often $k = 0.1$) for results that are always very "exact". This observation is quite surprising given the sensitivity shown in other recent references dealing with other configurations [49, 91, 171]. For this reason, a more in-depth mesh sensitivity analysis should be performed and these calculations will need to be confronted with other methods, such as the coning motion method [265] for symmetric spin-stabilized projectiles, or indicial methods for fin-stabilized projectiles [87], in order to better control the range of validity of this k -parameter.

9.2.3 AoA Limitations

Even if some calculations have focused on angles of attack up to 15° , it is a fact that still higher inclinations have not yet been covered by the presented approaches. The knowledge of these wide angle coefficients is, among others, necessary for maneuverability [89]: even the low angular rates associated with maneuvers can have large effects on the asymmetric loads in the boundary layer [74]. And again, this becomes even more important for guided projectiles that do not have their propulsion to eventually compensate for these effects in the boundary layer. However, to go further in the analysis of the inclination, a RANS/LES approach seems again to be necessary to correctly predict the separation characteristics on the lee side of the projectile [54], which implies a much higher mesh resolution analysis (with appropriate meshing techniques) that cannot fit in the time frame of the present work.

9.3 Conclusion on Part II

Since pressure and shear forces are applied by the boundary layer on the projectile's walls, an accurate modeling of the boundary layer is paramount for a precise prediction of the force and moment coefficients, including the effects of Magnus because of spin. Due to their shape, the boundary layer around projectiles appears to be laminar only on a very small part of the projectile nose, and then becomes turbulent very quickly, due to the very high Re numbers. The modeling of the turbulence, with a view on the laminar-turbulent transition is therefore required.

Between the different aerodynamic coefficients of interest, we can distinguish the static coefficients and the dynamic coefficients, linked to the different damping phenomena generated over time, which are more difficult to determine because of their connection to unstable forces. While the first category is essential in all applications, the second category is involved in the design phase of weapon-ammunition system, in order to ensure optimum projectile stability. If the damping in pitching is for instance too small or too high, there is a risk that the projectile will not finish its trajectory with the right impact angle on its target, missing the desired effect (shaped charge, armour-piercing projectile, non-lethal impact [24], etc...). However, when a system is well designed, knowledge of the static coefficients alone is in most cases sufficient for a fairly accurate trajectory calculation.

Once the mesh convergence and the appropriate choice of the turbulence model have been rigorously performed, the determination of the static coefficients is quite straightforward and requires little processing. Two categories can be distinguished in the dynamic coefficients. On the one hand, the spin related effects being so dependent on the boundary layer properties, that although the numerical determination method is also quite direct, some refinements can still be necessary, beyond the impositions required by the static coefficients, and certainly when the yaw angle increases. On the other hand, even if the effects related to the pitch are "a priori" not very dependent on the boundary layer, the procedure for determining the pitch damping coefficients is much more complex, due to the sensitivity to the calculation initial conditions, which is in the case of the planar pitching method the frequency of the forced oscillation. It is therefore apparent that in the development of a new prototype, the geometrical design can only be done by iteration since the oscillation frequency is dependent on the pitching moment, from which the pitching damping is derived.

Part III

Small-Caliber Applications

This last part aims at presenting three specific small-caliber applications, which differ through their velocity regime and their geometrical configuration. While most research focuses on large caliber projectiles, for obvious reasons of range, time of flight and cost, it is nonetheless valuable to also consider the small caliber field of application, which also offers challenging features. An underlying advantage of this choice is naturally the possibility of carrying out some experimental testing with the means available in the Royal Military Academy's laboratories (ABAL & MECA).

The analysis presented here is for sure not the most extensive, given the infinite number of possible calculations and sensitivity analyses, but they provide the framework for what can/should be considered. The specific need in terms of use or development must otherwise dictate which other aspects have to be quantified and evaluated.

Chapter 10

Non-Lethal Application

This chapter is both a revision and an extension of the following publications:

- V. de Briey, I. Ndindabahizi, B.G. Marinus and M. Pirlot, "Aerodynamical CFD Study of a non-lethal 12-Gauge fin-stabilized projectile". Human Factors and Mechanical Engineering for Defense and Safety, 2019. doi:[10.1007/s41314-019-0020-x](https://doi.org/10.1007/s41314-019-0020-x) [24].
- V. de Briey, A. de la Filolie, B.G. Marinus and M. Pirlot. "Aerodynamic Characterization of a Non-Lethal Finned Projectile at Low Subsonic Velocity". AIAA Aviation Forum, 2019. Dallas (US). doi:[10.2514/6.2019-3696](https://doi.org/10.2514/6.2019-3696) [23].

Exterior ballistics is especially known for its applications at very high velocities, in particular to ensure precision performance and sufficient kinetic energy at impact. The field of non-lethal weapons, which appeared after the 2000s, changes the standards somewhat since the ranges of engagement are much shorter and the main constraint on impact for a rigid projectile is to remain below a certain velocity threshold to avoid serious and permanent injuries [185]. CFD references in ballistics mentioning results well below 0.5 Mach are uncommon and the need to validate the techniques already presented becomes a necessity for non-lethal applications, given their increasing development.

To characterize the trajectory of a low subsonic fin-stabilized projectile with a low angle of attack, the use of a Point-Mass Model (PMM - sec 3.8), taking into account only gravity and a constant zero-yaw drag coefficient, seems "operationally" justified given the short-range nature of the applications and the limited required computing resources. This means that this approach does not take into account the attitude of the projectile in flight and when it hits the target, neglects

any possible instability in flight. The use of non-lethal or less-lethal projectiles where serious injuries must absolutely be avoided requires however that the impact conditions are perfectly controlled.

This work starts from a 12-gauge finned-geometry to numerically and experimentally predict static and dynamic aerodynamic coefficients at different angles of attack (drag, lift and pitching moment) and low velocities, up to Mach 0.3. A comparison of trajectories is then performed to determine the relevance of using a more complex model than the PMM for this type of application.

10.1 Methodology

10.1.1 Computational Approach

The main study focused on low subsonic velocities to analyze more deeply the viscous effect on the profiles. The different static coefficients were computed according to the methodology presented in chapter 8. A typical non-lethal fin-stabilized 12-gauge geometry was used (Fig.10.1). In this configuration, the body of the projectile is wider than the wingspan, thereby influencing the role of the fins.

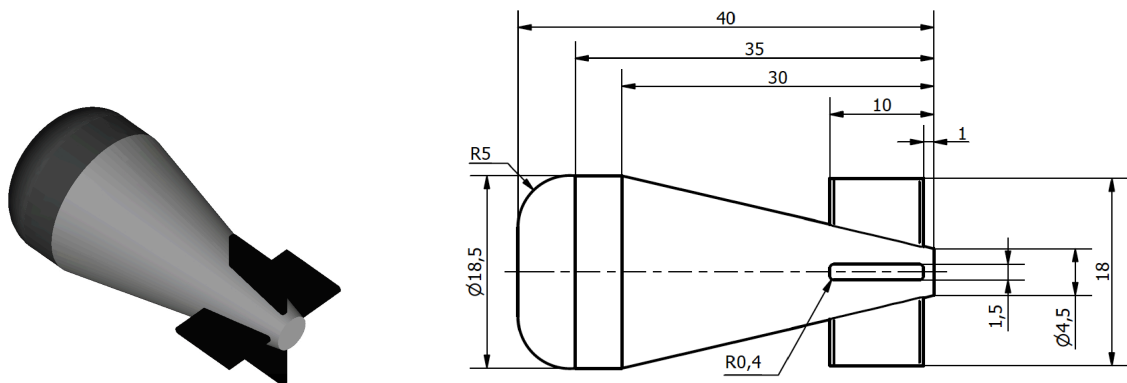


Figure 10.1: 12-GAUGE finned projectile dimensions in mm.

The final mesh used for the steady RANS simulations of the full projectile in free-air consists of 1.5 million tetrahedral elements with a prismatic (hexahedral) boundary layer mesh comprising 40 layers resulting in an average value for y^+ of 1 along the adiabatic no-slip walls¹. The domain extends to 15 projectile-lengths where pressure-far-field conditions are applied together with the desired angle of attack.

The presented results were computed at Mach 0.3, where it was possible to achieve a five orders magnitude decrease in the normalized residuals. Good convergence was also obtained at Mach 0.1, but with a much higher order of magnitude.

For the dynamic derivatives, the input parameters are taken from table 9.2.2. Given the low speeds, the time steps used both for the sweep method and for the determination of the pitch damping could be taken, "from a physical point of view", much larger than for the previous calculations. However, with these time steps, it was impossible to converge. Nevertheless, by reducing the time step by a factor of 1000 and by multiplying the time expression by a factor of 1000 in the "named expressions" (Sec. 8.4), the convergence was successfully achieved.

10.1.2 Experimental Approach

- **Wind-tunnel**

By means of an aerodynamic force balance (Fig.10.2), the three static coefficients (drag, lift and pitching moment) were measured in a low turbulence wind tunnel going up to Mach 0.1 for angles of attack from -20 to 20 degrees. The bodies are at scale 3 to match the Reynolds number with those of the flight of the scale 1 projectile when flying at Mach 0.3. In both cases the regime remains incompressible given the low velocity regime. The scale 3 bodies have a diameter of 5.565 cm for the test section of 60 by 60 cm. Corrections for walls were applied following reference [248].

In parallel, two different visualizations of the boundary layer were made in order to validate the CFD predictions regarding transition: infrared thermography and oil-flow visualization. Attention was mainly focused on the nose of the projectile and the flow behavior on the front part at different angles of attack.

¹Given the low velocities, the first cell wall distance could be expanded to $3.1 \cdot 10^{-6}$ m



Figure 10.2: Left : Aerodynamic balance for drag, lift and pitch measurements. Right : IR FlexCam for the temperature profiles visualization.

- **InfraRed Thermography**

InfraRed Thermography (IRT) [103, 221] was used to assess the state of the boundary layer transition, that depends on differences in model surface temperature caused by variations in the surface heat transfer rate. To accurately measure the changes in temperature occurring as a result of laminar-to-turbulent transition, the Noise Equivalent Temperature Difference (NETD) should be lower than 2 K. The IR FlexCam Ti50 was therefore used with a 0.07 K NETD and a spectral range from $8\mu\text{m}$ to $14\mu\text{m}$.

The most successful model materials for infrared thermography have low thermal conductivity and large emissivity. Two kinds of material were then used to print the projectiles for the experimental testing: a polyurethane foam called obomodulan and an anthracite resin, with the properties listed in Tab.10.1.

Table 10.1: Thermal properties of the projectiles.

	Obomodulan	Resin
Emissivity	0.6	0.91
Thermal conductivity [W/(m · K)]	0.17	0.028

- **Surface oil-flow visualization**

In the second visualization method, the projectile was coated with a proprietary oils and pigments mixture for surface flow visualizations.

10.2 Results

10.2.1 Experimental comparison of the static coefficients

The drag and lift coefficients obtained with the wind tunnel measurements and the RANS computations are shown in figure 10.3. Both graphs include axial force coefficients C_x and normal force coefficients C_y as well as the drag force and lift force coefficients C_D and C_L determined on the basis of the representation shown in Figure 3.14. References dealing with coefficients are sometimes not very explicit about the formulation (if they use F_X and F_N or D and L) and might suggest that they are equivalent, but the current example shows that these forces deviate significantly.

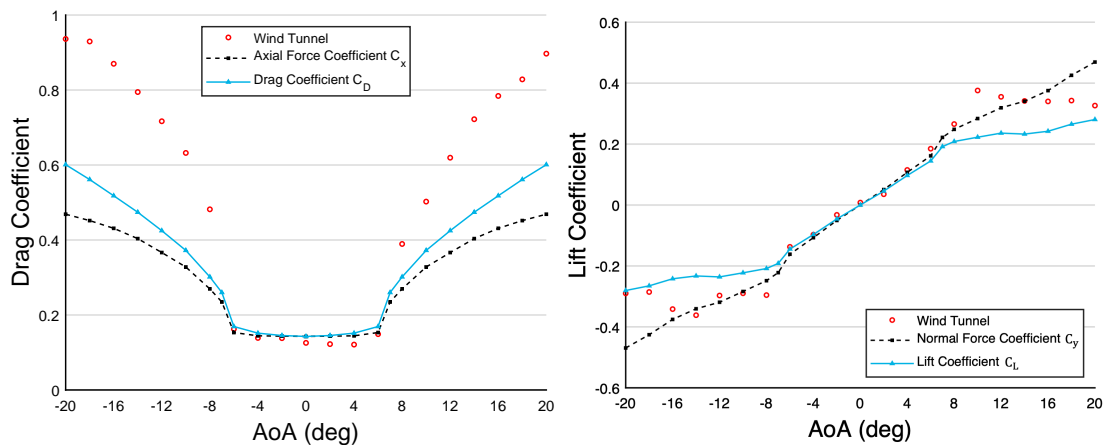


Figure 10.3: Wind Tunnel experiments compared with numerical results for the Drag and Lift Force Coefficients as a function of the Angle of Attack (AoA), according to the representation of Fig. 3.14.

At the time of writing, it is unclear why both methods give such a different behavior in terms of drag and lift at angles of attack higher than 6 degrees. Investigations have to be continued to assess the role of the wind tunnel dimensions in the measurements. The upcoming arrival of a new wind tunnel at the Military Academy should encourage the research process of the coefficients and the influence of the walls on the measurement.

Remarkably, the results for the pitch moment coefficient (Fig.10.4) are much better than for the other coefficients (Fig.10.3), which is in this context the most important for the determination of the dynamic coefficients.

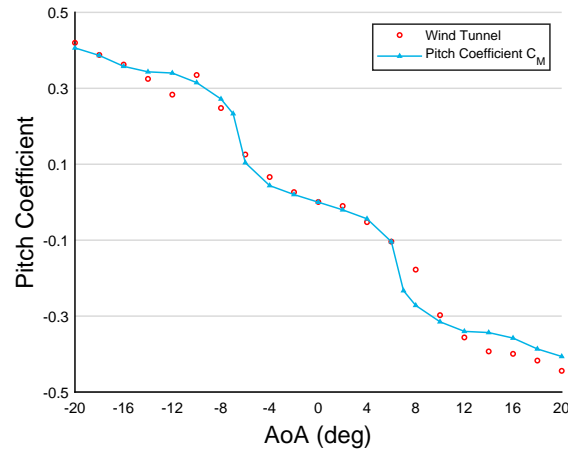


Figure 10.4: Wind Tunnel experiments compared with numerical results for the Pitch Moment Coefficient as a function of the Angle of Attack.

10.2.2 Dynamic Coefficients

Figures 10.5 and 10.6 show the history of the lift and pitch coefficients with respect to time and then with respect to the amplitude of the forced oscillation. Four calculations based on forced oscillations of frequencies varying between $k = 0.01$ and $k = 0.5$ have been performed to assess the sensitivity². The representation as a function of the number of timesteps indicates a certain delay of the projectile in starting its oscillatory movement, which is reduced as the initial oscillation speed decreases. From the second oscillation, the motion becomes periodic and it is then possible to represent the figure on the right and to calculate the pitch damping force or moment, based on the formulas 9.18 and 9.21 and the representation of figure 9.15.

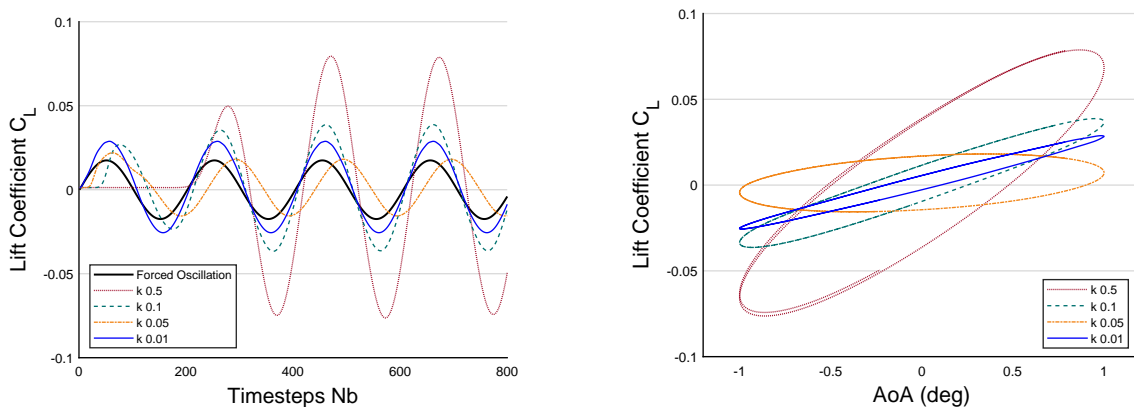


Figure 10.5: Lift coefficient response for different forced oscillation frequencies with $A = 1^\circ (= 0.017\text{rad})$.

² k being the reduced pitch frequency of the forced oscillation $\frac{\omega d}{2V}$ (Sec. 9.2.2)

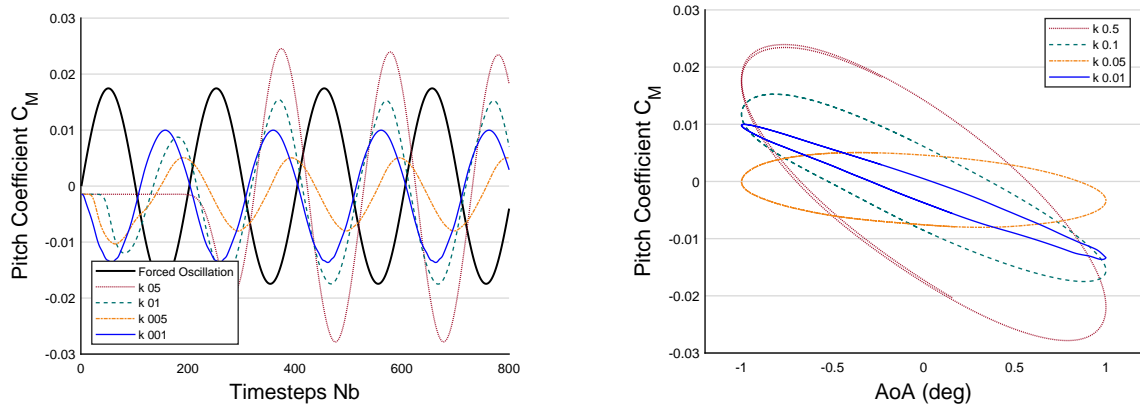


Figure 10.6: Pitch moment coefficient response for different forced oscillation frequencies with $A = 1^\circ (= 0.017\text{rad})$.

Finally, figure 10.7 summarizes the pitch damping force and moment coefficients as a function of k and indicates again an important dependency on the frequency. On the basis of the natural frequency calculated with an angle of 1° , k is equal to 0.07. The values of the coefficients are therefore taken as $(C_{N_{\dot{\alpha}}} + C_{N_q}) = 25$ and $(C_{M_{\dot{\alpha}}} + C_{M_q}) = -12^3$ for the trajectory calculations. These values have been taken constant given the short range of this projectile flying at largely subsonic speed.

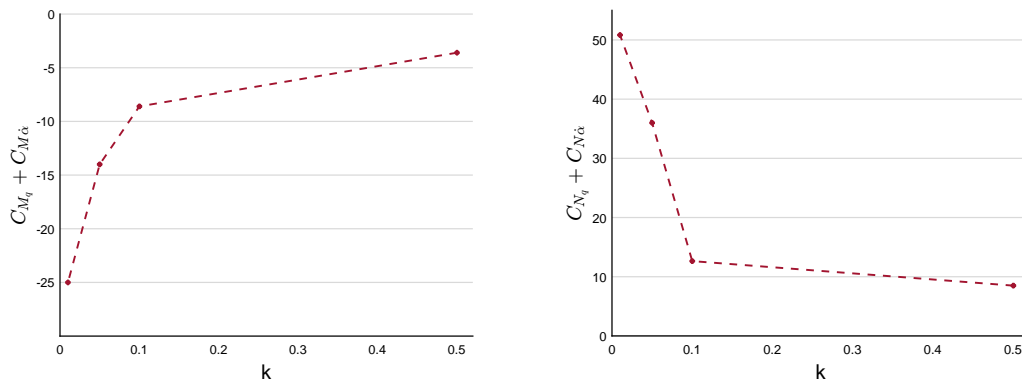


Figure 10.7: Pitch moment coefficient response for different forced oscillation frequencies k with $A = 1^\circ (= 0.017\text{rad})$ and $N = 200$ global iterations per oscillation.

³AeroFI gives a value of -10.

10.2.3 Boundary Layer Analysis

Despite the discrepancies for large angles observed between numerical and experimental results, both series feature a change in behavior between 6 and 8 degrees. At this stage, there is a break in the shape of these curves, pushing to investigate further the effects in the boundary layer.

Figure 10.8 is a collection of the different results obtained at 0° . The upper graph from the numerical simulations shows the pressure and skin friction coefficients along the intersection of the upper body with a plane collocated with a pair of fins. The projectiles at the bottom of the figure are the IRT (up) and oil (down) visualizations taken in the wind tunnel.

The flow is observed from left to right. On the IRT image the areas of lower temperature coincide with blue color while the regions of higher temperatures are red. Reynold's analogy relates the convective heat transfer in the boundary layer from the heated wall with the momentum transfer (i.e. the skin friction coefficient). Hence a thermogram bears the indicators of events occurring in the boundary layer and having an impact on its convective properties. A separation bubble is noticeable from the oil visualization on the front of the cylindrical part of the nose as well as on the front of the fins, at the leading edge. The fore separation bubble is clearly visible on the IRT image whereas the bubbles on the front of the fins are much less obvious because of the thickness of the fins and the resulting faster cooling. These observations are confirmed by the skin friction distribution which becomes negative due to the recirculating flow.

As surface pressure is generally a good indicator of separation, the separation bubbles are confirmed on the upper graphic by a plateau in the pressure coefficient distribution. In this case it results in a continuing low-pressure zone and an area generating potentially more drag.

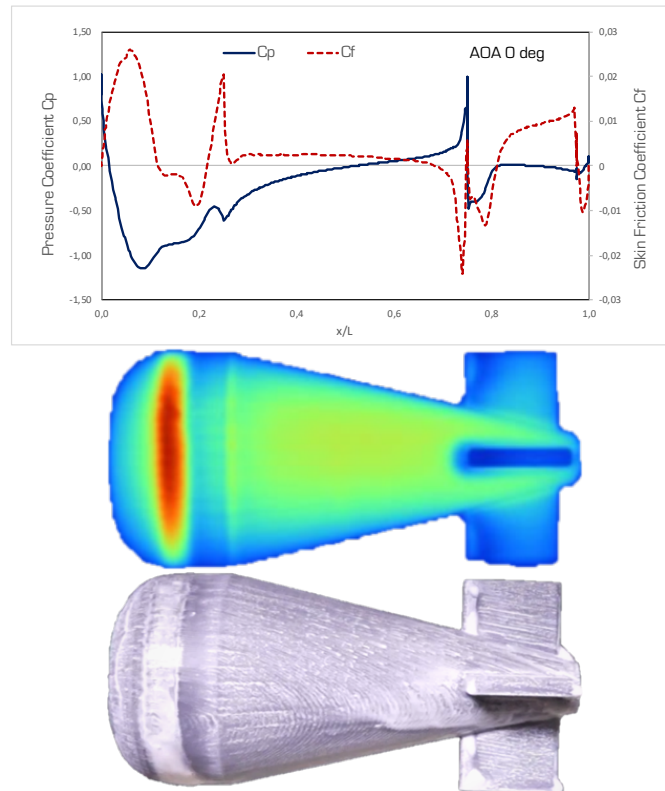


Figure 10.8: Pressure and Skin Friction Coefficients along the projectile for comparison with experimental visualizations at 0° . Lower temperature in blue and higher temperatures in red.

When we observe the evolution of the c_p - and c_f -curves between 4 and 10 degrees, as shown in figure 10.9, we clearly observe a change of evolution between 6 and 8 degrees that has an influence on the force coefficients from figure 10.3 and 10.4. In figure 10.9, the exposed (windward) side and unexposed (leeward) side are respectively shown on the left-hand and right-hand columns. For each angle the skin friction and pressure coefficient distributions are shown together with the corresponding thermogram. The flow on the exposed side at 4° bears also a flow-induced laminar separation bubble that is located as in the 0° -case. The evolution of the pressure and skin friction on the exposed side is similar to that of the symmetrical 0° -case but for the incipient separation at the junction between the cylindrical part and the cone section which is well attached in the CFD-results whereas the IRT-image wears the traces of separation at the junction. The flow on the unexposed side results in the same flow-induced laminar separation and consequent recirculation bubble although downstream of the reattachment point on the cylindrical part, the flow now separates again due to the junction. The separated flow does not reattach but it does not result at this angle in a significant low-pressure zone on the leeward side.

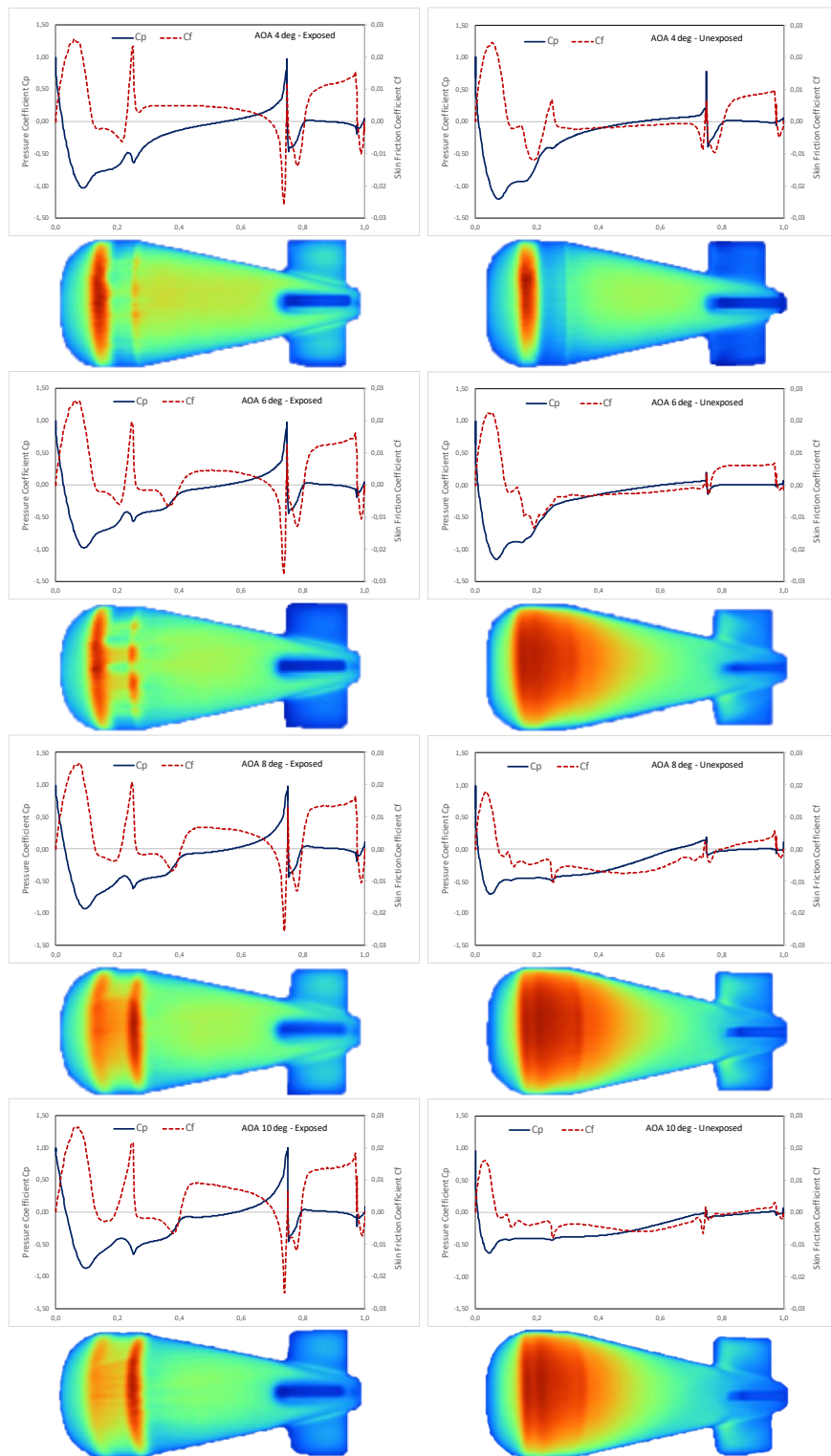


Figure 10.9: Pressure and skin friction coefficients along the exposed (windward) and unexposed (leeward) sides for different angles of attack (4, 6, 8 and 10 degrees) together with the corresponding IRT-images.

At 6° , the flow differs significantly from the 4° -case in that a second recirculation bubble forms downstream of the first reattachment. The fore recirculation bubble results from laminar separation located along the cylindrical part of the body where the adverse pressure gradient is steep. The second bubble is wall-induced in nature since the flow separates at the junction of the cylindrical body with the cone section on the exposed side. The flow later reattaches on the cone section although this is more difficult to see from the thermograms because of the turbulent character of the whole flow in that zone. On the unexposed side, the flow separates along the cylindrical part due to pressure-induced laminar separation and remains separated. This results in a low-pressure zone on the cone section that affects the drag coefficient.

At higher angles (8° and 10°), the exposed side features the same successive flow-induced and wall-induced recirculation bubbles. The pressure and skin friction distributions are hardly impacted by the change in angle of attack. The high drag coefficients found in figure 10.3 for these angles originate from the axial extent of the low-pressure zone on the cone section of the unexposed side. This zone differs significantly from the 6° -case both in its extent and its magnitude.

10.3 Trajectory Computations: PMM versus 6-DOF

The problem of the projectile orientation at impact was emphasized in the introduction to this chapter. This orientation is directly linked to the pitch damping moment, but especially to the type of initial perturbations encountered. A comparative calculation is performed for several ranges, considering first no initial perturbations. The results are shown in figure 10.10 for three angles of elevation: $QE = 2^\circ$, $QE = 5^\circ$ and $QE = 10^\circ$. The comparison between the 6DoF and the PMM indicates no significant difference in range up to 150m. After that, the deviation becomes non-negligible but given the application, higher ranges are not really expected...

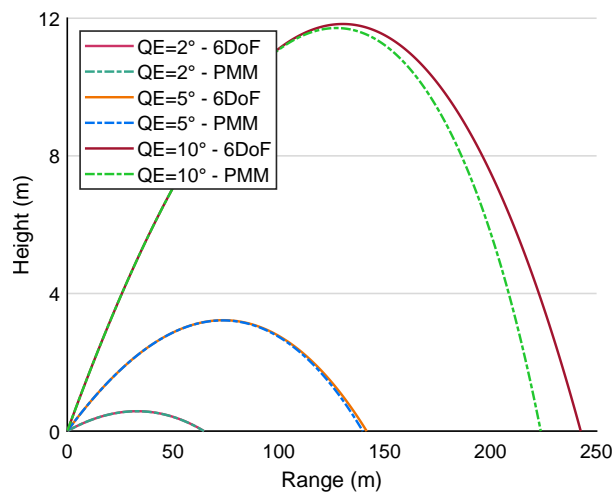


Figure 10.10: PMM vs 6DoF comparison for three elevation angles QE and no initial perturbations.

Nevertheless, the difficulty inherent to this type of application is not so much the projectile itself, but rather the control of the launching conditions. Laboratory experiments with a basic pneumatic assembly have been carried out to try to quantify the dispersion (Fig. 10.11), and several factors immediately alter these launching conditions. Since this projectile has fins, a smooth tube was used, with the addition of a sabot at the rear to provide closure in the tube and a good propulsion behind the projectile. However, the obturation is not guaranteed as with a standard projectile, generating oscillations in the tube and immediately at the exit. Afterwards, the presence of the sabot, which disengages from the projectile in flight (Fig. 10.12), also generates angular perturbations on the trajectory of the projectile. These observations therefore lead to focus more on the optimization of the launcher than on the projectile itself.

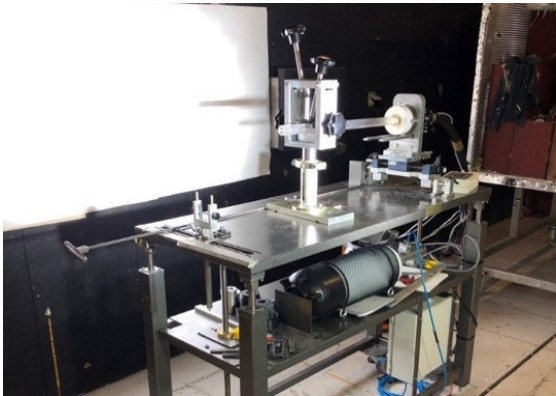


Figure 10.11: Pneumatic launcher with smooth barrel cal 12.

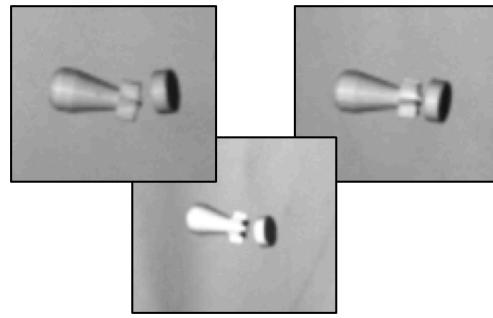


Figure 10.12: Separation of the sabot behind the projectile at the tube exit.

To translate this numerically, figure 10.13 illustrates trajectories with the same initial velocity ($MV = 100m/s$), the same tube inclination angle ($QE = 2^\circ$) and various initial perturbations which remain in quite reasonable order of magnitudes. We realize with the high dispersion in height and in drift that the quality of the trajectory model finally takes second place in relation to the launching conditions.

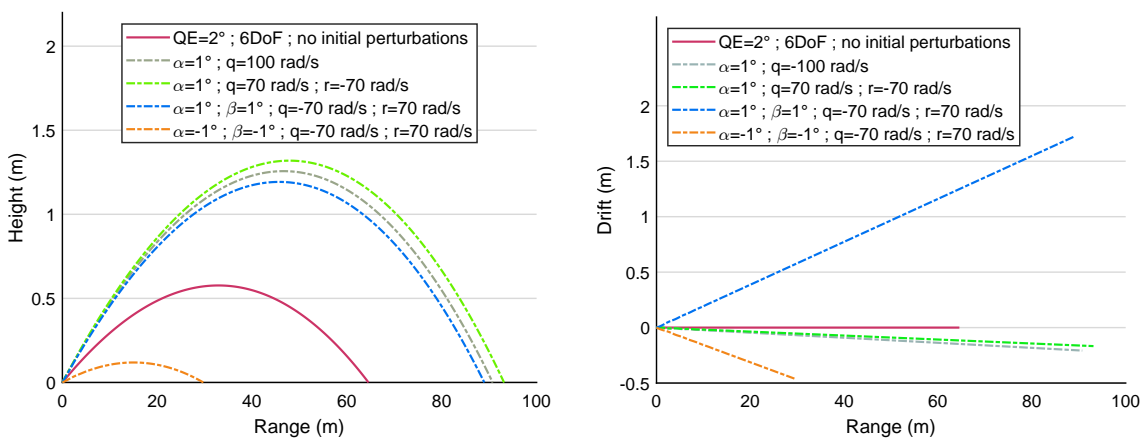


Figure 10.13: PMM vs 6DoF comparison for three elevation angles QE and no initial perturbations.

This being mentioned, figure 10.14 shows the pitch and yaw angles for the extreme configuration in terms of initial conditions represented in figure 10.13 and it turns out that despite the perturbations and the large deviation angles, the projectile is able to recover its stability, reflecting a good design.

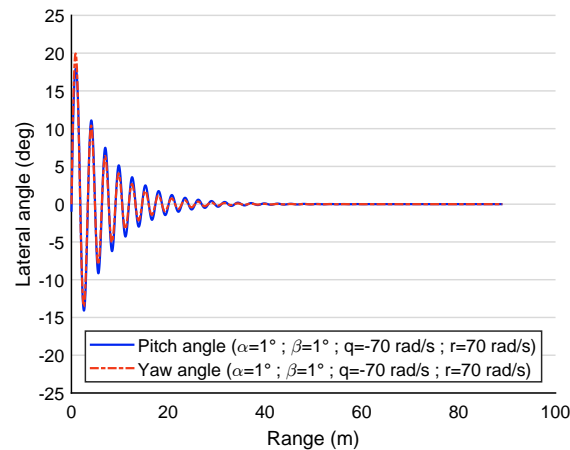


Figure 10.14: Pitch and yaw angles for extreme initial conditions.

10.4 Conclusion on the non-lethal field...

In addition to determining the static and dynamic aerodynamic coefficients required to calculate the projectile trajectory, a detailed analysis and numerical/experimental comparison of the boundary layer was carried out at low velocity. This analysis allows a better understanding of how the positioning of a complex geometry influences the generation of pressure and viscous forces applied to the projectile. In a rather encouraging way, flow-induced (adverse pressure-gradient) and wall-induced (junction between cylindrical part and cone section) separation are commonly predicted by the calculations and identified on the wind tunnel visualizations. Those distinct behaviors explain the sudden drag jump, and the break in the lift and pitch curves when the angle of attack grows.

The low speed range inherent to non-lethal projectiles, which is not often addressed in exterior ballistics studies, has been highlighted and deserves further investigation in terms of control of launch conditions in order to optimize fire control and to guarantee the expected impact conditions. The added value of a 6-DoF model over a PMM was analyzed and seems negligible in height and range as long as the launch conditions are not disrupted. But the slightest destabilization makes the PMM inappropriate and knowledge of the pitch damping coefficient becomes necessary to optimize stabilization following minor disturbances, even at these low velocities.

Chapter 11

Precision Ammunition & Transonic Domain

This chapter is both a revision and an extension of the following publication:

- V. de Briey, A. Moumen, B.G. Marinus, M.Pirlot “Influence of the Transonic Crossing for Precision Ammunition”. 31th International Symposium on Ballistics, Hyderabad (IN). 2019. doi:[10.12783/ballistics2019/33109](https://doi.org/10.12783/ballistics2019/33109) [25].

Although trajectography for small-caliber and long-range projectiles in particular, seems to be mastered since a long time, it is not totally mastered within transonic or even subsonic range. The trend for precision ammunition is always to hit a smaller target with a higher probability at an ever-increasing distance. The last two decades revealed many new calibers, new weapon features and a large number of trajectory software to reach this goal. However, there is no unanimous criterion yet to define properly and scientifically why a projectile is better than another one. The existing software are often drag based (Sec. 3.8), with a fitting established to match real firing, but they do not account specifically for the sharp changes in aerodynamic forces when the projectiles reach the transonic zone. Nonetheless, the transonic domain has to be crossed by precision ammunition when reaching high operational ranges with the classical propulsion and its inherent muzzle velocities.

The transonic domain has raised many questions since the appearance of flying objects at high velocities, and despite numerous studies on the subject, even in ballistics [145, 196, 198, 199, 216], it still conceals many mysteries. Some aeroballistic articles define the transonic regime as a region of critical aerodynamic behavior where aerodynamic coefficients have been found to increase by as much as 100% for classical small caliber ammunition [164, 195]. Many practical recipes have proved their worth in the field, but the added value of flow analysis via CFD for more systematic predictions of trajectories is not to be trivialized, certainly in a context where adjustments during real firings tend to be reduced to a minimum. It is obvious that internal and intermediate ballistics (quality and quantity of powder, quality and dimensions of casings, muzzle accessories, etc...) have a huge influence on the first part of the flight and so on the precision (reproducibility) of the shots that must cross the transonic domain, but the present chapter focuses on the intrinsic aerodynamic quality of projectiles.

The .338 inch Lapua Magnum projectile¹, in operational use with Belgian Defense snipers, will be here specifically considered. Depending on the brand, those .338 projectiles become subsonic at ranges varying between 1200 and 1400m, but the hit expectation for this weapon system is around 1600m on a human target. For the benchmark of these munitions, two aspects are above all important: the evolution of drag in the different regimes and the stability in flight. It is clear that no projectile will be able to present a C_{D_0} curve without a significant "drop" around Mach 1, but some geometries allow a smoother transition.

The geometrical specificity's of these "sniper" projectiles in the velocity range from Mach 1.2 down to Mach 0.8 will be aerodynamically analyzed using CFD, to better perceive how these projectiles do behave through the transonic domain. Since numerical simulations have limited value without an experimental basis, this part presents also by means of relatively new density sensitive visualization techniques (Schlieren + Background Oriented Schlieren), the quantification of the density around the projectile as well as the various shocks propagating in the transonic domain.

¹Caliber .338-in. = 8.58 mm

11.1 Methodology

Three types of projectiles in caliber .338 inch were studied.

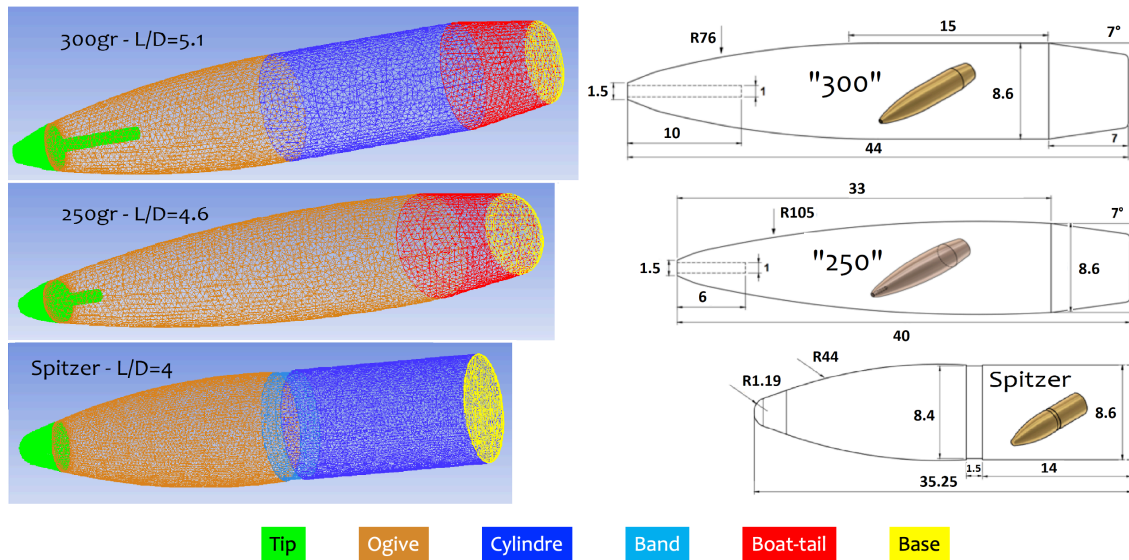


Figure 11.1: Dimensions of the three configurations studied in .338 in - all dimensions in mm.

The two first geometries in figure 11.1 are Hollow Point Boat-tail (HPBT) projectiles, specially developed for long range shooting, used in precision weapons, for marksmen and snipers. The "300 gr."² projectile is a geometry quite identical to the one found on the market, with a discontinuity between the ogive and the cylindrical part, while the "250 gr."³ geometry has been voluntarily deprived of its cylindrical part and is thus constituted of an ogive and then directly of a boat-tail. This difference will become important when comparing experimental and numerical images. They are both provided with a boat tail of the same dimensions, as well as an open tip at the nose, hence the name **Hollow Point** (See Box 11.1). The **Spitzer** bullet is mainly used for hunting. It does not have any slanted end and has a central groove between the ogive and the cylindrical part.

Except for the hole at the nose of the HPBT projectiles, the three configurations were considered as plain and monolithic for the calculation of the position of the center of gravity and the main moments of inertia.

²300 gr. (grains) \approx 19.4 g.

³250 gr. (grains) \approx 16.2 g.

Box 11.1: The Hollow Point controversy...

Hollow Point (HP) projectiles are part of the "**dum-dum**" class of projectiles. Dum-Dum was a town in Calcutta where the British Army had an ammunition factory where they developed in 1897 a bullet with a round nose with a jacket of copper-nickel covering a lead core, with the exception of a hole on the tip where the lead was bare. The goal of these projectiles was to cause a maximum of damage due to their size and the fact that they would fragment and mushroom inside the body. This ammunition caused so much human damage that it was considered as inhuman by the Hague Convention of 1899 which prohibited any projectile causing "superfluous injury or unnecessary suffering"*. To this day, all projectiles designed to fragment or to deform under the name "Hollow Point" or "dum-dum" are prohibited in the armed forces (only **Full Metal Jacket** projectiles may be used). Since then, conflicts have changed, and so has the discriminating performance of projectiles, but armed forces still cannot use Hollow Point projectiles, even when they are constructed with the intent to deform to avoid over-penetration. These projectiles are therefore mainly used for hunting and by police forces.



The Hollow Point Boat Tail projectiles discussed in this chapter are so named, not because they have the vocation to be deformed, but because of the method by which they are manufactured: the jacket of the projectile is placed from back to front and the tip is meticulously cut, leaving a very small hole, hence the name. This manufacturing process allows a better control of the regularity of the jacket between each projectile, increasing the quality of the ammunition, often referred as "match grade ammunition" for marksmen. However, when the first ammunition bearing the name HPBT appeared for snipers in the Defense inventories, the legal advisers reacted directly and the procedures are still ongoing to justify this equivocal and miscalculated appellation.

*www.weaponslaw.org

11.1.1 Experimental Approach

In order to support the numerical simulation results, the flow field around the different projectiles flying at various velocities in the transonic zone was visualized using two density sensitive visualization techniques during real firings, namely the Schlieren and the Background-Oriented Schlieren (BOS) techniques [96, 146, 182, 243, 249].

Both techniques exploit the light ray deflection passing through the refracting index gradient associated with a density gradient. The Schlieren technique has the advantage of high sensitivity and real time results, i.e. no need to post-process the obtained images to retrieve the information. On the other hand, this method suffers from several drawbacks such as the necessity of costly optical instruments (mirrors, lenses...), the difficulty to properly align the set-up, the optical issues such as the chromatic aberration, and the fact that only a qualitative study can be conducted with a limited field of view. To overcome these disadvantages, the BOS technique is used in combination with the classical technique. Indeed, this relatively new visualization technique is a quantitative and cost-effective diagnostic tool. The BOS set-up is composed of a high-speed camera that focuses sharply on a natural or synthetic background [146, 182]. Then, at least two images of this background without and with the flow in-between the camera and the background are recorded.

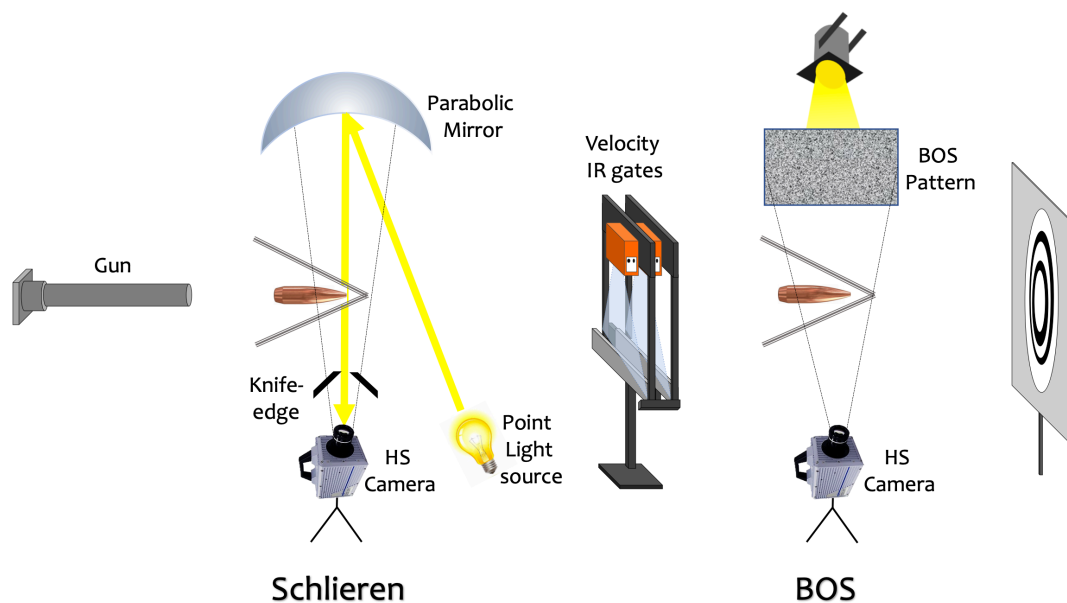


Figure 11.2: Experimental setup for the flow visualization around the projectile: Classical Schlieren technique on the left, BOS technique on the right.

The 'flow-on' image, as the projectile passes within the camera field of view, will be artificially distorted. This pixel shift (distortion) will be evaluated in comparison with the non-disturbed image, usually using a cross correlation or an Optical-Flow algorithm. These evaluation results in two displacement maps, namely the horizontal and vertical displacements relatives to the first derivative of the refraction index in the horizontal direction $\partial\rho/\partial x$ and in the vertical direction $\partial\rho/\partial y$ [249]. The experimental set-up implemented for those tests is shown in figure 11.2. Two Photron FASTCAM SA-X2 cameras were equipped with two Nikon lenses with a focal length $f = 135$ mm for the BOS part, sharply focusing on the background, and $f = 200$ mm for the classical Schlieren, focusing on the projectile trajectory. Both cameras were running at a frame rate of 15 000 frame/s and 4.2 μs exposure time. The double-pass Schlieren system is also composed of a point light source, a lens and a parabolic mirror. For the BOS, the optimized pattern was printed on a transparent film and was backlighted and placed at a distance from the projectile trajectory equal to 1.3m. The post-processing tool used during this experience was PIVLab[243].

BOS research is also in progress to study the effects of intermediate ballistics on the dynamics of the projectile at the muzzle [153].

11.1.2 Computational Approach

The CFD methodology was validated according to the investigations carried out in chapter 8 on the SOCBT geometry. The final meshes used to visualize the development of the shock waves for the steady RANS simulations of the full projectile in free-air consists typically of 4 million elements with a prismatic boundary layer comprising 50 layers resulting in an average value for y^+ of 1 along the adiabatic no-slip walls. This number of elements is significant for such simple geometries due to the high refinement outside the boundary layer for flow visualization. A comparison of aerodynamic coefficients was also done for coarser meshes to assess the necessity of the fine mesh resolution. In order to capture the jump in coefficients in the transonic zone, sweep computations were used, with 40 inner iterations to achieve a convergence of at least 2 orders of magnitude of the normalized residuals. Zero-yaw drag results for HPBT geometries were compared with firing experiments and the different static coefficients (drag, lift and pitch) were calculated at 3° AoA as a function of Mach. For the flow visualization, density gradient contours (numerical Schlieren) were created to complete the information of the Mach contours. In order to obtain those gradient contours it is necessary to keep the temporary solver memory from being freed, with the aim to detect density jumps, as well as for the BOS method. The first results are encouraging and have brought to light the possibility to quantify the density jumps of very precise phenomena visualized by the BOS.

11.2 Results

11.2.1 Flow Visualization

The images presented below (Fig.11.3-11.7) are presented by decreasing speeds, all geometries combined. For each speed we can see on the left the experimental visualizations as well as the CFD visualizations on the right. In the present phase of the study, shocks dissipate more quickly on numerical images, but this is due to the mesh size, which should be even finer to allow the tracking of disturbances. We must therefore focus on the birth of phenomena close to the wall where the C_p are in good agreement with experiments and not on the dissipation. On all the images, we can see that the relative orientations of shocks and intensities of the density gradients at the different speeds are quite well respected between experiments and CFD. The narrow shock wave close to the tip is clearly observed, opening and moving away as the speed decreases. Similarly, the triangular expansion and shock system occurring at the connection of the boattail near Mach 1 are very well marked on the different numerical Schlieren and CFD (Fig. 11.5-11.6).

As underlined in the description of the projectiles, the projectile "250" from the simulations does not have a cylindrical part, and therefore no geometrical discontinuity with the front of the projectile. This explains why no expansion zone is visible on the CFD visualizations in figure 11.3, figure 11.5 and figure 11.6 compared to the experiments.

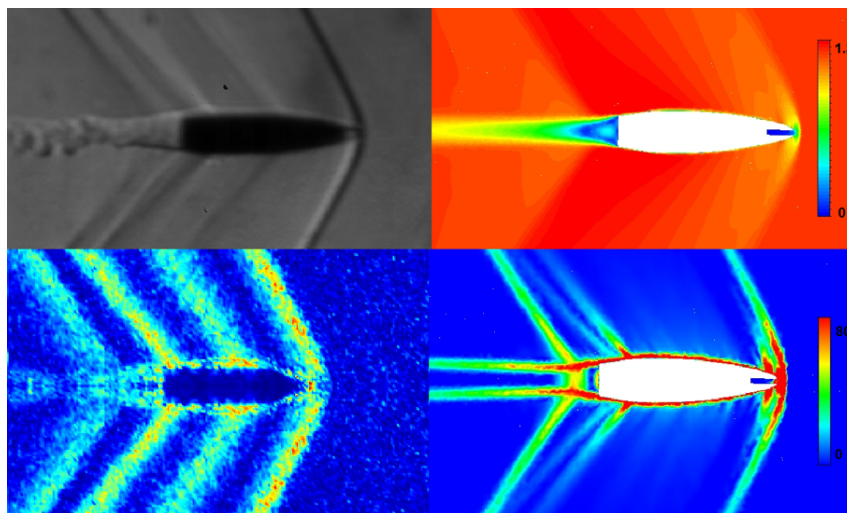


Figure 11.3: Projectile 250 at Mach 1.2: Experiments on the left (classical Schlieren at the top, BOS at the bottom), CFD contours on the right (Mach at the top, density gradient at the bottom).

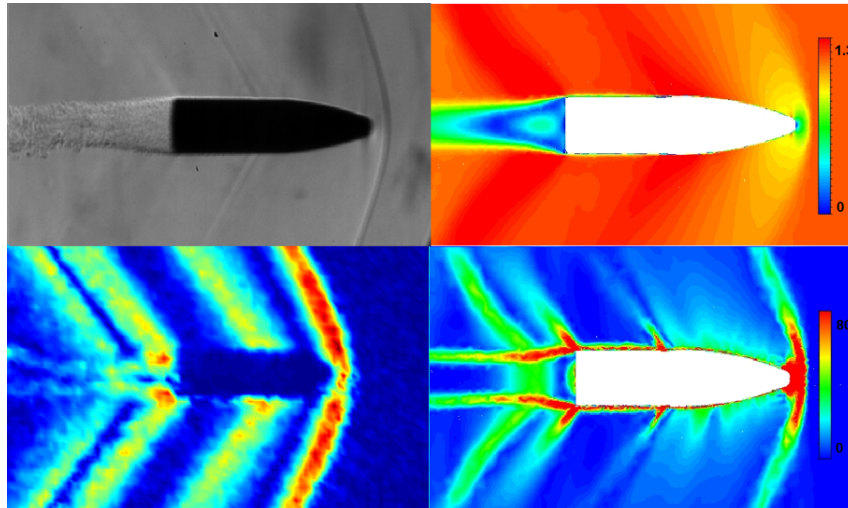


Figure 11.4: Spitzer projectile at Mach 1.15: Experiments on the left (classical Schlieren at the top, BOS at the bottom), CFD contours on the right (Mach at the top, density gradient at the bottom).

Figure 11.4 demonstrates the added value of numerical Schlieren if we are interested in the effect of the rotating band or any other indentation in the projectile. Indeed, the Mach contours do not show any macroscopic disturbance at the groove (pressure and conventional density profiles would return the same), whereas the numerical Schlieren as the experimental images mark this area and its extend beyond the immediate vicinity of the wall (as could wrongly be inferred from looking at the Mach contours solely).

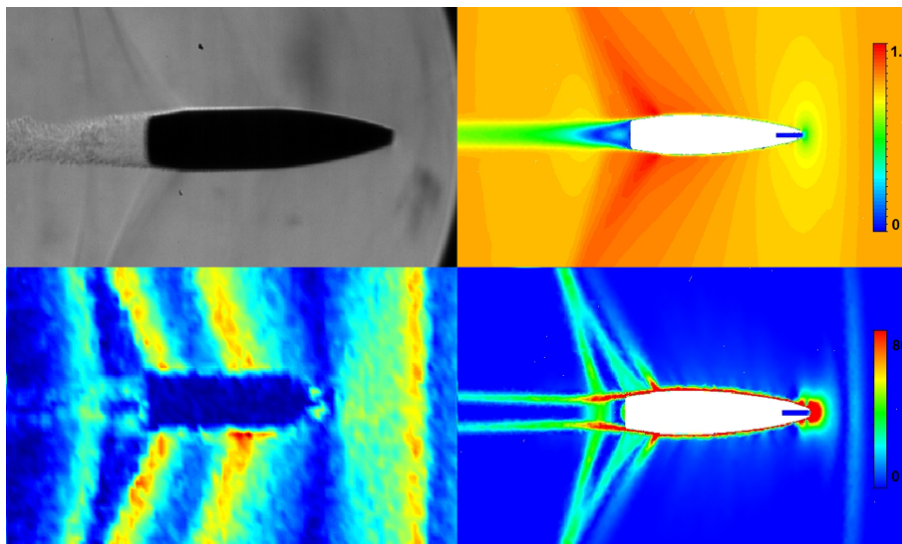


Figure 11.5: Projectile 250 at Mach 1.02: Experiments on the left (classical Schlieren at the top, BOS at the bottom), CFD contours on the right (Mach at the top, density gradient at the bottom).

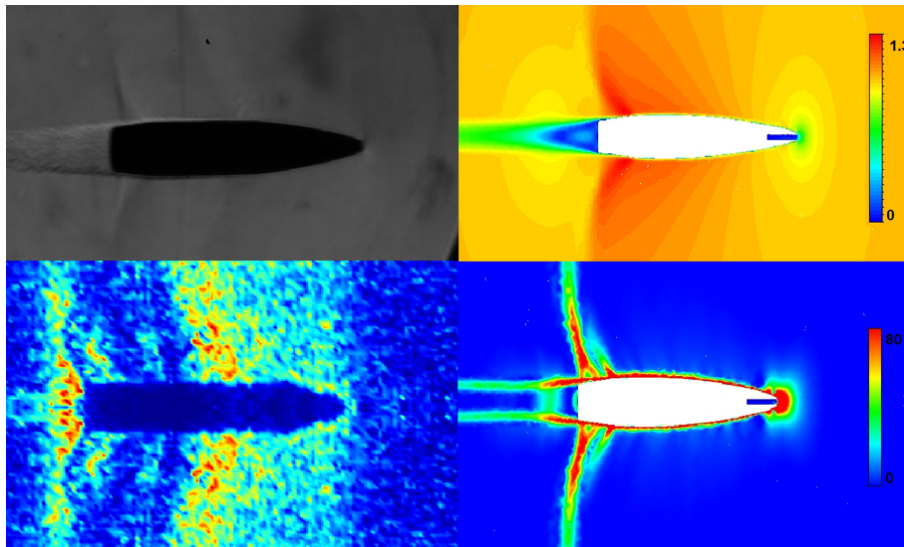


Figure 11.6: Projectile 250 at Mach 0.97: Experiments on the left (classical Schlieren at the top, BOS at the bottom), CFD contours on the right (Mach at the top, density gradient at the bottom).

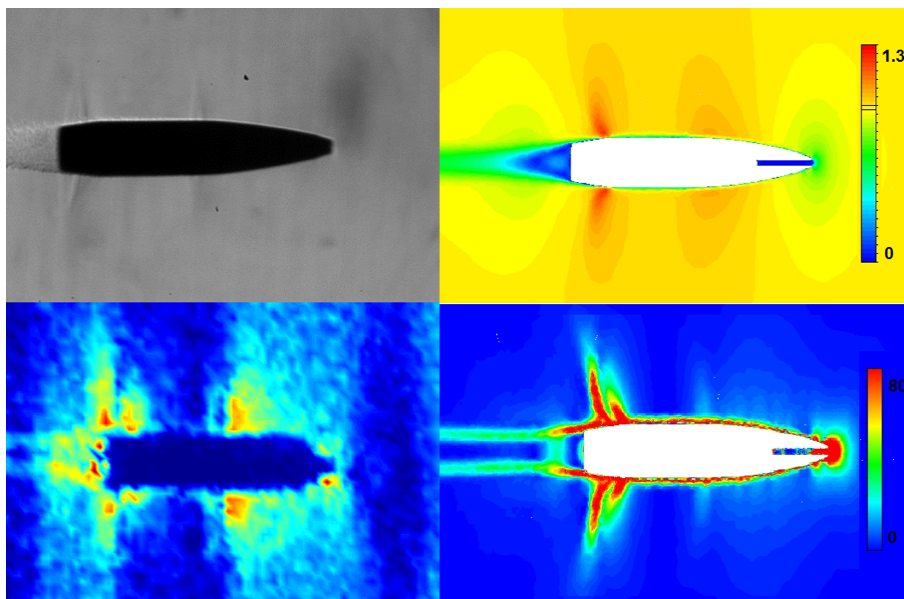


Figure 11.7: Projectile 300 at Mach 0.93: Experiments on the left (classical Schlieren at the top, BOS at the bottom), CFD contours on the right (Mach at the top, density gradient at the bottom).

An extensive study including CFD, wind tunnel and spark-range firings was done by the Army Research Laboratory [57, 217, 218, 259] to identify the influence of rifling grooves on different 5,56 mm projectiles in the supersonic domain. The conclusion of this research finally declared that the effort made to take the grooves in consideration experimentally and in CFD did not yield a significant improvement in that flight domain. Based on those results, further CFD investigations should however be continued in the transonic range, to assess the sensitivity of specific precision ammunition to the grooves in that regime.

In addition to the qualitative analysis that has just been presented, a quantification of the density near the projectile has been done by means of CFD and BOS technique (performed by Capt A. Moumen (ABAL) [154]). Figure 11.8 shows the CFD contour where the measurements were taken, while figure 11.9 shows the analogy obtained at the three distances. At the entrance of the transonic domain, where the shock waves are still very present, both techniques capture the same sudden changes in density, which naturally gives confidence in the simulation.



Figure 11.8: Numeric density contours with three parametric zones where the density was evaluated using the BOS technique on the .338-in. 300gr.-projectile.

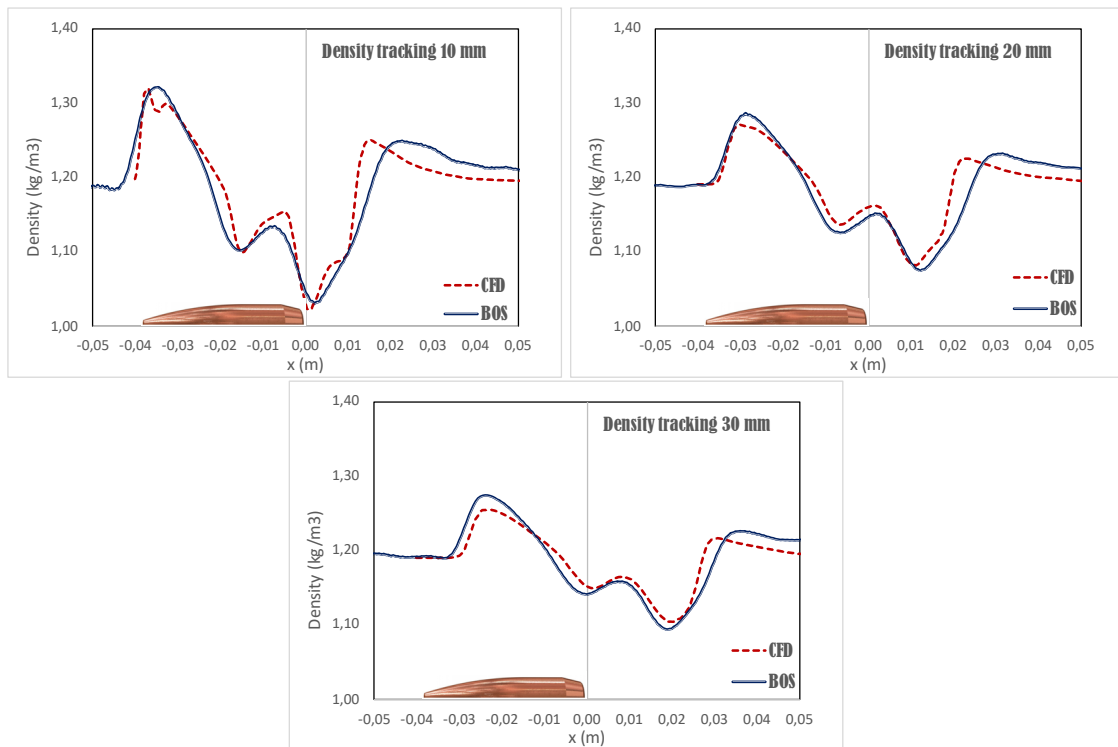


Figure 11.9: Density tracking at three distances from the 300 gr.-projectile wall.

11.2.2 Aerodynamic Coefficients

Zero-Yaw drag

Unlike experimental techniques, CFD allows to isolate the different parts of a body to study their respective contributions. This is a major asset in the development of new projectiles or in a benchmark analysis, to identify the elements that can cause more drag for instance, and improve the shape. This process is already done in large caliber for artillery [123] and is also developed in semi-empirical codes like McDrag [136]. The drag comparison for the .338-in. projectiles is shown in figures 11.10-11.13 where the drag is first given for the three configurations from figure 11.1. Experimental firing measurements (Box. 3.3) positively complement the numerical results for the 300 gr. and Spitzer projectiles. Drag is then compared in figure 11.11 for both HPBT projectiles with regard to the junction of the cylindrical part and the ogive, and the results are quite similar.

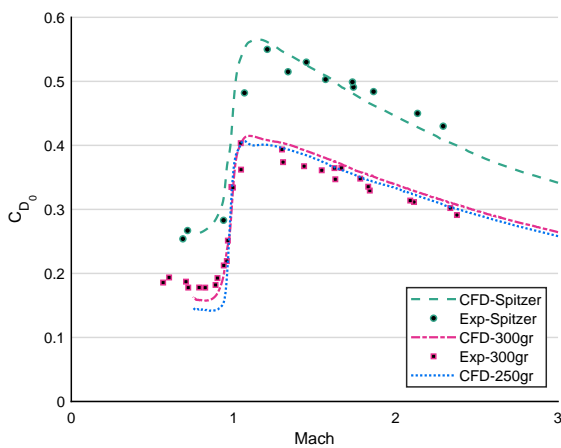


Figure 11.10: Total Zero Yaw Drag Coefficient for all geometries.

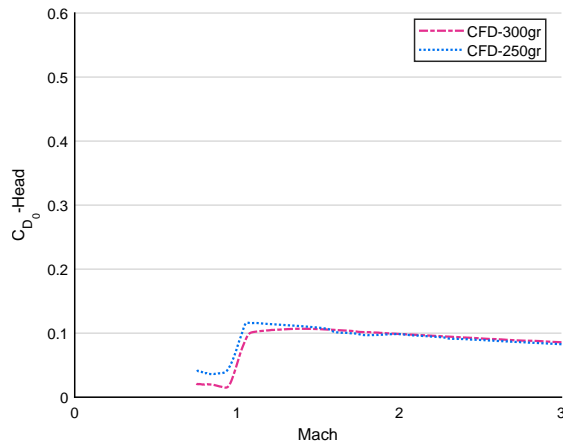


Figure 11.11: Body drag (Ogive+Cylinder) comparison between the 250 and 300 gr. projectiles.

At the tip, it is not surprising that the three results are similar in figure 11.12, the Spitzer projectile being slightly higher due to the somewhat larger surface area. The boat tail effect, however, is very clear in figure 11.13: it allows a significantly less abrupt separation and consequently a much lower drag.

A simulation with a 300 gr.-projectile was also performed with a closed and flat tip, and the results are totally equivalent at the drag level. This proves that this open-tip does not present at first sight any aerodynamic disadvantage for long-distance shooting. In general, if we compare the respective contributions we can see that the front of the projectile has less influence on the drag than the rear,

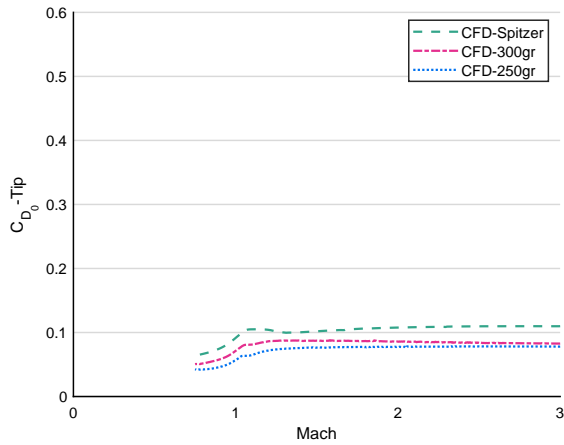


Figure 11.12: Tip drag for all geometries.

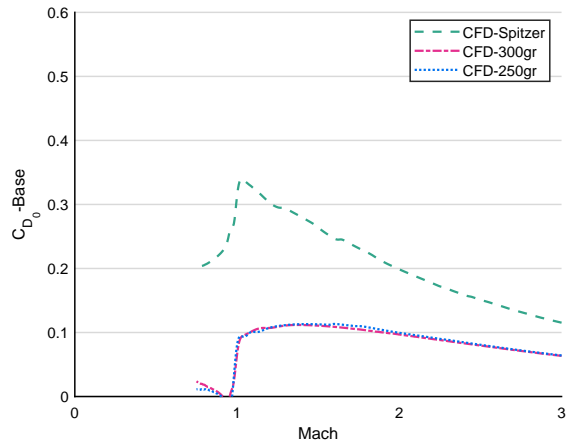


Figure 11.13: Base drag for all geometries.

because of the separation at the boattail. The entire profile development must therefore focus on the rear part, at least for flat-trajectory projectiles.

Other steady coefficients

Figures 11.14-11.15 compare respectively the lift and pitch coefficients for all three projectiles with steady (SS) and quasi-steady (Sweep) simulations, to observe the variations in the transonic domain. Due to its lower L/d ratio, the Spitzer projectile has a lower pitch coefficient, implying (all other parameters remaining constant) a better gyroscopic stability.

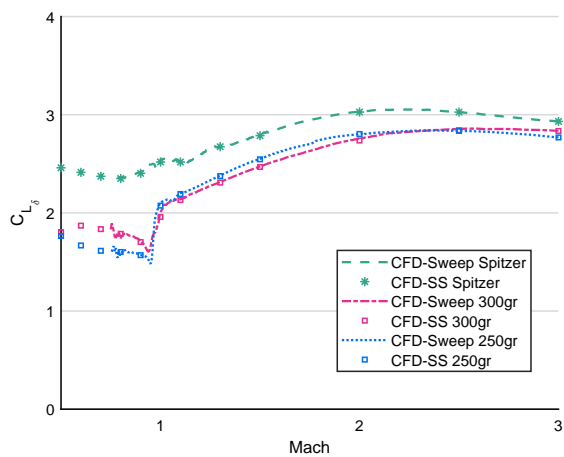


Figure 11.14: Lift coefficient for all geometries.

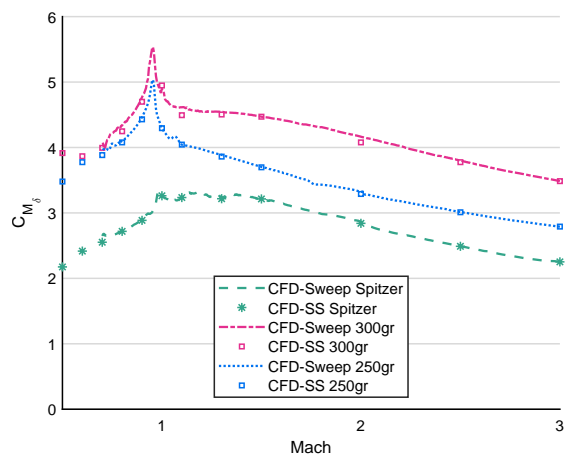


Figure 11.15: Pitch moment coefficient for all geometries.

Dynamic coefficients

The spin damping and Magnus moment coefficients are shown in figures 11.16-11.17. Chapter 9 had expressed some limitations on the determination of the Magnus moment with steady-state methods, nevertheless it is rather the order of magnitude that is evaluated here in a relative way between the different projectiles. As for the Spinner configuration (Fig.9.12), the velocity components in the boundary layer tend to change in the transonic zone, resulting in negative coefficient values.

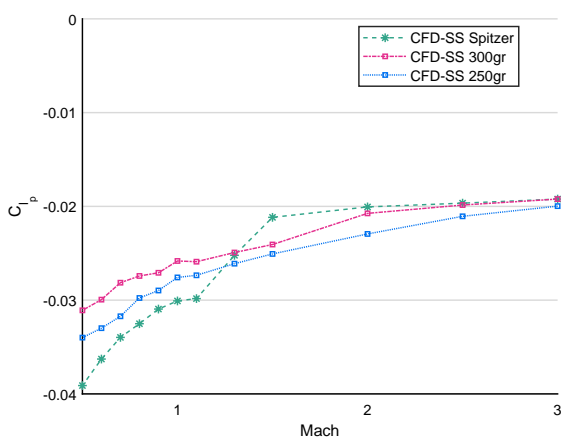


Figure 11.16: Spin damping coefficient for all geometries.

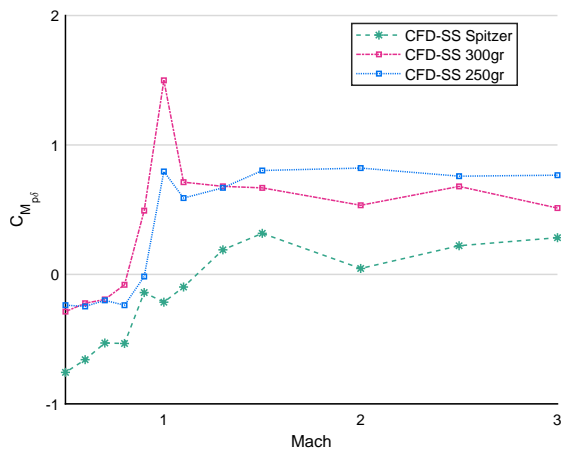


Figure 11.17: Magnus moment coefficient for all geometries.

Values for the pitch damping coefficients are given in table 11.2 dealing with stability. These values have been determined for a value of $k=0.07$, estimated on the basis of the 300 gr. projectile characteristics, but have not been subjected to sensitivity analysis. They will be directly confronted with the conclusions obtained in the stability analysis.

11.3 Stability Analysis

As for the non-lethal application, one may wonder what is the added value of a complex model where it is common practice to use a model requiring little input data... However, rather than comparing trajectories where "random" initial conditions would inevitably generate deviations, a comparative stability study of the projectiles is carried out below, on the basis of the linear theory presented in section 3.6 (Eq. 3.104-3.107) and resumed in chapter 5 (Eq. 5.5-5.10) dealing with

stability. CFD data determined in the previous section⁴ were used for analysis. A comparison is made for the Spitzer and 300 gr. projectiles (Tab. 11.1) at three critical speeds: Mach 2.5 for the muzzle velocity and then at Mach 1.1 and 0.9 for the borders of the transonic domain.

Table 11.1: Geometric data allowing the stability analysis ($T_w = 27.6$ cal/turn).

	Spitzer	300 gr.
m (kg)	0.0162	0.0194
I_x (kg.m ²)	$1.2 E^{-7}$	$1.4 E^{-7}$
I_y (kg.m ²)	$1.17 E^{-6}$	$1.98 E^{-6}$
L/d	4.1	5.1

Table 11.2 gives for the three Mach Numbers, the determined coefficients as well as the gyroscopic and dynamic stability factors. In chapter 5, two conditions were mentioned, namely $S_g > 1$ to guarantee gyroscopic stability and $S_g > 1/(S_d(2 - S_d))$ for dynamic stability ($0 < S_d < 2$). While the first condition is observed in all cases, dynamic stability is lacking in two cases at transonic speeds. This is also illustrated in figure 11.18, where the pitch damping moment coefficient values calculated with CFD are given, together with the allowable stability margins calculated using the linear theory. For the 300 gr. projectile at Mach 1.1 and the Spitzer projectile at Mach 0.9, the computed values are outside the theoretical stability range. Moreover, we can see here the interaction in stability between the Magnus moment and the pitch damping moment. When $C_{M_{p\delta}}$ is negative (values in red for the Spitzer projectile in table 11.2), the admissible range of $(C_{M_q} + C_{M\dot{\alpha}})$ to guarantee the dynamic stability is restricted and gets closer to zero. Conversely, as at Mach 1.1, the Magnus coefficient is still high for the 300 gr. projectile, its stability margin is more negative in terms of pitch damping coefficient.

In addition to taking a step back from the linear theory and its many simplifications, two in-depth analyses should nevertheless be followed if a concrete situation arose: perform the sensitivity study on k for transonic velocities specifically, by separating the two projectiles to have a confirmation on the $(C_{M_q} + C_{M\dot{\alpha}})$ values, and refine the mesh in the boundary layer to have better predictions of the Magnus moment which directly affects the stability calculation. If the trends are confirmed, this reinforces the instability problem in the transonic domain but will give direct indications on how to reduce them by adapting the design with respect to the inappropriate coefficients. It is also necessary to specify that the ro-

⁴Even if the approach is quantified, it remains valid only for monolithic projectiles.

tation speed p in the present cases is considered with a constant ratio $\frac{pd}{2V}$. Yet, with the use of the 6DoF model, this speed would have been proportionally reduced by the spin damping coefficient C_{l_p} , not considered here for a more "conceptual" analysis.

Table 11.2: Stability factors computations based on aerodynamic coefficients calculated using CFD.

	Ma 2.5		Ma 1.1		Ma 0.9	
v (m/s)	850		370		300	
p (rad/s)	22500		9800		8000	
	Spitzer	300 gr.	Spitzer	300 gr.	Spitzer	300 gr.
C_D	0.4	0.3	0.6	0.4	0.25	0.18
$C_{L\delta}$	3	2.8	2.5	2.1	2.4	1.7
$C_{M\delta}$	2.5	3.8	3.2	4.6	3	4.7
$C_{M_{p\delta}}$	0.2	0.7	-0.1	0.7	-0.1	0.5
$C_{M_q} + C_{M\dot{\alpha}}$	-26	-18	-6	-4	-11	-20
S_g	2.9	1.53	2.27	1.27	2.41	1.24
S_d	0.34	1.28	0.37	4.03	0.21	0.85
$1/S_d(2 - S_d)$	1.76	1.09	1.64	-0.12	2.66	1.02
SG_{Miller}	3.5	2.2	2.64	1.68	2.48	1.58

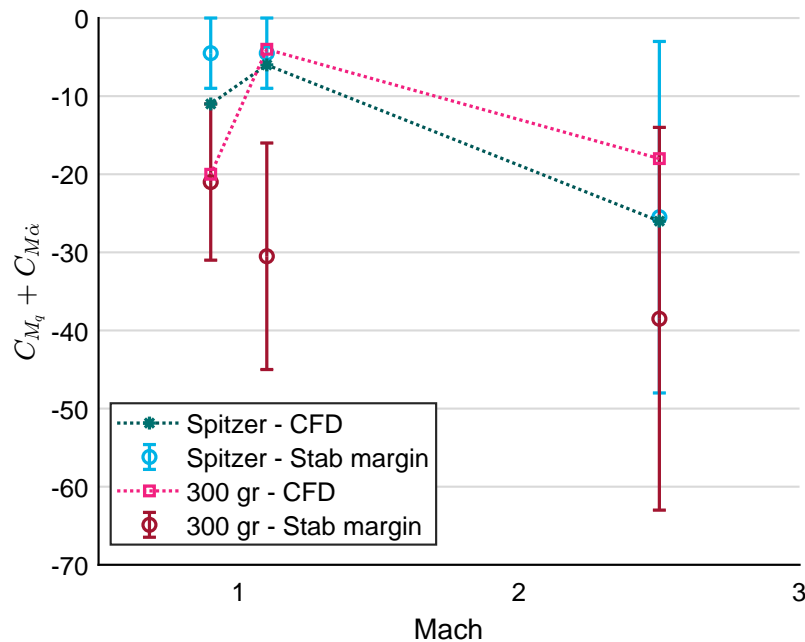


Figure 11.18: Pitch Damping coefficient with stability margins based on linear analysis.

The parameter SG_{Miller} listed in table 11.2 is, like the BC in section 3.8, a simple way to evaluate gyroscopic stability without having to determine aerodynamic coefficients [143]. Equation 11.1⁵ is somehow an empirical approximation of the stability factor S_g (Eq. 5.5) "calibrated" for a pitch coefficient $C_{M\delta} = 2.5$. According to the calculations made for the different spin-stabilized projectiles discussed so far, this is indeed a recurrent order of magnitude. The values obtained in table 11.2 give an idea of the validity of this formula since the results are always slightly higher than what S_g gives but the trends are correctly reproduced for both projectiles through the different velocities.

$$SG_{Miller} = \frac{5.58m}{Tw^2d^3\frac{L}{d}(1+(\frac{L}{d})^2)} \frac{\rho_{ICAO}}{\rho} Ma^{1/3} \quad (11.1)$$

11.4 Conclusion on long-range shooting...

The transonic domain has to be crossed by precision ammunition when reaching high operational ranges with the classical propulsion we know. Using experimental methods and literature, the aim of this study was to calibrate numerical models on long-range projectiles to capture transonic phenomena occurring towards some segments of the flight, both qualitatively and quantitatively. Three geometries were analysed in more detail, qualitatively by means of Schlieren and Background-Oriented Schlieren (BOS) visualizations and quantitatively by means of the BOS and CFD techniques, with the possibility to compare different projectiles on the basis of the drag footprint "by parts" and their stability by means of the different stability factors evaluated.

These promising first results have brought to light several numerical challenges. The sensitivity of the geometries to be prone to flow separation will be further investigated, to give an idea of the maximum angle of attack the projectile can perform without generating excessive disturbances in the boundary layer. This would be of direct interest in studying the stability and feasibility of still longer distance trajectory projectiles, where the angle of attack will inevitably increase.

⁵The given equation is to be used with SI units. The original equation is given for grains and inches, and the factor 5.58 is then 30.

Chapter 12

Mass Unbalance

The models commonly used to simulate projectile trajectories consider as a basic hypothesis that the center of gravity of the projectile corresponds to the geometric center of the projectile, located on the longitudinal symmetry axis of the projectile. Following this basic assumption, the widely used 6-DoF Model (Sec. 3.2) computes the position of the center of gravity as a function of time by solving twelve kinematic differential equations...

However, some applications cannot be subject to this hypothesis of coincidence given the nature of the projectile, which can either contain different asymmetric components such as a parachute, internal moving solid parts or different types of liquid payloads to name but a few [39, 48, 144, 160], or for maneuvering reasons where external asymmetry¹ is precisely what is wanted [42, 81].

The first approaches studying the unbalance used the tricyclic theory (Sec. 3.6) [163, 245] to quantify the initial conditions and in particular the effect of asymmetry on the first maximum yaw angle for spin-stabilized artillery projectiles [98]. As its name suggests, this linear theory gives closed-form solutions and takes into account a third mode of oscillation in addition to the nutation and precession of the projectile, with a magnitude equal to the angle between the unbalanced projectile's normal axis of inertia and the balanced projectile's normal axis of inertia. Since the tricyclic theory is based on an analytical approach by solving a linear differential equation, it implies constant aerodynamic coefficients,

¹A distinction is made between a static unbalance, caused by a center of gravity offset, and a dynamic unbalance, which consists of a misalignment between the principal axis of inertia and the axis of symmetry. Although these are independent properties, the two types almost always occur together [137].

nonthrusting projectile, small angles, and a constant roll velocity, which does not allow for aerodynamic variations as the projectile slows down along its trajectory. Nonetheless, this theory proved for rotationally symmetric projectiles that the first maximum yaw levels produced by mass asymmetries can cause important decreases in range and drift perturbations, even after satisfying the fundamental ballistic similitude criterion (identical shape, mass, and moments of inertia) [97]. Experimental campaigns have also confirmed these results using projectiles equipped with intern ballast and yaw probes [190]. In order to verify the damping rate following disturbances during the development phase of specific projectiles, experimental campaigns have also used these results to deliberately induce a yaw angle by introducing a mass asymmetry inducing a small principal-axis misalignment [159].

The tricyclic theory has been first extended to include Liquid-Fill Effects [161, 255], taking advantage of the similarity between the payload-induced side moment and the Magnus moment. The nutation rate was then determined for artillery projectiles by using the assumption that the liquid payload only influences its damping and not its angular frequency.

In the same idea, Cooper[42] extends the theory recognised by all to the modeling of control canards, also generating asymmetries, but allowing a better control of the trajectory. Analyze of the dynamic stability of projectiles exhibiting asymmetries was also given. Those extended linear-theories have of course the same limitations as the original theory but again, it can have important impact on the designs and allows to avoid inadequate designs early in the design process. Other studies focused more on the impact zone, again for artillery projectiles, supplementing the standard 6-DoF equations with constant angles for the dynamic unbalance and considering the aerodynamic coefficients of balanced projectiles [48, 102].

The conclusion of all these studies is that it is above all the initial conditions that are most decisive for the final range/drift, since if the conditions of stability are reached at the start, the unbalance can be compensated, and even used, for control authority in smart weapon applications for instance. Therefore, Frost[82] and Rogers[187] evaluated control authority of fin-stabilized and spin-stabilized projectiles equipped with an internal transverse rotating or translating part respectively, that can be controlled to an arbitrary position. The unbalance is

deployed only in flight so that there is no misalignment during launch and therefore no yaw amplified by any asymmetry at the start of the trajectory. A model with seven degrees of freedom was then implemented to take into account the controllable internal component. This approach was then again extended with a mass translating along the axis of symmetry in order to demonstrate that projectiles with variable stability exhibit greater control authority than highly stable standard rounds, leading to improved circular error probable² (CEP) performance with limited control force [188].

The purpose of this chapter is to use the methods detailed in the previous chapters to determine the aerodynamic coefficients of geometrically symmetric projectiles but with a fixed mass asymmetry (principal axis misalignment and CG offset) to complement previous findings for small caliber. In addition to having to take into account the evolution as a function of the yaw angle and the Mach number for the calculation of the coefficients, the 6 DoF model has been adapted to also take into account the unbalance position in flight without any modification of the twelve differential equations.

12.1 Mass unbalance in small caliber

The standard aerodynamic coefficients (with and without mass unbalance) were computed for both 9-mm and .308-in. bullets with validation data for the balanced .308-inch projectile [137]. The complete approach with mass unbalance is however presented below for a 9-mm round ogive projectile with a cylindrical body (Fig. 12.1). This projectile was chosen because it was possible to test it fairly easily in practice since it is designed to be fired with handguns at short distances. The computations for longer projectiles with a boat tail gave very similar trends numerically but could not be tested experimentally at effective range. The inherent difficulty linked to the choice of the 9-mm projectile is its velocity regime, which necessarily falls within the transonic regime. As this regime has already been the subject of previous chapter and publication [25], the same numerical methodology has been applied here. Its small L/d ratio also gives it a better stability, reinforcing somewhat the conclusions made.

²CEP = Radius of a circle centered on the middle point of impact, whose boundary is expected to include 50% of the impacts.

12.2 Experimental Approach

To effectively become aware of the effect of an unbalance in small caliber, .308-in monolithic copper projectiles were first fitted with an aluminum side insert. Unfortunately, although the projectiles exited the tube intact, the insert could not withstand the centrifugal force in the open air and almost systematically separated.

Another simple solution already used in the past [127, 137] was therefore applied by drilling a hole at the rear of the projectile (hence the ease of a cylindrical body). The technique worked, but only for a wide and shallow hole (leading to a smaller unbalance) because the solution with a deeper hole generated a tear in the front of the jacket due to the gas pressure during the acceleration in the tube.

Figure 12.1 illustrates this projectile of mass m , from which a mass m_E has been removed. The center of m_E is positioned at an axial distance l_E from the projectile's unbalance center of gravity CG_U , and at a distance r_E off the axis of symmetry. In the present case where the mass is removed to the rear of the original center of gravity with respect to the nose of the projectile, the distance l_E is defined as negative. The angle ε is the dynamic unbalance angle between the symmetry axis and the new axial moment of inertia. It is also necessary to define in the yz transverse plane to the projectile (Fig. 12.2), the roll orientation angles of the removed mass ϕ_0 , and of the new center of gravity Φ_0 , which are according to geometric reasoning, 180° out of phase with each other.

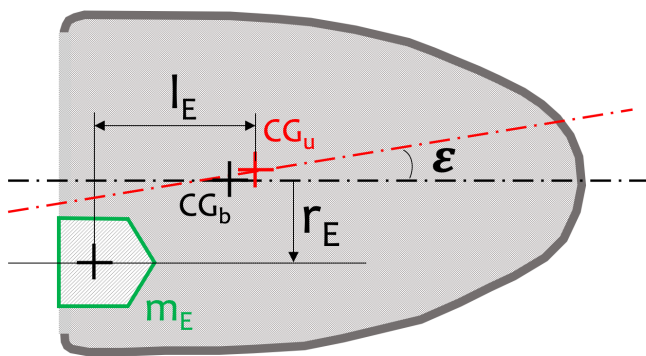


Figure 12.1: Schematic representation of a 9-mm caliber projectile from which a piece has been removed (green contour) to generate an unbalance.

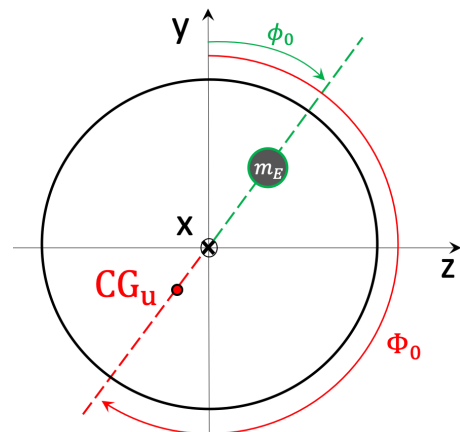


Figure 12.2: Angular definition of m_E and the new CG position.

The dispersion of the projectiles with the characteristics computed with SolidWorks³ and shown in Table 12.1, was compared at different distances from the target for an identical powder charge. The distances Δx and Δr are the offsets of the unbalanced CG_U with respect to the balanced CG_B (these values are especially used in the numerical part). The 9-mm tube used had a twist of 28.2 cal/tr with a length of 19 cm, allowing 3/4 of a revolution at the muzzle. Thanks to this data, it was possible for each shot to determine the position of the unbalance at its exit of the tube, to analyze the dispersion and correlate with the numerical and analytical models.

	Nominal	Unbalanced
Mass m (g)	7.4	6.9
Removed Mass m_E (g)	0	0.5
r_E (m)	/	$1.25 E^{-3}$
l_E (m)	/	$4.2 E^{-3}$
Avg v_0 (m/s)	426	440
Δv_0 (m/s)	2	5
I_x (kg.m ²)	$6.2 E^{-8}$	$5.9 E^{-8}$
I_y (kg.m ²)	$1.15 E^{-7}$	$1.11 E^{-7}$
I_z (kg.m ²)	$1.15 E^{-7}$	$1.09 E^{-7}$
I_{xy} (kg.m ²)	0	$-2 E^{-9}$
Tw (cal/tr)	28.2	28.2
Δx (m)	0	$3.7 E^{-4}$
$\Delta y = \Delta r$ (m)	0	$1.5 E^{-4}$

Table 12.1: 9-mm bullet characteristics with and without mass unbalance.

12.3 Analytical predictions

In the linear theory (Sec. 3.6), equation 3.114 showed the term K_T being the amplitude of the trim pitch and yaw angle. This parameter has not been discussed so far but it was represented in figure 3.33 for a projectile with an asymmetry in the fins. Figure 12.3 represents the equivalent situation with the gyroscopically stabilized 9-mm projectile with an unbalance. The amplitude of the arm K_T which can be assimilated here to the dynamic unbalance angle ε from figure 12.1, is given in equation 12.1 and gives a simple mathematical relation between a small dynamic unbalance due to mass asymmetry and the size of the trim arm that has to be added to the epicyclic pitching and yawing motion [137].

$$K_T = \frac{m_E r_E l_E}{I_y - I_x + \frac{I_x^2 M}{I_y P^2}} \quad (12.1)$$

³<https://www.solidworks.com/domain/design-engineering>

Based on the amplitude K_T and the gyro stability factor S_g (Eq. 5.5), an expression for the first maximum yaw angle δ_{MAX} , referred as "Kent's formula" [107, 156], can be derived:

$$\sin(\delta_{MAX}) = \left(2\frac{I_y}{I_x} - 1\right) \left(\frac{K_T}{\sqrt{1 - 1/S_g}}\right) \quad (12.2)$$

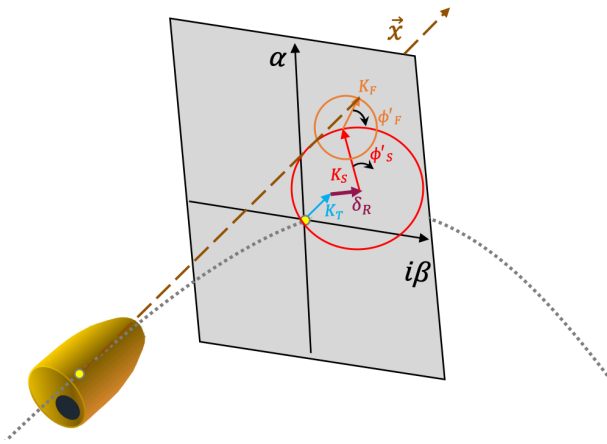


Figure 12.3: Schematic Tricyclic trim pitch and yaw arm K_T

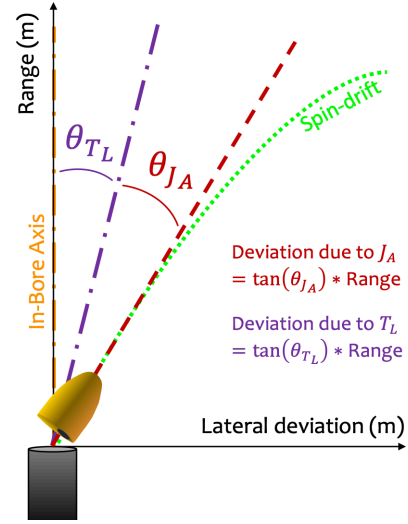


Figure 12.4: Schematic illustration of the different deviations that can accumulate, in this case to the right.

In the continuity of the tricyclic theory, McCoy [137] addresses the concepts of Aerodynamic Jump and Drift, which he extends analytically to quantify the effect of mass asymmetries, with the concept of Lateral Throwoff.

- The **Aerodynamic Jump** J_A , is caused by an initial yaw and initial yaw rate, at the instant of separation from the gun muzzle. Aerodynamic Jump changes the line of departure of the trajectory and J_A is the tangent of the deviation angle θ_{J_A} , as illustrated in figure 12.4. The specific contribution of a **dynamic unbalance** generated by the withdrawal of a small mass (I_x misalignment) is defined as follows:

$$J_A = \tan(\theta_{J_A}) = i \left(\frac{2\pi}{T_w}\right) \left(\frac{m_{ERE} l_E}{m d^2}\right) \left(\frac{C_{L_\delta}}{C_{M_\delta}}\right) e^{i\phi_0} \quad (12.3)$$

- The **Lateral Throwoff** T_L is the name given to the trajectory deviation caused by mass asymmetry or in-bore yawing [127] (Eq. 12.4). This deviation specific to static unbalanced projectiles (CG-offset) is thus to be added to the Aerodynamic Jump and drift already present for any spinning projectile, as shown in figure 12.4.

$$T_L = \tan(\theta_{T_L}) = i\left(\frac{2\pi}{T\omega}\right)\left(\frac{m_{E^rE}}{md}\right)e^{i\Phi_0} \quad (12.4)$$

For spin-stabilized field artillery projectiles fired at high elevation angles, these two effects can be neglected compared to the drift induced by the curvature. But for small and fast projectiles fired at short and medium range, Aerodynamic Jump and Lateral Throwoff are much more important to be accounted for.

On the basis of the data from table 12.1, it is thus possible to predict a deviation of the mean point of impact based simply on the initial conditions linked to the mass asymmetry. Considering then a 9-mm projectile whose unbalance at the muzzle was positioned at 270° (unbalance in the chamber at 0°), the offsets must be oriented at 180° according to formulas 12.3 & 12.4. Based on the values of C_{L_δ} & C_{M_δ} determined numerically at a speed of Mach 1.5 (Fig. 12.8-12.9), the values in table 12.2 are calculated and can be used for comparison with experimental firing and numerical predictions. According to figure 12.4, the values of J_A and T_L will still need to be multiplied by the firing distance (in meter) to determine the deviation.

$K_T \approx \varepsilon$	2.8°
δ_{MAX}	7.8°
J_A	0.0048
T_L	0.0021

Table 12.2: 9-mm bullet with unbalance: analytical offset predictions.

12.4 Comparison live firing with analytical predictions

Four series of shots were performed at 10m, 16m, 28m and 50m with each time about fifteen shots of which half were chambered with the unbalance up and the other half with the unbalance down. Each series was started with a calibration based on three nominal shots (without unbalance) where no dispersion was noticed, except at 50m where the three impacts were spaced 2cm apart. Figure 12.5 represents the deviation of the Middle Point of Impact (MPI) from the nominal impacts, as well as the CEP-dispersion observed as a function of the firing distance (error bars). These experimental results are compared with the analytical predictions detailed in previous section (J_A & T_L from table 12.2). Regarding the MPI, the results are very close and the dispersion observed with increasing distance can as usually be attributed to the dispersion in velocity, but also to the uncertainty on the position of the unbalance at the muzzle, and to the dimensions of this unbalance, drilled manually.

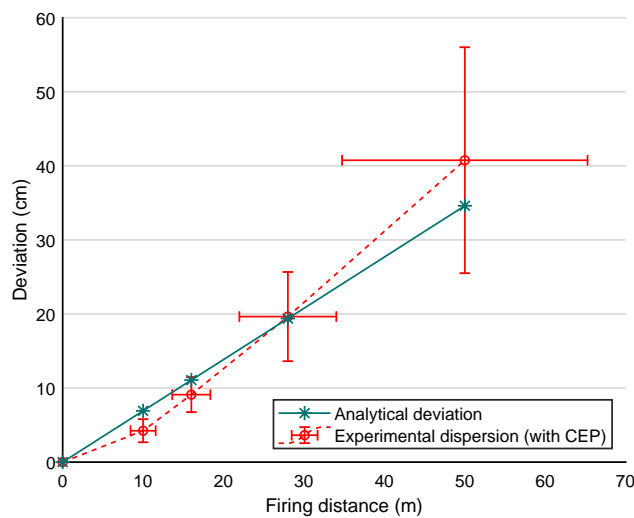


Figure 12.5: Experimental and analytical MPI deviations due to a mass unbalance.

The orientation of the impacts with respect to the center was systematically respected, either upwards if the hole was chambered downwards ($\phi_0 = 270^\circ$; $\Phi_0 = 90^\circ$), or downwards if the hole was chambered upwards ($\phi_0 = 90^\circ$; $\Phi_0 = 270^\circ$), in agreement with the analytical predictions (three quarter turns in the tube minus one quarter turn due to unbalance). This could also be observed using a high speed camera placed at the muzzle to visualize the angular displacements related to the presence of the unbalance (Fig.12.6).

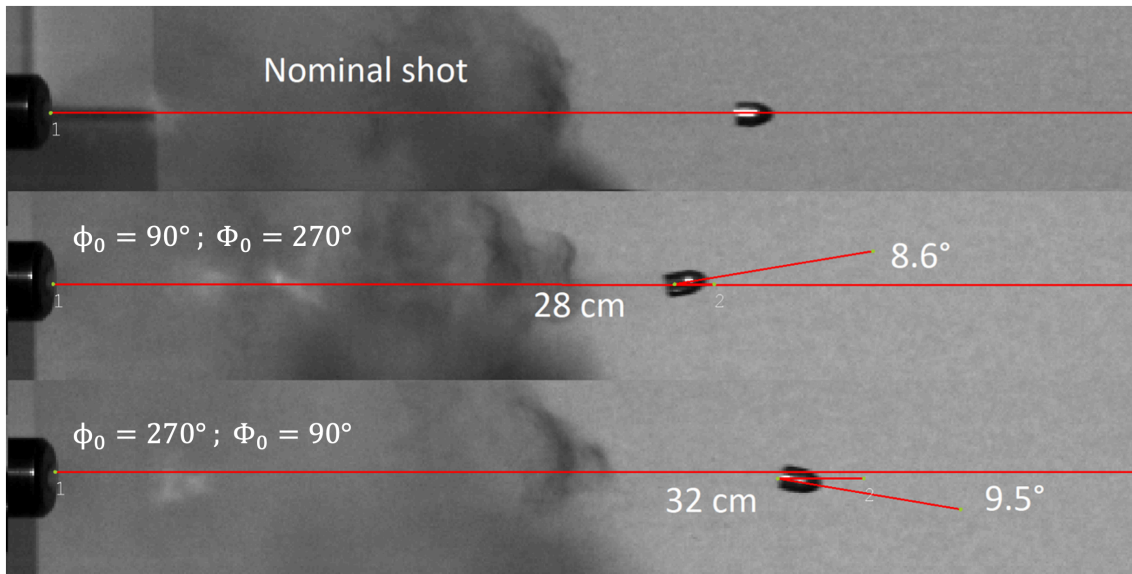


Figure 12.6: Visualization with the high speed camera of the departure of the projectile according to the position of the unbalance.

A maximum yaw angle is systematically observed around 30 cm from the muzzle and two complete vertical oscillations in the first meter are performed, which are reversed depending on whether the unbalance was placed at 0° or 180° .

Given this very similar analytical-empirical comparison, it is noticeable that at short range, the effects related to the unbalance in the air can only be negligible compared to the in-bore effects, generating a deflection in the immediate environment of the muzzle. Moreover, the tube-projectile combination used, generated an over-stabilization of the projectile at the muzzle ($S_g > 20$), biasing the tests somewhat in air, since the rotations at the muzzle were largely damped by the spin rate. Only the deflection angle was still present at the target.

12.5 Numerical Results

12.5.1 Aerodynamic coefficients without unbalance

Static coefficients

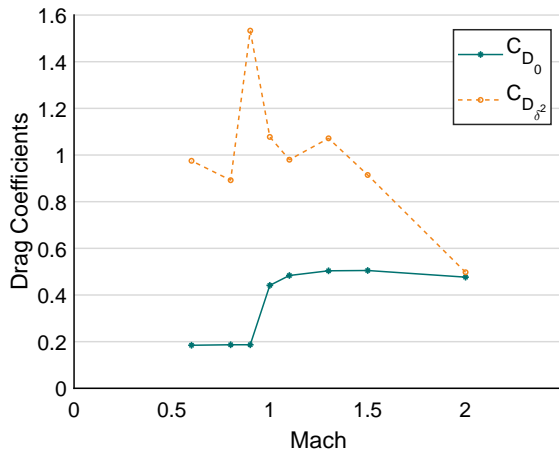


Figure 12.7: Drag coefficients for a 9-mm balanced projectile.

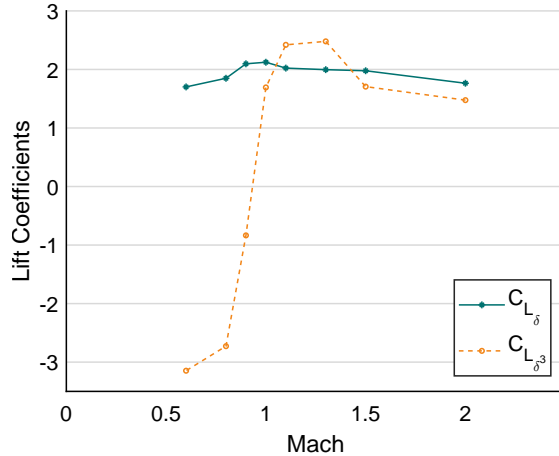


Figure 12.8: Lift coefficients for a 9-mm balanced projectile.

The static coefficients obtained in figures 12.7-12.9 are in line with the coefficients already obtained in small-caliber spin-stabilized projectiles, C_{D_0} being higher than for a long distance projectile, given the tangent ogive and the flat base. We also observe that the second and third order coefficients are quite small⁴, so they will be neglected in the following. The linear pitch coefficient (Fig. 12.9) is visibly lower than for long distance projectiles, due to the smaller L/d ratio.

Dynamic coefficients

The spin damping coefficient C_{l_p} is given in figure 12.10, while a constant value of -5 was considered for the pitch damping coefficient ($C_{M_{\dot{\alpha}}} + C_{M_q}$), as little variations was observed in the considered velocity range.

⁴Since they still have to be multiplied by $\sin^2 \delta$ or $\sin^3 \delta$.

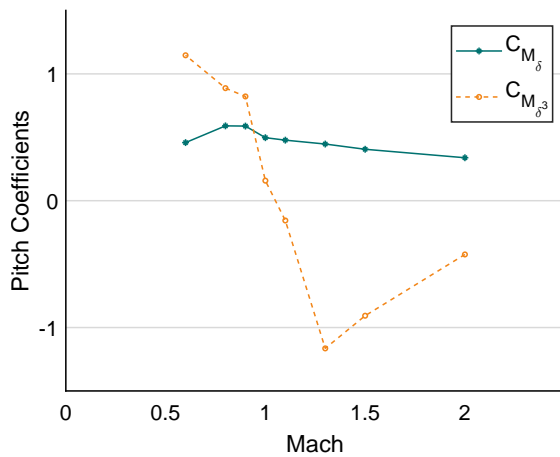


Figure 12.9: Pitch coefficients for a 9-mm balanced projectile.

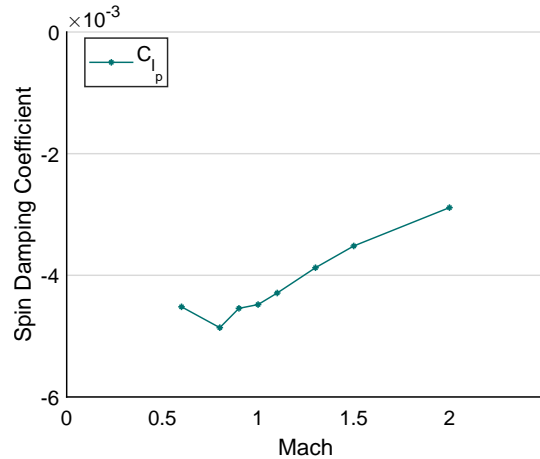


Figure 12.10: Spin damping coefficient for a 9-mm balanced projectile.

12.5.2 Aerodynamic coefficients with unbalance

In order to determine the influence of the unbalance on the different moment coefficients (Magnus being neglected), several calculations were carried out by placing the center of gravity (CG) at different locations in relation to the geometric center of the projectile. These different positions are illustrated in figure 12.11: the numbers correspond to the orientation of the new CG with respect to the symmetry axis, while the small letters *a*, *b* and *c* correspond to the radial distance Δr between the CG and the symmetry axis, *c* being the most important offset. The radial offsets $\Delta r = \sqrt{\Delta y^2 + \Delta z^2}$ were taken equal to 0.1, 0.3 and 0.5 mm while the offsets in *x* were varied between -0.5 and 2 mm with respect to the projectile nose.

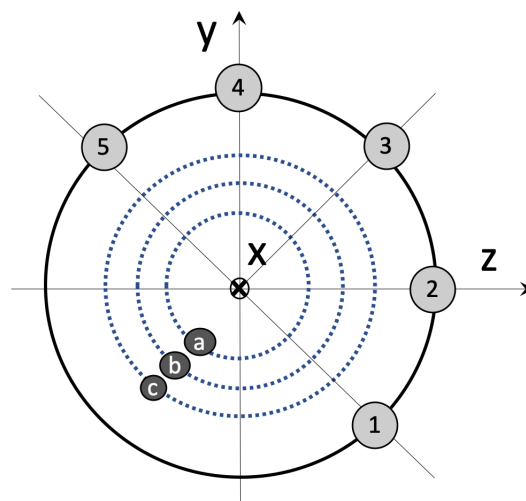


Figure 12.11: Different positions of the unbalance in the *yz* plane of the projectile.

Quasi-steady calculations were carried out at different velocities, varying the angle of attack from -15 to 15 degrees for all configurations from figure 12.11. Due to the symmetry of the problem, a number of configurations was redundant, but allowed to confirm the obtained results. Furthermore, the trends obtained for the pitching moment and spin damping moment are very clear: the lateral shift of the center of gravity has no influence on the pitching moment coefficient (Position 3 = Position 5) while the vertical shift has no influence on the spin damping moment coefficient (Position 3 = Position 1).

The presence of the unbalance has also no influence on the calculation of the force coefficients, only the moment coefficients must be determined on the basis of the position of this unbalance on its path. Since CFD allows to isolate the respective contributions, a first analysis is performed based on a lateral displacement of the CG, then to cumuler it with a longitudinal displacement.

Offset in y and z

Considering the orientation cases presented in figure 12.11, with the largest deviation (radius c), figures 12.12-12.13 represent the influence of a radial unbalance on the pitch and spin damping respectively, at a speed of Mach 1.1. Compared to the nominal coefficient (center of gravity = geometric center), the pitch coefficient is always shifted upwards for negative offsets and downwards for positive offsets in y -direction. In addition, for the spin damping, there is no offset at 0° but the slope of the curve changes completely as the unbalance z -deviation increases.

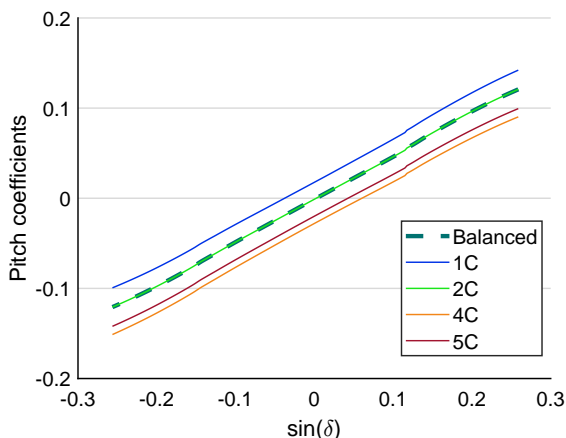


Figure 12.12: Pitch moment coefficient evolution as a function of the yaw angle, for different unbalanced projectiles (radial offset).

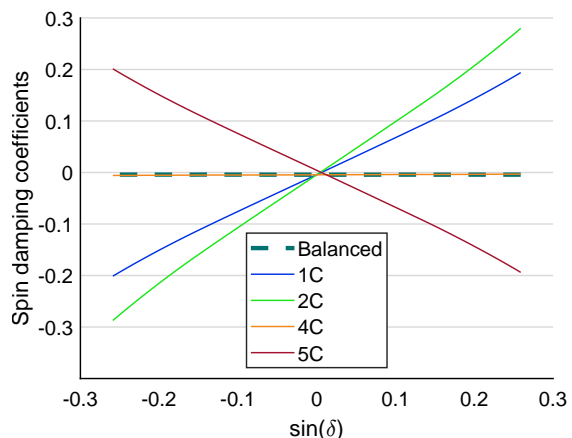


Figure 12.13: Spin damping moment coefficient evolution as a function of the yaw angle, for different unbalanced projectiles (radial offset).

The magnitude of the pitch offset and the spin damping slope change are also function of the velocity regime, as it can be seen in figures 12.14-12.15 for all the velocities. However, for each case considered, these variations remain almost constant in each velocity domain, i.e. supersonic and subsonic. Once again an abrupt change in the transonic transition is noticeable.

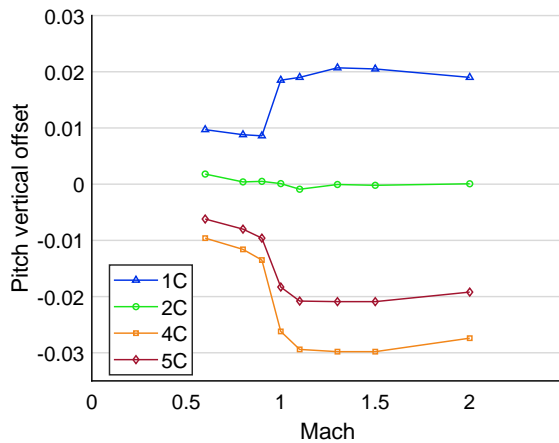


Figure 12.14: Vertical shift in pitch moment coefficient as a function of the velocity, for the unbalanced projectiles considered in figure 12.12.

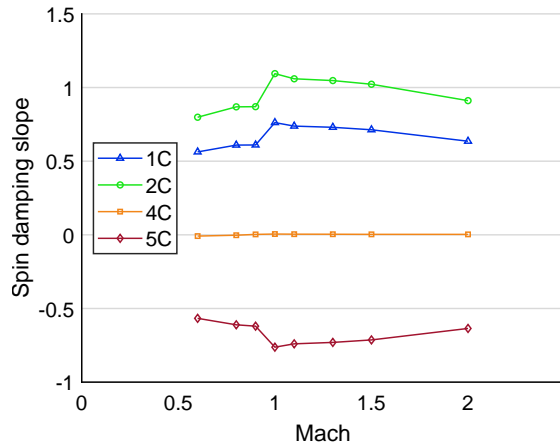


Figure 12.15: Slope increment in spin damping moment coefficient as a function of the velocity, for the unbalanced projectiles considered in figure 12.13.

The average slopes of the pitch moment coefficients (linear term) from figure 12.12 were plotted in figure 12.16 in relation to the speed, and we find back the coefficient C_{M_δ} already presented in figure 12.9. Similarly, the independent terms of the linear interpolations of figure 12.13 are compared to the C_{l_p} from figure 12.10 and the correlation is very good.

The coefficient shifts for all cases (1a until 5c) were then plotted as a function of the normalized center of gravity offset (divided by the caliber) and it can be seen in figures 12.18-12.19 that for both velocity regimes the trends are again linear. The linear interpolation of these two straight lines then makes it possible to consider an increment to the pitch and spin damping coefficients with respect to the y and z position of the center of gravity. It should be noted, however, that the increment in spin is proportionally much more significant than the increment in pitch.

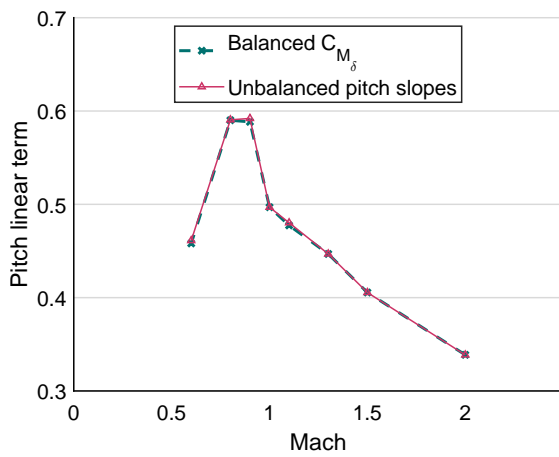


Figure 12.16: Average pitch slopes as a function of the velocity, for the unbalanced projectiles considered in figure 12.12.

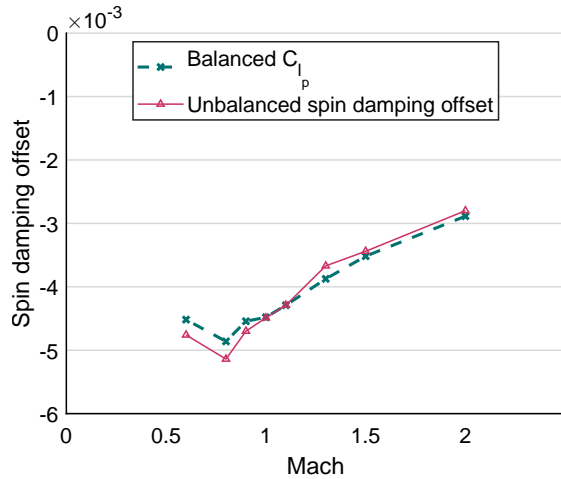


Figure 12.17: Average spin damping offset as a function of the velocity, for the unbalanced projectiles considered in figure 12.13.

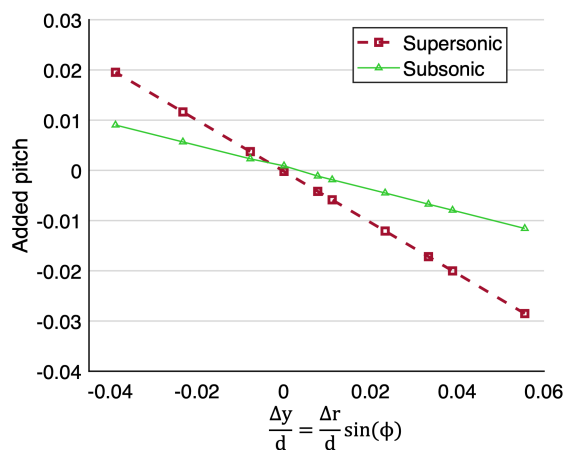


Figure 12.18: Linear pitch contribution to be added as a function of the radial vertical offset of the CG.

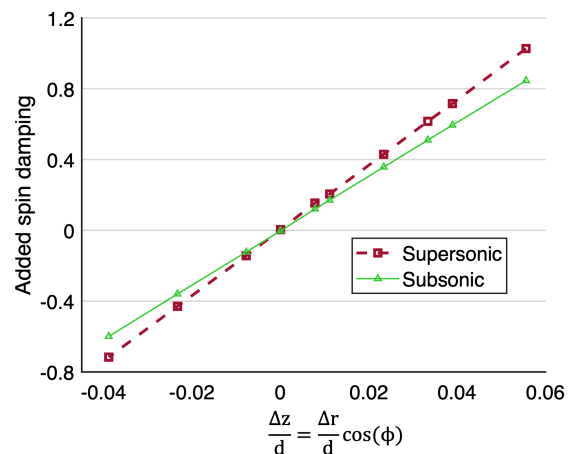


Figure 12.19: Linear spin damping contribution to be added as a function of the radial horizontal offset of the CG.

Offset in x

In the same way as for the radial offset, different longitudinal offsets Δx have been considered. While the influence on the spin damping is quite negligible (always for angles lower than 15°), a variation in the slope of the nominal pitch moment coefficient appears, independently of the radial offset Δr . Figure 12.20 shows the curves for three x -offsets cumulated to the radial offsets of case 5c. This angle increment evolves also linearly as a function of the velocity, which again allows to represent the angular increment with respect to the distance of the offset Δx in a linear way, as shown in figure 12.21. Therefore, the nominal angular coeffi-

cient can be corrected if the CG should move along the longitudinal axis of the projectile.

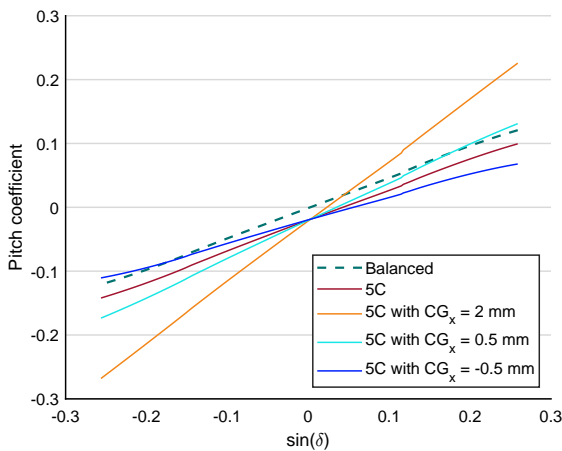


Figure 12.20: Pitch moment coefficient evolution as a function of the yaw angle, for different unbalanced projectiles (radial + longitudinal offset).

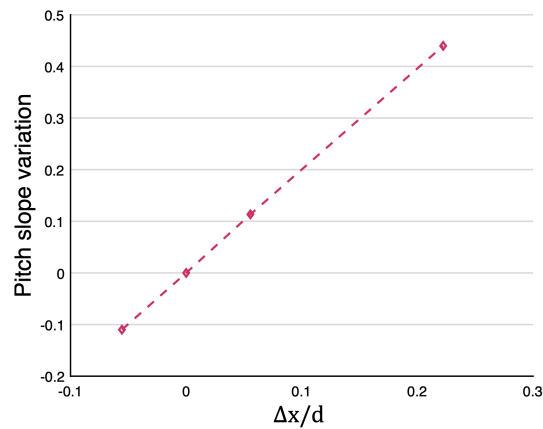


Figure 12.21: Linear pitch contribution to be added as a function of the longitudinal offset of the CG.

Finally, the pitch and spin damping coefficients for an unbalanced projectile are defined according to the following expressions:

Pitch coefficient:

$$C_{M,U} = l \frac{\Delta r}{d} \sin \phi + \left(C_{M_\delta} + m \frac{\Delta x}{d} \right) \sin \delta + C_{M_{\delta^3}} \sin \delta^3 \quad (12.5)$$

Spin damping coefficient:

$$C_{l_p,U} = C_{l_p} + \left(n \frac{\Delta r}{d} \cos \phi \right) \sin \delta \quad (12.6)$$

where l, m, n are constants determined by means of the angular slopes from graphs 12.18, 12.21 and 12.19 respectively. These constants will vary for each type of projectile, just as the balanced projectile coefficients do. Calculations for the .308-in projectile gave similar linear results.

Calculations were performed at 5 orientations and 3 radial distances, as well as at 3 longitudinal distances for one fixed radial distance, which constituted a large and redundant set of 18 "calculation points" allowing the verification of the obtained trends. However, given the linear pattern of the deviations, only 6 points with different radial and longitudinal offsets are finally needed for further analysis.

12.5.3 6-DoF computations

The advantage of numerical simulations is again to be able to consider variations by isolating the different contributions and exaggerating them. First, 6-DoF calculations have been performed without considering any initial perturbation, to visualize only the effects of the unbalance in the air. A first comparison is made at 50 m by exaggerating the decentering of the CG_U compared to the experiments performed ($\Delta x = 2$ mm and $\Delta r = 1$ mm). It can be seen in figures 12.22-12.23 that despite the variations in frequency and amplitude of the pitch and yaw, the differences in range and drift are quite minimal. This tendency is further confirmed by calculation at longer distances.

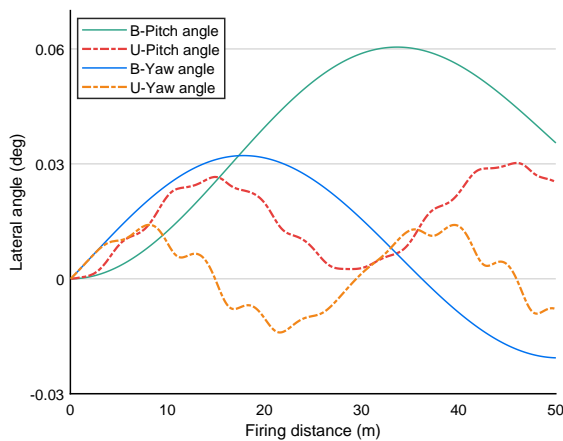


Figure 12.22: Pitch and yaw angles for a balanced (B) and unbalanced (U) projectile without initial perturbations. $QE=1.4$ mils and $MV=460$ m/s.

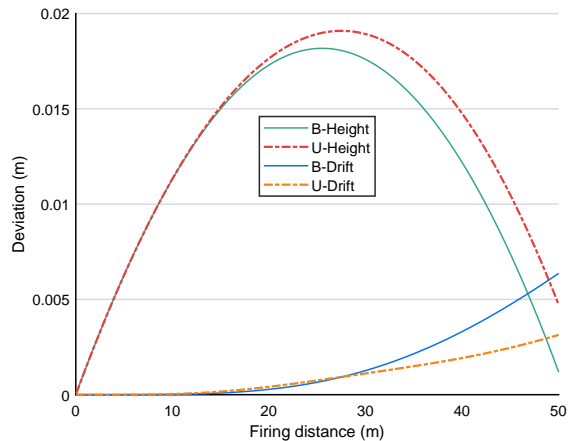


Figure 12.23: Height and drift deviations for a balanced (B) and unbalanced (U) projectile without initial perturbations. $QE=1.4$ mils and $MV=460$ m/s.

However, given the amplitude of the oscillations observed at the muzzle using the high speed camera (about 8° - figure 12.6), a transverse rotation speed $r_0 = \pm 500$ rad/s was added in the initial conditions of the 6-DOF calculation in order to obtain the same order of amplitude at 30 cm from the muzzle, with and without unbalance. Figure 12.24 represents the pitch motion for positive and negative vertical oscillation rates (positive or negative r) and the same unbalance as in the experiments. Given the overstabilization of the projectile, it is clear here that the oscillations are rapidly damped. A zoom on these oscillations on the first meter is given in figure 12.25, where we find indeed the two oscillations observed with the high speed camera, as well as the first maximum angle δ_{max} about 8° , which was shown in figure 12.6 and calculated analytically in table 12.2. While the first oscillations are similar between the balanced and unbalanced projectiles,

a deviation at impact is observed, which is in fact compensated by the presence of the unbalance. At 50 m, the unbalance tends to reduce the vertical offset (Fig. 12.26), independently of the vertical initial orientation, with orders of magnitude that fall within the range of the measurements obtained in figure 12.5. We also see in figure 12.27 that the lateral deviation is very small, reinforcing the idea that the presence of the unbalance causes very directional muzzle oscillations. If we had introduced $q_0 = \pm 500 \text{ rad/s}$ instead of $r_0 = \pm 500 \text{ rad/s}$, which corresponds to a laterally loaded unbalance, the deflection at impact would have been lateral. This was confirmed experimentally but within 20 m, for safety reasons in the laboratory.

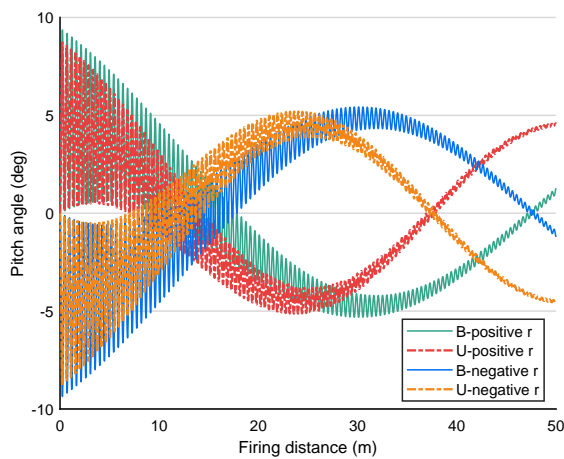


Figure 12.24: Pitch angle for a balanced (B) and unbalanced (U) projectile with $r = \pm 500 \text{ rad/s}$. $QE=1.4 \text{ mils}$ and $MV=460 \text{ m/s}$.

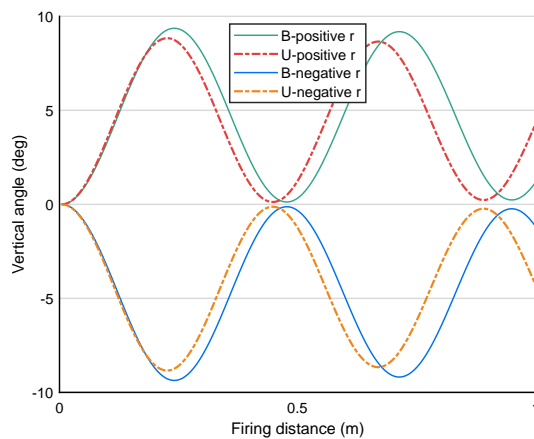


Figure 12.25: Zoom on the first meter from figure 12.24.

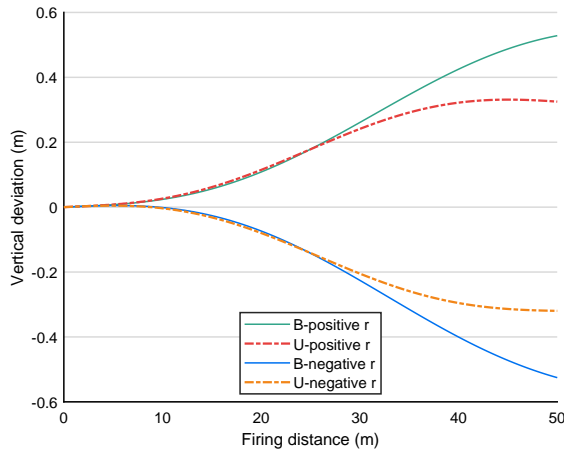


Figure 12.26: Vertical deviation for a balanced (B) and unbalanced (U) projectile with $r = \pm 500 \text{ rad/s}$. $QE=1.4 \text{ mils}$ and $MV=460 \text{ m/s}$.

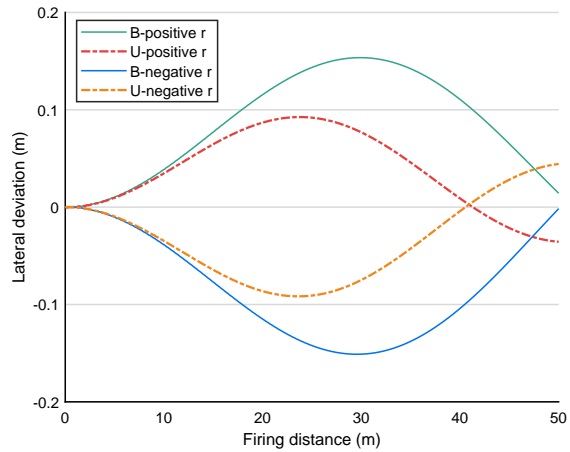


Figure 12.27: Horizontal deviation for a balanced (B) and unbalanced (U) projectile with $r = \pm 500 \text{ rad/s}$. $QE=1.4 \text{ mils}$ and $MV=460 \text{ m/s}$.

12.6 Conclusion on the mass unbalance...

The results experienced with large calibers could be extended to small calibers at small range, with both experimental and numerical visualizations: it appears very clearly that the effects related to the presence of the unbalance are much more important at the exit of the tube, than in air, since the orientation problems are quickly compensated by the gyroscopic effect whereas the direction of the trajectory is definitely deviated.

However, the effort must continue for other types of small-caliber projectiles, in order to validate the numerical method at longer range, and to be able to quantify to what extent the presence of an unintentional unbalance can be supported by the conventional gyroscopic stabilization (without over-stabilization). Conversely, the numerical method for determining the coefficients with unbalance could be an interesting asset, also for small calibers, to deliberately trigger a dispersion or a marked deviation (short range projectiles), without having to go through heavy experimental test campaigns. This could be a way to "control" the initial conditions by exaggerating them.

Part IV

Conclusions

Conclusions

A first part of this work was devoted to the most widespread trajectography models and their implementation in LabVIEW, following a simplifying philosophy, because the compromise between lightness and accuracy of the calculations is an important notion to consider, certainly for an operational application like this one.

The six degrees of freedom (6-DoF) model was certainly a big block, but despite that the 12 nonlinear, coupled, first-order differential equations are repeated in many articles, including the transformation matrices to switch between the reference frames, the "between-lines" and "between-matrices" have also been detailed to enable the understanding and the ulterior optimizations of the programs. All this with the effort to follow the conventions of the ballistic reference frame and keeping in mind the educational role. The 6-DoF model allows to compute the flight of any symmetric or inertial asymmetric projectile (spin- or fin-stabilized) and was validated with published results on conventional projectiles. Its parameters include a complete set of static and dynamic contributions, including Magnus and pitch damping forces and moments.

All the implemented models have their strengths in terms of either accuracy or simplicity, but globally, regardless of the analysis level, the fact remains that the need for accurate aerodynamic coefficients is omnipresent and crucial. Even the linear theory, which emits many simplifications, cannot be used without a set of "starting" coefficients.

For the determination of these coefficients, CFD was then addressed all the way from steady 2D axisymmetric computations up to full 3D unsteady non symmetric computations at angle of attack. Aerodynamic coefficients being dependent on both the Mach number and the angle of attack, but also on the Reynolds number and the shape of the projectile, a rigorous evaluation of the influence of these parameters was carried out. The intermittency transition γ -SST model was chosen for its ability to treat the external wall-bounded flows with a boundary layer subjected to adverse pressure gradients. The systematic approach allowed the determination of the coefficient curves as a function of the Mach number at zero incidence, but also at angle of attack up to 15° for the determination of the coefficient derivatives (second and third order). Results for spin- as for fin-stabilized projectiles were finally compared to experimental and empirical data on canonical geometries already widely studied and referenced, to demonstrate the ability to deal with the different projectile's shapes.

The pitch damping was determined on the basis of the response of the projectile to a forced oscillation about its center of gravity. This response having proven to be strongly dependent on the input frequency of the forced oscillation, the method requires therefore a good preliminary estimate of the natural frequency of the projectile. However, from many publications related to ballistics, this reduced frequency seems to be chosen according to good practice, without any further argumentation, while other sectors in aeronautics have also demonstrated this crucial dependence.

In addition to explicitly link the first two parts, the third part of this work finally addresses three applications in the field of small caliber. The first one considers a finned projectile at very low speed, putting forward, besides the projectile's stability problem itself to maintain its non-lethal character, the problem of the launching conditions (i.e. initial perturbations), which must be properly mastered to start any trajectory calculation. Experimental and numerical fluid dynamics were used to gain insight into the behavior of the boundary layer in several flight conditions.

The second application brings us to the "critical" transonic domain, through a comparative study between projectiles used in a caliber commonly used for long-distance firing. Different projectile shape characteristics have been put forward, with their direct effects in terms of aerodynamic properties. Given the "relatively" flat trajectories, the linear theory was also applied to compare the different stabilities on the basis of data calculated with CFD. Besides the gyroscopic stability which is relatively easy to determine, we showed the connection between the Magnus and pitch damping moments and their influence on the dynamic stability, leading to a possible destabilization in the transonic domain.

The third and last application extends the conclusions drawn in large caliber projectiles presenting an unbalance, to a small-caliber 9-mm projectile with a fixed unbalance. An original numerical approach is used to quantify the moment coefficients for unbalanced projectiles and the results at short range converge with the analytical predictions and experimental measurements: the very directional effects related to the position of the unbalance could be demonstrated.

Although ballistics is a branch of mechanics, the departments of Ballistics and Mechanical Engineering from the Royal Military Academy are relatively distant in terms of research. Some of the goals of this work was therefore to extend the respective techniques: on one side to create a global and efficient research tool for exterior ballistics, on the other side to enlarge the fluid mechanics applications in the supersonic range.

As the ABAL department is both solicited by operational users for specific and concrete issues, and also by industry for background studies, it is valuable to rely on rigorously home-developed tools allowing flexibility of use, with always the possibility of optimizing the basic skeleton according to the particular needs of the clients. Of course, existing sources should not be ignored and this is the reason why a whole chapter summarized the different programs and contributions already made in terms of trajectography.

Research and optimization perspectives

"Je mehr ich weiß, desto mehr erkenne ich, dass ich nichts weiß."

- Albert Einstein -

This sentence has never seemed so true for me and as all learning leads to a lot of questions, this last part aims to compile the points of attention and the developments to be considered in the future. Many interesting projects in the field can for sure be initiated in the short and medium terms. The different aspects will be formulated according to the structure of this work.

Rigid Body Dynamics

Trajectory models

In this part we can dissociate the optimization and the improvement of the current 6-DoF code. The optimization implies in particular the use of quaternions, variable time steps (depending on the curvature and the integration error) and implicit integration methods and/or a RK7 scheme to compare with the BALCO model which will be soon available to NATO members. A more efficient and open-source language for this type of application could also be considered, such as Julia, Python or C++ [177].

The improvement part would consider the implementation of a 7-DoF module (again which could be confronted with BALCO and HTraj) as well as an indirect integration also for the 6-DoF model, by optimizing the numerical methods according to the type of application (direct/ indirect fire/ means of aiming/ uphill-downhill/ ...).

Going into the NABK and the different linked software packages to be aware of all the latest developments around the trajectory would not be an easy task either: Although the new purchases are black boxes and it is no longer necessary to implement firing solutions ourselves (as it was the case in the past with "Artyfire" for artillery [72]) it is important to keep an external ballistic computing capacity for "everyday" operational issues and to continue maintaining academic knowledge.

Error Budget

Another PhD research in ABAL department is ongoing and will require, among others, exterior ballistics inputs. It is entitled : "*Measure effectiveness at system of systems level based on non-deterministic discrete event model*". The goal of this research is to propagate uncertainties (errors) on input parameters of the models throughout the complete simulation chain (internal, external and terminal ballistics), in order to evaluate the uncertainties (errors) on the output quantities (accuracy or lethality). The uncertainty propagation is done by means of Monte Carlo simulations. For a high number of input parameters with uncertainty, the cost of the simulations can be prohibitively high. Therefore, fast simulation algorithms (discrete event) need to be used to speed up simulation times. The research also explores the use of macroscopic models (surrogate models) to propagate the errors. For these types of simulations, it is also important to use accurate models. Improved accuracy goes hand in hand with more complexity. Complex models take more time to solve and there is a need to accurately represent the behavior of the system using simple models.

With this in mind, and the added complexity of UQ in CFD, a contrary approach starting from a "ballistic" error budget could be considered. For ballistic applications where a dispersion margin is already systematically present, it would be more conceivable to ask from which margin of error brought by the aerodynamic coefficients the dispersion at the target is altered, or in other words: what is the acceptable margin of error on the coefficients, which would in a way allow to anticipate the cost of the CFD-simulations but especially of their optimization?

Computational Fluid Dynamics

Mesh Quality & RANS/LES methods

Setting up a good and accurate mesh (which will often be labeled as a "beautiful" mesh) is almost an art in itself, and is certainly one of the most time-consuming parts, in terms of "human" processing. This is one of the reason why the unstructured and "almost" automatic approach in ICEM-CFD was used in this work. However, some RANS calculations have shown their limitations, and before one can truly conclude that it is only a turbulence-modeling limitation, one should first consider optimizing the mesh to further reduce the uncertainty on the spatial discretization.

Furthermore, different RANS/LES approaches will have to be envisaged in the near future. Many hybrid RANS/LES techniques are constantly being developed, in the form of zonal or non-zonal approaches [122]. While zonal methods are still preferred for wall-bounded flows where only the parts including complex flow physics are scale-resolved, non-zonal methods are suggested for flows dominated by large coherent structure and strong unsteady profiles. Both methods can nevertheless be compared on the basis of the available means, the flight conditions and the desired aerodynamic parameters. In any case, these methods will require the implementation of more complex but more regular meshes with specific methods (such as solution adaptive mesh refinement (AMR) with overset-mesh methodology [54].)

With "refined" techniques, the influence of large angles of attack, the influence of grooves, but also the roughness of the projectile surface, will be studied with more confidence, especially for more complex geometries where it is also necessary to evaluate the interaction of flows due to the different added features (moving fins, canards, nozzle, etc...) [278].

Experimental Aerodynamics

As mentioned in this work, the arrival of a supersonic wind tunnel at the Academy will allow new research in terms of static and dynamic stability coefficients, for in-house experimental confirmation in controlled conditions on top of ballistic tests with their inherent variability in muzzle and fly out conditions.

Applications in continuous growth

Guided Ammunition

The development of Guidance, Navigation & Control (GNC) algorithms is constantly progressing, as a consequence of the increased demand for target hit accuracy and cost reductions, in various types of defenses. Without going into the complexity and sophistication of the missiles' integrated sensors, flight dynamics developments have allowed the evolution of canard guided spin-stabilized projectiles with the integration of course correction fuse, impulse jets, translating masses or fin deflectors [242], but until now in large caliber (> 76 mm) and for very large trajectories. The knowledge of this field opens the door to medium and small calibers and the challenge of being able to do the same with smaller masses and bodies more sensitive to air resistance...

Although the concept of RBD/CFD coupling seems to have become more affordable in the US ARL [260], closer to home for instance, the different departments of ISL have already well formalized the fundamentals of these guidance and control algorithms and are developing in-house numerical simulation codes, supported by wind-tunnel experiments and free flight tests, to acquire the aerodynamics of a new generation of guided projectiles, together with flight control algorithms and optimal guidance laws for trajectory control [242].

Supercavitating underwater ammunition

Only air as a flight environment has been addressed in this work, but an interesting application that deserves attention is the optimization of water-borne ammunition. The operational need to fire in and from water is very present but the projectiles currently developed are not able to maintain their stability and lose all effectiveness in water. Small-caliber developments of supercavitating underwater ammunition have already appeared on the market and seem to give good results, but only a few experimental studies with supporting analytical models really describe the physical challenge [65, 78, 241].

References

- [1] AEP-96. *The Six/Seven Degrees of Freedom Guided Projectile Trajectory Model - Edition A Version 1*. 2016.
- [2] A. Altufayl and den Heijer W.L. "Development of a 6 DOF Trajectory Simulation Model for Asymmetric Projectiles". MA thesis. North-West University - South Africa, 2019.
- [3] M.J. Amoruso. *Euler Angles and Quaternions in Six Degrees of Freedom Simulations of Projectiles*. US Army ARL, 1996.
- [4] J.D. Anderson. "Ludwig Prandtl's Boundary Layer". In: *Physics Today* 58.12 (2005). DOI: [10.1063/1.2169443](https://doi.org/10.1063/1.2169443).
- [5] J.D. Anderson. *Hypersonic and High Temperature Gas Dynamics*. Ed. by J.A. Schetz. second edition. AIAA Education Series, 2006. DOI: [10.2514/4.861956](https://doi.org/10.2514/4.861956).
- [6] Inc. ANSYS. *ANSYS Fluent User's & Theory Guide 2021 R1*.
- [7] Inc. ANSYS. *ANSYS ICEM CFD User Manual 17.0*.
- [8] Inc. ANSYS. *DesignModeler User's Guide 14.5*.
- [9] Inc. ANSYS. *Workbench User's Guide 15.0*.
- [10] AOP-37. *NATO Armaments Ballistic Kernel - Volume 1-4*. 2013.
- [11] AOP-4355. *The Lieske Modified Point Mass and Five Degrees of Freedom Trajectory Models - Edition A, Version 1*. 2017.
- [12] AOP-4655. *An engineering model to estimate aerodynamic coefficients - Edition 1*. 2014.
- [13] AOP-53. *AeroFI, NATO Technical Shareable Software (NTSS) for the Determination of Aerodynamic Coefficients - Version 1.3*.
- [14] AOP-65. *Firing techniques to determine ballistic data for fire control systems - Edition C, Version 1*. 2013.
- [15] Arrow Tech Associates. *The Free Flight Aerodynamic Range*. Aberdeen Proving Ground, MD: BRL Report-1048, 1958.

- [16] Arrow Tech Associates. *PRODAS V3 Technical Manual*. Burlington, VT, USA, 2002.
- [17] Arrow Tech Associates. *Advanced Training for the Weapons Designer*. South Burlington, Vermont: Course Catalog, 2013.
- [18] B. Barnett. *Trajectory Equations for a Six-Degree-of-Freedom Missile*. Picatinny Arsenal, Dover, USA: Technical Memorandum FRL-TM-25, 1962.
- [19] B. Barnett. *Trajectory Equations for a Six-Degree-of-Freedom Missile Using a Fixed-Plane Coordinate System*. Picatinny Arsenal, Dover, USA: Technical Report 3391, 1966.
- [20] B. Ben Amma, S. Melliani, and L. S. Chadli. "A Fourth Order Runge-Kutta Gill Method for the Numerical Solution of Intuitionistic Fuzzy Differential Equations". In: *Springer Nature Switzerland AG 2019* (2019). doi: [10.1007/978-3-030-02155-9_5](https://doi.org/10.1007/978-3-030-02155-9_5).
- [21] V. A Bhagwandin and J. Sahu. *Numerical Prediction of Pitch Damping Stability Derivatives for Finned Projectiles*. Aberdeen Proving Ground, MD: ARL Report-TR-6725, 2013. doi: [10.2514/1.A32734](https://doi.org/10.2514/1.A32734).
- [22] V.A. Bhagwandin. "Numerical Prediction of Roll Damping and Magnus Dynamic Derivatives for Finned Projectiles at Angle of Attack". In: *30th AIAA Applied Aerodynamics Conference*. New Orleans, Louisiana, 2012. doi: [10.2514/6.2012-2905](https://doi.org/10.2514/6.2012-2905).
- [23] V. de Briey et al. "Aerodynamic Characterization of a Non-Lethal Finned Projectile at Low Subsonic Velocity". In: *AIAA Aviation 2019 Forum, Dallas*. 2019. doi: [10.2514/6.2019-3696](https://doi.org/10.2514/6.2019-3696).
- [24] V. de Briey et al. "Aerodynamical CFD Study of a non-lethal 12-Gauge fin-stabilized projectile". In: *Human Factors and Mechanical Engineering for Defense and Safety* (2019). doi: [10.1007/s41314-019-0020-x](https://doi.org/10.1007/s41314-019-0020-x).
- [25] V. de Briey et al. "Influence of the Transonic Crossing for Precision Ammunition". In: *31th International Symposium on Ballistics, Hyderabad*. 2019. doi: [10.12783/ballistics2019/33109](https://doi.org/10.12783/ballistics2019/33109).
- [26] B.T. Burchett. "Unscented Filtering for Munition Parameter Estimation using Onboard Sensor Telemetry". In: *AIAA AVIATION Forum*. Dallas, TX, 2019. doi: [10.2514/6.2019-3162](https://doi.org/10.2514/6.2019-3162).
- [27] G. Buresti. "A note on Stokes' hypothesis". In: *Acta Mech* 226 (2015), pp. 3555–3559. doi: [10.1007/s00707-015-1380-9](https://doi.org/10.1007/s00707-015-1380-9).
- [28] T. Bykerka, D. Verstraete, and J. Steelant. "Low speed longitudinal dynamic stability analysis of a hypersonic waverider using unsteady Reynolds

- averaged Navier Stokes forced oscillation simulations". In: *Aerospace Science and Technology* (2020). DOI: [10.1016/j.ast.2020.105883](https://doi.org/10.1016/j.ast.2020.105883).
- [29] D.E Carlucci and S.S. Jacobson. *Ballistics: Theory & Design of Guns & Ammunition*. CRC Press - Taylor & Francis Group, 2008. ISBN: 978-1-4200-6618-0.
- [30] L. Carvalho and G. Filo. *CFD analysis of drag force for different nose cone design*. 2019.
- [31] R. Cayzac et al. "Magnus Effect: Physical Origins and Numerical Prediction". In: *Journal of Applied Mechanics* 78.5 (2011). DOI: [10.1115/1.4004330](https://doi.org/10.1115/1.4004330).
- [32] E. Celens. "A physically more direct and mathematically more simple approach to the modified point mass trajectory model". In: *10th International Symposium on Ballistics*. San Diego, California, 1987.
- [33] I.B. Celik et al. "Procedure for estimation and reporting of uncertainty due to discretization in CFD Applications". In: *Journal of Fluids Engineering* 7.130 (2008), pp. 1–4. DOI: [10.1115/1.2960953](https://doi.org/10.1115/1.2960953).
- [34] L. Chaffois, P. Chabin, and G. Bersano. *DART Projectile – IM tests Assessment*. EURENCO & OTO MELARA, 2015.
- [35] G.T. Chapman and D.B Kirk. "A Method for Extracting Aerodynamic Coefficients from Free-Flight Data". In: *AIAA Journal* 8.4 (1970), pp. 753–758. DOI: [10.2514/3.5752](https://doi.org/10.2514/3.5752).
- [36] L.K. Cheng, C. Smorenburg, and J. van Bree. "Projectile Orientation Measurement (POM) system". In: *OPTRO 2005* (2005).
- [37] H. Choi and P. Moin. "Grid-point requirements for large eddy simulation: Chapman's estimates revisited". In: *Physics of Fluids* 24 (2012). DOI: [10.1063/1.3676783](https://doi.org/10.1063/1.3676783).
- [38] F.A. Chughtai, J. Masud, and S. Akhtar. "Unsteady aerodynamics computation and investigation of magnus effect on computed trajectory of spinning projectile from subsonic to supersonic speeds." In: *The Aeronautical Journal* 123.1264 (2019), pp. 863–889. DOI: [10.1017/aer.2019.32](https://doi.org/10.1017/aer.2019.32).
- [39] K.K. Cobb and R.H. Whyte. "Effects of moving components on the motion of a 20-mm projectile". In: *11th AIAA Aerodynamics Testing Conference*. New York, 1983, pp. 94–103. DOI: [10.2514/6.1980-428](https://doi.org/10.2514/6.1980-428).
- [40] R.A. Collins and Miller W.A. *Several Models of Six Degree of Freedom Equations of Motion for a Ballistic Missile*. Inglewood, California: Air Force Ballistic Systems Division Technical Note BSD-TDR-62-22, 1962.
- [41] G.R. Cooper. "Influence of Yaw Cards on the Yaw Growth of Spin-Stabilized Projectiles". In: *Journal of Aircraft* 38.2 (2001). DOI: [10.2514/2.2784](https://doi.org/10.2514/2.2784).

- [42] G.R. Cooper, F. Fresconi, and M.E. Costello. "Flight stability of an asymmetric projectile with activating canards". In: *Journal of Spacecraft and rockets* 49.1 (2012), pp. 130–135. doi: [10.2514/1.A32022](https://doi.org/10.2514/1.A32022).
- [43] G.R. Cooper, P. Weinacht, and J.F. Newill. *Another Analytical Approach to Predicting Munition Trajectories*. Aberdeen Proving Ground, MD: ARL-TR-3948, 2006.
- [44] D. Corriveau. "Validation of the NATO Armaments Ballistic Kernel for use in small-arms fire control systems." In: *Defence Technology* 13 (2017), pp. 188–199. doi: [10.1016/j.dt.2017.04.006](https://doi.org/10.1016/j.dt.2017.04.006).
- [45] D. Corriveau and A. Dupuis. "System Modeling of a 40mm automatic Grenade Launcher (U)". In: *58th Aeroballistic Range Association Meeting* (2007).
- [46] M. Costello, S. Gatto, and J. Sahu. "Using CFD/RBD Results to Generate Aerodynamic Models for Flight Simulation". In: *AIAA Atmospheric Flight Mechanics Conference and Exhibit*. Hilton Head, South Carolina, 2007. doi: [10.2514/6.2007-6582](https://doi.org/10.2514/6.2007-6582).
- [47] M. Costello and J. Sahu. "Using computational fluid dynamic/rigid body dynamic results to generate aerodynamic models for projectile flight simulation". In: *Proceedings of the Institution of Mechanical Engineers, Part G: Journal of Aerospace Engineering* (2008). doi: [10.1243/09544100JAERO304](https://doi.org/10.1243/09544100JAERO304).
- [48] M.E. Costello and D.P. Anderson. "Effect of internal mass unbalance on the terminal accuracy and stability of a field artillery projectile". In: *AIAA Atmospheric Flight Mechanics Conference*. San Diego, CA, 1996, pp. 814–821. doi: [10.2514/6.1996-3447](https://doi.org/10.2514/6.1996-3447).
- [49] A.A. Da Ronch et al. "Computation of Dynamic Derivatives Using CFD". In: *28th AIAA Applied Aerodynamics Conference*. Chicago, Illinois, 2010. doi: [10.2514/6.2010-4817](https://doi.org/10.2514/6.2010-4817).
- [50] Valcartier Defence Research Establishment. "Ballistic Range Technology". In: (1970). URL: <https://apps.dtic.mil/dtic/tr/fulltext/u2/713915.pdf>.
- [51] J.M. Delery. "Physics of Vortical Flows". In: *Journal of Aircraft* 29.5 (1992), pp. 856–876. doi: [10.2514/3.46256](https://doi.org/10.2514/3.46256).
- [52] H. Demailly. "Identification des coefficients aérodynamiques d'un projectile à partir de mesures prises en vol". PhD thesis. Université d'Orléans, 2011.

- [53] J. DeSpirito. "Effects of Base Shape on Spin-stabilized Projectile Aerodynamics". In: *26th AIAA Applied Aerodynamics Conference*. Honolulu, Hawaii, 2008. DOI: [10.2514/6.2008-6738](https://doi.org/10.2514/6.2008-6738).
- [54] J. DeSpirito. "CFD aerodynamic characterization of 155-mm projectile at high angle-of-attack". In: *35th AIAA Applied Aerodynamics Conference*. Denver, Colorado, 2017. DOI: [10.2514/6.2017-3397](https://doi.org/10.2514/6.2017-3397).
- [55] J. Despirito and K. Heavey. "CFD Computation of Magnus Moment and Roll Damping Moment of a Spinning Projectile". In: *AIAA Atmospheric Flight Mechanics Conference and Exhibit* (2004). DOI: [10.2514/6.2004-4713](https://doi.org/10.2514/6.2004-4713).
- [56] J. DeSpirito and P. Plostins. "CFD Prediction of M910 Projectile Aerodynamics: Unsteady Wake Effect on Magnus Moment". In: *AIAA Atmospheric Flight Mechanics Conference and Exhibit*. Hilton Head, South Carolina, 2007. DOI: [10.2514/6.2007-6580](https://doi.org/10.2514/6.2007-6580).
- [57] J. DeSpirito and S.I. Sifton. *Capabilities for Magnus Prediction in Subsonic and Transonic Flight*. Aberdeen Proving Ground, 2008.
- [58] J. DeSpirito, S.I. Sifton, and P. Weinacht. *Navier-Stokes Predictions of Dynamic Stability Derivatives: Evaluation of Steady-State Methods*. Aberdeen Proving Ground, MD, 2008.
- [59] J. DeSpirito, S.I. Sifton, and P. Weinacht. "Navier-Stokes Predictions of Dynamic Stability Derivatives: Evaluation of Steady-State Methods". In: *Journal of Spacecraft and Rockets* (2009). DOI: [10.2514/1.38666](https://doi.org/10.2514/1.38666).
- [60] K. Diakakis, G. Papadakis, and S.G. Voutsinas. "Assessment of transition modeling for high Reynolds flows". In: *Aerospace Science and Technology* 85 (2019), pp. 416–428. DOI: [10.1016/j.ast.2018.12.031](https://doi.org/10.1016/j.ast.2018.12.031).
- [61] E.R. Dickinson. *Production of Firing Tables for Cannon Artillery*. Aberdeen Proving Ground, MD: BRL report 1371, 1967.
- [62] DRDC. *Defence R&D Canada Valcartier: Aeroballistic Range - Munitions Experimental Test Centre (METC)*. Information Brochure, 2007.
- [63] M.R. Driels. *Advanced Weaponneering - Third Edition, Volume 2*. USA: AIAA Education Series, 2020, pp. 53–71.
- [64] M.R. Driels. *Weaponneering: An introduction - Third Edition, Volume 1*. USA: AIAA Education Series, 2020, pp. 81–107.
- [65] O. Dullum. "Ballistics of Supercavitating Projectiles". In: *30th International Symposium on Ballistics*. Long Beach, CA, 2017.

- [66] L.D. Duncan and B.F. Engebos. *A Six Degree of Freedom Digital Computer Program for Trajectory Simulation*. White Sands Missile Range, New Mexico: AD664116 - ECOM 5158, 1967.
- [67] L.D. Duncan and R.J. Ensey. *Six Degree of Freedom Digital Simulation Model for Unguided Fin-Stabilized Rockets*. White Sands Missile Range, New Mexico: AD452106, 1964.
- [68] M.C. Dunn, B. Shotorban, and A. Frendi. "Uncertainty Quantification of Turbulence Model Coefficients via Latina Hypercube Sampling Method." In: *Journal of Fluids Engineering* 133.4 (2011). DOI: [10.1115/1.4003762](https://doi.org/10.1115/1.4003762).
- [69] A.D. Dupuis. *Aeroballistic Range and Wind Tunnel Tests of the Basic Finner Reference Projectile From Subsonic to High Supersonic Velocities*. Defense Research Establishment: Valcartier, Canada, 2002.
- [70] A.D. Dupuis and W. Hathaway. *Aeroballistic Range Tests of the Basic Finner Reference Projectile at Supersonic Velocities*. Defense Research Establishment: Valcartier, Canada, 1997.
- [71] A.D. Dupuis and W. Hathaway. *Aeroballistic Range Tests of the Air Force Finner Reference Projectile*. Defense Research Establishment: Valcartier, Canada - TM 2002-008, 2002.
- [72] G. Dyckmans. *Artyfire: Rekenprocedures - Baanberekening*. Artillery School - Studiebureau, 1996.
- [73] Firing Tables Branch ARDEC Element. *FCT 155-AM-B: Introduction to Fire Control Trajectories*. Aberdeen Proving Ground, 1995.
- [74] L. Ericsson. "Missile dynamics including high alpha maneuvers". In: *27th AIAA Aerospace Sciences Meeting and Exhibit*. Reno, Nevada, 1989. DOI: [10.2514/6.1989-330](https://doi.org/10.2514/6.1989-330).
- [75] N. Ferguson. *Civilization: The West and the Rest*. USA: Penguin Books, 2011.
- [76] M. Fischer and W. Hathaway. *Aeroballistic Research Facility Data Analysis System (ARFDAS)*. Air Force Armament Laboratory AFATL-TR-88-48, 1988.
- [77] P. Flores. *Concepts and Formulations for Spatial Multibody Dynamics*. 2015. Chap. 4. Euler Angles, Bryant Angles and Euler Parameters, pp. 15–20. DOI: [10.1007/978-3-319-16190-7_4](https://doi.org/10.1007/978-3-319-16190-7_4).
- [78] H. Forouzani, B. Saranjani, and R. Kamali. "A Study on the Motion of High Speed Supercavitating Projectiles". In: *Journal of Applied Fluid Mechanics* 11.6 (2018). DOI: [10.29252/jafm.11.06.28807](https://doi.org/10.29252/jafm.11.06.28807).
- [79] E.H. Fowler et al. "The Aerodynamics of a Spinning Shell". In: *Proceedings of the Royal Society of London* (1920), pp. 199–205.

- [80] F. Fresconi and T. Harkins. "Aerodynamic Characterizations of Asymmetric and Maneuvering 105-, 120-, and 155-mm Fin-Stabilized Projectiles Derived From Telemetry Experiments". In: *AIAA Atmospheric Flight Mechanics Conference*. Portland, Oregon, 2011. doi: [10.2514/6.2011-6268](https://doi.org/10.2514/6.2011-6268).
- [81] F. Fresconi et al. "Flight Behavior of an Asymmetric Body through Spark Range Experiments Using Roll Yaw Resonance for Yaw Enhancement". In: (2015). doi: [10.2514/6.2016-0782](https://doi.org/10.2514/6.2016-0782). URL: <https://apps.dtic.mil/dtic/tr/fulltext/u2/a623629.pdf>.
- [82] G.W. Frost and M.F. Costello. *Control Authority of a Projectile Equipped With an Internal Unbalanced Part*. ARL-CR-555, 2004.
- [83] A.C. Fung and G. Zimmermun. "Digital Simulation of Rotational Kinematics". In: *Goddard Space Flight Center Greenbelt* (1969).
- [84] E. Gagnon and A. Vachon. "Comparison of Computer Codes for Projectile Trajectory Simulation". In: *31st International Symposium on Ballistics*. Vol. 1. Hyderabad, India, 2019, pp. 591–605. doi: [10.12783/ballistics2019/33097](https://doi.org/10.12783/ballistics2019/33097).
- [85] A. Gerasimov. *Guidelines for Setting up Laminar-Turbulent Transition Cases in ANSYS CFD*. European Technology Group ANSYS UK - Ltd Version 2.0, 2014.
- [86] S.L. Gerhard. *Equations of Motion for Missiles with Six Degrees of Freedom*. Picatinny Arsenal, Dover, N.J.: Feltman research & Engineering Laboratories, 1960.
- [87] M. Ghoreyshi et al. "Indicial Methods for the Numerical Calculation of Dynamic Derivatives". In: *AIAA Journal* (2016). doi: [10.2514/1.J055444](https://doi.org/10.2514/1.J055444).
- [88] D.N Gkritzapis et al. "Modified Linear Theory for Spinning or Non-Spinning Projectiles". In: *The Open Mechanics Journal 2* (2008), pp. 6–11. doi: [10.2174/1874158400802010006](https://doi.org/10.2174/1874158400802010006).
- [89] P. Gnemmi et al. "Flowfield Around Spike-Tipped Bodies for High Attack Angles at Mach 4.5". In: *Journal of Spacecraft and Rockets* 40.5 (2003), pp. 622–631. doi: [10.2514/2.6910](https://doi.org/10.2514/2.6910).
- [90] C. Gorié et al. "Epistemic uncertainty quantification for Reynolds-averaged Navier-Stokes modeling of separated flows over streamlined surfaces." In: *Physics of Fluids* 31.3 (2019). doi: [10.1063/1.5086341](https://doi.org/10.1063/1.5086341).
- [91] C. Guo and Y. Ren. "The computation of the pitch damping stability derivatives of supersonic blunt cones using unsteady sensitivity equations." In: *Advances in Aerodynamics* 1.17 (2019). doi: [10.1186/s42774-019-0018-3](https://doi.org/10.1186/s42774-019-0018-3).

- [92] D. Guo. "Time-Accurate Simulation of Longitudinal Flight Mechanics with Control by CFD/RBD Coupling". In: *Applied Mechanics and Materials* 226-228 (2012), pp. 788–792. doi: [10.4028/www.scientific.net/AMM.226-228.788](https://doi.org/10.4028/www.scientific.net/AMM.226-228.788).
- [93] M. Hainz L.C. Costello. "Modified Projectile Linear Theory for Rapid Trajectory Prediction". In: *Journal of Guidance, Control and Dynamics* 28 (2005), pp. 1006–1014. doi: [10.2514/1.8027](https://doi.org/10.2514/1.8027).
- [94] K. Heavey and J. Sahu. *Application of Computational Fluid Dynamics to a Monoplane Fixed-Wing Missile With Elliptic Cross Sections*. Aberdeen Proving Ground: ARL-TR-3549, 2005.
- [95] Ch. Hirsch. *Numerical Computation of Internal & External Flows*. 2nd ed. Vol. 1. UK: John Wiley and Sons, 2007. ISBN: 978-0-7506-6594-0.
- [96] A. Hirschberg. "Schlieren and Shadowgraph Techniques: Visualizing Phenomena in Transparent Media". In: *European Journal of Mechanics* 21.4 (2002). doi: [10.1016/S0997-7546\(02\)01191-3](https://doi.org/10.1016/S0997-7546(02)01191-3).
- [97] A.E. Hodapp and LaFarge R.A. "A Ballistic Similitude Design Criterion for Artillery Projectiles". In: *Journal of Guidance Control and Dynamics* 7.5 (1984), pp. 631–633. doi: [10.2514/3.19907](https://doi.org/10.2514/3.19907).
- [98] A.E. Jr. Hodapp. "Effect of Mass Asymmetry on Ballistic Match of Projectiles". In: *Journal of Spacecraft and Rocket* 13.12 (1976), pp. 757–760. doi: [10.2514/3.57137](https://doi.org/10.2514/3.57137).
- [99] M. Holden et al. "Experimental Studies in LENS I and X to Evaluate Real Gas Effects on Hypervelocity Vehicle Performance". In: *45th AIAA Aerospace Sciences Meeting and Exhibit*. Reno, Nevada, 2007. doi: [10.2514/6.2007-204](https://doi.org/10.2514/6.2007-204).
- [100] *ISO 2533 Standard Atmosphere - First Edition (1975) + Addendum 2 (1997)*. Geneva, Switzerland.
- [101] I.D. Jacobson. "Influence of Boundary Layer Transition on the Magnus Effect on a Spinning Body of Revolution". PhD thesis. University of Virginia, 1970.
- [102] S. Jankovic, J. Gallant, and E. Celens. "Dispersion of an artillery projectile due to its unbalance". In: *18th International Symposium Ballistics*. San Antonio, 1999, pp. 128–141.
- [103] L. Joseph, A. Borgoltz, and W. Devenport. "Infrared thermography for detection of laminar-turbulent transition in lowspeed wind tunnel testing". In: *Experiments in Fluids* (2016). doi: [10.1007/s00348-016-2162-4](https://doi.org/10.1007/s00348-016-2162-4).

- [104] D.S. Joshi et al. *Magnus Effect on spinning Bodies of revolution*. University of Virginia, 1979.
- [105] M. Kato and B. Launder. "The modeling of turbulent flows around stationary and vibrating square cylinders". In: *9th Symposium on Turbulent Shear Flows*. 1993.
- [106] L.D. Kayser and F. Whiton. *Surface Pressure Measurements on a Boattailed Projectile Shape at Transonic Speeds*. Aberdeen Proving Ground, Maryland: ARBRL- MR-03161 - AD A1 13520, 1982.
- [107] J. Kelley and E. McShane. *On the Motion of a Projectile with Small or Slowly Changing Yaw*. 1944.
- [108] R. Kent. *An Elementary Treatment of the Motion of a Spinning Projectile About its center of Gravity*. Aberdeen Proving Ground: BRL, 1937.
- [109] M. Kiani. "Local geoid height approximation and interpolation using moving least squares approach". In: *Geodesy and Geodynamic* 11.2 (2020), pp. 120–126. DOI: [10.1016/j.geog.2019.12.003](https://doi.org/10.1016/j.geog.2019.12.003).
- [110] A. Ko et al. "Prediction and Analysis of the Aerodynamic Characteristics of a Spinning Projectile Based on Computational Fluid Dynamics". In: *International Journal of Aerospace Engineering* 2020 (2020). DOI: [10.1155/2020/6043721](https://doi.org/10.1155/2020/6043721).
- [111] J. Kokes, M. Costello, and J. Sahu. "Generating an aerodynamic model for projectile flight simulation using unsteady time accurate computational fluid dynamic results". In: *WIT Transactions on Modelling and Simulation* (2007). DOI: [10.2495/CBAL070041](https://doi.org/10.2495/CBAL070041).
- [112] D.G. Kovacs et al. "An Experimental Approach to Determine the Aerodynamic Pitch Damping Coefficient of Slender Bodies in the Transonic Regime". In: *AIAA Aviation 2020 Forum (Virtual Event)*. 2020. DOI: [10.2514/6.2020-3105](https://doi.org/10.2514/6.2020-3105).
- [113] P.K. Kundu, I.M. Cohen, and D.R. Dowling. *Fluid Mechanics (Fifth Edition)*. Ed. by Academic Press. 2012. ISBN: 9780123821003. DOI: [10.1016/B978-0-12-382100-3.10001-0](https://doi.org/10.1016/B978-0-12-382100-3.10001-0).
- [114] K. Kurbatskii and F. Montanari. "Application of Pressure-Based Coupled Solver to the Problem of Hypersonic Missiles with Aerospikes". In: *45th AIAA Aerospace Sciences Meeting and Exhibit*. Reno, Nevada, 2007. DOI: [10.2514/6.2007-462](https://doi.org/10.2514/6.2007-462).

- [115] R.B. Langtry. "A Correlation-based Transition Model Using Local Variables for Unstructured Parallelized CFD Codes". PhD thesis. Germany: University of Stuttgart, 2006. DOI: [10.18419/opus-1705](https://doi.org/10.18419/opus-1705).
- [116] W. Lanz, W. Odermatt, and G. Weihrauch. "Kinetic Energy Projectiles: Development History, State of the art, Trends". In: *19th International Symposium of Ballistics* Interlaken, Switzerland (2001). DOI: [10.1051/20100642017](https://doi.org/10.1051/20100642017).
- [117] B. E. Launder and D. B. Spalding. *Lectures in Mathematical Models of Turbulence*. Academic Press, 1972. ISBN: 0124380506.
- [118] S. Lee, Y. Choi, and H. Chung. "Forced Oscillation Wind Tunnel Tests for Dynamic Characteristics of Aircraft". In: *AIAA Aviation Forum*. Dallas, TX, 2019. DOI: [10.2514/6.2019-3605](https://doi.org/10.2514/6.2019-3605).
- [119] F. Lesage. *Navier-Stokes Prediction of Pitch Damping Coefficients for Projectiles*. Centre de Recherche pour la Défense Valcartier, 1997.
- [120] R.F. Lieske and R.L. McCoy. *Equations of motion of a rigid projectile*. Aberdeen Proving Ground, MD: BRL report 1244, 1964.
- [121] R.F. Lieske and M.L. Reiter. *Equations of motion for a modified point mass trajectory*. Aberdeen Proving Ground, MD: BRL report 1314, 1966.
- [122] Y. Lin, J. Wang, and M. Savill. "Embedded large eddy simulation of transitional flow over NACA0012 aerofoil". In: *Journal of Aerospace Engineering* 235.2 (2021), pp. 189–204. DOI: [10.1177/0954410020939797](https://doi.org/10.1177/0954410020939797).
- [123] A.M. Lipanov, S.A. Korolev, and I.G. Rusyak. "Optimization of aerodynamic form of projectile for solving the problem of shooting range increasing". In: *AIP Conference Proceedings*. 2017. DOI: [10.1063/1.5007543](https://doi.org/10.1063/1.5007543).
- [124] B. Litz. *Modern Advancements in Long Range Shooting*. Vol. 2. USA: Applied Ballistics Laboratory, 2014. Chap. 10.
- [125] V.V. Lunev. *Real Gas Flows with High Velocities*. CRC Press, 2009. Chap. 1 - Gas dynamic model and equations of gas flows. ISBN: 9781138116146.
- [126] G. S. Makeich and I. A. Kryukov. "Aerodynamics and Flight Dynamics Simulation of Basic Finner Supersonic Flight in Aeroballistic Experiment". In: *Journal of Physics: Conference Series* (2018). DOI: [10.1088/1742-6596/1009/1/012009](https://doi.org/10.1088/1742-6596/1009/1/012009).
- [127] F.W. Mann. *The Bullet's Flight from Powder to Target*. New York: Munn and Company, 1909.
- [128] B.G. Marinus. "Multidisciplinary Optimization of Aircraft Propeller Blades". PhD thesis. Royal Military Academy, 2011.

- [129] B.G. Marinus. *CO016 : Numerical Modeling*. Royal Military Academy - Provisional Course Notes, 2013.
- [130] B.G. Marinus and W. Bosschaerts. *ES312a : Fluid Dynamics*. Royal Military Academy, 2018.
- [131] A.B. Markov. *A Nonlinear Six Degree of Freedom Ballistic Aerial Target Simulation Model*. Alberta, Canada: Defence Research Establishment Suffield : AD-A144 052, 1984.
- [132] D.W. Martin. *Runge-Kutta Methods for Integrating Differential Equations on High Speed Digital Computers*. 1958.
- [133] J.C. Martin. "On Magnus Effects Caused by Boundary Layer Displacement Thickness on Bodies of Revolution at Small Angles of Attack". In: *Journal of the Aeronautical Sciences* 24.6 (1957), pp. 421–429. doi: [10.2514/8.3872](https://doi.org/10.2514/8.3872).
- [134] B. Martinez et al. "Stereovision Based Determination of Aerodynamic Coefficients for a Wind Tunnel Model in Free Rotational Motion". In: *Aerodynamic Measurement Technology and Ground Testing Conference*. 2019. doi: [10.2514/6.2018-3804](https://doi.org/10.2514/6.2018-3804).
- [135] R.L. McCoy. *Aerodynamic and Flight Dynamic Characteristics of the New Family of 5.56 mm NATO Ammunition*. Aberdeen Proving Ground, MD: BRL-MR-3467 - AD-A162 133, 1985.
- [136] R.L. McCoy. "McDrag" - *A computer Program for Estimating the Drag Coefficients of projectiles*. Aberdeen Proving Ground, MD: ARBRL TR-02293, 1981.
- [137] R.L. McCoy. *Modern Exterior Ballistics: The Launch and Flight Dynamics of Symmetric Projectiles*. Schiffer Publishing Ltd. : Atglen, PA, 1999.
- [138] M. Meldi, D. Lucor, and P. Sagaut. "Quantification of the effects of uncertainties in turbulent flows through generalized Polynomial Chaos." In: *Journal of Physics Conference Series* 318.4 (2011). doi: [10.1088/1742-6596/318/4/042055](https://doi.org/10.1088/1742-6596/318/4/042055).
- [139] F.R. Menter. "Two-Equation Eddy-Viscosity Turbulence Models for Engineering Applications". In: *AIAA Journal* 32.8 (1994), pp. 1598–1605. doi: [10.2514/3.12149](https://doi.org/10.2514/3.12149).
- [140] F.R. Menter et al. "A Correlation-Based Transition Model Using Local variables - Part I: Model Formulation". In: *Journal of Turbomachinery* (2006). doi: [10.1115/1.2184352](https://doi.org/10.1115/1.2184352).
- [141] B. Mi, H. Zhan, and B. Chen. "New Systematic CFD Methods to Calculate Static and Single Dynamic Stability Derivatives of Aircraft". In: *Hindawi*:

- Mathematical Problems in Engineering* 2017 (2017). DOI: [10.1155/2017/4217217](https://doi.org/10.1155/2017/4217217).
- [142] A. Mielke, C. Klatt, and C. Mundt. "Magnus effect for Finned Bodies in Supersonic Flows". In: *AIAA Aviation Forum*. Dallas, TX, 2019. DOI: [10.2514/6.2019-3164](https://doi.org/10.2514/6.2019-3164).
- [143] D. Miller. *A New Rule for Estimating Rifling Twist: An Aid to Choosing Bullets and Rifles*. Precision Shooting, 2005, pp. 43–48.
- [144] M.C. Miller. "Flight instabilities of Spinning Projectiles Having Non- Rigid Payloads". In: *Journal of Guidance, Control, and Dynamics* 5.2 (1982), pp. 150–157. DOI: [10.2514/3.56152](https://doi.org/10.2514/3.56152).
- [145] M.C. Miller. "Surface Pressure Measurements on a transonic spinning projectile". In: *Journal of Spacecraft and Rockets* 22 (1985), pp. 112–118. DOI: [10.2514/3.25718](https://doi.org/10.2514/3.25718).
- [146] T. Mizukaki. "Background-Oriented Schlieren for Large-Scale and High-Speed Aerodynamic Phenomena". In: *53rd AIAA Aerospace Sciences Meeting*. Florida, 2015. DOI: [10.2514/6.2015-1692](https://doi.org/10.2514/6.2015-1692).
- [147] C. Montalvo and M. Costello. "Estimation of Projectile Aerodynamic Coefficients Using Coupled CFD/RBD Simulation Results". In: *AIAA Atmospheric Flight Mechanics Conference* (2010). DOI: [10.2514/6.2010-8249](https://doi.org/10.2514/6.2010-8249).
- [148] F.G. Moore. *Approximate Methods for Weapon Aerodynamics*. Progress in Astronautics and Aeronautics. Vol. 186. 2000. ISBN: 1-56347-399-2.
- [149] F.G. Moore and T.C. Hymer. *The 2002 Version of the Aeroprediction Code: Part 1 - Summary of new Theoretical Methodology*. Dahlgren Division Naval Surface Warfare Center-Virginia: NSWCDD/TR-01/108, 2002.
- [150] F.G. Moore and T.C. Hymer. "2002 Version of the Aeroprediction Code (AP02)". In: *Journal of Spacecraft and Rockets* 41 (2004). DOI: [10.2514/1.9196](https://doi.org/10.2514/1.9196).
- [151] F.G. Moore and T.C. Hymer. "2005 Version of the Aeroprediction Code (AP05)". In: *Journal of Spacecraft and Rockets* 42 (2005). DOI: [10.2514/1.7970](https://doi.org/10.2514/1.7970).
- [152] F.G. Moore and L.Y. Moore. *2009 Version of the Aeroprediction Code: The AP09*. 2008.
- [153] A. Moumen et al. "Visualization of Muzzle Flow and Projectile in Flight Flow Using the Background Oriented Schlieren Technique". In: *31th International Symposium in Ballistics*. Hyderabad, India, 1989. DOI: [10.12783/ballistics2019/33107](https://doi.org/10.12783/ballistics2019/33107).

- [154] A. Moumen et al. "Visualization and analysis of muzzle flow fields using the Background-Oriented Schlieren technique". In: *Journal of Visualization* (2020). DOI: [10.1007/s12650-020-00639-w](https://doi.org/10.1007/s12650-020-00639-w).
- [155] L. Muller et al. "Wind tunnel measurements of the dynamic stability derivatives of a fin-stabilized projectile by means of a three-axis freely-rotating test bench". In: *AIAA Aviation 2020 Forum (Virtual Event)*. 2020. DOI: [10.2514/6.2020-2782](https://doi.org/10.2514/6.2020-2782).
- [156] Ch. Murphy. *Stability Criteria of the Kelley-McShane Linearized Theory of Yawing Motion*. Aberdeen Proving Ground, MD: BRL report-853, 1953.
- [157] Ch. Murphy. *The measurement of Non-Linear Forces And Moments By Means of Free Flight Tests*. Aberdeen Proving Ground, MD: BRL Report-974, 1956.
- [158] Ch. Murphy. *Free Flight Motion of Symmetric Missiles*. Aberdeen Proving Ground, MD: BRL Report-1216, 1963. DOI: [10.21236/ad0442757](https://doi.org/10.21236/ad0442757).
- [159] Ch. Murphy. "Yaw Induction by Mass Asymmetry". In: *Journal of Spacecraft and Rockets* 14.8 (1977), pp. 511–512. DOI: [10.2514/3.57231](https://doi.org/10.2514/3.57231).
- [160] Ch. Murphy. "Influence of Moving Internal Parts on Angular Motion of Spinning Projectiles". In: *Journal of Guidance and Control* 1.2 (1978), pp. 117–122. DOI: [10.2514/3.55753](https://doi.org/10.2514/3.55753).
- [161] Ch. Murphy. "Angular motion of a spinning projectile with a viscous liquid payload". In: *Journal of Guidance, Control and Dynamics* 6 (1983), pp. 280–286. DOI: [10.2514/3.19830](https://doi.org/10.2514/3.19830).
- [162] B. Narizzano. *HTRAJ V 1.00 Six Degree of Freedom Trajectory Simulation User's Guide*. Army ARDEC, 2011.
- [163] J.D. Nicolaidis. *On the Free Flight Motion of Missiles have Slight Configurational Asymmetries*. BRL-858. Aberdeen Proving Ground, Maryland, 1953.
- [164] C. Nietubicz, W. Sturek, and K. Heavey. "Computations of Projectile Magnus Effect at Transonic Velocities". In: *AIAA Journal* 23 (1985), pp. 998–1004. DOI: [10.2514/3.9030](https://doi.org/10.2514/3.9030).
- [165] C.J. Nietubicz and K. Opalka. *Supersonic Wind Tunnel Measurements of Static and Magnus Aerodynamic Coefficients for Projectile Shapes with Tangent and Secant Ogive Noses*. Aberdeen Proving Ground, Maryland: ARBRL-MR-02991, 1980.
- [166] C.J. Nietubicz, W.B. Sturek, and K.R. Heavey. *Computations of Projectile Magnus Effect at Transonic Velocities*. Aberdeen Proving Ground, Maryland: BRL-TR-02515, 1983.

- [167] T. A. Nygaard and R. L. Meakin. "Aerodynamic Analysis of a Spinning Missile with Dithering Canards". In: *Journal of Spacecraft and Rockets* 41.5 (2004), pp. 726–734. doi: [10.2514/1.13075](https://doi.org/10.2514/1.13075).
- [168] E. Oktay and H. Akay. "CFD predictions of dynamic derivatives for missiles". In: *40th AIAA Aerospace Sciences Meeting & Exhibit*. 2002. doi: [10.2514/6.2002-276](https://doi.org/10.2514/6.2002-276).
- [169] ONERA. "Le code de prévision aérodynamique de l'ONERA : "MISSILE"." In: *Symposium on Missile Aerodynamics*. Sorrento, Italy, 1998.
- [170] International Civil Aviation Organization. *Standard Atmosphere - Tables and Data for Altitudes to 65800 Feet*. Langley Aeronautical Laboratory: NACA Report-1235, 1955.
- [171] F. Paglia et al. "Pitching aerodynamic damping in a free fall phase: Background theories and numerical analyses". In: *7th European Conference for Aeronautics and Space Sciences (EUCASS)*. 2017. doi: [10.13009/EUCASS2017-550](https://doi.org/10.13009/EUCASS2017-550).
- [172] S.H Park, Y. Kim, and J.H. Kwon. "Prediction of Damping Coefficients Using the Unsteady Euler Equations". In: *Journal of Spacecraft and Rockets* 40.3 (2003), pp. 356–362. doi: [10.2514/2.3970](https://doi.org/10.2514/2.3970).
- [173] S.H. Park and J.H. Kwon. "Navier-Stokes Computations of Stability Derivatives for Symmetric Projectiles". In: *AIAA Aerospace Sciences*. Reno, Nevada, 2004. doi: [10.2514/6.2004-14](https://doi.org/10.2514/6.2004-14).
- [174] S.H. Park and J.H. Kwon. "Navier–Stokes Computation of Pitch–Damping Coefficients Using Steady Coning Motions". In: *Journal of Spacecraft and Rockets* 41.5 (2004), pp. 754–761. doi: [10.2514/1.2024](https://doi.org/10.2514/1.2024).
- [175] M. Pechier, P. Guillen, and R. Cayzac. "Magnus Effect over Finned Projectiles". In: *AIAA J. of Spacecraft and Rockets* 38.4 (1998), pp. 542–549. doi: [10.2514/2.3714](https://doi.org/10.2514/2.3714).
- [176] R.A. Pennekamp. *A large-caliber Yaw Inducer*. Aberdeen Proving Ground: BRL TR-3794, 1989.
- [177] H.Z. Peter. *Advanced Six Degrees of Freedom Aerospace Simulation and Analysis in C++, Second Edition*. American Institute of Aeronautics and Astronautics, Inc., 2014. ISBN: 978-1-62410-252-3. doi: [10.2514/4.102523](https://doi.org/10.2514/4.102523).
- [178] P. Plostins, J.A. Bornstein, and Ch.O. White. *The Transitional Ballistics, Aeroballistics and Jump Characteristics of a 25-mm-AP Training Projectile with base-bleed*. Aberdeen Proving Ground, Maryland: ARBRL- TR-2888, 1988.

- [179] P. Plostins, R.L. McCoy, and B.A. Wagoner. *Aeroballistic Performance of the 25-mm Range Limited Training Projectile*. Aberdeen Proving Ground, Maryland: ARBRL- MR-3886, 1991.
- [180] C. Qingshan and M. Ju. "The multi-level Monte Carlo method for simulations of turbulent flows". In: *Monthly Weather Review* (2019). DOI: [10.1175/MWR-D-18-0053.1](https://doi.org/10.1175/MWR-D-18-0053.1).
- [181] C.A. Rabbath and D. Corriveau. "A comparison of piecewise cubic Hermite interpolating polynomials, cubic splines and piecewise linear functions for the approximation of projectile aerodynamics". In: *Defence Technology* 15 (2017), pp. 741–757. DOI: [10.1016/j.dt.2019.07.016](https://doi.org/10.1016/j.dt.2019.07.016).
- [182] M. Raffel. "Background-Oriented Schlieren (BOS) techniques". In: *Experiments in Fluids* 56 (2015), p. 60.
- [183] D.A. Randall. *The Navier-Stokes Equation*. Department of Atmospheric Science Colorado State University, Fort Collins, Colorado 80523, 2007.
- [184] R.P. Reklis and W. Sturek. *Surface Pressure Measurements on Slender Bodies at angle of attack in Supersonic Flow*. Aberdeen Proving Ground: ARBRL-MR-02876, 1978.
- [185] C. Robbe. "Experimental Evaluation of the Thoracic Impact of Non-Lethal Projectiles". PhD thesis. Royal Military Academy - Université Liège, 2013.
- [186] B. Robins. *New Principles in Gunnery*. London, 1742.
- [187] J. Rogers and M.F. Costello. "Flight Dynamics and Control Authority of a Projectile Equipped with a Controllable Internal Translating Mass". In: *AIAA Atmospheric Flight Mechanics Conference and Exhibit*. South Carolina, 2007. DOI: [10.2514/6.2007-6492](https://doi.org/10.2514/6.2007-6492).
- [188] J. Rogers and M.F. Costello. "A Variable Stability Projectile Using an Internal Moving Mass". In: *AIAA Atmospheric Flight Mechanics Conference and Exhibit*. Atlanta, Georgia, 2008. DOI: [10.2514/6.2008-7116](https://doi.org/10.2514/6.2008-7116).
- [189] W.K. Rogers. *The Transonic Free Flight Range*. Aberdeen Proving Ground, Maryland: BRL Report-1044, 1958.
- [190] L.R. Rollstin and A.E. Jr. Hodapp. "Experimental Evaluation of Artillery Projectile Impact Errors Induces by Principal-Axis Misalignment". In: *Journal of Spacecraft and Rockets* 16.5 (1979), pp. 316–318. DOI: [10.2514/3.57664](https://doi.org/10.2514/3.57664).
- [191] C. Rosema, J. Doyle, and Blake W. Auman L. M and. *Missile Datcom, User's Manual 2011 Revision*. Report Nr AFRL-RB-WP-TR-2011-3071: Wright-Patterson Air Force Base - US Air Force Research Laboratory, 2011.

- [192] D.H. Rudy and J.C. Strikwerda. "Boundary Conditions for Subsonic Compressible Navier-Stokes Calculations". In: *Computers and Fluids* 9 (1981), pp. 327–338. doi: [10.1016/0045-7930\(81\)90005-0](https://doi.org/10.1016/0045-7930(81)90005-0).
- [193] S.M. Sabot, G.L. Winchenbach, and G.T. Chapman. "Comparison of various drag coefficient expansions using polynomials and splines". In: *Journal of spacecraft* 23 (1986), pp. 259–263. doi: [10.2514/3.25107](https://doi.org/10.2514/3.25107).
- [194] N.V. Sahinidis. "Optimization under uncertainty: state-of-the-art and opportunities." In: *Computers & Chemical Engineering* 28 (2011), pp. 971–983. doi: [10.1016/j.compchemeng.2003.09.017](https://doi.org/10.1016/j.compchemeng.2003.09.017).
- [195] J. Sahu. "Numerical Computations of Transonic Critical Aerodynamic Behavior". In: *AIAA Journal* 28 (1990), pp. 807–816. doi: [10.2514/3.25123](https://doi.org/10.2514/3.25123).
- [196] J. Sahu. *Transonic Navier-Stokes Computations for a spinning body of revolution*. BRL-TR 3265, 1991.
- [197] J. Sahu. "Advanced Time-accurate CFD/RBD Simulations of projectiles in free flight". In: *DODUGC* 1 (2005), pp. 86–91. doi: [10.1109/DODUGC.2005.7](https://doi.org/10.1109/DODUGC.2005.7).
- [198] J. Sahu. "Unsteady Free flight Aerodynamics of a Spinning Projectile at A High Transonic Speed". In: *AIAA AFM Meeting*. Honolulu, HI, 2008. doi: [10.2514/6.2008-7115](https://doi.org/10.2514/6.2008-7115).
- [199] J. Sahu. "Computations of unsteady aerodynamics of a spinning body at Transonic Speeds". In: *27th AIAA Applied Aerodynamics Conference*. 2009. doi: [6.2009-3852](https://doi.org/6.2009-3852).
- [200] J. Sahu. "Virtual Fly-Out Simulations of a spinning Projectile from Subsonic to Supersonic Speeds". In: *29th AIAA Atmospheric Flight Mechanics Conference*. Honolulu, Hawaii, 2011. doi: [10.2514/6.2011-3026](https://doi.org/10.2514/6.2011-3026).
- [201] J. Sahu. *Time-Accurate Numerical Prediction of Free Flight Aerodynamics of a Finned Projectile*. Aberdeen Proving Ground: ARL-TR-3603.
- [202] J. Sahu, M. Costello, and C. Montalvo. "Development and Application of Multidisciplinary Coupled Computational Techniques for Projectile Aerodynamics". In: *7th International Conference on Computational Fluid Dynamics*. Hawaii, 2012. doi: [ICCFD7-4504](https://doi.org/ICCFD7-4504).
- [203] J. Sahu and F. Fresconi. "Flight Behaviors of a Complex Projectile using a Coupled CFD-based Simulation Technique: Free Motion". In: *33rd AIAA Applied Aerodynamics Conference, Aviation Forum*. Dallas, TX, 2015. doi: [10.2514/6.2015-2585](https://doi.org/10.2514/6.2015-2585).

- [204] J. Sahu and F. Fresconi. "Fast Generation of Aerodynamics Data for a Canard-Controlled Body with Thrust-Vector Control". In: *AIAA Aviation Forum*. Dallas, TX, 2019. doi: [10.2514/6.2019-3163](https://doi.org/10.2514/6.2019-3163).
- [205] J. Sahu, F. Fresconi, and K. Heavey. "Unsteady Aerodynamics of a Finned Projectile at a Supersonic Speed with Jet Interaction". In: *AIAA Aviation 2014 Forum*. Atlanta, GA, 2014. doi: [10.2514/6.2014-3024](https://doi.org/10.2514/6.2014-3024).
- [206] J. Sahu and K.R. Heavey. *Parallel Numerical Computations of Projectile Flow Fields*. Aberdeen Proving Ground: ARL-TR-2019, 1999.
- [207] J. Sahu et al. "Recent Applications of Structured and Unstructured Grid Techniques to Complex Projectile and Missile Configurations". In: *Eight International Grid Generation and Computational Field Simulations*. Honolulu, HI, 2002.
- [208] Jubaraj Sahu. "Numerical Computations of Dynamic Derivatives of a Finned Projectile Using A Time-Accurate CFD Method". In: *AIAA Atmospheric Flight Mechanics Conference and Exhibit*. Hilton Head, South Carolina: American Institute of Aeronautics and Astronautics, 2007. doi: [10.2514/6.2007-6581](https://doi.org/10.2514/6.2007-6581).
- [209] Jubaraj Sahu, Karen R Heavey, and Aerospace Engineer. "Time-Accurate Computations for Rapid generation of missile aerodynamics". In: *AIAA Atmospheric Flight Mechanics Conference August (2010)*, pp. 1-22. doi: [10.2514/6.2010-8248](https://doi.org/10.2514/6.2010-8248).
- [210] T. Sailaranta and A. Siltavuori. *AeroFi – TECHNICAL REPORT T-285, rev. 5.2*. 2010.
- [211] J. Serpieri. "Cross-Flow Instability: Flow diagnostics and control of swept wing boundary layers". PhD thesis. TU Delft Aerodynamics (ORCID 0000-0003-4173-2681), 2018. doi: [10.4233/uuid:3dac1e78-fcc3-437f-9579-048b74439f55](https://doi.org/10.4233/uuid:3dac1e78-fcc3-437f-9579-048b74439f55).
- [212] J.J.S. Shang. "Landmarks and new frontiers of computational fluid dynamics". In: *Advanced Aerodynamics 1.5* (2019). doi: [10.1186/s42774-019-0003-x](https://doi.org/10.1186/s42774-019-0003-x).
- [213] M.A. Shilo. *Six Degree of Freedom Flight Dynamic Model of a MK-82 Store*. Melbourne, Australia: Department of Defence, Technical Note AD-A277 065, 1994.
- [214] J. Siewert and B. Whyte. *Spinner 2004 : A New version*. Arrow Tech presentation.

- [215] S. Silton and P. Weinacht. "Effect of rifling grooves on the performance of small-caliber ammunition". In: *26th Army Science Conference*. 2008.
- [216] S.I. Silton. "Navier-Stokes Computations for a Spinning Projectile From Subsonic to Supersonic Speeds". In: *Journal of Spacecraft and Rockets* 42.2 (2002), pp. 223–231. doi: [10.2514/1.4175](https://doi.org/10.2514/1.4175).
- [217] S.I. Silton and B.E. Howell. *Aerodynamic and Flight Dynamic Characteristics of 5.56-mm Ammunition: M855*. Aberdeen Proving Ground, MD: ARL-TR-5182, 2010. doi: [10.21236/ada530895](https://doi.org/10.21236/ada530895).
- [218] S.I. Silton and B.E. Howell. "Predicting the Dynamic Stability of Small-Caliber Ammunition". In: *25th International Symposium on Ballistics* (2011).
- [219] Sidra Silton. "Navier-Stokes Predictions of Aerodynamic Coefficients and Dynamic Derivatives of a 0.50-cal Projectile". In: *29th AIAA Applied Aerodynamics Conference*. Honolulu, Hawaii, 2011. doi: [10.2514/6.2011-3030](https://doi.org/10.2514/6.2011-3030).
- [220] Sidra I. Silton. "Quasi-Steady Simulations for the Efficient Generation of Static Aerodynamic Coefficients at Subsonic Velocities". In: *35th AIAA Applied Aerodynamics Conference*. Denver, Colorado, 2017. doi: [10.2514/6.2017-3398](https://doi.org/10.2514/6.2017-3398).
- [221] B. Simon et al. "Infrared thermography for dynamic detection of laminar-turbulent transition". In: *Experiments in Fluids* (2016). doi: [10.1007/s00348-014-2178-9](https://doi.org/10.1007/s00348-014-2178-9).
- [222] F. Simon et al. "Reynolds-Averaged Navier-Stokes/Large-Eddy Simulations of Supersonic Base Flow". In: *AIAA Journal* 44.11 (2006), pp. 2578–2590. doi: [10.2514/1.21366](https://doi.org/10.2514/1.21366).
- [223] F. Simon et al. "RANS/LES Simulations of Projectiles with and without Rotation in the Subsonic and Transonic Regimes". In: *23rd International Symposium on Ballistics*. Tarragona, Spain, 2007.
- [224] F. Simon et al. "Zonal-Detached-Eddy Simulation of Projectiles in the Subsonic and Transonic Regimes". In: *AIAA JOURNAL* 45 (2007), pp. 1606–1619. doi: [10.2514/1.26827](https://doi.org/10.2514/1.26827).
- [225] F. Simon et al. "Numerical simulation of magnus force control for projectiles configurations". In: *Computers Fluids* (2008), pp. 965–968. doi: [10.1016/j.compfluid.2008.09.006](https://doi.org/10.1016/j.compfluid.2008.09.006).
- [226] G. Soave. "Equilibrium constants from a modified Redlich-Kwong equation of state." In: *Chemical Engineering Science* 27.6 (1972), pp. 1197–1203. doi: [10.1016/0009-2509\(72\)80096-4](https://doi.org/10.1016/0009-2509(72)80096-4).

- [227] A. Sowa. *NATO shareable Software Developing true Suite Supporting National Operational, Fire Control Systems*. 2008.
- [228] J. F. Stalnaker and M. A. Robinson. *Computation of Stability Derivatives of Spinning Missiles Using Unstructured Cartesian Meshes*. AIAA-2002-2802, American Institute of Aeronautics and Astronautics, 2002. doi: [10.2514/6.2002-2802](https://doi.org/10.2514/6.2002-2802).
- [229] STANAG-4172. *5.56 Ammunition (Linked or otherwise) - Edition 2*. 1993.
- [230] STANAG-4500. *Procedures to Determine Field Artillery Muzzle Velocity Management, Interchangeability and Prediction - Edition 1*. 1998.
- [231] STANAG-4537. "NATO Armaments Ballistic Kernel (NABK)". In: (2015).
- [232] STANREC-4618. *The 6/7 degrees of freedom guided projectile trajectory model - Edition 1*. 2016.
- [233] W. Sturek. *Boundary-Layer Studies On Spinning Bodies Of Revolution*. Aberdeen Proving Ground: BRL report AD-785 688, 1973.
- [234] W. Sturek and L.B. Schiff. *Computation of the Magnus Effect for slender bodies in supersonic flow*. Aberdeen Proving Ground: ARBRL-TR-02384, 1981.
- [235] W.B. Sturek and L.B. Schiff. "Computations of the Magnus Effect for Slender Bodies in Supersonic Flow". In: *AIAA Journal* 12 (1982), pp. 1724–1731.
- [236] W.B. Sturek et al. "Applications of computational fluid dynamics to the aerodynamics of army projectiles". en. In: *Journal of Spacecraft and Rockets* 31.2 (1994), pp. 186–199. doi: [10.2514/3.26422](https://doi.org/10.2514/3.26422).
- [237] W.M. Swanson. "The Magnus Effect: A Summary of Investigations to Date". In: *Journal of Basic Engineering* (1961), p. 461. doi: [10.1115/1.3659004](https://doi.org/10.1115/1.3659004).
- [238] C.H. Tai, Y.L. Tian, and J.L. Liou. "High-resolution upwind viscous flow solver on SOCBT configuration with turbulence models". en. In: *Finite Elements in Analysis and Design* 18.2 (1994), pp. 237–257. doi: [10.1016/0168-874X\(94\)90105-8](https://doi.org/10.1016/0168-874X(94)90105-8).
- [239] V.E. Terrapon. *AERO0004: Turbulent Flows – Lectures 1,10,11*. Université de Liège, 2018.
- [240] Z. Terze, A. Müller, and D. Zlatar. "Singularity-free time integration of rotational quaternions using non-redundant ordinary differential equations". In: *Multibody System Dynamics* 38 (2016), pp. 201–225. doi: [10.1007/s11044-016-9518-7](https://doi.org/10.1007/s11044-016-9518-7).
- [241] D.N. Thai et al. "Ballistics of Supercavitating Projectiles". In: *Advances in Military Technology* 13.2 (2018). doi: [10.3849/aimt.01243](https://doi.org/10.3849/aimt.01243).

- [242] S. Theodoulis and P. Wernert. "Flight Dynamics Control for Smart Munition: The ISL Contribution." In: 50.1 (2017), pp. 15512–15517. doi: [10.1016/j.ifacol.2017.08.2127](https://doi.org/10.1016/j.ifacol.2017.08.2127).
- [243] W. Thielicke and E.J. Stamhuis. "PIVlab – Towards User-friendly, Affordable and Accurate Digital Particle Image Velocimetry in MATLAB". In: *Journal of Open Research Software* 2 (2014).
- [244] S. Tuling. "Modelling of Dynamic Stability Derivatives Using CFD". In: *25th International Congress of the Aeronautical Sciences* (2006).
- [245] H.R. Vaughn. *A detailed development of the tricyclic theory*. Sandia Laboratories, 1968.
- [246] H.R. Vaughn and G.G. Wilson. "Effect of Yaw of Repose on Ballistic Match of Similar Projectiles". In: *AIAA Journal* 9 (1971), pp. 1208–1210. doi: [10.2514/3.6344](https://doi.org/10.2514/3.6344).
- [247] H.K. Versteeg and W. Malalasekera. *An introduction to Computational Fluid Dynamics: The Finite Volume Method*. Pearson Education Limited, 1995. Chap. 2-3. ISBN: 0-582-21884-5.
- [248] E. Villeneuve. *Mesures expérimentales de l'impact des revêtements hydrophobes et surperhydrophobes sur la traînée et la portance d'un profil aérodynamique propre et glacé*. Université du Québec, 2011.
- [249] N.A. Vinnichenko, A.V. Uvarov, and Y.Y. Plaksina. "Accuracy of Background Oriented Schlieren for Different Background Patterns and Means of Refraction Index Reconstruction". In: *15th International Symposium on Flow Visualization*. Minsk, Belarus, 2012.
- [250] K.E. Von Krueger. "An evaluation of Yuma Proving Grounds ballistic arsenal scoring methods". MA thesis. Naval Postgraduate School - Monterey, California., 2005.
- [251] D. Walters and D. Cokljat. "A three-equation eddy-viscosity model for Reynolds-averaged Navier-Stokes simulations of transitional flows". In: *Journal of Fluids Engineering* 130.12 (2008), pp. 121–401. doi: [10.1115/1.2979230](https://doi.org/10.1115/1.2979230).
- [252] R.K. Walters. *Numerical Integration Methods for Ballistic Rocket Trajectory simulation programs*. Atmospheric Sciences Laboratory White Sands Missile Range, New Mexico, AD658064, 1967.
- [253] Y.M. Wang et al. "Local Geoid Determination". In: *Encyclopedia of Geodesy*, Springer International Publishing (2016). doi: [10.1007:978-3-319-02370-0_53-1](https://doi.org/10.1007/978-3-319-02370-0_53-1).

- [254] J. Wauters. "Development and Application of Surrogate-Assisted Optimization under Uncertainty Strategies for Unmanned Aerial Vehicles". PhD thesis. Department of Electromechanical Systems and Metals Engineering (ESME) - Universiteit Gent, 2020.
- [255] D.J. Weber. "Simplified Method for Evaluating the Flight Stability of Liquid-Filled Projectiles". In: *Journal of Spacecraft and Rockets* 31.1 (1994), pp. 130–134. DOI: [10.2514/3.26412](https://doi.org/10.2514/3.26412).
- [256] P. Weinacht. "Navier–Stokes Predictions of the Individual Components of the Pitch-Damping Sum". In: *Journal of Spacecraft and Rockets* 35.5 (1998). DOI: [10.2514/2.3390](https://doi.org/10.2514/2.3390).
- [257] P. Weinacht. "Prediction of Pitch-Damping of Projectiles at Low Supersonic and Transonic Velocities". In: *Proceedings of the 36th Aerospace Sciences - AIAA-98-0395*. Reno, 1998. DOI: [10.2514/6.1998-395](https://doi.org/10.2514/6.1998-395).
- [258] P. Weinacht. "Projectile Performance, Stability, and Free-Flight Motion Prediction Using Computational Fluid Dynamics". In: *Journal of Spacecraft and Rockets* 41.2 (2004), pp. 257–263. DOI: [10.2514/1.1037](https://doi.org/10.2514/1.1037).
- [259] P. Weinacht. "Validation and Prediction of the Effect of Rifling Grooves on Small-Caliber Ammunition Performance". In: *AIAA Atmospheric Flight Mechanics Conference and Exhibit* (2006). DOI: [10.2514/6.2006-6010](https://doi.org/10.2514/6.2006-6010).
- [260] P. Weinacht. "Virtual wind tunnel Experiments for Small Caliber Ammunition Aerodynamic Characterization". In: *23rd International Symposium on Ballistics*. Terragona, Spain, 2007. DOI: [MD21005-5066](https://doi.org/MD21005-5066).
- [261] P. Weinacht, G.R. Cooper, and J.F. Newill. *Analytical Prediction of Trajectories for High-Velocity Direct-Fire Munitions*. Aberdeen Proving Ground, MD: ARL-TR-3567, 2005.
- [262] P. Weinacht, J.F. Newill, and Conroy P. *Conceptual design approach for small-caliber aeroballistics with application to 5.56-mm ammunition*. Aberdeen Proving Ground, MD: ARL-TR-3620, 2005.
- [263] P. Weinacht and W.B. Sturek. "Navier-Stokes Predictions of Pitch Damping of Finned Projectiles Using Steady Coning Motion". In: *Proceedings of the 8th AIAA Aerodynamics Conference - AIAA-90-3088*. Portland, OR, 1990. DOI: [10.2514/6.1990-3088](https://doi.org/10.2514/6.1990-3088).
- [264] P. Weinacht and W.B. Sturek. "Navier-Stokes predictions of static and dynamic aerodynamic derivatives for high L/D finned projectiles." In: *AGARD Conf. Proc., AGARD-CP-493, Paper 20*. 1990.

- [265] P. Weinacht and W.B. Sturek. "Computation of the roll characteristics of a finned projectile." In: *Journal of Spacecraft and Rockets* 33.5 (1996). doi: [10.2514/3.26836](https://doi.org/10.2514/3.26836).
- [266] P. Weinacht, W.B. Sturek, and L.B. Schiff. "Navier–Stokes Predictions of Pitch Damping for Axisymmetric Projectiles". In: *Journal of Spacecraft and Rockets* 34.6 (1997). doi: [10.2514/2.3306](https://doi.org/10.2514/2.3306).
- [267] J. M. Weiss and W. A. Smith. "Preconditioning applied to variable and constant density flows". In: *AIAA Journal* 33.11 (1995), pp. 2050–2057. doi: [10.2514/3.12946](https://doi.org/10.2514/3.12946).
- [268] P. Wernert, S. Theodoulis, and Morel Y. "Flight dynamics properties of 155 mm spin-stabilized projectiles analyzed in different body frames". In: *AIAA Atmospheric Flight Mechanics Conference and Exhibit*. Toronto, Canada, 2010. doi: [10.2514/6.2010-7640](https://doi.org/10.2514/6.2010-7640).
- [269] K.O. West. *Comparison of Free-flight Spark Range and Wind Tunnel Test Data for a Generic Missile Configuration at Mach Numbers From 0.6 to 2.5*. AFATL-TR-81-87; Air Force Armament Laboratory: Eglin Air Force Base, FL, 1981. doi: [10.2514/6.1982-1365](https://doi.org/10.2514/6.1982-1365).
- [270] P. Wey. *BALCO User's Guide, AOP-50 NATO technical shareable software - V1.0b, Edition 1*. 2015.
- [271] P. Wey et al. "Determination of Aerodynamic Coefficients from Shock Tunnel Free Flight Trajectories". In: *Aerodynamic Measurement Technology and Ground Testing Conference*. New Orleans, Louisiana, USA, 2012. doi: [10.2514/6.2012-3321](https://doi.org/10.2514/6.2012-3321).
- [272] P. Wey et al. "BALCO 6/7-DoF Trajectory Model". In: *29th International Symposium of Ballistics*. Edinburgh, Scotland, 2016.
- [273] R.H. White. *Aerodynamic coefficients of the M483A1 determined from sparkrange tests*. Ballistic Research Laboratory, Aberdeen Proving Ground, Maryland: BRL Report-CR-59, 1991.
- [274] D.C. Wilcox. *Turbulence Modeling for CFD*. DCW Industries, Inc. La Canada, California, 1998.
- [275] M. Wilder et al. "Free-Flight Measurements of Convective Heat Transfer in Hypersonic Ballistic-Range Environments". In: *39th AIAA Thermophysics Conference*. Miami, FL, 2007. doi: [10.2514/6.2007-4404](https://doi.org/10.2514/6.2007-4404).
- [276] H. Xiao and P. Cinnella. "Quantification of model uncertainty in RANS simulations: A review." In: *Progress in Aerospace Sciences* (2019). doi: [10.1016/j.paerosci.2018.10.001](https://doi.org/10.1016/j.paerosci.2018.10.001).

-
- [277] S. Yoon et al. "A Miniaturized Magnetic Induction Sensor Using Geomagnetism for Turn Count of Small-Caliber Ammunition". In: *Sensors* (2006), pp. 712–726. doi: [10.3390/s6070712](https://doi.org/10.3390/s6070712).
- [278] J. Zhang, J. Lei, and J. Niu. "Numerical investigation of aerodynamic characteristics of free-spinning tail projectile with canards roll control". In: *Aerospace Engineering* (2020). doi: [10.1177/0954410020953316](https://doi.org/10.1177/0954410020953316).
- [279] Z. Zhang, C. Meng, and Y. Wang. "Six-Dimensional Ballistics of a certain Howitzer Projectile Considered with Dynamic Unbalance". In: *31st International Symposium on Ballistics*. Vol. 1. Hyderabad, India, 2019, pp. 828–836. doi: [10.12783/ballistics2019/33121](https://doi.org/10.12783/ballistics2019/33121).